SÃO PAULO STATE UNIVERISTY
Graduate Program in Mechanical Engineering
Campus Bauru

JEAN PAULO CARNEIRO JUNIOR

STRATEGIES FOR ATTENUATION BAND ENHANCEMENT OF ONE-DIMENSIONAL FINITE PERIODIC STRUCTURES

Bauru
2025

SÃO PAULO STATE UNIVERISTY
Graduate Program in Mechanical Engineering
Campus Bauru

Jean Paulo Carneiro Junior

Strategies for attenuation band enhancement of one-dimensional finite periodic structures

Thesis presented to the Graduate Program in Mechanical Engineering as part of the requirements for obtaining the title of Doctor in Mechanical Engineering from the Faculty of Engineering, São Paulo State University (UNESP), Campus Bauru.

Concentration area: Modelling and Design of Mechanical Systems.

Prof. Dr. Paulo J. Paupitz Gonçalves
Supervisor

Prof. Dr. Michael John Brennan
Co-supervisor

Bauru
2025

C289s

Carneiro Junior, Jean Paulo
Strategies for attenuation band enhancement of one-dimensional finite periodic structures / Jean Paulo Carneiro Junior. -- Bauru, 2025
207 p. : il., tabs., fotos

Tese (doutorado) - Universidade Estadual Paulista (UNESP), Faculdade de Engenharia, Bauru
Orientador: Paulo José Paupitz Gonçalves
Coorientador: Michael John Brennan

1. Longitudinal vibration. 2. Flexural vibration. 3. Super attenuation band. 4. Vibration neutraliser/absorber. 5. Transfer matrix method. I. Título.

Sistema de geração automática de fichas catalográficas da Unesp. Dados fornecidos pelo autor(a).

UNIVERSIDADE ESTADUAL PAULISTA

Câmpus de Bauru

ATA DA DEFESA PÚBLICA DA TESE DE DOUTORADO DE JEAN PAULO CARNEIRO JUNIOR, DISCENTE DO PROGRAMA DE PÓS-GRADUAÇÃO EM ENGENHARIA MECÂNICA, DA FACULDADE DE ENGENHARIA - CÂMPUS DE BAURU.

Aos 30 dias do mês de julho do ano de 2025, às 8h, no(a) Via sistemas de videoconferência e outras ferramentas para comunicação a distância, realizou-se a defesa de TESE DE DOUTORADO de JEAN PAULO CARNEIRO JUNIOR, intitulada **STRATEGIES FOR ATTENUATION BANDS ENHANCEMENT OF ONE-DIMENSIONAL FINITE PERIODIC STRUCTURES** . A Comissão Examinadora foi constituída pelos seguintes membros: Prof. Dr. PAULO JOSÉ PAUPITZ GONÇALVES (Orientador(a) - Participação Presencial) do(a) Departamento de Engenharia Mecânica / Faculdade de Engenharia - UNESP, Prof. Dr. JOSÉ ROBERTO DE FRANÇA ARRUDA (Participação Virtual) do(a) Departamento de Mecanica Computacional / Universidade Estadual de Campinas - UNICAMP, Prof. Dr. THIAGO DE PAULA SALES (Participação Virtual) do(a) Divisão de Engenharia Mecânica / Instituto Tecnológico de Aeronáutica, Prof. Dr. FABIO MAZZARIOL SANTICIOLLI (Participação Presencial) do(a) Departamento de Engenharia Mecânica / Universidade Estadual Paulista, Profa. Dra. CAMILA GIANINI GONSALEZ BUENO (Participação Virtual) do(a) Departamento de Engenharia Mecânica / Faculdade de Engenharia de Ilha Solteira - UNESP. Após a exposição pelo doutorando e arguição pelos membros da Comissão Examinadora que participaram do ato, de forma presencial e/ou virtual, o discente recebeu o conceito final: Aprovado . Nada mais havendo, foi lavrada a presente ata, que após lida e aprovada, foi assinada pelo(a) Presidente(a) da Comissão Examinadora.

Prof. Dr. PAULO JOSÉ PAUPITZ GONÇALVES

gov.br Documento assinado digitalmente
PAULO JOSE PAUPITZ GONCALVES
Data: 04/08/2025 09:21:14-0300
Verifique em https://validar.iti.gov.br

PROPOSTA DE ALTERAÇÃO DO TÍTULO

A COMISSÃO EXAMINADORA PROPÕE A ALTERAÇÃO DO TÍTULO DO TRABALHO DO ALUNO **JEAN PAULO CARNEIRO JUNIOR** DE: **"STRATEGIES FOR ATTENUATION BANDS ENHANCEMENT OF ONE-DIMENSIONAL FINITE PERIODIC STRUCTURES"**

PARA:

STRATEGIES FOR ATTENUATION BAND ENHANCEMENT OF ONE-DIMENSIONAL FINITE PERIODIC STRUCTURES

30 de julho de 2025.

gov.br
Documento assinado digitalmente
PAULO JOSE PAUPITZ GONCALVES
Data: 04/08/2025 09:19:50-0300
Verifique em https://validar.iti.gov.br

Prof. Dr. Paulo José Paupitz Gonçalves
Orientador

ACKNOWLEDGEMENTS

The journey that culminated in this thesis was shaped by many people to whom I would like to express my sincere gratitude. First and foremost, I would like to express my deepest gratitude to my beloved wife, Thaina. Through moments of joy and challenges alike, and no matter where this journey has led me, she has been a constant source of support, patience, understanding, and unwavering companionship, and I am profoundly thankful for her presence by my side throughout all these years. This thesis is dedicated to her. I am also deeply grateful to my parents, Jean and Rosana, through whom I extend my thanks to my brother João and grandmothers, who have been pillars of my life.

I would like to thank Dr. Mike Brennan and Dr. Paulo Paupitz for their friendly and generous supervision – for teaching and exemplifying not just how to be a researcher, but how to be a *good* researcher. I am especially grateful to Dr. Vinicius Germano, who, alongside the professors, served as both mentor and friend (he taught me the essential criteria for achieving good experimental results). This thesis is fundamentally the product of this group teaching, guidance, and patience, and for that, I am profoundly thankful.

I would like to thank the friends I made along the way, from Dourados, Ilha Solteira, and Auckland, to Bauru. These friends became my second family with whom I shared moments of joy and sorrow, opportunities and doubts, motivation and perseverance. I would like to thank you very much, and I am certain that my glass will never be empty among them.

I would like to thank the people who opened the doors for my research wherever I went. I am especially thankful to Professor Rodrigo Borges and Douglas Bueno, who offered me valuable opportunities and mentorships. I also extend my heartfelt thanks to my supervisors in Auckland, Professors Vladislav Sorokin and Brian Mace, for their warm welcome, insightful teachings, and important discussions.

I gratefully acknowledge the Mechanical Engineering Department of the Faculty of Engineering of Ilha Solteira and Bauru for the provided infrastructure to develop this work. I gratefully acknowledge the financial supports of São Paulo Research Foundation (FAPESP) by grants 2019/19335-9, 2022/09543-6 and 2018/15894-0.

There is no subject so old that something new
cannot be said about it.
Fyodor Dostoevsky

ABSTRACT

Recently, a growing number of studies have employed periodicity to manipulate the wave propagation in structural systems. Owing to this unique property, periodic structures can function as mechanical filters within the so-called stop bands. In recent years, significant research efforts have been dedicated to optimising such systems, with a particular focus on broadening the stop bands and lowering their operational frequency range. However, despite these advances, knowledge gaps concerning the design of finite periodic structures remain. Similarly, existing literature does not clearly define the operational limits of simplified linear periodic systems, which could otherwise serve as a foundation for the development of more complex configurations. The main motivation of this thesis is to develop strategies and techniques to enhance the performance of finite periodic structures in terms of vibration attenuation and control. To this end, one-dimensional periodic waveguides, both mono- and multi-coupled, have been investigated using various analytical approaches. Analytical models were developed based on receptance matrix and dynamic stiffness formulations. Vibration transmission was analysed with an emphasis on displacement transmissibility, incorporating the transfer matrix method. Two primary strategies were explored in this thesis to improve the attenuation bands. The first concerns the effects of asymmetry, while the second focuses on the integration of the Bragg and local resonance stop bands. In the first strategy, rods with internal cross-sectional discontinuities are examined. Second, Euler–Bernoulli beams with external translational and rotational discontinuities were analysed. Furthermore, the effect of local resonance as a vibration attenuation mechanism was assessed, and the key control parameters were identified. Finite structure models were compared to traditional infinite-system approaches based on wave transmission characteristics. Analytical and numerical developments provided insights into the physical phenomena responsible for the observed effects. These results, validated through experimental procedures, demonstrate that the strategies investigated hold significant potential for practical application in vibration control and mitigation.

Keywords: Longitudinal vibration, Flexural vibration, Rods, Beams, Asymmetric cell, Super attenuation band, Neutraliser, Attenuation band prediction.

RESUMO

Recentemente houve um número crescente de estudos com o emprego de periodicidade, objetivando manipular a propagação de ondas em estruturas. Devido a essa propriedade particular, as estruturas periódicas possuem a capacidade de atuar como filtros mecânicos nas chamadas bandas de parada. Nos últimos anos, muitas pesquisas foram realizadas com foco na otimização desses sistemas, visando o alargamento das bandas de parada e a redução da sua frequência de operação. No entanto, mesmo com os avanços recentes, ainda há lacunas de conhecimento no que diz respeito a projetos de estruturas periódicas finitas. Da mesma forma, a literatura não delimita claramente os limites operacionais dos sistemas periódicos lineares simplificados, os quais poderiam fundamentar o desenvolvimento de sistemas mais complexos. A principal motivação desta tese é desenvolver estratégias e técnicas que melhorem o desempenho de estruturas periódicas finitas em termos de atenuação e controle de vibração. Para isso, são investigados guias de ondas periódicos unidimensionais, tanto monoacoplados quanto multiacoplados, por meio de diferentes abordagens. Usam-se modelos analíticos com base na abordagem das matrizes de receptância e da rigidez dinâmica. A transmissão de vibração é analisada com ênfase na transmissibilidade de deslocamentos, utilizando também o método da matriz de transferência. Nesta tese, são exploradas duas estratégias para aprimorar as bandas de atenuação. A primeira refere-se aos efeitos da assimetria, enquanto a segunda aborda a união entre bandas de parada de Bragg e de ressonância local. Na primeira estratégia, investigam-se barras com descontinuidade interna na seção transversal. Na segunda, analisam-se vigas de Euler-Bernoulli com descontinuidades externas do tipo translacional e rotacional. Além disso, avalia-se o efeito da ressonância local como mecanismo de atenuação, identificando seus principais fatores de controle. Modelos de estruturas finitas são comparados com abordagens tradicionais de sistemas infinitos, com base na transmissão de ondas. Os desenvolvimentos analíticos e numéricos permitem compreender os fenômenos físicos que causam os efeitos investigados. Esses resultados, validados por meio de procedimentos experimentais, demonstram que as estratégias exploradas apresentam alto potencial para o projeto e a aplicação prática no controle e mitigação da vibração.

Palavras-chave: Vibração longitudinal, Vibração flexural, Barras, Vigas, Célula assimétrica, Super banda de atenuação, Neutralizador, Predição de banda de atenuação.

LIST OF FIGURES

Figure 1.1. Schematic illustration of the range of applications of periodic structures in vibration control. (a) Illustrates the application of periodic foundations in the attenuation of vibrations from ground. (b) Illustrates the application of local resonance in aircraft fuselage insulation panels to mitigate transmitted sounds. 2

Figure 1.2. Thesis conceptual framework and problem statements 3

Figure 1.3. Historical timeline presenting milestones and notable contributions in the study of periodic structures. 5

Figure 2.1. Illustrations of (a) longitudinal and (b) bending waves motion in one-dimensional waveguides. The deformation is exaggerated for clarity. 16

Figure 2.2. Illustrative examples of wave in (a) non-dispersive (longitudinal waves in a rod) and (b) dispersive medium (bending waves in a beam). Wave packet built up from a sum of cosine functions with different frequencies. 19

Figure 2.3. Diagram of a linear system subject to unidirectional forces and displacements 21

Figure 2.4. General finite structure composed of *N* elements with multiple coupling coordinates. 23

Figure 2.5. Transformations between receptance, dynamic stiffness and transfer matrices for the general finite structure subject to loading and displacements. 26

Figure 2.6. Pictorial representation of complete structure transfer matrix determination. 27

Figure 2.7. Waveguides with periodic segment of large number of cells and details in the *n*-th cell 28

Figure 2.8. Stop band formation in periodic structure. (a) Dispersion diagram, where $\left|\mathrm{Re}\{\psi\}\right|$ in thick grey line and $-\left|\mathrm{Im}\{\psi\}\right|$ in thin black line. (b) Displacement transmissibility and (c) receptances considering a single cell. Point receptance in thick grey lines and transfer receptance in thin black lines. Vertical lines highlight the transmissibility features frequencies. 33

Figure 3.1. Thin uniform rod under longitudinal vibration (a) with coordinate *x*, displacement *u*, Young's modulus *E*, mass density ρ and cross-sectional area *S*. (b) Differential element of the rod with stress action. 37

Figure 3.2. Uniform rod truncation process. (a) Infinite rod. (b) Semi-infinite rod and (c) finite rod. 40

Figure 3.3. General finite mono-coupled periodic structure composed of *N* cells and a detail in the *n*th (a) symmetric and (b) asymmetric cells with different configurations: (i) $\alpha > 1$, (ii) $\alpha < 1$ and all cases $\gamma = 1$. 43

Figure 3.4. Attenuation band and bounding frequencies analysis of a periodic structure comprising symmetric cells. Displacement transmissibility of (a) a single cell and and (b) multiple cells; thick grey line, $N = 3$; thin black line, $N = 6$, with $\alpha = 0.5$ or $\alpha = 2$. (c) Point receptance of a single cell with $U_R = 0$ with $\alpha = 0.5$ in thick grey line and $\alpha = 2$ in thin black line. The bounding frequencies are given by the expression in Tab. 3.1 50

Figure 3.5. Attenuation band and bounding frequencies analysis of a periodic structure comprising single symmetric cell in thick grey lines and single asymmetric cell in thin black lines. (a) $\alpha = 2$ and (b) $\alpha = 0.5$. (i) Displacement transmissibility. (ii) point receptance in L with $U_R = 0$. The bounding frequencies are given by the expression in Tab. 3.1 and highlighted by the vertical lines. 53

Figure 3.6. Attenuation band and bounding frequencies analysis of a periodic structure comprising multiples asymmetric cells with area ratio (a) $\alpha = 2$ and (b) $\alpha = 0.5$. (i) Displacement transmissibility. (ii) Point receptance and (iii) transfer receptance. Thick gray lines corresponds to structure with $N = 3$ and thin black lines to $N = 6$ 56

Figure 3.7. Partition of the structure to determine the vibration between the periodic cells or substructures. 58

Figure 3.8. Minimum displacement transmissibility between the excitation at the left of the structure and the ends of the cells for (a) 1 cell, (b) 3 cells, and (c) 6 cells. The thick grey line is for symmetric cells and the thin black line is for asymmetric cells, both with $\alpha = 2$ 59

Figure 3.9. The attenuation band for the asymmetric cell and the stop band for the symmetric cell as a function of the area ratio α. The upper bound corresponds to the attenuation band for a single asymmetric cell. 60

Figure 3.10. Experimental setup showing a periodic structure consisting of three nylon asymmetric cells, with the inset giving the dimensions of a single cell. The structure was excited with the impact hammer on the centre line of the structure at the left- and right-hand ends, and the transmissibility was measured using the left and right accelerometers. 63

Figure 3.11. Comparison of experimental results with theoretical developments. (a) cells oriented to give an attenuation band ($\alpha = 1.71$). (b) cells oriented to give a band of frequencies in which there is amplification ($\alpha = 0.58$). Experiment results, thin black line; theoretical, thick grey line. Figures on the right are photos of the investigated structure. 64

Figure 4.1. Vibration of a Euler–Bernoulli beam. (a) Beam under free vibration and properties. (b) Displacements and deformations in bending. 69

Figure 4.2. Host beam with an attached discontinuity. (a) Infinite beam and wave components generated by the source and the discontinuity. (b) Section of the beam in the vicinity of the attachment, showing the incident and reflected waves generated by the discontinuity, among which the right-going propagating waves compose the transmitted wave. (c) Types of couplings considered, these being translational and rotational neutralisers. 72

Figure 4.3. Typical behaviour of the dynamic stiffness (a) modulus and (b) real part of either a translational or rotational vibration neutraliser. 78

Figure 4.4. Infinite beam wave transmission ratio for an attached translational neutraliser, in thick grey line, and rotational neutraliser, in thin black line. 79

Figure 4.5. Host beam with an attached discontinuity. (a) Semi-infinite beam and wave components generated by the source and the discontinuity. (b) Section of the beam in the vicinity of the attachment, showing the incident and reflected waves generated by the discontinuity, among which the right-going propagating waves compose the transmitted wave. 80

Figure 4.6. Semi-infinite beam wave transmission ratio for an attached translational neutraliser, in thick grey line, and rotational neutraliser, in thin black line. 82

Figure 4.7. Schematic of a finite Euler-Bernoulli beam with a device attached at point a. 83

Figure 4.8. Comparison of the effect that either a (a) translational or (b) rotational vibration neutraliser, has on a free-free beam, excited by a force at one end, in thin black lines, with a bare beam in thick grey lines. (i) Displacement transmissibility. (ii) Transfer receptance. 87

Figure 4.9. Theoretical curves for infinite, semi-infinite and finite beams based on the expressions in Table 4.1. (b) Translational neutraliser; and (b) rotational neutraliser. (i) Infinite and semi-infinite beams wave transmission ratio. (ii) Displacement transmissibility. 91

Figure 4.10. Models to characterise the dynamic behaviour of the beam-like neutraliser. 93

Figure 4.11. Measurements to characterise the dynamic behaviour of the beam-like neutraliser. (a) Comparison between the neutraliser theoretical and experimental accelerances. (b) real part of the measured and modelled dynamic stiffness of the neutraliser. Experimental results in solid black lines and theoretical results in solid grey lines. 94

Figure 4.12. Experimental setup (not to scale) (a) infinite beam (sandbox at each end of the host beam), (b) semi-infinite beam (sandbox at one end of the host beam), and (c) finite beam. 96

Figure 4.13. Experimental measurements, in thin black lines, and theoretical model, in thick grey lines, for wave transmission ratio on a (a) infinite and (b) semi-infinite beams; and transmissibility on a (c) finite beam. 99

Figure 5.1. General rod with an attached device at it central point. 104

Figure 5.2. Dynamic behaviour, expressed in the form of transmissibility and drive-point receptance, of the rod with different types of couplings. (a) Transmissibility for an attached axial neutraliser with dynamic characteristics of (i) stiffness, (ii) combined and (iii) mass. (b) Point receptance of the system in (a) imposing displacement restriction at the right end. (c) transmissibility for an attached (i) grounded spring and (iii) concentrated mass. 106

Figure 5.3. Single-span beam with discontinuity attached force and displacements components. The attachment is assumed to be a translational or a rotational neutraliser. 109

Figure 5.4. Methods of visualizing transmissibility. (a) Composite view. (b) Top view with reference to a unit. (c) Transmissibility of the shaded planes indicated in (a) – front views. 110

Figure 5.5. Transmissibility top views assuming (a) a translational neutraliser with $\mu_w = 0.2$ and (b) rotational neutraliser with $\chi_\theta = 0.2$; and close-up in the (i) δ and (ii) β tuning conditions. 111

Figure 5.6. Super attenuation band formation using a translational neutraliser with $\mu_w = 0.2$ and (i) $l/\lambda_w = 0.946$ and (ii) $l/\lambda_w = 1.186$. (a) transmissibility. (b) Point (grey) and transfer (black) receptances. (c) Point receptance with constrained right-end. system. Solid lines and dash-dot lines refer to the system and bare host beam, respectively. 114

Figure 5.7. Supper attenuation band formation using a rotational neutraliser with $\chi_\theta = 0.2$ and (i) $l/\lambda_\theta = 0.780$ and (ii) $l/\lambda_\theta = 1.570$. (a) transmissibility. (b) Point (grey) and transfer (black) receptances. (c) Point receptance with constrained right-end. system. Solid lines and dash-dot lines refer to the system and bare host beam, respectively. 116

Figure 5.8. Transmissibility top views assuming attached neutralisers. (i) Translational neutraliser with $\mu_w = 0.2$ and (ii) rotational neutraliser with $\chi_\theta = 0.2$. (a) rotational displacement for a force source. (b) translational displacement for a moment source. (c) rotational displacement for a moment source. 122

Figure 5.9. Experimental setup (not to scale) showing the schematic representation of the system and its experimental implementation. 125

Figure 5.10. Experimental results for the super attenuation band using a translational neutraliser. (a) Translational displacement transmissibilities. (b) point and (c) transfer receptances. Tuning conditions (i) δ and (ii) β. Model in grey thick solid lines and measures in thin black lines. 128

Figure 5.11. Experimental results for the super attenuation band using a rotational neutraliser. (a) Translational displacement transmissibilities. (b) point and (c) transfer receptances. Tuning conditions (i) δ and (ii) β. Model in grey thick solid lines and measures in thin black lines. 131

Figure 5.12. General periodic beam with translational or rotational vibration neutraliser attached to centre of the *n*-th cell. 132

Figure 5.13. Translational displacement transmissibility of a finite periodic beam of three cells with translational neutralisers. (a) Top view of the transmissibility as a function of l/λ_w. (b) Transmissibility in the specific configurations in (i) $l/\lambda_w = 0.94596$ and (ii) $l/\lambda_w = 1.18610$. Thick grey lines, without structural damping, and thin black lines with loss factor of 0.001. 134

Figure 5.14. Translational displacement transmissibility of a finite periodic beam of three cells with rotational neutralisers. (a) Top view of the transmissibility as a function of l/λ_θ. (b) Transmissibility in the specific configurations in (i) $l/\lambda_\theta = 1.56995$ and (ii) $l/\lambda_\theta = 1.83250$. Thick grey lines, without structural damping, and thin black lines with loss factor of 0.001. 135

Figure 5.15. Translational displacement transmissibility of a finite periodic beam with (a) translational neutraliser and (b) rotational neutraliser, assuming $N=1$, in thick grey lines; and $N=3$ in thin black lines. 136

Figure B.1. Schematic illustration of the experimental setup. 156

Figure B.2 Experimental setup photograph. 157

Figure B.3. Schematic illustration of the experimental setup 159

Figure B.4. Experimental setup (not to scale) on a (a) infinite beam (sandbox at each end of the host beam), (b) semi-infinite beam (sandbox at one end of the host beam), and (c) finite beam. 161

Figure B.5. Experimental setup photograph. 162

Figure B.6. Photograph demonstrating the arrangement for simulating semi-infinite boundary conditions. 163

Figure B.7. Experimental setup (not to scale) of a finite beam with attachments at its centre position. 165

Figure B.8. Photograph of the physical system used in the experiments with translational (left) and rotational (right) neutralizer. Dashed boxes show details of the coupled devices. 166

Figure C.1. Wave transmission ratio for beam with discontinuity consisting on a concentrated mass or grounded rotational spring, thick grey line; and grounded line spring or pure moment of inertia, thin blue line. 170

Figure C.2. Transmissibility for finite beams with different types of (a) mass-like and (b) stiffness-like behaviours. (i) Translational and (ii) rotational discontinuities. Complete transmissibility, Eqs. (4.20a,b), in grey thick lines and approximated form transmissibility, Eqs. (4.21a,b), in blue thin lines. 173

Figure D.1. Beam with a rotational device attached. (a) Schematic representation of the designed beam structure with imposed force and measured displacement. (b) Detail on the attached device. 175

Figure D.2. Schematic representation of the beam-like moment resonator. (a) Real separated device diagram. (b) Approximated lumped system. 176

Figure D.3. Experimental setup and device details. 177

Figure D.4. Experimental and theoretical results comparison. (a) Bare host beam. (b) Beam with attached device system. Experimental transfer accelerance in thin black lines. Theoretical transfer accelerance in thick grey lines. 178

Figure D.5. Different forms of the (a) translational and (b) rotational dynamic stiffnesses. Expressions given by Eqs. (D.2a,b) in dash-dot lines, Eqs. (D.5a,b) in solid thick lines, Eqs. (D.7a,b) in solid thin lines, Eqs. (D.8a,b) in blue dotted lines and Eqs. (D.9a,b) in red dotted lines. 183

Figure D.6. Experimental and theoretical results comparison for the system shown in Fig. D.3 and assuming the model expressed by Eq. (D.10). Experimental transfer accelerance in thin black lines and theoretical transfer accelerance in thick grey lines. 184

LIST OF TABLES

Table 3.1. Key features of the lowest stop and attenuation bands for structures containing a finite array of *N* symmetric and asymmetric cells respectively. 61

Table 3.2. Summary of the experimental results in terms of attenuation band and minimum transmissibility compared with the predictions and bound limits..... 64

Table 4.1. Expressions for the displacement transmissibilities and wave transmission ratios. 89

Table 5.1. Formation of the super attenuation band in a rod and single-span beam under different conditions. 124

Table 5.2. Comparison between the experimental e theoretical super attenuation band boundary frequencies for the single-span beam under different conditions. 130

Table B.1. Experimental setup. 157

Table B.2. Periodic rod properties 158

Table B.3. Equipment setup. 160

Table B.4. Neutraliser properties. 160

Table B.5. Equipment setup. 163

Table B.6. Host beam properties. 164

Table B.7. Equipment setup 167

Table B.8. Host beam and neutraliser properties. 167

Table D.1. Properties of the host beam and attached device 177

LIST OF SYMBOLS AND ABBREVIATIONS

LATIN SYMBOLS

Symbol	Description
A	Propagating wave amplitude
B	Evanescent wave amplitude
c	Spatial phase velocity
D	Dynamic stiffness
E	Young's modulus
F	General force amplitude
f	Frequency in Hertz
I	Second moment of area
k	Wavenumber
L	Structure length
l	Element length
M	Bending moment
m	Element mass
N	Number of cells
n	n-th cell
R	Receptance
S	Cross-sectional area
s	Spring characteristic stiffness
T	Element of the transfer matrix
t	Time variable
t	Transmission coefficient
U	Complex amplitude of longitudinal displacement
u	Longitudinal displacement in time domain
v	Propagating wave function
W	Complex amplitude of transversal displacement
w	Transversal displacement in time domain
X	General displacement
x	Space variable

GREEK LETTERS

Symbol	Description
α	Cross-sectional area ratio
B	Dynamic stiffness matching parameter for β tuning condition
β	SAB tuning condition
χ	(Characteristic) stiffness ratio
Δ	Dynamic stiffness matching parameter for δ tuning condition
δ	SAB tuning condition
γ	Length ratio
ε	Young's modulus ratio
η	Loss factor
Θ	Complex amplitude of rotational displacement
θ	Rotational displacement in time domain
κ	Wavenumber ratio
λ	Wavelength
μ	(Characteristic) Mass ratio
ξ	Hamonic excitation
ρ	Mass density
σ	Longitudinal stress
ϕ	Spatial wave phase
φ	Transfer matrix eigenvalue
ψ	Propagating constant
Ω	Non-dimensional frequency parameter
ω	Temporal frequency in radians per second

MATRICES AND VECTORS

Symbol	Description
D	Dynamic stiffness matrix
R	Receptance matrix
T	Transfer matrix
u	Displacement vector
f	Loading vector
q	State vector
Ψ	Floquet multipliers matrix

SUPERSCRIPTS

Symbol	Description
[*n*]	*n*-th system kinetic and kinematic property or ratio
-	Left-going wave indicator
+	Right-going wave indicator
T	Transpose

SUBSCRIPTS

Symbol	Description
min	Minimum property value
F	Referred to force excitation
g	Referred to group velocity
I	Relating to the position in which the property is valued in the structure
i	i-th element (or sub-element) property
J	Relating to the position in which the property is valued in the structure
L	Structure left-end property
P	Relating to the position in which the property is valued in the structure
p	Referred to phase velocity
R	Structure right-end property
X	Referred to general displacement
w	Referred to translational motion
θ	Referred to rotational motion
∞	Property of an infinite structure

ACRONYMS

Symbol	Description
PS	Pass band
SB	Stop band
LR	Local resonance
TR	Displacement transmissibility of a single cell
str	Structure
Sym	Symmetric
Asy	Asymmetric
SAB	Super attenuation band
QSAB	Quasi-Super attenuation band

SPECIAL NOTATIONS

Symbol	Description
$[\ ]$	Matrix
$\{\ \}$	Vector
$\lvert\ \rvert$	Absolute value of a number
$\sqrt{\ }$	Square-root of a number
e	Exponential
j	Imaginary number $\sqrt{-1}$
$\mathrm{Re}\{\ \}$	Real part of a number
$\mathrm{Im}\{\ \}$	Imaginary part of a number
$\mathrm{d}^n(\ )/\mathrm{d}(\ )^n$	*n*-order ordinary differential
$\partial^n(\ )/\partial(\ )^n$	*n*-order partial differential

CONTENTS

1 INTRODUCTION 1

1.1 BACKGROUND 1

1.2 LITERATURE REVIEW 4

1.2.1 Foundational works 4

1.2.2 Early engineering applications and vibration control developments 6

1.2.3 Recent advances and matastructures 7

1.3 OBJECTIVES 12

1.4 CONTRIBUTIONS TO KNOWLEDGE 13

1.5 THESIS OUTLINE 13

2 MODELLING FINITE CONTINUOUS PERIODIC STRUCTURES: THEORETICAL FOUDATIONS 15

2.1 INTRODUCTION 15

2.2 WAVE MOTION CONCEPTS 15

2.2.1 Phase velocity and dispersion relation 17

2.3 RECEPTANCE, DYNAMIC STIFFNESS AND TRANSFER MATRIX FORMULATION 19

2.3.1 Definitions of the receptance and dynamic stiffness approach 20

2.3.2 Relationship between the dynamic stiffness and receptance matrices approach and transfer matrix method 22

2.3.3 Complete dynamic stiffness and receptance matrices of combined systems using the transfer matrix for a periodic structure 26

2.4 DISPERSION DIAGRAM AND ATTENUATION BANDS IN PERIODIC STRUCTURES. 27

2.4.1 Dispersion relation and filtering properties of periodic structures 28

2.4.2 Relationship of dispersion diagram and transmissibility 29

2.5 CHAPTER REMARKS 35

3 THE EFFECT OF ASYMMETRY ON ATTENUATION BAND ENHANCEMENT IN MONO-COUPLED METASTRUCTURES 36

3.1 INTRODUCTION 36

3.2 MODELLING UNIFORM RODS UNDER LONGITUDINAL VIBRATION 36

3.2.1 Longitudinal waves in rods 36

3.2.2 Transfer matrix of uniform rods 39

3.3 FINITE PERIODIC STRUCTURE COMPRISING *N* CELLS 42
3.3.1 Symmetric cell 44
3.3.2 Asymmetric cell 51
3.4 ATTENUATION THROUGH SYMMETRIC AND ASYMMETRIC MONO-COUPLED STRUCTURES 57
3.5 EXPERIMENTAL VALIDATION 62
3.6 ON THE OTHER CONDITIONS OF THE PERIODIC CELL 65
3.7 CHAPTER REMARKS 66
4 CONTROLLING VIBRATION TRANSMISSION IN A BEAM WITH EXTERNAL DISCONTINUITIES 68
4.1 INTRODUCTION 68
4.2 MODELLING UNIFORM BEAMS UNDER BENDING VIBRATION 68
4.2.1 Free wave motion in beams 68
4.2.2 Wave transmission of an infinite beam 71
4.2.3 Wave transmission of semi-infinite beam with an attached discontinuity 79
4.2.4 Modelling a finite beam with an attached discontinuity 82
4.3 EXPERIMENTAL DEMONSTRATIONS 92
4.3.1 Characterisation of the neutraliser 92
4.3.2 Host beam with neutraliser attached 95
4.4 LOCAL RESONANCE EFFECT IN BEAMS AND RODS 100
4.5 CHAPTER REMARKS 101
5 EFFECTS OF COUPLING LOCAL RESONANCE BAND AND BRAGG STOP BAND IN BEAMS 103
5.1 INTRODUCTION 103
5.2 COUPLING LOCAL RESONANCE BAND AND BRAGG BAND GAP: THE SUPER ATTENUATION BAND 103
5.3 THE FORMATION OF THE SUPER ATTENUATION BAND IN SINGLE-SPAN BEAMS 108
5.3.1 The tuning conditions of the super attenuation band 110
5.3.2 Discussions on tuning conditions 117
5.4 ON THE FORMATION OF THE SUPPER ATTENUATION BAND IN OTHER SOURCE AND RESPONSE CONDITIONS 119
5.5 EXPERIMENTAL DEMONSTRATIONS 125

5.5.1 Super attenuation band with a translational vibration neutraliser 126
5.5.2 Super attenuation band with a rotational vibration neutraliser 129
5.6 On the Formation of the Super Attenuation Band in Periodic Beams 132
5.7 Chapter Remarks 136
6 FINAL REMARKS 138
6.1 main Conclusions 138
6.2 Recommendations for further works 140
6.3 List of publications 140
REFERENCES 143
APPENDIX A. DETERMINATION OF THE TRANSFER MATRIX FOR A MONO-COUPLED PERIODIC STRUCTURE CONTAINING N CELLS (EQ. (3.13)) 154
APPENDIX B. SUPPLEMENTARY DETAILS OF EXPERIMENTAL PROCEDURES AND ADDITIONAL RESULTS 156
B.1. Experimental details for the procedure on a periodic rod composed of three asymmetrical cells 156
B.2. Experimental details for the procedure on a beam-like vibration neutraliser 159
B.3. experimental details for the procedure on an infinite, semi-infinite and finite beam 161
B.4. experimental details for the procedure on the formation of the super attenuation band 165
APPENDIX C. EFFECTS OF ATTACHING LUMPED PARAMETERS ON BEAMS 168
C.1. Wave transmission across discontinuities in an infinite beam 168
C.2. Transmissibility of finite beam with external discontinuities 171
APPENDIX D. THEORETICAL AND EXPERIMENTAL ANALYSIS OF BEAM-LIKE ROTATIONAL NEUTRALISER 174
D.1. The pure rotary inertia and the practival behaviour 174
D.2. modelling the beam-like rotational neutraliser 179

1 INTRODUCTION

1.1 BACKGROUND

The investigation of structural vibrations in periodic systems has a long and distinguished history, commencing with the seminal work of Brillouin (1953) and the contributions of Mead (1996). This field has experienced a resurgence of interest in recent times, driven by advancements in metamaterial-engineered structures with enhanced capabilities for filtering structural wave propagation (HUSSEIN *et al*., 2014). The applications of periodic structures are wide-ranging from mitigating ground vibrations in civil construction to improving acoustic performance in aerospace, automotive, and mechanical systems (FARAJIAN *et al*., 2022; WANG *et al*., 2019) – as illustrates Fig. 1.1.

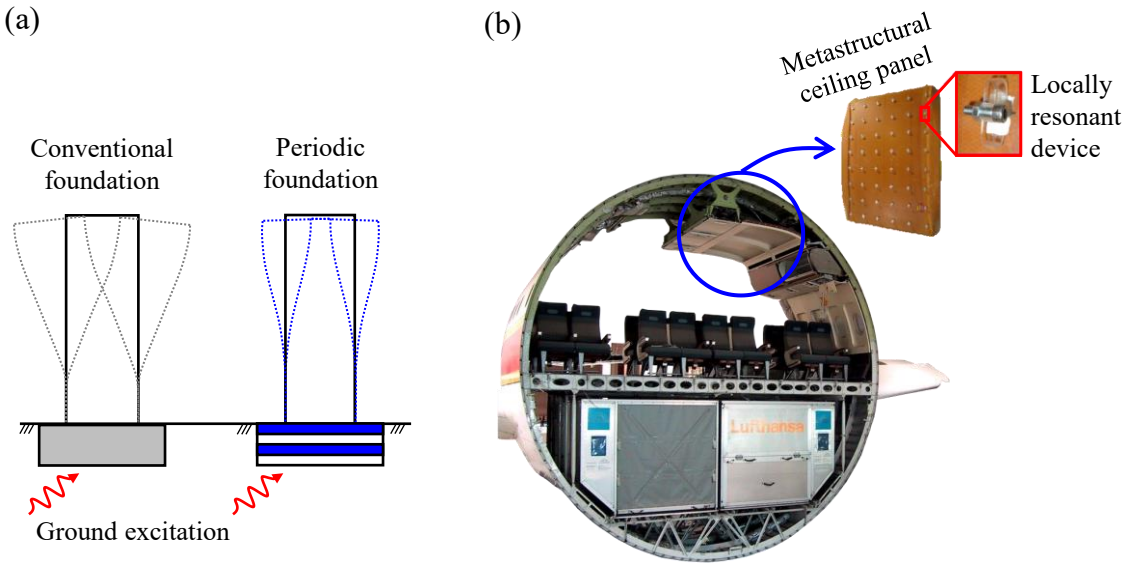
Periodic structures are characterised by their composition of multiple identical structural elements, named *cells*, joined together end to end to form the whole structure (MEAD, 1996). The cells are modeled according to their geometric and material properties, to reorganize the wave propagation and present stop bands (bandgaps) in certain frequency bands, that is, regions of frequency where the waves do not propagate (BRILLOUIN, 1953), as initially studied by Rayleigh (1877). This characteristic allows these systems to act as mechanical filters (SANTOS *et al*., 2023).

Recent developments have focused on optimising stop bands and understanding the effects of wave propagation in finite and infinite structures (FABRO *et al*., 2021; HOLLKAMP *et al*., 2019; HULL; CRAY, 2014; YEH; HARNE, 2019). However, despite these advances, practical design challenges remain. Most of the research on periodic structures has concentrated on stop bands and dispersion curves (XIAO; WEN, 2020; YING; NI, 2018), with minimal investigation into practical designs for finite structures, which constitutes a knowledge gap.

Different methods have been used in the study of periodic structures, considering the large application fields, as can be found in the literature. Almeida *et al.* (2022) applied the concept of periodicity to reduce the sound power level in a refrigeration compressor based on the analysis of finite elements (FEM), spectral elements (SEM), and plane wave expansion methods (PWE). Nobrega *et al.* (2016) presented a study of rods composed of metamaterials and concluded that the wave finite element method (WFEM) presents good convergence and is more suitable for modelling complex structures. Carneiro Jr. *et al.* (2021a; 2021b; 2021c)

have focused their efforts on improving the stop band considering geometric periodicity in rods and beams, using the Transfer Matrix approach. These works resulted in physical understandings of these zones introducing the concept of attenuation band to differentiate between finite and infinite systems. However, producing these at low frequency with a broad range, without adding much mass or constraints to the structure, is still challenging.

Figure 1.1. Schematic illustration of the range of applications of periodic structures in vibration control. (a) Illustrates the application of periodic foundations in the attenuation of vibrations from ground. (b) Illustrates the application of local resonance in aircraft fuselage insulation panels to mitigate transmitted sounds.



Source: Assembled by the author, using references (CHENG Z.; SHI *et al*., 2017; MUSEUM, 2024; ALVES PIRES *et al*., 2022).

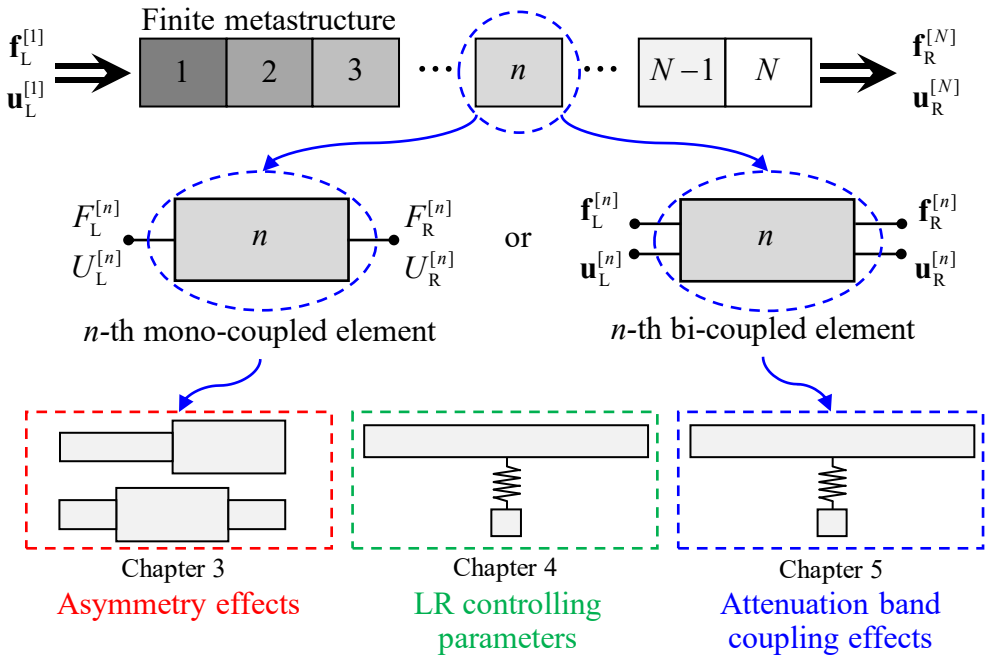
In addition to exploring various models, the literature presents a range of techniques and strategies aimed at maximizing vibration reduction and broadening the frequency bandwidth over which this reduction is achieved. These objectives collectively form the basis of the concept known as attenuation band enhancement.

In recent years, significant research efforts have been directed toward employing Bragg scattering and local resonance effects (LR) to expand stop bands. Yu *et al.* (2008) was the first to observe the coupling between these two attenuation mechanisms. Recent studies have provided substantial advancements in the understanding of this phenomenon, supported by laboratory experiments demonstrating the formation of super stop bands in mono-coupled systems (CLEANTE *et al.*, 2022; CLEANTE *et al.*, 2023; GONÇALVES *et al.*, 2021). Despite

these advances, a knowledge gap remains regarding the behaviour and implications of this phenomenon in multi-coupled systems.

The discussions outlined thus far underscore the need for further research to complement existing studies on enhancing vibration attenuation and addressing the previously identified knowledge gaps. This thesis aims to explore two strategies to improve the performance of periodic metastructures in vibration reduction and control. The analysis focuses on two systems: rods subjected to quasi-longitudinal vibration and beams subjected to pure bending vibration. Figure 1.2 illustrates the proposed systems strategies and the overarching conceptual framework employed to model them: A finite metastructure composed of N cells, which are modeled in the form of mono-coupled rods, where the effects of asymmetry are investigated (using internal discontinuity) and bi-coupled beams, where the effects of attenuation band coupling are investigated (using external discontinuity).

Figure 1.2. Thesis conceptual framework and problem statements.



Source: author.

1.2 LITERATURE REVIEW

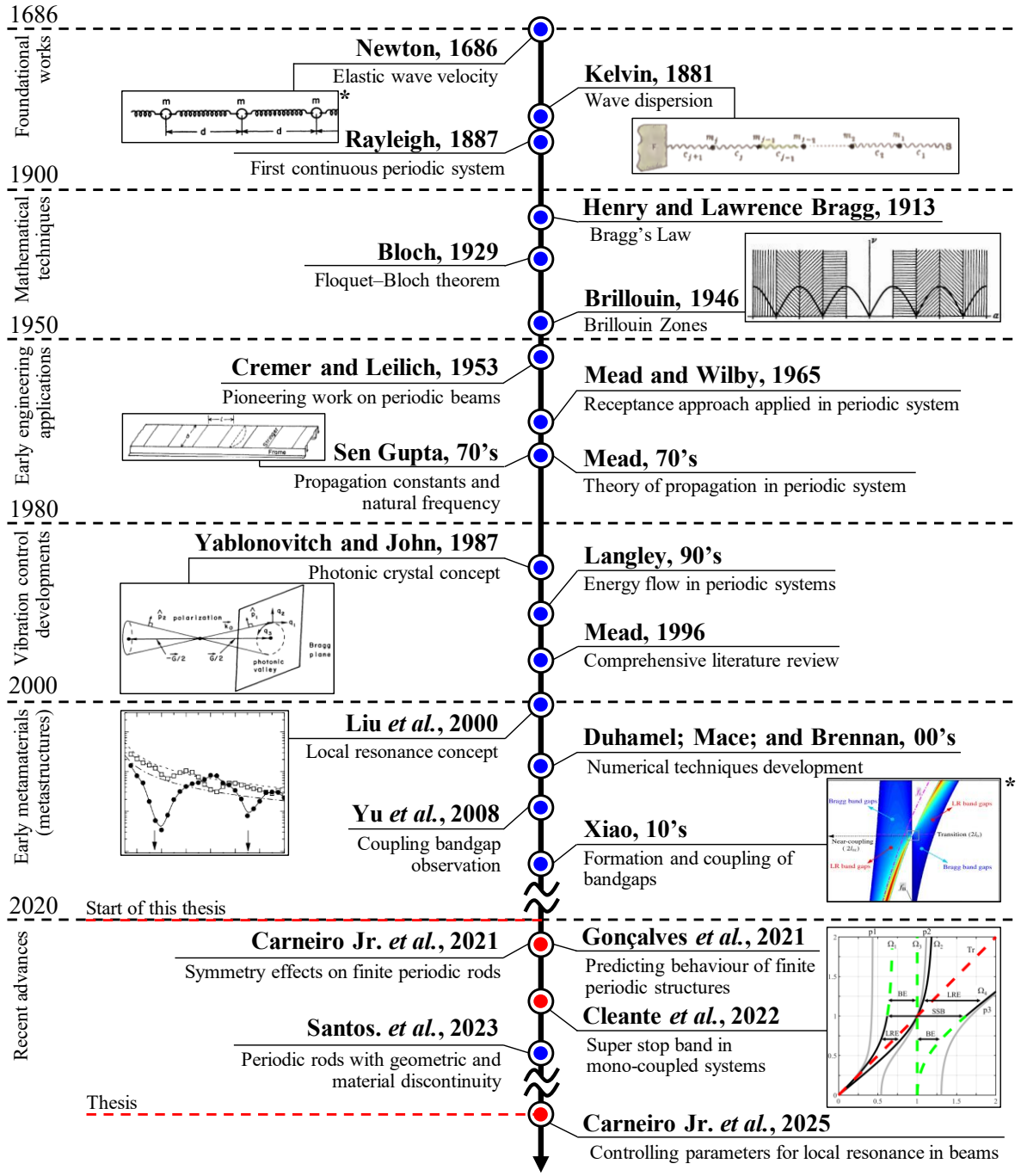
The background outlined in the previous section is further developed here to position this thesis within the broader field of research on periodic structures. The rationale is summarized in Figure 1.3, which presents a timeline linking historical milestones and key contributions to the foundation of this thesis. For a more detailed discussion, readers are encouraged to consult the comprehensive reviews by Mead (1996), Hussein (2014), Banerjee (2019), and Muhammad (2022).

1.2.1 Foundational works

A periodic structure is defined as a system composed of identical elements arranged in a manner that reorganizes the propagation of waves (MUHAMMAD; LIM, 2022). According to Brillouin's (1953) historical analysis, the first investigation into periodic structures can be traced back to Isaac Newton (1686), who explored this concept in his efforts to derive an expression for the velocity of sound in air. Rayleigh (1887) advanced the field by investigating a continuous periodic structure, specifically a stretched string with periodic, continuous variations in density along its length, undergoing transverse harmonic vibrations (MEAD, 1996).

From 1900 to 1950, substantial advancements were achieved in the development of mathematical methods for examining increasingly intricate systems such as crystal lattice structures and electrical circuits. These methodologies have since proven invaluable for subsequent studies in the engineering of continuous periodic structures. One of the most significant theoretical advances in the early 20th century was *Bragg scattering* theorem, formulated by the father-and-son team William Henry Bragg and William Lawrence Bragg (BRAGG; BRAGG, 1913). This law describes how wavefronts scattered by lattice planes interfere constructively or destructively under specific conditions, establishing a precise relationship between the wavelength and scattering angle. Bloch (1929) extended Floquet's earlier analysis by introducing a theorem governing the propagation of plane waves in periodic media. Floquet-Bloch's theorem asserts that, in an infinite and non-dissipative lattice, the amplitude variations of a wave as it traverses between unit cells are unaffected by the specific location of the cell within the lattice. As a result, the wave propagation properties of a periodic system can be entirely understood by examining just one unit cell.

Figure 1.3. Historical timeline presenting milestones and notable contributions in the study of periodic structures.



Source: author. Subfigures extracted from the cited works. *Special cases extracted from (BRILLOUIN, 1953; XIAO *et al.*, 2013a).

In the mid-20th century, Brillouin (1946) consolidated and expanded the knowledge in this field with his seminal book, Wave Propagation in Periodic Structures. This work synthesized prior developments and introduced the theory of stop bands in one-dimensional and multidimensional crystal lattices, relating these findings to energy flow, impedance, and the equivalence of electrical systems. It also established the concept of the *Brillouin zone*, which remains fundamental in wave propagation studies.

1.2.2 Early engineering applications and vibration control developments

After 1950, the analysis and application of periodic structures in engineering experienced growth. Cremer and Leilich (1953) conducted pioneering research on beams subjected to flexural wave motion with periodic point supports or masses. A few years later, Miles (1956) investigated the natural frequencies of beams with multiple supports, laying the groundwork for continuous mono-coupled systems.

The subsequent decades saw substantial advancements in the study of wave propagation in continuous periodic systems. For instance, Mead and Wilby (1965) utilized receptance functions to study beams with periodically spaced rigid joints subjected to random vibrations. Their work incorporated the effects of rotational and transverse stiffness into receptance calculations and derived attenuation and phase constants for flexural wave motion. Later, Sen Gupta (1970) applied the receptance matrix principle to analyse rib-skin structures, demonstrating how propagation constants could be used to determine the natural frequencies of one-dimensional periodic systems (SEN GUPTA, 1971). This principle was further generalized by Denys Mead, who extended the theory to both mono- and multi-coupled structures, complementing earlier studies on crystal lattices (MEAD, 1973; MEAD, 1975a; 1975b; MEAD; BANSAL, 1978).

Although the properties of periodic media have long been investigated, their potential for enabling innovative technological applications has only recently been recognized. Yablonovitch (1987) and John (1987) independently proposed the concept of photonic crystals in their groundbreaking studies on dielectric structures. This concept was later adapted for acoustic and elastic waves, leading to the development of *phononic crystals* (HUSSEIN *et al*., 2014).

The design of passive periodic structures for vibration control remains a prominent area of research, largely building upon work conducted in the late 20th century. Langley, for example, extensively analysed energy flow in one- and two-dimensional periodic systems (LANGLEY *et al.*, 1997; LANGLEY, 1994a; 1994b; 1994c). Many of these studies focused on Bragg scattering phenomena, as explored by researchers such as Sigalas (1992), Economou (1994), and Kushwaha (1996). This is also evident in Mead's (1996) comprehensive literature review, which highlights the enduring significance of these earlier findings in contemporary investigations of periodic structures.

1.2.3 Recent advances and matastructures

During the first decade of the 21st century, numerical techniques for investigating periodic structures underwent rapid development. Between 2000 and 2024, the number of publications in this field increased by over 70%[1]. Many of these studies applied wave-based methods, with notable contributions from researchers (DUHAMEL *et al*., 2006; MACE *et al*., 2005; MENCIK, 2018, 2014; WAKI *et al*., 2009). Among the most widely employed approaches are the Wave Finite Element Method (WFEM) (HOANG *et al*., 2020; LEI; LIU, 2024; NOBREGA *et al*., 2016), the Wave Spectral Element Method (WSEM) (GOPALAKRISHNAN; RAUT, 2019), and the plane wave expansion method, all of which are extensively discussed in the literature (DAL POGGETTO; SERPA, 2021; LIAO *et al.*, 2024).

Alternative methodologies have also been explored, notably those using state vector formulations to relate the amplitudes of incoming and outgoing waves within a structure (BRENNAN *et al*., 1997; GONSALEZ-BUENO, 2019; SANTOS, 2018). These methods are grounded in the relationship between the cell transfer matrix and the propagation constant – based in the Bloch-Floquet theorem relation. In several studies, these approaches have been utilised to examine the influence of geometry on one-dimensional periodic waveguides (FABRO *et al*., 2019; NICOLETTI; BACHOUR, 2020; NUNES *et al*., 2022). Recent work by Santos and collaborators extended these investigations to beams and rods (SANTOS *et al*., 2021, 2023).

[1] Estimate obtained using Scopus Metrics for the term "periodic structures".

In practical engineering situations, the design of periodic structures should meet specific requirements, such as the vibration attenuation required within a prescribed frequency range (attenuation band), in addition to the physical limitations of the structure. However, many studies into periodic structures concentrate on the determination of stop bands and dispersion curves, which results in a knowledge gap in terms of the design of practical periodic structures, such as the overall length of the structures. Part of this gap was filled by Carneiro Jr. *et al.* (2021) for stepped rods and constitutes one of the attenuation band enhancement strategies presented in this thesis. Their finds were later proven in other forms of discontinuities (DA SILVA *et al*., 2024).

Comparative studies of finite and infinite systems have demonstrated that the attenuation bands of sufficiently large finite structures closely approximate those of infinite systems (CLEANTE *et al*., 2022; DOMADIYA *et al*., 2016; WEI, J. PETYT, 1997). However, when a periodic structure is truncated to a finite size, *localised resonant modes*, recently also known as truncation resonances (or truncation modes), emerge within the stop bands. This was initially observed by Born (1942) and uncovered theoretically by Wallis (1957). Recently, this phenomenon was observed by Carneiro Jr. *et al.* (2021), and it has been shown that the prominent displacement occurs near the boundaries of the structure and is influenced by the symmetry of the cells and applied boundary conditions. Other researchers have confirmed these findings and further demonstrated that, in certain cases, truncation resonances can be harnessed for energy harvesting, sensing, waveguiding, and phononic flow control, where localised modes or specific frequency responses are desired (AL BA'BA'A *et al*., 2023; PARK *et al*., 2024; ROSA *et al*., 2023). In this thesis, however, the objective is to enhance the attenuation bands and, consequently, to avoid the occurrence of this phenomenon.

Additionally, significant progress has been made in optimization and design of periodic structures, particularly efforts aimed at broadening stop bands (BOUKADIA *et al.*, 2020; SHENG *et al.*, 2020). Some researchers have developed theories for estimating stop bands in beams, rods, and shafts with periodic arrays of resonators (WANG *et al*., 2023; XIAO *et al*., 2011; XIAO; WEN, 2020). However, in these cases, there is an additional stop band mechanism known as *local resonance effect*, that requires further investigation to enhance the understanding and application of these systems.

1.2.3.1 The local resonance effect

Most of the research cited in the previous sections has investigated periodic structures based on the intrinsic stop band mechanism of this system, that is, the Bragg scattering band. This mechanism represents regions of destructive interference between incident and reflected waves, which occur when the wavelengths are comparable to the dimensions of the periodic units. Consequently, this type of stop band typically forms in the low-frequency range only for large structures (SILVA, 2015). However, at the turn of the millennium, another mechanism emerged, driven by advancements in research on phononic crystals: the local resonance band.

The local resonance band is characterised by a narrow frequency band with profound localised vibration reduction, governed by the effect induced in the structure by a system such as a vibration absorber (GONÇALVES *et al*., 2021; LIU *et al*., 2000). Liu *et al.* (2000) were the first to conceptualize this mechanism while investigating a three-dimensional structure with metallic spheres coated with polymeric material. This arrangement induces local resonance in the substructural elements. When the periodic chain was subjected to acoustic waves, the medium exhibited a stop band at a wavelength significantly below than that associated with stop band generation based on the spatial periodicity of the impedance mismatch areas, which leads to the Bragg scattering band.

The unveiling of this local resonance band mechanism has expanded the horizons of investigations into phononic crystals and the emergence of metamaterials (LI; WANG, 2021; RAGHAVAN; PHANI, 2013; YU *et al*., 2006, 2008). Indeed, what characterizes a metamaterial is the unique property of this phenomenon, which results in unconventional behaviour in periodic systems. As discussed by Hussein *et al.* (2014), the prefix “meta” in this context is derived from the Greek language to signify the notion of “after” or “beyond” and is linked to the idea of a material exhibiting properties that transcend those of conventional materials.

Furthermore, in this thesis, it is necessary to clarify the nomenclature of the suffix “material” and “structure.” Rosa *et al.* (2021) delves into this distinction. As discussed previously, there is a fundamental difference between infinite and finite media. The former aligns with the hypotheses of classical physical theorems, such as Floquet-Bloch, and is defined as “material”, as it provides a fundamental description of the modal wave propagation properties of the medium under investigation, independent of overall size and external

boundary conditions. Such media possess intrinsic properties, such as Young's modulus and density. A "structure", on the other hand, is composed of a finite number of elements, is subject to boundary conditions, and is defined by extrinsic characteristics, such as stiffness and mass. Therefore, the medium investigated in this thesis is best described as a metastructure.

1.2.3.2 The super stop band

The local resonance effect has been explored in periodic structures in various ways. Xiao *et al.* (2012) investigated beams using a series of resonators tuned to the same natural frequency. Other studies present the strategy of tuning the resonators to different natural frequencies, thereby widening the attenuation region (HU *et al*., 2021; SILVA *et al*., 2020; SUGINO *et al*., 2016). Even so, although a significant reduction in vibration was obtained, the bandwidth for this stop band remained narrow (SUGINO *et al.*, 2016).

An alternative strategy for widening the stop band was initially observed by Yu *et al.* (2008), who attached vibration absorbers to a pipe conveying fluid and demonstrated that a wider stop band could be formed by changing the size of the cell. Later, using a uniform string with periodically attached vibration absorbers, Xiao *et al.* (2011) showed that the phenomenon observed by Yu *et al.* (2008) was due to the complete coupling of the Bragg and local resonance stop bands, which occurs when the absorber is appropriately tuned. In subsequent year, Xiao *et al.* (2012) investigated a multi-degree-of-freedom vibration absorber attached to a rod and demonstrated that a local resonance stop band can coexist with the stop band.

Recently, Gonçalves *et al.* (2021) investigated the formation of a super stop band behaviour in a finite periodic structure by studying a single mono-coupled symmetric cell with an attached vibration absorber. Their results demonstrated that the stop band related to the Bragg effect is predominantly due to the added mass or stiffness attributed to the vibration absorber, depending on whether its natural frequency is smaller or greater than the free-free natural frequency of the host cell. Additionally, the authors introduced a new concept of the super stop band, characterizing this attenuation region by its smooth curve behaviour and wide bandwidth in transmissibility.

This strategy has also been employed in multi-coupled structures. Hao *et al.* (2019) demonstrated that stop band effects coupling can be created on a dispersive waveguide, provided it is mono-coupled, due to periodically spaced simple supports. A similar conclusion

was presented by Carneiro Jr. *et al.* (2023), who investigated the super stop band using the receptance and transfer matrix methods in beams with periodically distributed rotational resonators and hinge couplings at the ends. The coupling of stop band effects to suppress flexural wave propagation in beams with periodically attached vibration absorbers was also examined in other works (LIU; HUSSEIN, 2012; XIAO *et al.*, 2013a; 2013b).

This phenomenon has continued to be investigated in recent studies. Li *et al.* (2022) proposed a single-phase metastructural beam consisting of a host beam and a periodic array of local resonators, which was analysed both theoretically and experimentally. The authors demonstrated that the proposed beam achieves a vibration attenuation bandwidth more than four times that of conventional systems. Luo *et al.* (2024) investigated this phenomenon in a metastructure composed of partial-interaction composite beams, with an emphasis on civil engineering applications, showing a significant reduction in transmission.

Advancements in the understanding of the stop band coupling phenomenon in finite structures was achieved by Cleante *et al.* (2022; 2023). In these studies, the authors explored mono-coupled systems analytically and experimentally, considering symmetric and asymmetric cells. In their investigation the dynamic features and the transmissibility of a single cell are determined, the physical mechanisms behind the super stop band formation and the influence of damping are described. The results show that a smooth super stop band only occurs when the vibration absorber is tuned to the free-free natural frequency of the single host cell. However, as will be shown in this thesis, there is other tuning condition, when the vibration absorber is tuned to the fixed-fixed natural frequency of the single host cell.

Although some research has been conducted on the coupling of Bragg stop bands and local resonance, such as the studies cited above, no investigation has presented this phenomenon in the context of a super stop band in multi-coupled systems, that is, a region of attenuation characterized by a wide bandwidth and smooth behaviour. To understand the formation of super stop bands in multi-coupled systems, it is necessary to examine the effect of local resonance in these types of structures.

As seen in the aforementioned studies, local resonance is induced by the coupling of resonant appendages in host systems, which are often modelled as vibration absorbers or neutralisers. Carneiro Jr. *et al.* (2025) investigated the dynamics behind the formation of the local resonance effect in a bi-coupled system, coupling translational and rotational resonators in infinite, semi-infinite, and finite beams. Their findings demonstrated that the translational or

rotational type creates a dip in the displacement transmissibility, which corresponds to an anti-resonance in the transfer receptance. This behaviour depends solely on the local interaction between the neutraliser and the beam, such that the boundary effects of the beam may be neglected. This work has supported the development of research on the formation of super stop bands in beams, which represents one of the strategies for improving the attenuation bands presented in this thesis.

1.3 OBJECTIVES

The main objective of this thesis is to develop and explore new techniques and strategies for improving the performance of periodic structures in terms of vibration attenuation and bandwidth. This objective stems from questions regarding the theoretical and practical limits of linear periodic systems. The development of this thesis can be divided into the following secondary objectives:

1. To derive simplified transmissibility expressions to predict the dynamic behaviour of periodic structures.
2. To explain the effects of cell symmetry and asymmetry on attenuation band enhancement for finite periodic structures.
3. To explore and characterise the local resonance effect in beams and rods using a vibration neutraliser.
4. To investigate and demonstrate the formation of the super attenuation band as a strategy for enhancing attenuation bands in periodic structures.

1.4 CONTRIBUTIONS TO KNOWLEDGE

The contributions of this thesis are as follows:

- Analytical expressions have been developed to predict the behaviour of an *N* periodic cell rod structure.
- Simplified expressions have been derived to estimate the bandwidth and the minimum transmissibility for periodic rods and beams. This contribution was published in (CARNEIRO JR. *et al*., 2021a, 2021b)
- It has been demonstrated that a properly oriented finite mono-coupled array of asymmetric cells outperforms a comparable array of symmetric cells in terms of attenuation band. This contribution was published in (CARNEIRO JR et al., 2021a)
- The factors that govern the local resonance effect in beams have been determined. This contribution was published in (CARNEIRO JR. *et al*., 2025).
- The dynamic behaviour of the super attenuation band in mono- and multi-coupled periodic structures has been characterized under two tuning conditions, governed by a receptance matching criterion. This contribution was published in (CARNEIRO JR. *et al*., 2023).

1.5 THESIS OUTLINE

The thesis consists of 6 chapters and 4 appendices. Chapter 1 presents the main purpose of this research, a brief literature review, the objectives of the work, followed by the contributions to knowledge.

Chapter 2 presents the theoretical foundation of the systems discussed in this thesis. The fundamental definitions and relations between receptance, dynamic stiffness and the transfer matrix are presented. These combine with theoretical concepts on wave in elastic structures to discuss the relationship between stop band and attenuation band.

Chapter 3 investigates vibration attenuation in a finite structure comprising *N* periodic rods. Of particular interest was the behaviour of the structure when the cells are either symmetric or asymmetric and the orientation of the cells with respect to the vibration source,

in terms of the frequency range in which there is vibration attenuation, and maximum attenuation within this range. The discontinuity of these cases was provided by a cross-sectional area change. It is demonstrated and discussed in this chapter how asymmetry can be applied to improve vibration attenuation and its limitations.

Chapter 4 extends the analysis to discontinuity in beams under flexural wave motion. The study introduces the concept of local resonance induced by external discontinuities. Using wave-based modelling and transfer matrix formulations, the chapter investigates infinite, semi-infinite and finite beams. In this analysis the discontinuity is comprised by a neutraliser attached to the host structure (cell). The physical mechanism behind the LR phenomena is discussed and the controlling parameters presented.

Chapter 5 investigates the super attenuation band formation in multi-coupled system represented by the Euler-Bernoulli beam model. Based on the approaches and investigations presented in the previous chapters, beams with coupled translational and rotational neutralisers were analysed under different conditions of excitation and response. The differences and similarities between the mono-coupled system and beam analysed are discussed. Numerical techniques and physical concepts, along with the control parameters and practical limitations of the system composed by N cells are presented. Theoretical developments are supported by experimental results.

Chapter 6 presents the final remarks and main conclusions of the thesis, along with recommendations for future work and a list of publications.

Appendix A present the determination of the transfer matrix for a periodic structure containing N cells using the Cayley-Hamilton theorem.

Appendix B presents the technical and procedural details of the experimental results presented throughout this thesis.

Appendix C presents the theoretical foundations and controlling factors of the wave transmission in infinite beams with attached lumped parameters.

Appendix D presents theoretical models to describe beam-like rotational neutralisers.

2 MODELLING FINITE CONTINUOUS PERIODIC STRUCTURES: THEORETICAL FOUDATIONS

2.1 INTRODUCTION

Periodic structures can assume different configurations, both regarding the assembly of their substructures, material composition and how they are subjected to external forces. Nevertheless, it is reasonable to consider that Newton's laws and continuity relations remain applicable to the structure, regardless of its complexity, as well as to its substructures. This often simplifies the analysis of the dynamic behaviour. In the study of vibrations, these kinematic and kinetic relations can be conveniently expressed using receptance or dynamic stiffness functions, which provide a clear physical perspective on the phenomena investigated. These techniques offer powerful tools for analysing linear structures by leveraging their ability to decompose complex systems into manageable substructures.

This chapter presents the methodology used in this thesis, which is divided into three main parts. The first presents a theoretical foundation based on wave motion in elastic structures. The second part presents the foundations in the approach using dynamic stiffness, receptance, and transfer matrix matrices. The last part combines the previous theoretical discussions to explain the filtering properties of periodic structures and draws the comparison between dispersion relation and transmissibility.

This chapter builds upon concepts presented in previous studies – particularly textbooks Wave Motion in Elastic Solids (GRAFF, 1991), Passive Vibration Control (MEAD, 1999), Advanced Applications in Acoustics, Noise and Vibration (FAHY; WALKER, 2004), and Sound and Structural Vibration (FAHY; GARDONIO, 2007) –, extending their application to the modelling of periodic structures.

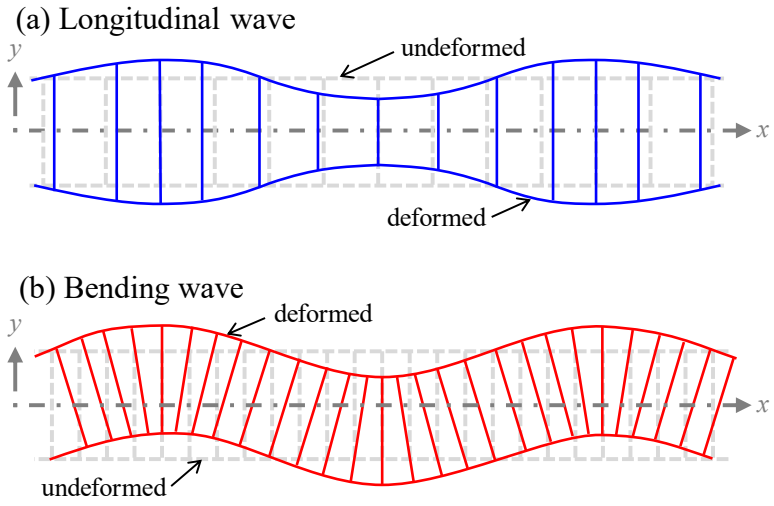
2.2 WAVE MOTION CONCEPTS

In a structure, whether finite or infinite, vibrational energy is transferred from one part to another in the form of a wave. This elastic wave motion is characterized as a phenomenon in which a physical quantity, such as energy, propagates through a medium without the transport of matter (FAHY; GARDONIO, 2007). In this context, the concept of elastic wave propagation will be used to guide the modelling of homogeneous rods and beams.

The types of waves propagating in the one-dimensional systems analysed in this thesis are illustrated in Fig. 2.1. A longitudinal wave is an in-plane wave in which the motion of the particles in the medium is parallel to the direction of wave propagation, with the particles vibrating around their individual equilibrium positions. It is important to note that there is some out-of-plane displacement due to the Poisson's contraction phenomena (*i.e.*, lateral strains) As a result of this phenomenon, structures whose dimensions in all directions are not significantly larger than the wavelength – such as one-dimensional rods as depicted in Fig. 2.1(a) – exhibit lateral displacements (CREMER *et al.*, 1973). Consequently, purely longitudinal motion does not occur in these cases; instead, the motion is described as *quasi-longitudinal*. The model adopted in this thesis is based on the pure longitudinal motion hypothesis.

The other type of wave is the flexural or bending wave, characterized by translational displacement and rotation, as shown in Fig. 2.1(b). In this type of wave motion, the deformation of the medium is governed by bending moments and shear forces. It should be noted that flexural waves are out-of-plane waves.

Figure 2.1. Illustrations of (a) longitudinal and (b) bending waves motion in one-dimensional waveguides. The deformation is exaggerated for clarity.



Source: Fahy and Gardonio (2007) adapted.

A propagating wave that is harmonic in time and space, can be represented by (BRENNAN *et al.*, 2016a)

$$v(x,t) = A\sin(\omega t \pm kx) \tag{2.1a}$$

or

$$v(x,t) = A\cos(\omega t \pm kx)\,, \tag{2.2a}$$

where A is the wave amplitude, ω is the angular frequency, t is the time variable, k is the wavenumber and x is the space variable.

For waves propagating in the positive or negative x direction, the argument takes the form $-kx$ or $+kx$, respectively. The wavenumber is a fundamental concept in harmonic wave motion and can be expressed by the relation (CREMER *et al.*, 1973)

$$k = \frac{2\pi}{\lambda} \tag{2.3}$$

where λ is the wavelength. Note that k is inversely proportional to the wavelength. It follows that the wavenumber can be described in the form of a *spatial frequency*, which physically means that the spatial phase changes per unit distance (BRENNAN *et al.*, 2016a). Analogous to the spatial frequency, the *temporal frequency* ω is inversely proportional to the period, which is the temporal change of phase per unit time.

2.2.1 Phase velocity and dispersion relation

The relationship between the temporal frequency and the spatial frequency of the propagating wave defines the phase velocity, as in Eq. (2.3), that is

$$c = \frac{\omega}{k}\,. \tag{2.4}$$

Considering a wave propagating to the right, its phase can be described as $\phi = \omega t - kx$. For a constant phase ϕ_p we can write (OSTACHOWICZ *et al.*, 2012)

$$x = \left(\frac{\omega}{k}\right)t - \frac{\phi_p}{k} = c_p t - \frac{\phi_p}{k}. \tag{2.5}$$

Consequently, a point of constant phase for each *k*, moves with this velocity c_p. An observer traveling in the direction of wave propagation at this velocity would perceive no change in the wave phase (FAHY; GARDONIO, 2007). From the concept of spatial phase, the distance that a wave travel between the two distinct time instants is ϕ_p / k.

Considering now two right-going propagating waves, with same amplitudes *A*, but with different frequencies and wavenumbers. Each wave propagates with phase velocity c_1 and c_2. These can be summed because of the principle of superposition to give

$$v(x,t) = \bar{A}\sin\left(\left(\frac{\omega_1 + \omega_2}{2}\right)t - \left(\frac{k_1 + k_2}{2}\right)x\right) \tag{2.6}$$

where

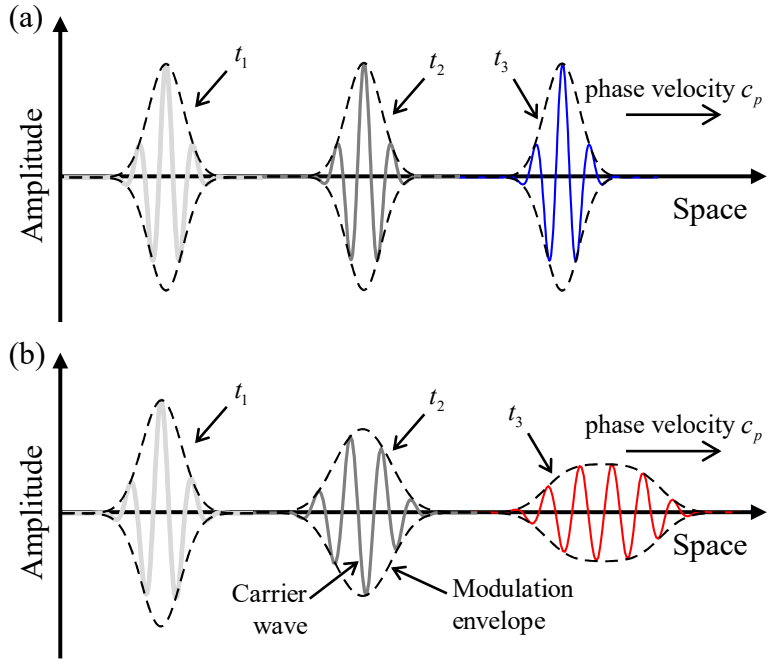
$$\bar{A} = 2A\cos\left(\left(\frac{\omega_1 - \omega_2}{2}\right)t - \left(\frac{k_1 - k_2}{2}\right)x\right).$$

The combined wave has mean frequency of $(\omega_1 + \omega_2)/2$ and mean wavenumber $(k_1 + k_2)/2$, consequently, its propagates with the phase velocity $c_p = (\omega_1 + \omega_2)/(k_1 + k_2)$. Now, the envelope of the combined waves $\bar{A}$ does not propagate at this phase velocity. It propagates at the group velocity, which is the velocity at which the energy in the combined wave is transported and given by (CREMER *et al.*, 1973)

$$c_g = \frac{\omega_1 - \omega_2}{k_1 - k_2}. \tag{2.7}$$

In the limiting case Eq. (2.7) becomes $c_g = \mathrm{d}\omega/\mathrm{d}k$. The group velocity represents the rate at which the frequency changes with respect to the wavenumber. For waves with a phase velocity that is independent of frequency – known as non-dispersive waves – $c_g = c_p$. This is the case of longitudinal waves in rods, as will be discussed later. However, for dispersive waves, where the phase velocity depends on frequency, the group velocity differs from the phase velocity, this is, $c_g \neq c_p$ (BRENNAN *et al.*, 2016a; CREMER *et al.*, 2005; GRAFF, 1991). This is the case of the bending waves in beams. In a non-dispersive structural medium, a vibration pulse generated at a specific point will travel through the structure without distortion. Conversely, if the wave is dispersive, the pulse will change shape as it propagates through the structure. This effect is illustrated in Fig. 2.2.

Figure 2.2. Illustrative examples of wave in (a) non-dispersive (longitudinal waves in a rod) and (b) dispersive medium (bending waves in a beam). Wave packet built up from a sum of cosine functions with different frequencies.



Source: author.

2.3 RECEPTANCE, DYNAMIC STIFFNESS AND TRANSFER MATRIX FORMULATION

The main objects investigated in this thesis include *linear finite* structures. In this sense, the methods of receptance and dynamic stiffness emerge as advantageous tools. This section

introduces the basic definitions and equations governing receptance, dynamic stiffness, and transfer matrix and demonstrates how these concepts are applied in the modelling of combined systems.

The origins and developments of the approach explored in this thesis lie in the foundations of mobility and impedance methods in structural dynamics, which stem from interconnected progress in mechanical and electrical sciences (GARDONIO; BRENNAN, 2002). These methods allow the analysis of mechanical structures in terms of measurable properties, such as force and velocity (mobility/impedance) or force and displacement (receptance/dynamic stiffness), without high-frequency limitations, providing a powerful alternative to traditional methods such as finite element analysis (GARDONIO; BRENNAN, 2004; MCMAHON, 2014; SANTOS *et al*., 2021).

One of the greatest advantages is the interchangeability of the receptance, dynamic stiffness, and transfer matrix approaches. These approaches have evolved to encompass multi-degree-of-freedom systems and flexible, distributed mechanical systems, and researchers continue to refine then to apply at variety of fields (AL BA'BA'A *et al*., 2023; HAN *et al*., 2012; LEE; THOMPSON, 2001).

2.3.1 Definitions of the receptance and dynamic stiffness approach

In general, the receptance and dynamic stiffness are reciprocal frequency response functions; thus, the former is also called *dynamic flexibility*. While receptance is defined as the complex harmonic displacement (response) due to a real unit of force (source), dynamic stiffness is the complex harmonic force required to produce a real unit of displacement (MEAD, 1999, p. 71).

Figure 2.3 shows a linear mono-coupled system with a single displacement coordinate X and two forces F applied to its ends. Following the definitions, it is possible to express the receptance and dynamic stiffness, respectively, by,

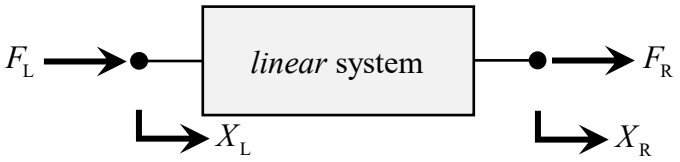
$$R(\omega) = \left.\frac{X_{\mathrm{L}}(\omega)}{F_{\mathrm{L}}(\omega)}\right|_{F_{\mathrm{R}}=0} \quad \text{and} \quad D(\omega) = \left.\frac{F_{\mathrm{L}}(\omega)}{X_{\mathrm{L}}(\omega)}\right|_{X_{\mathrm{R}}=0} \tag{2.8a,b}$$

where ω is the frequency in radians per second and the subscripts L and R represent the left and right ends, respectively. Note that in Eq. (2.8) the boundary conditions $F_{\mathrm{R}} = 0$ and $X_{\mathrm{R}} = 0$ were imposed. In fact, other conditions could be imposed, such as assuming $F_{\mathrm{L}} = 0$ and $F_{\mathrm{R}} \neq 0$ or even $X_{\mathrm{L}} = 0$ and $X_{\mathrm{R}} \neq 0$, which would result in other forms of receptance and dynamic stiffness. The form of Eq. (2.8) is called the driving point (or simply *point*) receptance and driving point dynamic stiffness, since the response and excitation are evaluated at the same positions L. If, on the other hand, the response and excitation are evaluated at different positions, the term *transfer* is adopted, as in the transfer receptance relation between the right-end displacement due to the left-end force expressed by $R(\omega) = X_{\mathrm{R}} / F_{\mathrm{L}}\big|_{F_{\mathrm{R}}=0}$. Therefore, the general way of expressing the receptance and the dynamic stiffness in the systems is given by

$$R_{\mathrm{IJ}}(\omega) = \left.\frac{X_{\mathrm{I}}(\omega)}{F_{\mathrm{J}}(\omega)}\right|_{F_{\mathrm{P}\neq\mathrm{J}}=0} \text{ and } D_{\mathrm{IJ}}(\omega) = \left.\frac{F_{\mathrm{I}}(\omega)}{X_{\mathrm{J}}(\omega)}\right|_{X_{\mathrm{P}\neq\mathrm{J}}=0}, \tag{2.9a,b}$$

where the subscripts I, J and P denote the analysis points of the components. It is evident that if $\mathrm{I} = \mathrm{J}$, one results in the point frequency response functions $R_{\mathrm{II}} = 1/D_{\mathrm{II}}$ and $R_{\mathrm{JJ}} = 1/D_{\mathrm{JJ}}$, or $\mathrm{I} \neq \mathrm{J}$, the transfer frequency response functions $R_{\mathrm{IJ}} = 1/D_{\mathrm{JI}}$ and $R_{\mathrm{JI}} = 1/D_{\mathrm{IJ}}$, imposing the appropriate boundary conditions.

Figure 2.3. Diagram of a linear system subject to unidirectional forces and displacements.



Source: author.

As shown, the terms point and transfer do not refer to the nature of the excitation, for example, a point force, but rather to the excitation point. Thus, in multidirectional or multi-coupled systems, a cross-point receptance can be observed. In future chapters, these functions will also be discussed, such as the complex harmonic transverse displacement due to the real unit of bending moment imposed on a beam. Furthermore, this excitation point implies geometric limitations of the different evaluated systems. As discussed by Cremer (2005, p. 236), in practical cases, a geometric limitation is that the excitation area is much smaller than

the governing wavelength, so the excitation region effectively behaves as a point (upper limit); however, this area cannot be much smaller than the depth of the structure; otherwise, the force applied to a very small area would deform the structure (lower limit).

The relations presented for the receptance and dynamic stiffness are analogous to other frequency response functions, depending on the kinematic variable used (GARDONIO; BRENNAN, 2004, p. 397). When the variables are velocity, mobility and mechanical impedance are obtained; and when the variables are acceleration, inertance or accelerance and apparent mass are obtained (BRENNAN; TANG, 2023, p. 23). This particularity of the models is an advantage from an experimental perspective, allowing easy evaluation of the frequency response functions with different measurement devices.

2.3.2 Relationship between the dynamic stiffness and receptance matrices approach and transfer matrix method

Vibrating systems can be observed in various ways. If, for example, the system shown in Fig. 2.3 represents a transmission path, the state at the ends may be sufficient to evaluate it; on the other hand, if the objective is to evaluate the way in which the vibration changes throughout the system, it becomes important to describe the elements that constitute it. Practical systems are finite structures with defined boundary conditions that, in general, can be divided into smaller parts. The definitions and concepts discussed in the preceding section remain consistent for both the whole and individual parts.

Figure 2.4 represents a system composed of *N* elements. Each element interacts with the adjacent elements through relations of continuity and equilibrium and can form various arrangements of properties. For example, if described as *N* identical elements, a homogeneous structure results; on the other hand, if the properties alternate in defined periods, a periodic structure, or even a graded structure results.

Another important parameter that constitutes the structures is highlighted in the detail of the *n*-th element in Fig. 2.4: the multiple coupling coordinates. From this, we can deduce the displacement vectors **u** and load vectors **f** of dimension i x 1, depending on the number *i* of the coupling coordinates of the motion. This also gives rise to the nomenclature mono-coupled, bi-coupled or multi-coupled. Therefore, the structure where the motion occurs, say, exclusively in the *x*-direction, results in a mono-coupled system with components $\mathbf{u}^{[n]} = \left\{ X_{\mathrm{L}}^{[n]}, X_{\mathrm{R}}^{[n]} \right\}^{\mathrm{T}}$ and

$\mathbf{f}^{[n]} = \left\{F_{\mathrm{L}}^{[n]}, F_{\mathrm{R}}^{[n]}\right\}^{\mathrm{T}}$, as illustrated by the simplification in the same figure. The superscript (T) denotes the transpose.

To predict the complete behaviour of the structure based on the dynamic behaviour of the substructures, it is necessary to know these elements accurately. It is now convenient to describe the dynamic stiffness in matrix form $\mathbf{f}^{[n]} = \mathbf{D}^{[n]}\mathbf{u}^{[n]}$, this is,

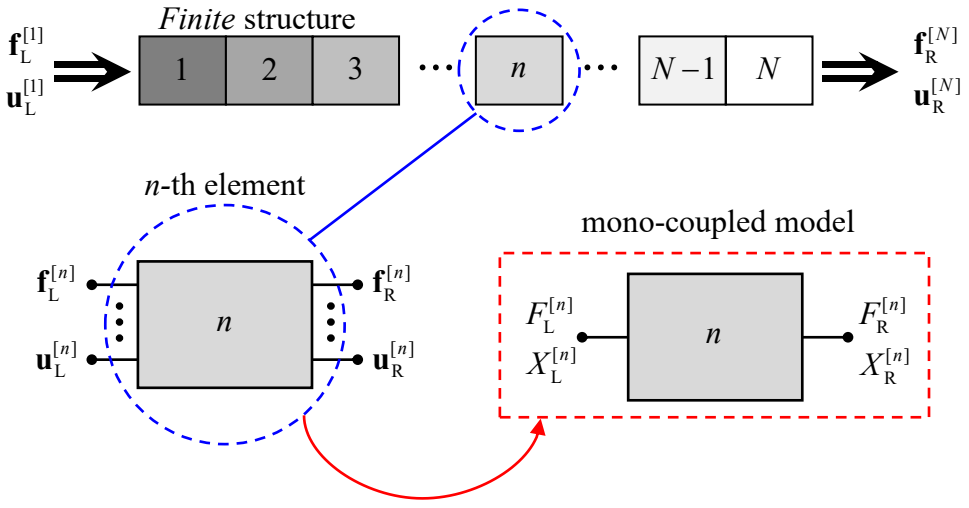
$$\begin{Bmatrix} \mathbf{f}_{\mathrm{L}}^{[n]} \\ \mathbf{f}_{\mathrm{R}}^{[n]} \end{Bmatrix} = \begin{bmatrix} \mathbf{D}_{\mathrm{LL}}^{[n]} & \mathbf{D}_{\mathrm{LR}}^{[n]} \\ \mathbf{D}_{\mathrm{LR}}^{[n]\,\mathrm{T}} & \mathbf{D}_{\mathrm{RR}}^{[n]} \end{bmatrix} \begin{Bmatrix} \mathbf{u}_{\mathrm{L}}^{[n]} \\ \mathbf{u}_{\mathrm{R}}^{[n]} \end{Bmatrix} \tag{2.10}$$

and receptance matrix form $\mathbf{u}^{[n]} = \mathbf{R}^{[n]}\mathbf{f}^{[n]}$ or

$$\begin{Bmatrix} \mathbf{u}_{\mathrm{L}}^{[n]} \\ \mathbf{u}_{\mathrm{R}}^{[n]} \end{Bmatrix} = \begin{bmatrix} \mathbf{R}_{\mathrm{LL}}^{[n]} & \mathbf{R}_{\mathrm{LR}}^{[n]} \\ \mathbf{R}_{\mathrm{LR}}^{[n]\,\mathrm{T}} & \mathbf{R}_{\mathrm{RR}}^{[n]} \end{bmatrix} \begin{Bmatrix} \mathbf{f}_{\mathrm{L}}^{[n]} \\ \mathbf{f}_{\mathrm{R}}^{[n]} \end{Bmatrix}, \tag{2.11}$$

where $\mathbf{D}^{[n]}$ and $\mathbf{R}^{[n]} = \left[\mathbf{D}^{[n]}\right]^{-1}$ are the dynamic stiffness and receptance matrices, respectively.

Figure 2.4. General finite structure composed of N elements with multiple coupling coordinates.



Source: author.

The relationships expressed in Eqs. (2.10) and (2.11) can be extended to any number of coupling coordinates and respective number of loads. The elements of matrices $\mathbf{D}^{[n]}$ and $\mathbf{R}^{[n]}$

are determined by applying different boundary conditions, i.e, continuity of the displacements and the equilibrium of forces.

Three important concepts of the dynamic stiffness/receptance method are implicit in these matrices: symmetry, reciprocity and passivity. From the symmetry results, the point dynamic stiffness at one end is equal to the point dynamic stiffness at the other end, that is, $F_{\mathrm{L}} / X_{\mathrm{L}}\big|^{[n]} = F_{\mathrm{R}} / X_{\mathrm{R}}\big|^{[n]}$. The principle of reciprocity in dynamic stiffness/receptance is the structural dynamics equivalent to the Maxwell-Betti theorem in structural statics (MEAD, 1999, p. 82) and results in the symmetry of the matrices (i.e, $\mathbf{D}_{\mathrm{LR}}^{[n]} = \mathbf{D}_{\mathrm{RL}}^{[n]\mathrm{T}}$). This reciprocity relation means that the harmonic force required in R to produce a harmonic displacement in L is equal to the force required in L to produce an equivalent harmonic displacement in R. The passivity results in terms greater than or equal to zero in the main diagonal elements (point dynamic stiffnesses or point receptances) (O'HARA, 1966).

An alternative method to represent these relationships is the transfer matrix. This representation describes the interaction between the state vectors at points L and R in the system. By considering the receptance matrix in Eq. (2.11), which can be rearranged to separate the loading and displacement in the form of

$$\begin{bmatrix} \mathbf{R}_{\mathrm{RR}}^{[n]} & -\mathbf{I} \\ \mathbf{R}_{\mathrm{LR}}^{[n]} & \mathbf{0} \end{bmatrix} \begin{Bmatrix} \mathbf{f}_{\mathrm{R}}^{[n]} \\ \mathbf{u}_{\mathrm{R}}^{[n]} \end{Bmatrix} = \begin{bmatrix} \mathbf{R}_{\mathrm{RL}}^{[n]} & \mathbf{0} \\ \mathbf{R}_{\mathrm{LL}}^{[n]} & \mathbf{I} \end{bmatrix} \begin{Bmatrix} -\mathbf{f}_{\mathrm{L}}^{[n]} \\ \mathbf{u}_{\mathrm{L}}^{[n]} \end{Bmatrix}, \tag{2.12}$$

where $\mathbf{0}$ and $\mathbf{I}$ are the zero and identity matrices, respectively. The transfer relation of the *n*th element is given by $\mathbf{q}_{\mathrm{R}}^{[n]} = \mathbf{T}^{[n]} \mathbf{q}_{\mathrm{L}}^{[n]}$ (RUBIN, 1967), this is,

$$\begin{Bmatrix} \mathbf{f}_{\mathrm{R}}^{[n]} \\ \mathbf{u}_{\mathrm{R}}^{[n]} \end{Bmatrix} = \begin{bmatrix} \mathbf{T}_{\mathrm{LL}}^{[n]} & \mathbf{T}_{\mathrm{LR}}^{[n]} \\ \mathbf{T}_{\mathrm{RL}}^{[n]} & \mathbf{T}_{\mathrm{RR}}^{[n]} \end{bmatrix} \begin{Bmatrix} -\mathbf{f}_{\mathrm{L}}^{[n]} \\ \mathbf{u}_{\mathrm{L}}^{[n]} \end{Bmatrix}, \tag{2.13}$$

in which

$$\begin{aligned}
\mathbf{T}_{\mathrm{LL}}^{[n]} &= \left[\mathbf{R}_{\mathrm{LR}}^{[n]}\right]^{-1}\mathbf{R}_{\mathrm{LL}}, \\
\mathbf{T}_{\mathrm{LR}}^{[n]} &= \left[\mathbf{R}_{\mathrm{LR}}^{[n]}\right]^{-1}, \\
\mathbf{T}_{\mathrm{RL}}^{[n]} &= \mathbf{R}_{\mathrm{RR}}^{[n]}\left[\mathbf{R}_{\mathrm{LR}}^{[n]}\right]^{-1}\mathbf{R}_{\mathrm{LL}}^{[n]} - \mathbf{R}_{\mathrm{LR}}^{[n]\mathrm{T}}
\end{aligned} \tag{2.14a-c}$$

and

$$\mathbf{T}_{\mathrm{RR}}^{[n]} = \mathbf{R}_{\mathrm{RR}}^{[n]}\left[\mathbf{R}_{\mathrm{LR}}^{[n]}\right]^{-1}. \tag{2.14d}$$

These four terms are also known as four-pole parameters, each of which has a specific physical meaning (MEAD, 1999, p. 92), and can be interpreted as:

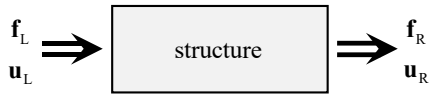
- $\mathbf{T}_{\mathrm{LL}}^{[n]}$, is related to the kinetic transmissibility between R and L when L is motionless;
- $\mathbf{T}_{\mathrm{RR}}^{[n]}$ is related to the kinematic transmissibility between R and L when motion is imposed at R and L is free.

The secondary diagonal carries the transfer frequency response functions:

- $\mathbf{T}_{\mathrm{LR}}^{[n]}$ is the transfer dynamic stiffness and represents the resistive forces in R when motion is imposed on the free end L;
- $\mathbf{T}_{\mathrm{RL}}^{[n]}$, on the other hand, is the transfer receptance and represents the motion in R owing to the imposition of loading on the blocked end L.

Just as the transfer matrix can be written from receptance, it can also be written from dynamic stiffness. The reverse is also consistent, so that $\mathbf{D}^{[n]}$ and $\mathbf{R}^{[n]}$ can be determined from $\mathbf{T}^{[n]}$. Figure 2.5 shows the transformation relation between the receptance, dynamic stiffness, and transfer matrices for a generic structure.

Figure 2.5. Transformations between receptance, dynamic stiffness and transfer matrices for the general finite structure subject to loading and displacements.



from / to	Receptance $\begin{Bmatrix}\mathbf{u}_L\\ \mathbf{u}_R\end{Bmatrix}=\mathbf{R}\begin{Bmatrix}\mathbf{f}_L\\ \mathbf{f}_R\end{Bmatrix}$	Transfer $\begin{Bmatrix}\mathbf{f}_R\\ \mathbf{u}_R\end{Bmatrix}=\mathbf{T}\begin{Bmatrix}\mathbf{f}_L\\ \mathbf{u}_L\end{Bmatrix}$	Dynamic Stiffness $\begin{Bmatrix}\mathbf{f}_L\\ \mathbf{f}_R\end{Bmatrix}=\mathbf{D}\begin{Bmatrix}\mathbf{u}_L\\ \mathbf{u}_R\end{Bmatrix}$
Receptance $\mathbf{R}=$	$\begin{bmatrix}\mathbf{R}_{LL} & \mathbf{R}_{LR}\\ \mathbf{R}_{LR}^{T} & \mathbf{R}_{RR}\end{bmatrix}$	$\begin{bmatrix}-\mathbf{T}_{LR}^{-1}\mathbf{T}_{LL} & -\mathbf{T}_{LR}^{-1}\\ -\left(\mathbf{T}_{LR}^{-1}\right)^{T} & -\mathbf{T}_{RR}\mathbf{T}_{LR}^{-1}\end{bmatrix}$	$\left[\mathbf{D}\right]^{-1}$
Transfer $\mathbf{T}=$	$\begin{bmatrix}\mathbf{R}_{LR}^{-1}\mathbf{R}_{LL} & -\mathbf{R}_{LR}^{-1}\\ \mathbf{R}_{LL}\mathbf{R}_{LR}^{-1}\mathbf{R}_{RR}-\mathbf{R}_{LR}^{T} & \mathbf{R}_{RR}\mathbf{R}_{LR}^{-1}\end{bmatrix}$	$\begin{bmatrix}\mathbf{T}_{LL} & \mathbf{T}_{LR}\\ \mathbf{T}_{RL} & \mathbf{T}_{RR}\end{bmatrix}$	$\begin{bmatrix}-\mathbf{D}_{RR}\mathbf{D}_{LR}^{-1} & \mathbf{D}_{RR}\mathbf{D}_{LR}^{-1}\mathbf{D}_{LL}-\mathbf{D}_{LR}^{T}\\ \mathbf{D}_{LR}^{-1} & -\mathbf{D}_{LR}^{-1}\mathbf{D}_{LL}\end{bmatrix}$
Dynamic Stiffness $\mathbf{D}=$	$\left[\mathbf{R}\right]^{-1}$	$\begin{bmatrix}-\mathbf{T}_{RL}^{-1}\mathbf{T}_{RR} & \mathbf{T}_{RL}^{-1}\\ \left(\mathbf{T}_{RL}^{-1}\right)^{T} & -\mathbf{T}_{LL}\mathbf{T}_{RL}^{-1}\end{bmatrix}$	$\begin{bmatrix}\mathbf{D}_{LL} & \mathbf{D}_{LR}\\ \mathbf{D}_{LR}^{T} & \mathbf{D}_{RR}\end{bmatrix}$

Source: Rubin (1967) adapted.

2.3.3 Complete dynamic stiffness and receptance matrices of combined systems using the transfer matrix for a periodic structure

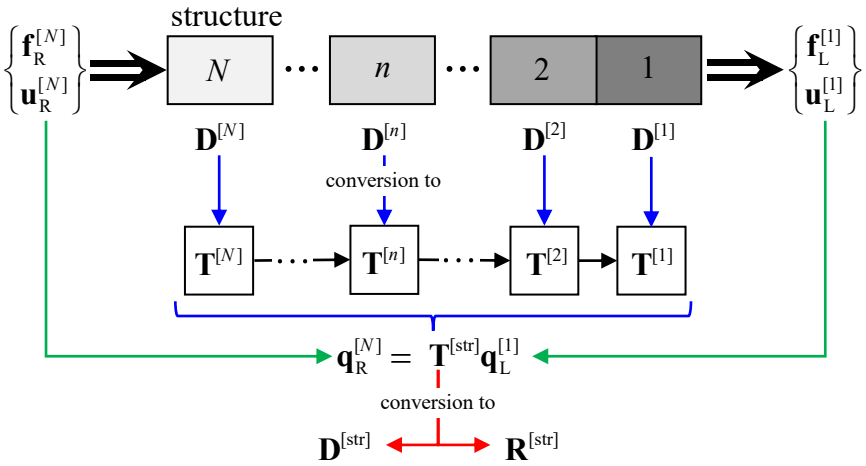
In addition to the important properties of the dynamics of the structure present in the transfer matrix, another significant advantage of this method is its computational and analytical efficiency. For example, the complete structure shown in Fig. 2.4, when described using the dynamic stiffness approach implies the assembly of a square matrix of dimension *N* times the number of coupling coordinates, which is often computationally and algebraically inefficient. In this section, the transfer matrix is used to overcome this condition.

Each element in Fig. 2.4 has a particular transfer matrix that interacts with neighbouring elements through a state with equilibrium and continuity conditions, that is, $\mathbf{u}_R^{[n]}=\mathbf{u}_L^{[n+1]}$ and $\mathbf{f}_R^{[n]}=-\mathbf{f}_L^{[n+1]}$. Hence, $\mathbf{q}_R^{[n+1]}=\mathbf{T}^{[n+1]}\mathbf{T}^{[n]}\mathbf{q}_L^{[n]}$. Expanding this relation, it is determined that the state at the ends of a structure subdivided into *N* elements is related through the product matrix of the individual transfer matrices of each element following the order of the left pre-multiplication by the subsequent element (RUBIN, 1967). In other words,

$$\mathbf{q}_{\mathrm{R}}^{[N]} = \mathbf{T}^{[\mathrm{str}]}\mathbf{q}_{\mathrm{L}}^{[1]} \tag{2.15}$$

where $\mathbf{T}^{[\mathrm{str}]} = \mathbf{T}^{[N]}\mathbf{T}^{[N-1]}\cdots\mathbf{T}^{[1]}$. Thus, for a periodic structure $\mathbf{T}^{[\mathrm{str}]} = \left[\mathbf{T}^{[n]}\right]^{N}$. By knowing $\mathbf{T}^{[\mathrm{str}]}$, the complete dynamic stiffness $\mathbf{D}^{[\mathrm{str}]}$ and complete receptance $\mathbf{R}^{[\mathrm{str}]}$ matrices of the structure can be obtained, as shown in Fig. 2.5. Figure 2.6 presents a pictorial representation of the development of Eq. (2.15).

Figure 2.6. Pictorial representation of complete structure transfer matrix determination.



Source: author.

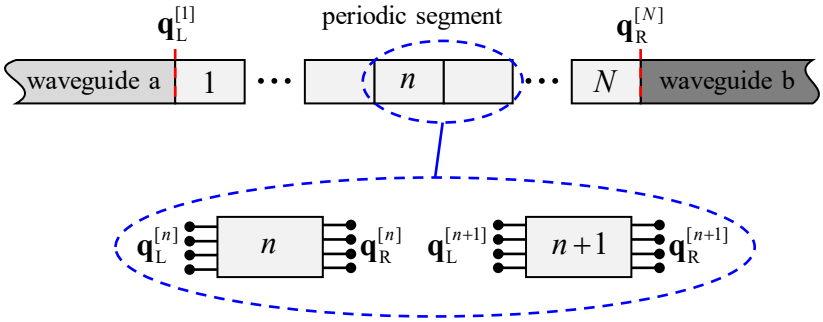
2.4 DISPERSION DIAGRAM AND ATTENUATION BANDS IN PERIODIC STRUCTURES.

Throughout the development of the field of periodic structures, significant research has been conducted on infinite cell systems (HUSSEIN *et al.*, 2014). These approaches provide deep insights into the fundamental physical behaviour of such systems. However, in engineering applications and practical implementations, systems are typically truncated – that is, they are finite in size and constrained by boundary conditions. Compared to infinite systems, considerably less research has been devoted to finite periodic systems. This section outlines the theoretical foundation of the attenuation properties of periodic structures and describes the methodology used to reconcile the physical concepts derived from dispersion curves with observations of transmissibility.

2.4.1 Dispersion relation and filtering properties of periodic structures

Consider the waveguide illustrated in Fig. 2.7, which consists of two semi-infinite sections connected by a periodic transmission path containing N unit cells, where N is very large. The design of periodic structures enables the creation of frequency ranges in which waves can propagate, known as pass bands (PB), and frequency ranges in which wave attenuation occurs, known as stop bands (SB) or band gaps (BRILLOUIN, 1953). Pass and stop bands arise from constructive and destructive wave interference across the periodic structure, respectively, and these effects combine with the overall structure.

Figure 2.7. Waveguides with periodic segment of large number of cells and details in the n-th cell.



Source: author.

According to Mace *et al.* (2023), the total vibration transmission between $\mathbf{q}_{\mathrm{R}}^{[N]}$ and $\mathbf{q}_{\mathrm{L}}^{[1]}$ is influenced by three primary factors. The first is the propagation constant, which governs the PB and SB characteristics of the periodic segment. The second is the impedance discontinuities at the two ends of the structure. The third factor involves internal resonance effects within the periodic segment, caused by successive reflections of Bloch waves that may interfere constructively or destructively.

The Bloch-Floquet theorem states that, for any structure composed of repetitive identical units, the state vector of two consecutive cells (or the change in wave amplitude) is independent of the specific location of the unit cell within the structure (BLOCH, 1929; IQBAL; KUMAR, 2024). According to this theorem, for the cells in the close-up in Fig. 2.7,

$$\mathbf{q}_{\mathrm{L}}^{[n+1]} = \boldsymbol{\psi}\mathbf{q}_{\mathrm{L}}^{[n]}, \tag{2.16}$$

where $\boldsymbol{\psi}$ is the diagonal matrix of the Floquet multipliers that relates the propagation constant (also known as Bloch parameters) ψ in the form e^{ψ}. The dimension of $\boldsymbol{\psi}$ depends on the number of degrees of freedom NDOF of the medium (or coupling coordinates). It has been established that there are 2NDOF distinct values of ψ at any given frequency (MEAD, 1975a); consequently, $\boldsymbol{\psi}$ is a 2x2 matrix for mono-coupled systems, and 4x4 matrix for bi-coupled.

The propagation constants are complex numbers that govern the characteristics of elastic wave propagation in periodic structures. The real part, known as the attenuation constant, quantifies the amplitude decay of wave propagation from one unit cell to the next. The imaginary part, referred to as the phase constant, describes the phase difference between two adjacent cells. When the propagation constant is purely imaginary, $\left|e^{\psi}\right| = 1$, indicating that waves propagate without attenuation, forming a pass band. Conversely, if a real component exists, such that $\left|e^{\psi}\right| \neq 1$, the wave amplitude is attenuated, corresponding to a stop band (MACE *et al*., 2023; MEAD, 1996; SANTOS, 2018). From this foundation, the relationship between frequency and the propagation constant is established. This relationship, known as the dispersion relation, is typically represented in the form of a dispersion diagram, as shown in the following section.

2.4.2 Relationship of dispersion diagram and transmissibility

The relation between the state vectors at the right and left ends of the *n* cell is given by Eq. (2.13). Combining the continuity and equilibrium relations with Eq. (2.13) and Eq. (2.16) leads to the eigenvalue problem expressed by

$$\mathbf{T}\mathbf{q}_{\mathrm{L}}^{[n]} = \boldsymbol{\psi}\mathbf{q}_{\mathrm{L}}^{[n]}, \tag{2.17}$$

in which the superscript [*n*] was omitted from the cell transfer matrix due to periodicity. The solution of Eq. (2.17) provides the values of the Floquet multipliers, from which the propagation constants are easily determined, so that their real and imaginary parts can be evaluated as functions of frequency.

Equation (2.17) is primarily useful for numerical investigations of periodic systems. However, for physical interpretation and analytical development, it may be convenient to write the eigenvalue problem from Eq. (2.12). In this case, Eq. (2.12) can be rewritten as

$$\mathbf{R}_{\mathrm{R}}\mathbf{q}_{\mathrm{R}}^{[n]} = \mathbf{R}_{\mathrm{L}}\mathbf{q}_{\mathrm{L}}^{[n]}. \tag{2.18}$$

Applying the boundary conditions mentioned above and combining the result with the Bloch-Floquet theorem yields the eigenvalue problem given by

$$\left[\mathbf{R}_{\mathrm{R}}\boldsymbol{\psi} - \mathbf{R}_{\mathrm{L}}\right]\mathbf{q}_{\mathrm{L}}^{[n]} = 0. \tag{2.19}$$

Equation (2.19) allows us to write the relationship between the propagation constants and cell receptances, which can be expressed in simple trigonometric functions depending on the course of the investigated system. For example, if the system in question is mono-coupled as in the simplified model in Fig. 2.4, one pair of ψ will exist at any given frequency, and Eq. (2.19) can be reduced to

$$\left(R_{\mathrm{LL}} + R_{\mathrm{RR}} - R_{\mathrm{LR}}\mathrm{e}^{\psi} - R_{\mathrm{RL}}\mathrm{e}^{-\psi}\right)F_{\mathrm{L}} = 0. \tag{2.20a}$$

Using $\mathrm{e}^{\psi} = \cosh\psi + \sinh\psi$ and applying the reciprocity principle, this can be written as

$$\left(R_{\mathrm{LL}} + R_{\mathrm{RR}} - 2R_{\mathrm{RL}}\cosh\psi\right)F_{\mathrm{L}} = 0. \tag{2.20b}$$

Therefore, in this example system, the propagation constant must satisfy

$$\cosh\psi = \frac{1 + R_{\mathrm{RR}}/R_{\mathrm{LL}}}{2\mathrm{TR}}, \tag{2.21}$$

where $\mathrm{TR} = R_{\mathrm{RL}}/R_{\mathrm{LL}}$ denotes the single cell displacement transmissibility. Note that if the cell is symmetric $R_{\mathrm{LL}} = R_{\mathrm{RR}}$, thus $\cosh\psi = 1/\mathrm{TR}$.

Denys Mead (1975a; 1975b) investigated wave propagation and natural modes in mono- and multi-coupled periodic systems using these relations, and basing the theory on these approaches. As recently demonstrated by Gonçalves *et al.* (2021), it is possible to predict the dynamic behaviour of the stop band in finite structures from the transmissibility of a single cell using these relations and the Caley-Hamilton theorem. Appendix A presents the authors' development to obtain, after some manipulations and assuming symmetrical cells, the relationship

$$\cosh N\psi = \frac{1}{X_{\mathrm{R}}^{[N]} / X_{\mathrm{L}}^{[1]}}. \tag{2.22}$$

Displacement transmissibility is the ratio of the generated motion to the imposed motion (CENEDESE *et al*., 2021). Physically, this can be interpreted as the motion at one point of the structure relative to the source motion at another point. However, it is necessary to observe other characteristics of this property for interpretation from the perspective of vibration propagation.

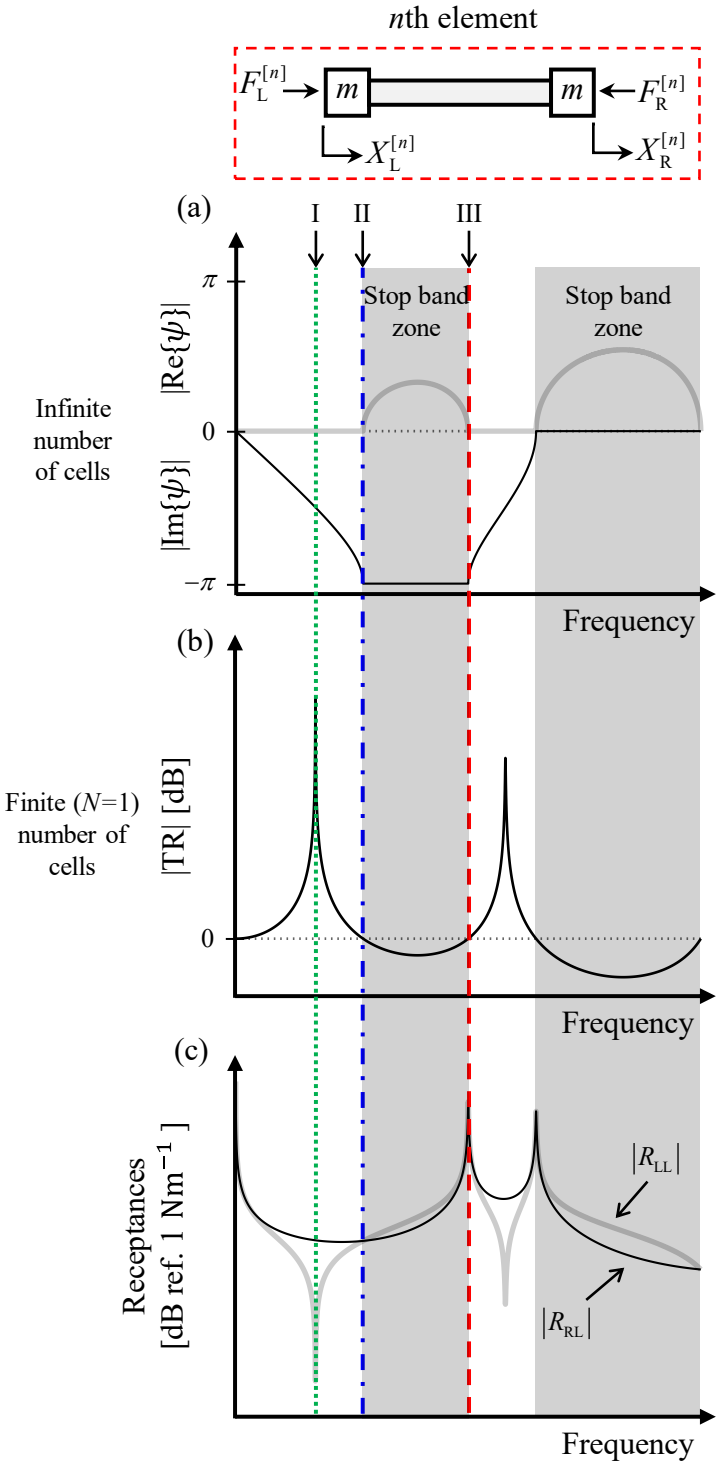
As discussed in Section 2.3.2, and in agreement with Eq. (2.21) the transmissibility is composed of the relationship between the point receptance matrix at R (say at the receiver) and the transfer receptance matrix between points R and L (receiver to source). In other words, the transmissibility matrix relates the frequency response functions between the two points. It is clear that this relationship results in a property that is independent of the source magnitude but rather of the structural points evaluated.

To illustrate the relationship of dispersion diagram and transmissibility, the cases comprising infinite and finite structures are presented in Fig. 2.8. The vibration propagating through the infinite periodic media is evaluated using the wave propagation constant. For a finite periodic structure with N cells, the displacement transmissibility is then calculated from Eq. (2.15). It is considered in the illustration a mono-coupled continuous system with periodic attachments of concentrated masses. A common representation for dispersion curves, transmissibility and correspondent receptances, is shown in Figs. 2.8(a), 2.8(b) and 2.8(c), respectively.

Figure 2.8(a) shows that the stop band occurs when ψ is real and $\mathrm{Im}\{\psi\} = 0$ or $\pm\pi$, which is highlighted by the shaded area. At frequencies where $\mathrm{Re}\{\psi\} = 0$ (purely imaginary), waves propagate without attenuation, thus a pass band.

The modulus of the displacement transmissibility calculated numerically for a single cell is plotted in Fig. 2.8(b). The point and transfer receptances that compose this transmissibility are plotted in Fig. 2.8(c). There are frequency ranges where the transmissibility is amplified (>1), stationary (=1) or reduced (<1). Of particular interest are the regions where it is reduced, and it converges with the stop band frequency zones. These regions are delimited by the points where the transmissibility is stationary, called boundary frequencies.

Figure 2.8. Stop band formation in periodic structure. (a) Dispersion diagram, where $\left|\mathrm{Re}\{\psi\}\right|$ in thick grey line and $-\left|\mathrm{Im}\{\psi\}\right|$ in thin black line. (b) Displacement transmissibility and (c) receptances considering a single cell. Point receptance in thick grey line and transfer receptance in thin black line. Vertical lines highlight the transmissibility feature frequencies.



Source: author.

Comparing the boundary and amplification frequencies with the behaviour presented by the receptances (highlighted by the vertical lines), the characteristics of transmissibility can be explained as follows:

I. The maximum point in an amplification band is the peaks in the transmissibility, which occurs due to the anti-resonance frequency in the point receptance. At these frequencies $|R_{\mathrm{LL}}| \to 0$ (point dynamic stiffness become large), which means that the source point is motionless (large required force to produce motion) and less than the motion at any other point in the structure. Therefore, a resonant-type peak appears;

II. This vertical line highlights the lower boundary frequency. At this frequency the magnitudes of point and transfer receptances are equal, so $\left|X_{\mathrm{R}}^{[N]} / X_{\mathrm{L}}^{[1]}\right| = 1$;

III. The upper boundary frequency highlighted in this case has particular significance because this corresponds to a free-free resonance frequency of the structure. At these frequencies the receptances become large, but their quotient remains finite and $\left|X_{\mathrm{R}}^{[N]} / X_{\mathrm{L}}^{[1]}\right| = 1$.

Although in this thesis the analyses focus on the transmissibility of displacements, there is also the transmissibility of forces, which is indicated in Eq. (2.14a). These two transmissibilities allow us to determine each other, and other frequency response functions of the systems in a relationship as given by Lage *et al.* (2014) and in the works conduced br Maia and other authors (MAIA *et al*., 2001; URGUEIRA *et al*., 2011). From these it is proven an important transmissibility theorem, which states that the displacement transmissibility from L to R when L is free is the same as the force transmissibility from R to L when L is fixed, i.e, $X_{\mathrm{R}}^{[n]} / X_{\mathrm{L}}^{[n]}\big|_{F_{\mathrm{L}}=0} = F_{\mathrm{L}}^{[n]} / F_{\mathrm{R}}^{[n]}\big|_{X_{\mathrm{L}}=0}$ (MEAD, 1999, p. 100).

The example illustrated in Figure 2.8 considers a symmetric cell, and in these cases the stop band bandwidth in the dispersion diagram is the same as the bandwidth where the transmissibility is attenuated. But this does not occur for structures composed of a few asymmetric cells. In these cases, it is convenient to refer to these zones in transmissibility as *attenuation bands* instead of stop bands. The effects of symmetry and asymmetry that influence the behaviour mentioned are discussed in the next chapter.

2.5 CHAPTER REMARKS

This chapter provided the theoretical foundation and methodological framework essential for understanding and modelling finite continuous periodic structures. Through the concepts of wave propagation, receptance, and transfer matrices, it highlighted the interplay between physical phenomena. The exploration of longitudinal and flexural waves, as well as their implications for dispersive and non-dispersive systems, provided essential insights into wave behaviour in elastic media.

The receptance and dynamic stiffness methodologies were explored as powerful tools for analysing linear systems. Based on these discussions and complementary materials, it is concluded that the dynamic stiffness matrix approach is advantageous for the combination of multiple elements. The receptance matrix approach, on the other hand, can be related to experimental procedures, and is therefore advantageous in these cases. The discussion on matrix relationships, symmetry, reciprocity, and passivity underlined the robustness and versatility of these methods for structural dynamic analysis. The integration of these approaches enables prediction of the behaviour of periodic structures based on the analysis of individuals cells, forming the analytical background for subsequent chapters.

The chapter culminated in a detailed analysis of the dispersion properties and transmissibility behaviour of periodic structures. Using the Bloch-Floquet theorem, the relationship between dispersion diagrams and transmissibility was elucidated, providing a direct link between theoretical wave behaviour and practical engineering applications. The methodology for identifying pass and stop bands, as well as attenuation zones in finite systems, was established, and defined as the latter as a convenient nomenclature for the investigations conducted in subsequent chapters.

As this thesis progresses, the methodologies established in this chapter will be extended to explore advanced topics on vibration attenuation enhancement. The following chapters will use the foundations presented here in different theoretical developments, experimental evaluations, and prediction strategies for periodic strucutres.

3 THE EFFECT OF ASYMMETRY ON ATTENUATION BAND ENHANCEMENT IN MONO-COUPLED METASTRUCTURES

3.1 INTRODUCTION

Vibration has the uncanny knack of finding ways to circumvent obstacles in its path, was one of Denys Mead's findings during his years of research (MEAD, 1999, p. 169). This observation underscores the inherent challenges in engineering solutions for controlling vibrations, regardless of whether the goal is to mitigate or harness them. The passive capacity of periodic structures to manipulate wave propagation, which leads to the formation of pass bands and stop bands, renders these systems highly appealing for various applications. However, much of the existing research has focused on infinite periodic systems, such as phononic crystals, leaving significant gaps in the understanding of the effects of boundary conditions, including the emergence of *resonant modes* (AL BA'BA'A *et al*., 2019). Addressing these gaps constitutes the primary objective of this chapter.

In this chapter, the approaches described in Chapter 2 are applied to fill the aforementioned knowledge gap. The aim is to investigate the dynamics of finite periodic structures composed of symmetric and asymmetric cells, specifically rods with varying cross sections, and to determine alternative strategies for their attenuation properties. Using displacement transmissibility, the study derives expressions for designing mono-coupled rod structures with parameters such as length, cross-section, cell orientation, and number of cells. The results presented in this chapter were published in Carneiro Jr. *et al.* (2021).

3.2 MODELLING UNIFORM RODS UNDER LONGITUDINAL VIBRATION

3.2.1 Longitudinal waves in rods

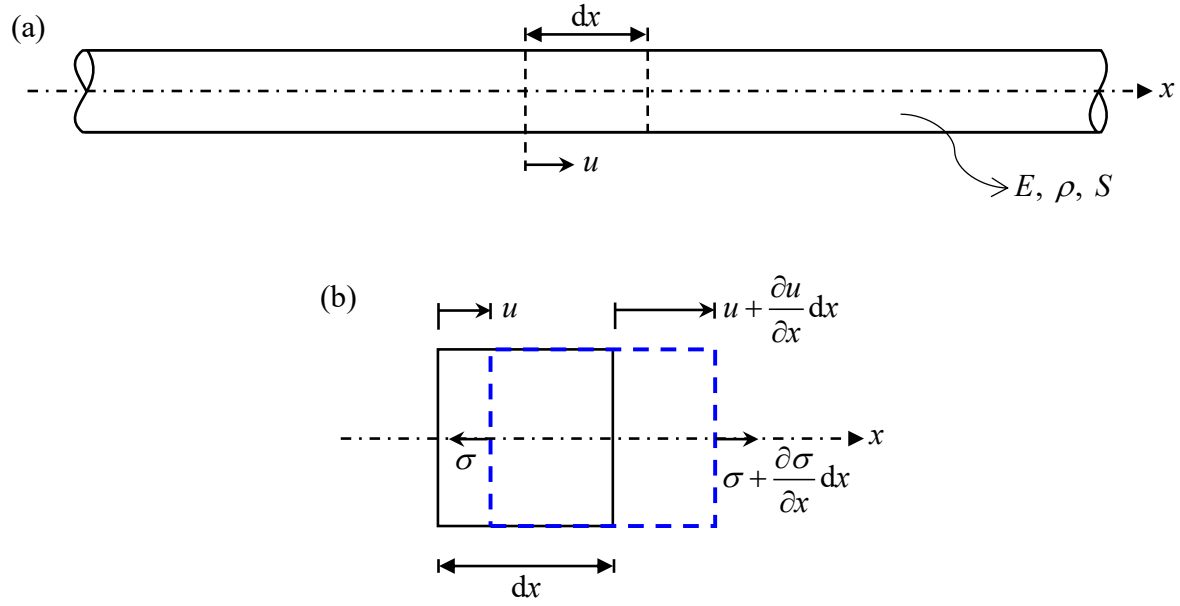
Consider the axial stress in a long, slender, supported rod, as shown in Fig. 3.1. It is assumed that lateral inertia effects associated with lateral contraction-expansion (Poisson's effects) can be neglected. This implies that a pure longitudinal motion is assumed. The

following hypotheses were based on the absence of body forces. According to Newton's law of motion, the equation of longitudinal motion for an element is given by (GRAFF, 1991)

$$\frac{\partial \sigma}{\partial x} = \rho \frac{\partial^2 u}{\partial t^2}, \tag{3.1}$$

where the coordinate x refers to the space variable along the length of the rod, the longitudinal displacement is represented by $u(x,t)$, σ represents the longitudinal stress and ρ the mass density.

Figure 3.1. Thin uniform rod under longitudinal vibration (a) with coordinate x, displacement u, Young's modulus E, mass density ρ and cross-sectional area S. (b) Differential element of the rod with stress action.



Source: Graff (1991) adapted.

From the linear elastic constitutive law (Hooke's law),

$$\sigma = E\frac{\partial u}{\partial x}, \tag{3.2}$$

where E is the Young's modulus. Combining Eq. (3.1) and Eq. (3.2) results in

$$E\frac{\partial^2 u}{\partial x^2} = \rho\frac{\partial^2 u}{\partial t^2} \text{ or } \frac{\partial^2 u}{\partial x^2} = \frac{1}{c^2}\frac{\partial^2 u}{\partial t^2} \tag{3.3a,b}$$

in which $c = \sqrt{E/\rho}$ is the phase velocity of the longitudinal waves in uniform rods. Note that this phase velocity is independent of frequency, such that a wave in a rod is non-dispersive.

Equations (3.3) have an harmonic solution in space and time, expressed by (BRENNAN *et al.*, 2016a)

$$u(x,t) = \left(A^{+}\mathrm{e}^{-\mathrm{j}kx} + A^{-}\mathrm{e}^{\mathrm{j}kx}\right)\mathrm{e}^{\mathrm{j}\omega t}, \tag{3.4}$$

where e is the exponential, $\mathrm{j} = \sqrt{-1}$, $k = \omega/c$ is the rod wavenumber, and A^{+} and A^{-} are the amplitudes of the right- and left-going propagating waves, respectively.

Equation (3.4) can be expressed as $u(x,t) = U(x)\mathrm{e}^{\mathrm{j}\omega t}$, in which

$$U(x) = A^{+}\mathrm{e}^{-\mathrm{j}kx} + A^{-}\mathrm{e}^{\mathrm{j}kx}. \tag{3.5}$$

Therefore, the relationship with the displacement and the stress of the unit uniform element can be related with the wave amplitudes as

$$\begin{Bmatrix} \sigma(x,\omega) \\ U(x,\omega) \end{Bmatrix} = \begin{bmatrix} \mathrm{j}Ek & -\mathrm{j}Ek \\ 1 & 1 \end{bmatrix} \begin{Bmatrix} A^{-}\mathrm{e}^{\mathrm{j}kx} \\ A^{+}\mathrm{e}^{-\mathrm{j}kx} \end{Bmatrix}. \tag{3.6}$$

Considering this infinite rod and assuming a harmonic axial force, such that $\xi_F(t) = F\mathrm{e}^{\mathrm{j}\omega t}$, from elastic constitutive law[2], Eq. (3.6) can be rewritten as

$$\begin{Bmatrix} F(x,\omega) \\ U(x,\omega) \end{Bmatrix} = \begin{bmatrix} \mathrm{j}ESk & -\mathrm{j}ESk \\ 1 & 1 \end{bmatrix} \begin{Bmatrix} A^{-}\mathrm{e}^{\mathrm{j}kx} \\ A^{+}\mathrm{e}^{-\mathrm{j}kx} \end{Bmatrix}, \tag{3.7}$$

where S is the cross-sectional area. Equation (3.7) represents the relationship between the vector of waves amplitudes and the state vector, given by the *transformation matrix*.

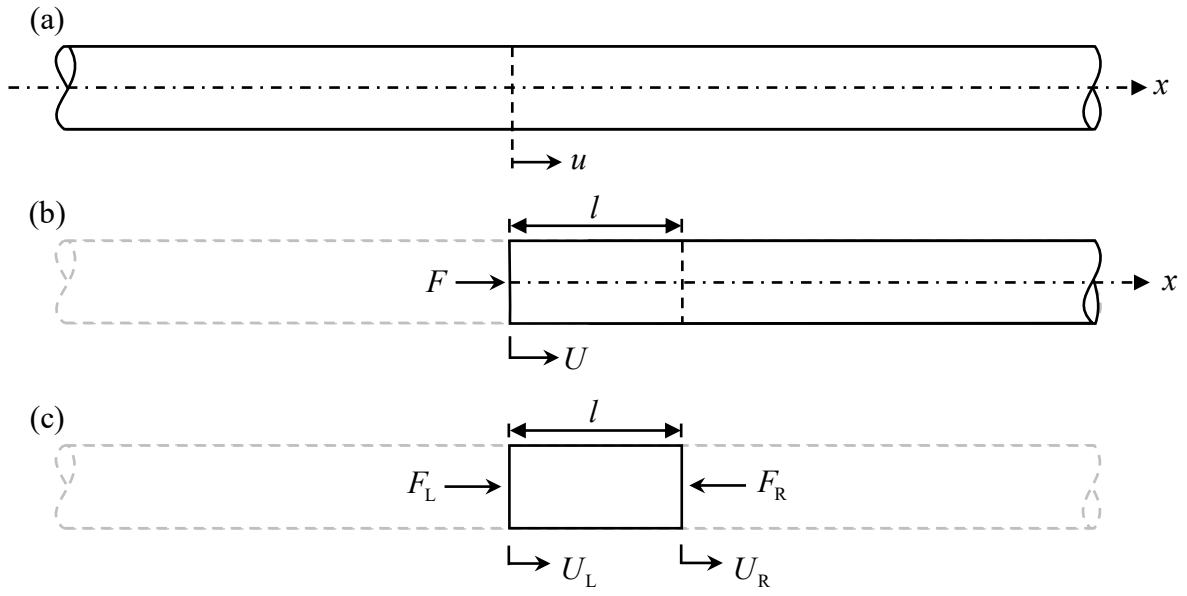
3.2.2 Transfer matrix of uniform rods

Wave amplitudes depend on the geometrical configuration, amplitude, and phase of the excitation force. They can be determined by applying appropriate boundary conditions. For example, considering a semi-infinite rod in which a force is applied at the free end at $x = 0$, as shown in Fig. 3.2(b), the boundary condition is $F = -ES\,\mathrm{d}U/\mathrm{d}x$. As result, the right-going wave amplitude is given by $A^{+} = -F/\mathrm{j}ESk$, and together with the continuity relations, the resistance of the rod to the imposed force can be expressed as

$$\frac{F}{U} = \mathrm{j}ESk = \mathrm{j}\omega S\sqrt{\rho E} = D_{\infty}. \tag{3.8}$$

[2] Note that $F = \int \sigma(x,\omega)\mathrm{d}S = \sigma S$.

Figure 3.2. Uniform rod truncation process. (a) Infinite rod. (b) Semi-infinite rod and (c) finite rod.



Source: author.

In fact, Eq. (3.8) is the point dynamic stiffness of the semi-infinite rod and can be interpreted as the relationship between the complex motion and the correspond ding force required to produce this motion (MEAD, 1999). This relationship is usually observed in the form of impedance, which relates velocity instead displacement with the force. Thus, differentiating the displacement with respect to time results in $F/\dot{U} = S\sqrt{\rho E}$, which is a real quantity and does not vary with frequency. Hence, as seen by the excitation force, a semi-infinite rod also acts as a viscous damper (BRENNAN *et al.*, 2016a).

In terms of the vibration propagation, it is convenient to investigate the state at distinct points in the rod. Thus, consider the truncation to a finite segment, with length *l* between points L and R, as shown in Fig. 3.2(c). Assuming $x = 0$ at L, we can rewrite Eq. (3.7) as

$$\begin{Bmatrix} F_{\mathrm{L}} \\ U_{\mathrm{L}} \end{Bmatrix} = \begin{bmatrix} D_{\infty} & -D_{\infty} \\ 1 & 1 \end{bmatrix} \begin{Bmatrix} A^{-} \\ A^{+} \end{Bmatrix}, \tag{3.9}$$

where the subscript L denotes the position in which the kinematic or kinetic property is evaluated. For $x = l$ at R, the state is expressed by

$$\begin{Bmatrix} F_{\mathrm{R}} \\ U_{\mathrm{R}} \end{Bmatrix} = \begin{bmatrix} D_{\infty} & -D_{\infty} \\ 1 & 1 \end{bmatrix} \begin{Bmatrix} A^{-}\mathrm{e}^{\mathrm{j}kl} \\ A^{+}\mathrm{e}^{-\mathrm{j}kl} \end{Bmatrix} \tag{3.10a}$$

or

$$\begin{Bmatrix} F_{\mathrm{R}} \\ U_{\mathrm{R}} \end{Bmatrix} = \begin{bmatrix} D_{\infty} & -D_{\infty} \\ 1 & 1 \end{bmatrix} \begin{bmatrix} \mathrm{e}^{\mathrm{j}kl} & 0 \\ 0 & \mathrm{e}^{-\mathrm{j}kl} \end{bmatrix} \begin{Bmatrix} A^{-} \\ A^{+} \end{Bmatrix}. \tag{3.10b}$$

The second matrix in Eq. (3.10b) is the spatial transformation matrix. Combining Eqs. (3.10b) and (3.9), it is found that the state vectors between points R and L of the uniform rod are related by

$$\begin{Bmatrix} F_{\mathrm{R}} \\ U_{\mathrm{R}} \end{Bmatrix} = \mathbf{T} \begin{Bmatrix} F_{\mathrm{L}} \\ U_{\mathrm{L}} \end{Bmatrix}, \tag{3.11}$$

where **T** denotes the rod transfer matrix given by

$$\mathbf{T} = \begin{bmatrix} D_{\infty} & -D_{\infty} \\ 1 & 1 \end{bmatrix} \begin{bmatrix} \mathrm{e}^{\mathrm{j}kl} & 0 \\ 0 & \mathrm{e}^{-\mathrm{j}kl} \end{bmatrix} \begin{bmatrix} D_{\infty} & -D_{\infty} \\ 1 & 1 \end{bmatrix}^{-1} = \begin{bmatrix} \cos(kl) & \mathrm{j}D_{\infty}\sin(kl) \\ \dfrac{\mathrm{j}}{D_{\infty}}\sin(kl) & \cos(kl) \end{bmatrix}. \tag{3.12}$$

The transfer matrix has important dynamic parameters for the system in each element, as discussed in the previous chapter, and is used to model the periodic rod in the next section.

3.3 FINITE PERIODIC STRUCTURE COMPRISING *N* CELLS

Figure 3.3 shows the structure of interest in this section, which consists of a periodic system comprising identical cells. Cells are composed of elements a and b, with different properties, and arranged in a symmetrical or asymmetrical manner in relation to the axis normal to excitation in the centre of the cell. Because the structure is periodic and continuous, there are several frequency ranges within which the vibration is attenuated, known as attenuation bands. The attenuation bands are the same as the stop bands (MEAD, 1975a), which are frequency ranges in an infinite structure where waves do not propagate if the structure is composed of mono-coupled symmetric cells. If the structure is composed of asymmetric cells, then the attenuation bands are not the same as the stop bands unless the structure is of infinite length. Section 2.4.2 has discussed the stop band/attenuation band relation.

Of particular interest in this chapter is the determination of the lower and upper cut-off frequencies of the attenuation band and the maximum attenuation in the lowest attenuation band of a finite periodic structure. To this end, the focus is on the transmissibility of the system, which is described based on the relations of the transfer matrix method, as presented in Chapter 2.

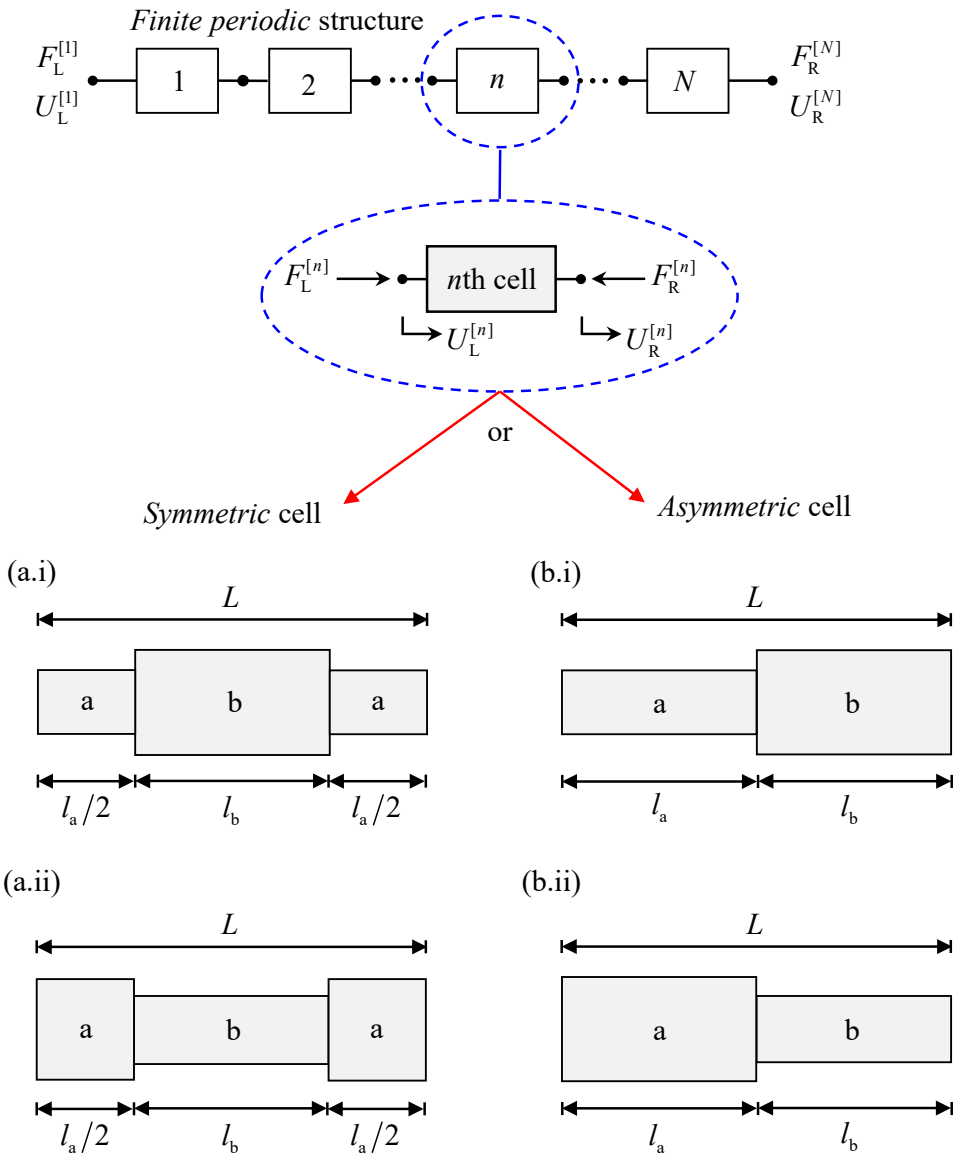
The transfer matrix of the complete structure is given by Eq. (2.15) due to the periodicity, i.e, $\mathbf{T}^{[\mathrm{str}]} = \left[\mathbf{T}^{[\mathrm{cell}]}\right]^{N}$. Some authors have investigated ways to express the power of the cell matrix (GONÇALVES *et al*., 2021; SANTOS, 2018). As shown in Appendix A, using the Cayley–Hamilton theorem, the structure transfer matrix can be written as

$$\mathbf{T}^{[\mathrm{str}]} = \begin{bmatrix} \cosh(N\psi) - (T_{\mathrm{LL}} - T_{\mathrm{RR}})\dfrac{\sinh(N\psi)}{2\sinh(\psi)} & \dfrac{T_{\mathrm{LR}}\sinh(N\psi)}{\sinh(\psi)} \\ \dfrac{T_{\mathrm{RL}}\sinh(N\psi)}{\sinh(\psi)} & \cosh(N\psi) + (T_{\mathrm{LL}} - T_{\mathrm{RR}})\dfrac{\sinh(N\psi)}{2\sinh(\psi)} \end{bmatrix}, \quad (3.13)$$

where $\psi = \operatorname{acosh}\left(\dfrac{T_{\mathrm{LL}} + T_{\mathrm{RR}}}{2}\right)$ (as given by Eq. (2.21) in Sec. 2.42) and T_{PP} are the single cell transfer matrix terms (the superscript [*n*] was omitted for simplicity). Thus, in the general case the displacement transmissibility for the structure with *N* cells is given by

$$\frac{U_R^{[N]}}{U_L^{[1]}} = \frac{2\sinh(\psi)}{2\sinh(\psi)\cosh(N\psi)+(T_{\mathrm{LL}}-T_{\mathrm{RR}})\sinh(N\psi)}. \tag{3.14}$$

Figure 3.3. General finite mono-coupled periodic structure composed of N cells and a detail in the nth (a) symmetric and (b) asymmetric cells with different configurations: (i) $\alpha>1$, (ii) $\alpha<1$ and all cases $\gamma=1$.



Source: Carneiro Jr. *et al.* (2021) adapted.

Four cases are considered, which are shown in Fig. 3.3. The first set involves symmetric cells shown in Fig. 3.3(a) and the second set comprises the asymmetric cells shown in Fig. 3.3(b). In approximation to practical systems, the continuous structure excited longitudinally is assumed according to the rod model.

To create an attenuation band by appropriately arranging the geometry of the rods, the same material was assumed for elements a and b, therefore the longitudinal wavenumber $k = \omega/\sqrt{E/\rho}$ (due to phase velocity) (CREMER *et al.*, 2005, p. 32) is equal for both segments. The cross-sectional areas and lengths of the rods could be changed with respect to each other, but keeping the total length of the cell $L = l_\mathrm{a} + l_\mathrm{b}$ constant. These relative changes are characterized by the parameters

$$\alpha = \frac{\text{cross-sectional area of b}}{\text{cross-sectional area of a}} = \frac{S_\mathrm{b}}{S_\mathrm{a}} \text{ and } \gamma = \frac{\text{length of b}}{\text{length of a}} = \frac{l_\mathrm{b}}{l_\mathrm{a}}. \tag{3.15a,b}$$

In the next sections, the area ratio α and the length ratio γ are investigated in order to determine the optimal parameters for improving the attenuation bands in the proposed structure. These are investigated according to the transfer matrix model that describes that the relationship between the forces and displacements at each end of a rod element is given accordingly Eq. (2.13), *i.e.*, $\mathbf{q}_\mathrm{R}^{[i]} = \mathbf{T}^{[i]}\mathbf{q}_\mathrm{L}^{[i]}$, where $\mathbf{q}_\mathrm{R}^{[i]} = \left\{F_\mathrm{R}^{[i]}, U_\mathrm{R}^{[i]} ES_i k\right\}^\mathrm{T}$, $\mathbf{q}_\mathrm{L}^{[i]} = \left\{F_\mathrm{L}^{[i]}, U_\mathrm{L}^{[i]} ES_i k\right\}^\mathrm{T}$ and the displacement are normalised by the rod properties.

3.3.1 Symmetric cell

As shown by Eq. (3.14), the displacement transmissibility of the complete structure is described as a function of the number of cells and terms of the main diagonal of the transfer matrix of a single cell. For a symmetric cell $T_\mathrm{LL} = T_\mathrm{RR}$, then $\psi = \operatorname{acosh}\left(T_\mathrm{LL}\right)$ and the displacement transmissibility for the complete structure with *N* cells can be simplified to $U_R^{[N]}/U_L^{[1]}\Big|^{[\mathrm{Sym}]} = 1/\cosh\left(N\psi\right)$ (Eq. 2.22). Noting that $\operatorname{acosh}\left(z\right) = \ln\left(z + \sqrt{z^2 - 1}\right)$, this transmissibility can be written as

$$\left.\frac{U_{\mathrm{R}}^{[N]}}{U_{\mathrm{L}}^{[1]}}\right|^{[\mathrm{Sym}]} = \frac{2}{\left(\frac{1}{\overline{T}}+\sqrt{\frac{1}{\overline{T}^2}-1}\right)^{N}+\left(\frac{1}{\overline{T}}+\sqrt{\frac{1}{\overline{T}^2}-1}\right)^{-N}}, \tag{3.16}$$

where the term $\overline{T} = 1/T_{\mathrm{LL}} = U_{\mathrm{R}}^{[n]}/U_{\mathrm{L}}^{[n]}$ is the longitudinal displacement transmissibility of a single cell.

As discussed in the previous chapter, the transmissibilities can be determined from the transfer matrix. The transfer matrix for the symmetric cell shown in Fig. 3.3(a) is the product of three transfer matrices, one for each rod segment, so that

$$\mathbf{T}^{[\mathrm{Sym}]} = \mathbf{T}^{[\mathrm{a}]}\mathbf{T}^{[\mathrm{b}]}\mathbf{T}^{[\mathrm{a}]}, \tag{3.17}$$

where

$$\mathbf{T}^{[\mathrm{a}]} = \begin{bmatrix} \cos\left(\frac{kL}{2(1+\gamma)}\right) & -\sin\left(\frac{kL}{2(1+\gamma)}\right) \\ \sin\left(\frac{kL}{2(1+\gamma)}\right) & \cos\left(\frac{kL}{2(1+\gamma)}\right) \end{bmatrix} \text{ and } \mathbf{T}^{[\mathrm{b}]} = \begin{bmatrix} \cos\left(\frac{kL\gamma}{1+\gamma}\right) & -\alpha\sin\left(\frac{kL\gamma}{1+\gamma}\right) \\ \frac{1}{\alpha}\sin\left(\frac{kL\gamma}{1+\gamma}\right) & \cos\left(\frac{kL\gamma}{1+\gamma}\right) \end{bmatrix}.$$

The coefficients of the trigonometric terms are given by the product of the wavenumber and segment length: for a, $k\,l_{\mathrm{a}}/2 = kL/2(1+\gamma)$ and for b $kl_{\mathrm{b}} = kL\gamma/(1+\gamma)$.

The transmissibility for the single symmetric cell is given

$$\overline{T}\Big|^{[\mathrm{Sym}]} = \left.\frac{U_{\mathrm{R}}^{[n]}}{U_{\mathrm{L}}^{[n]}}\right|^{[\mathrm{Sym}]}_{F_{\mathrm{R}}=0} = \frac{4\alpha}{(\alpha+1)^2\cos(kL)-(\alpha-1)^2\cos(kL\Lambda)}, \tag{3.18}$$

where $\Lambda = (\gamma - 1)/(\gamma + 1)$. Note that, unlike the area ratio, the influence of the length ratio is implicit only in the coefficient of the trigonometric term. Since the wavenumber is a spatial frequency inversely proportional to the spatial period, *i.e.*, to the wavelength λ (CREMER *et al.*, 2005, p. 32), the product $kL\Lambda$ can be interpreted as the difference between the ratio of the wavelength in each element of the cell.

To determine the ratio of the lengths of the rods elements γ, which minimizes the transmissibility, Eq. (3.18) is differentiated with respect to Λ and solved for $\partial\left|\overline{T}\right|^{[\mathrm{Sym}]}/\partial\Lambda = 0$, this is

$$\frac{-4(\alpha-1)^2\,\alpha kL\sin(kL\Lambda)}{\left[(\alpha+1)^2\cos(kL)-(\alpha-1)^2\cos(kL\Lambda)\right]^2}=0.$$

This leads to the condition that $\sin(kL\Lambda)=0$, which has solutions when $\Lambda = \pi(a-1)/kL$ for $a = 1,\ 2,\ ...,\ \infty$, where a is the order of attenuation bands from low to high frequencies. For the first stop band $a=1$, so that $\Lambda = 0$. This means that $\gamma = 1$ and consequently $l_a = l_b = l$, which when substituted into Eq. (3.18) results in (CARNEIRO JR. *et al.*, 2021)

$$\left|\overline{T}\right|^{[\mathrm{Sym}]} = \frac{4\alpha}{(\alpha-1)^2-(\alpha+1)^2\cos(2kl)}. \tag{3.19}$$

Equation (3.19) can now be investigated based on the area ratio. If α is greater (smaller) than unity, the cross-sectional area of the element b is greater (smaller) than the cross-sectional area of the element a. No attenuation (stop) band exists when $\alpha = 1$, in this case the transmissibility is simply $\left|\sec(2kl)\right|$. It is worth noting that in Eq. (3.19), substituting α with $1/\alpha$ yields the same transmissibility, indicating that the arrangements shown in Figures 3.3(ai) and 3.3(aii) produce identical outcomes.

Equation (3.19) is plotted in Fig. 3.4(a) as a function of l/λ, where $\lambda = 2\pi/k$ is a wavelength in the structure, for values of $\alpha = 0.5$ and $\alpha = 2$. To limit the peaks response, a loss factor of $\eta = 0.01$ is assumed to add some damping to the structure, such that its Young's modulus becomes complex and is given by $E(1+\mathrm{j}\eta)$ (CREMER *et al.*, 2005, p. 153). It can be seen that there is a frequency range in which $|T| \leq 1$. This corresponds to the stop band in which a wave in an infinite structure cannot propagate. The frequencies at the boundaries of the stop band can be determined by setting Eq. (3.19) to ± 1 (MEAD, 1975a). The resulting equation can be solved to give (CARNEIRO JR. *et al.*, 2021)

$$\left.\frac{l}{\lambda}\right|_{\text{lower}} = \frac{1}{\pi}\operatorname{atan}\sqrt{\alpha}, \qquad \left.\frac{l}{\lambda}\right|_{\text{ùpper}} = \frac{1}{\pi}\operatorname{atan}\sqrt{\frac{1}{\alpha}}, \qquad \text{for } \alpha < 1 \qquad (3.20a,b)$$

and

$$\left.\frac{l}{\lambda}\right|_{\text{lower}} = \frac{1}{\pi}\operatorname{atan}\sqrt{\frac{1}{\alpha}}, \qquad \left.\frac{l}{\lambda}\right|_{\text{upper}} = \frac{1}{\pi}\operatorname{atan}\sqrt{\alpha}, \qquad \text{for } \alpha > 1. \qquad (3.20c,d)$$

These frequency boundaries are shown in Fig. 3.4 as blue circles.

The minimum vibration transmission through the cell occurs when $l/\lambda = 1/4$. At this frequency $\cos(2kl) = -1$, and Eq. (3.19) becomes

$$\left.\overline{T}\right|_{\text{min}}^{[\text{Sym}]} = \frac{2}{\alpha + \alpha^{-1}}. \qquad (3.21)$$

This is shown in Fig. 3.4 as a green square.

Now investigating for multiple cells, the modulus of Eq. (3.16) is plotted in Fig. 3.4(b) for $N = 3$ and $N = 6$. The attenuation band is clear in the figure, where it can be seen that its bandwidth does not change as *N* increases – Eq. (3.20) holds true for these cases and gives the

boundary frequencies of the attenuation (stop) band irrespective of the number of cells in the periodic structure.

The minimum transmissibility can be obtained by substituting Eq. (3.21) into Eq. (3.16), which gives (CARNEIRO JR. *et al.*, 2021)

$$\left|\frac{U_{\mathrm{R}}^{[N]}}{U_{\mathrm{L}}^{[1]}}\right|_{\min} = \frac{2}{\alpha^{N}+\alpha^{-N}}. \tag{3.22}$$

When $\alpha^{2N} >> 1$, Eq. (3.22) can be approximated to $U_{\mathrm{R}}^{[N]}/U_{\mathrm{L}}^{[1]}\big|_{\min} \approx 2/\alpha^{N}$. The reciprocal of this value expresses the maximum attenuation that can be achieved within the attenuation (stop) band, *i.e.*,

$$\text{maximum attenuation} \approx \frac{\alpha^{N}}{2}.$$

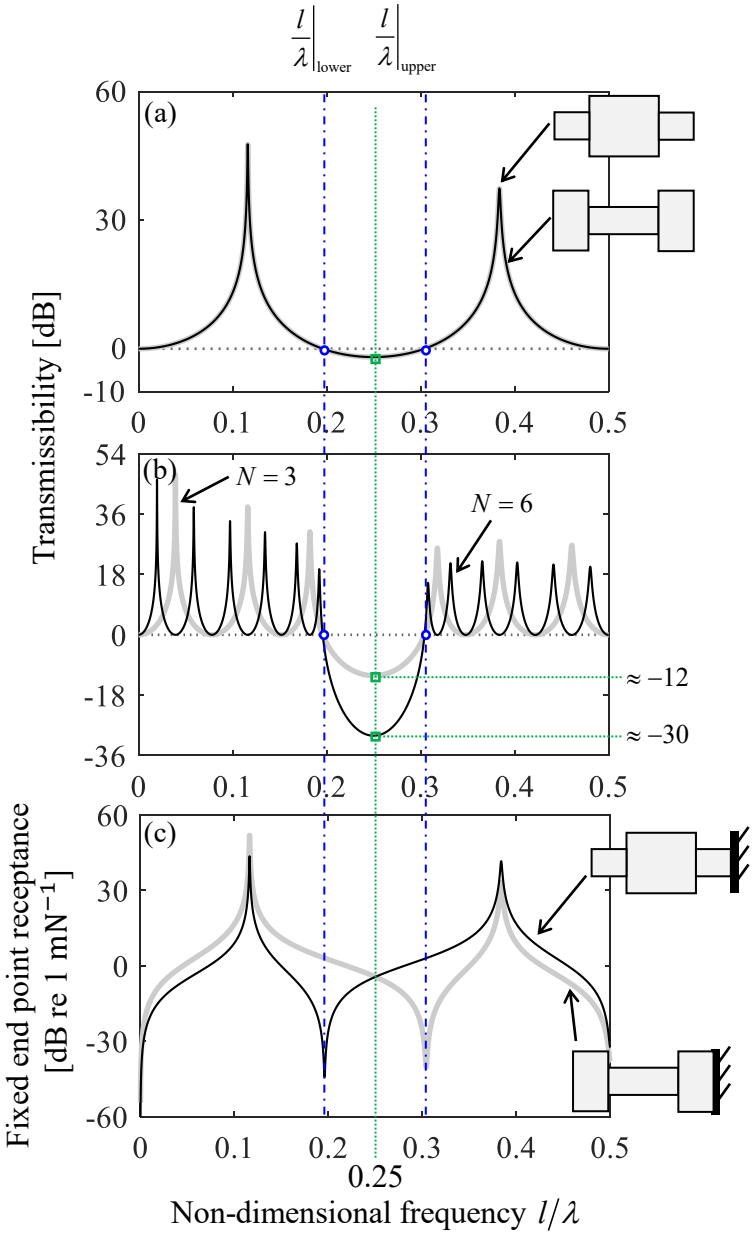
Provided this approximation holds, then the attenuation in dB increases linearly as the number of cells increases. It is shown in the Fig. 3.4(b) as a square is this maximum attenuation.

The minimum transmissibility frequency $l/\lambda\big|_{\min}$, together with the $l/\lambda\big|_{\text{lower}}$ and $l/\lambda\big|_{\text{upper}}$ frequencies, comprise the boundary frequencies of the attenuation band. In particular, the two latter are related to important parameters for structural dynamics. As discussed in Chapter 2, one of them occurs when the modulus of the point and transfer receptances tends to infinity, that is, at the natural frequency of the free-free cell. The dynamics of the other boundary frequency can be investigated from the point receptance when U_{R} is set to zero. In this case (GONÇALVES *et al*., 2021),

$$\left.\frac{U_{\mathrm{L}}}{F_{\mathrm{L}}}\right|_{U_{\mathrm{R}}=0} = \frac{R_{\mathrm{LL}}{}^{2}-R_{\mathrm{RL}}{}^{2}}{R_{\mathrm{LL}}}. \tag{3.23}$$

This expression is illustrated in Fig. 3.4(c). Note that the boundary frequencies highlighted by the dashed vertical lines correspond to anti-resonances of this receptance. This means that this frequency occurs at the natural frequency of the cell in the fixed-fixed boundary condition. Therefore if $\alpha > 1$, then $l/\lambda\big|_{\text{lower}}$ and $l/\lambda\big|_{\text{upper}}$ correspond to the free-free and fixed-fixed natural frequencies of the single cell (MEAD, 1975a). On the other hand, if $\alpha < 1$, then $l/\lambda\big|_{\text{lower}}$ and $l/\lambda\big|_{\text{upper}}$ correspond to the fixed-fixed and free-free natural frequencies, respectively, of the single cell.

Figure 3.4. Attenuation band and bounding frequencies analysis of a periodic structure comprising symmetric cells. Displacement transmissibility of (a) a single cell and and (b) multiple cells; thick grey line, $N=3$; thin black line, $N=6$, with $\alpha=0.5$ or $\alpha=2$. (c) Point receptance of a single cell with $U_{\mathrm{R}}=0$ with $\alpha=0.5$ in thick grey line and $\alpha=2$ in thin black line. The bounding frequencies are given by the expression in Tab. 3.1.



Source: author.

3.3.2 Asymmetric cell

Consider now the asymmetric cell shown in Fig. 3.3(b). For cells oriented as in this case the transfer matrix is given by the product of the matrices $\mathbf{T}^{[a]}$ and $\mathbf{T}^{[b]}$ of Eq. (3.17) rearranged in the form

$$\mathbf{T}^{[\mathrm{Asy}]} = \mathbf{T}^{[b]}\mathbf{T}^{[a]}\mathbf{T}^{[a]}. \tag{3.24}$$

As in the symmetric system, the transmissibility is the reciprocal of element 2,2 in the matrix $\left[\mathbf{T}^{[\mathrm{Asy}]}\right]^{-1}$, so that

$$\overline{T}\Big|^{[\mathrm{Asy}]} = \frac{U_{\mathrm{R}}^{[n]}}{U_{\mathrm{L}}^{[n]}}\bigg|_{F_{\mathrm{R}}=0}^{[\mathrm{Asy}]} = \frac{2}{(\alpha+1)\cos(kL)-(\alpha-1)\cos(kL\Lambda)}, \tag{3.25}$$

where $\Lambda = (\gamma-1)/(\gamma+1)$.

The optimum length of the elements is determined by applying the same procedure as in the previous section, *i.e.*, $\partial\left|\overline{T}\right|^{[\mathrm{Asy}]}/\partial\Lambda = 0$. From this it is found the optimum length ratio is $\gamma = 1$ so that $l_{\mathrm{a}} = l_{\mathrm{b}} = l$. Substituting this into Eq. (3.25) results in (CARNEIRO JR. *et al.*, 2021)

$$\overline{T}\Big|^{[\mathrm{Asy}]} = \frac{2}{(\alpha+1)\cos(2kl)-(\alpha-1)}. \tag{3.26}$$

Equation (3.26) is plotted in Fig. 3.5(i) as a function of l/λ for $\alpha = 2$ (a) and $\alpha = 0.5$ (b). As for the symmetric cell, a loss factor of $\eta = 0.01$ is assumed. For comparison, the transmissibility for the corresponding symmetric cell is also shown. It can be seen that there is a frequency range for the transmissibility of the asymmetric cell in which $\left|\overline{T}\right| \le 1$ for $\alpha = 2$,

but this does not correspond to the stop band shown in Fig. 3.5(a.i). It is thus called the attenuation band, which is larger than the stop band for this type of system. To determine the frequencies at the boundaries of the attenuation band, Eq. (3.26) is set to -1 as in the symmetric case, and the resulting equation solved to give

$$\left.\frac{l}{\lambda}\right|_{\text{lower}} = \frac{1}{2\pi}\operatorname{atan}\sqrt{\frac{2}{\alpha-1}} \quad \text{and} \quad \left.\frac{l}{\lambda}\right|_{\text{upper}} = \frac{1}{4}+\frac{1}{2\pi}\operatorname{atan}\sqrt{\frac{\alpha-1}{2}}, \quad \text{for } \alpha>1. \tag{3.27a,b}$$

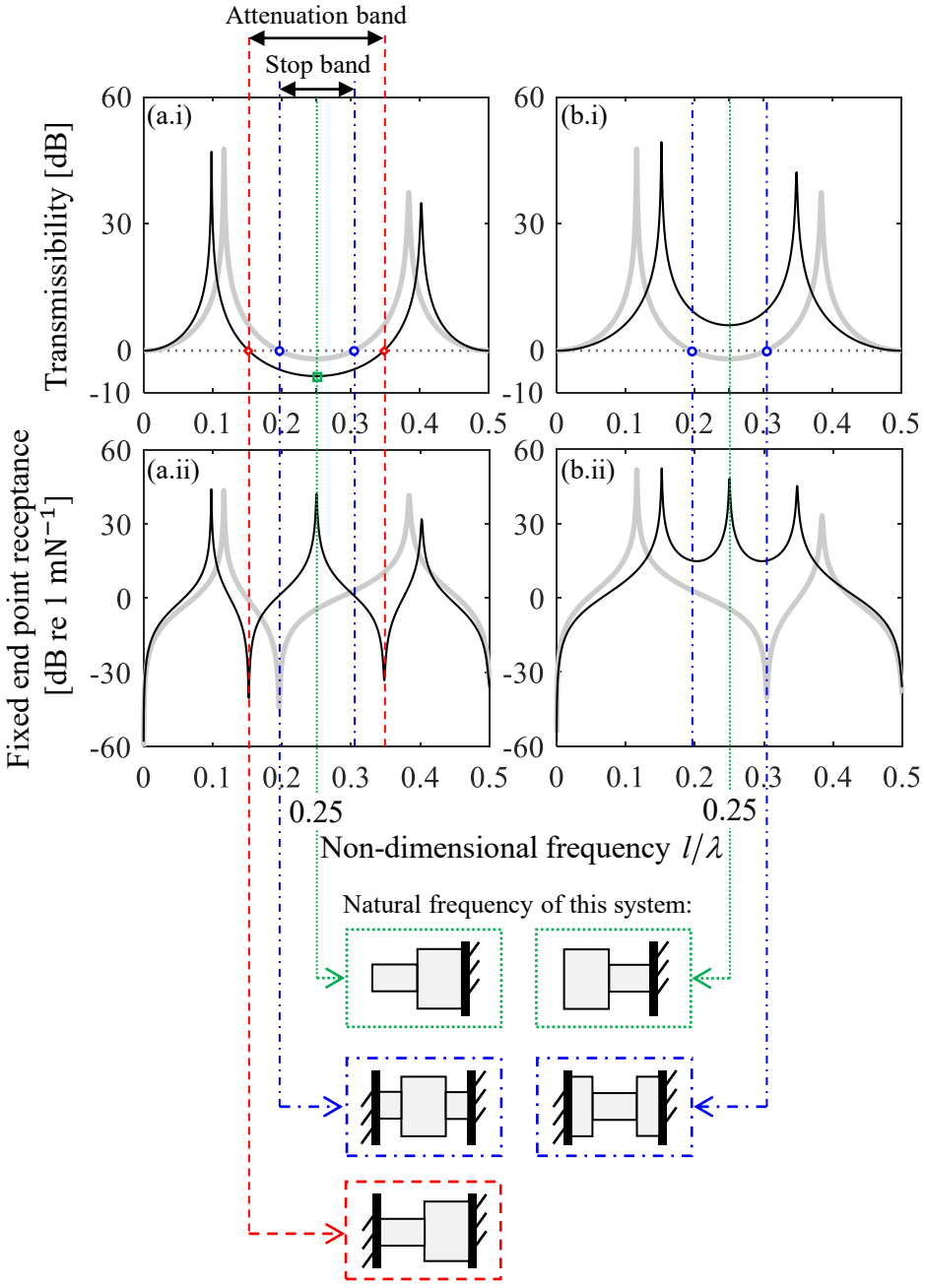
It can be seen in Fig. 3.5(b), where $\alpha = 0.5$, that an attenuation band does not exist for $\alpha \le 1$. When $\alpha > 1$, the minimum attenuation occurs at $l/\lambda = 1/4 = l/\lambda|_{\text{min}}$, as with the symmetric case. Substituting this into Eq. (3.26) results in

$$\left|\bar{T}\right|_{\text{min}}^{[\text{Asy}]} = \frac{1}{\alpha}. \tag{3.28}$$

This is shown in Fig. 3.5(a.i) as a square.

Figure 3.5(ii) shows the point receptance when $U_{\text{R}} = 0$, as expressed in Eq. (3.23), for the symmetric cell in the grey line and for the asymmetric cell in the black line. Note that the asymmetric cell presents boundary conditions at boundary frequencies different from those observed in the symmetric cell. In the current system, when $\alpha > 1$, $l/\lambda|_{\text{lower}}$ and $l/\lambda|_{\text{upper}}$ correspond to the natural frequencies of the fixed-fixed cell, whereas in the previous system, only one of them corresponded to such condition. Below the plots, the vertical lines guide the attenuation band boundary frequencies to the equivalent system natural frequency.

Figure 3.5. Attenuation band and bounding frequencies analysis of a periodic structure comprising single symmetric cell in thick grey lines and single asymmetric cell in thin black lines. (a) $\alpha = 2$ and (b) $\alpha = 0.5$. (i) Displacement transmissibility. (ii) point receptance in L with $U_{\mathrm{R}} = 0$. The bounding frequencies are given by the expression in Tab. 3.1 and highlighted by the vertical lines.



Source: author.

The attenuation band and bounding frequencies analysis of a periodic structure comprising multiples asymmetric cells are investigated in Fig. 3.6. In this figure the modulus of Eq. (3.14) is plotted for $N=3$ and $N=6$. Note that the bandwidth decreases as the number of cells increases. Similarly to the single cell, the minimum transmissibility for $\alpha>1$ occurs at $l/\lambda\big|_{\min}=1/4$. At this frequency, the off-diagonal terms in the transfer matrix are zero, and because of this, the minimum transmissibility for a periodic structure with *N* cells is simply the minimum transmissibility for a single cell raised to the *N*-th power, *i.e.*, (CARNEIRO JR. *et al.*, 2021)

$$\left|\frac{U_{\mathrm{R}}^{[N]}}{U_{\mathrm{L}}^{[1]}}\right|_{\min}=\frac{1}{\alpha^{N}}. \tag{3.29}$$

This is shown in Fig 3.6(a.i) as a square. Again, the maximum attenuation in dB increases linearly as the number of cells increases. For example, if the number of cells is doubled then the maximum attenuation in dB doubles (CARNEIRO JR. *et al.*, 2021). This can be verified in Fig. 3.6(a.i) by the horizontal lines that highlight the minimum transmissibilities.

It can be seen in Fig. 3.6(b.i) that there is not a clear broad frequency band of attenuation, because $\alpha<1$. The peak that tends to occurs at $l/\lambda=1/4$ when the number of cells increases is due to a quarter-wave resonance of the thinner rod element at the right-hand end of the structure: this is the truncation resonance effect. This phenomenon was explored numerically by Cunha (2017) also highlighting the distinctions between symmetry and asymmetry of cells. Essentially, this rod element acts as if it is base-excited by the remaining part of the periodic structure which has a high dynamic stiffness at this frequency (CARNEIRO JR. *et al.*, 2021). This demonstrates that it is important to orientate the cells correctly regarding to the position of the excitation source.

The reason why the orientation of an asymmetric cell with respect to source affects the transmissibility and hence the attenuation/amplification for a single cell can be determined by investigating the transmissibility of the cell in terms of receptance. Figure 3.6(ii) and 3.6(iii) shows the point and transfer receptances, respectively, for the evaluated structures in the correspondent transmissibility figures. The transfer receptance is independent of the orientation of the cell, *i.e.*, it is the same in each case, because of reciprocity, so the governing factor is the

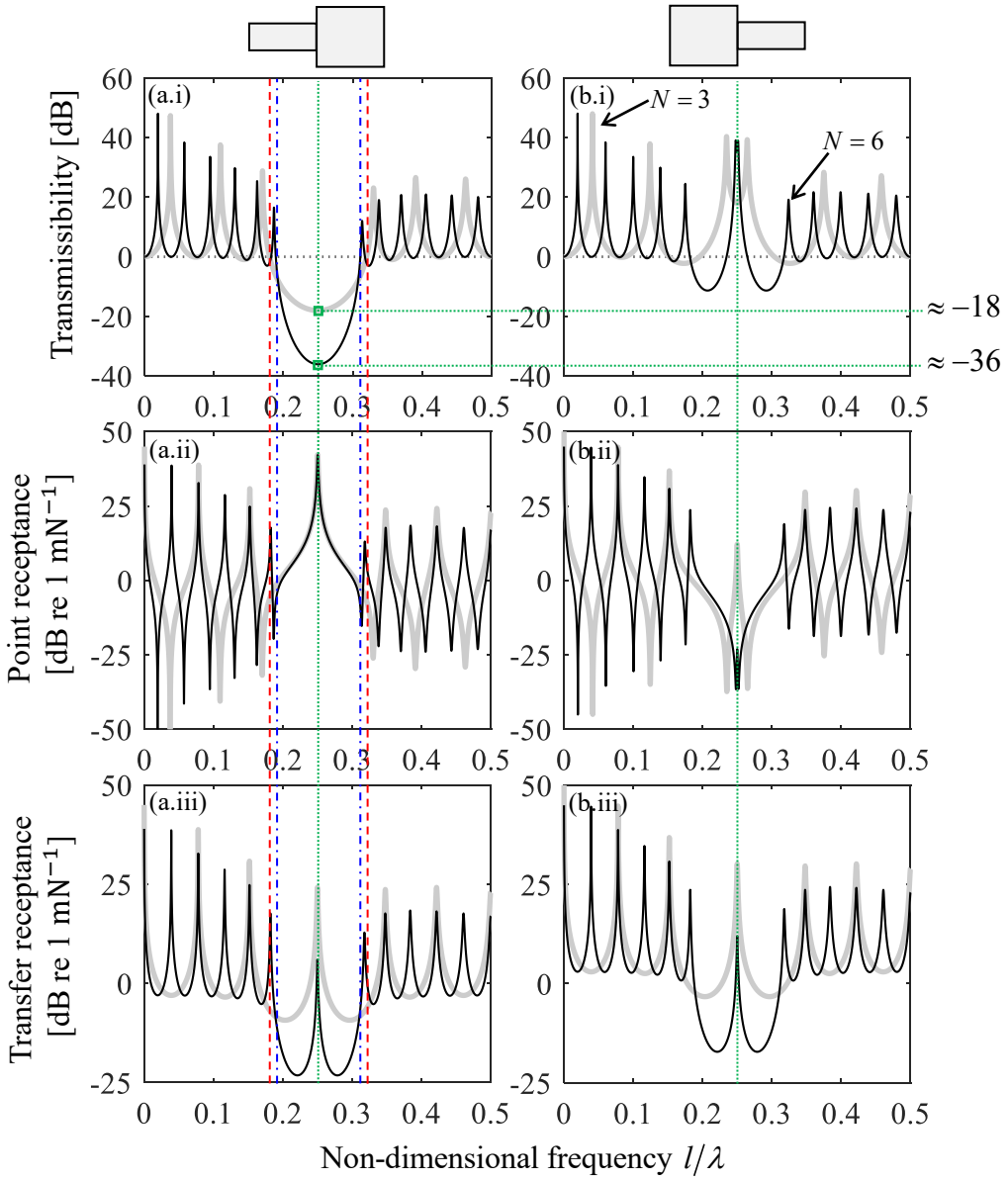
point receptance – which clearly changes significatively in the target band region, due to the structure orientation.

The point receptance of a homogeneous rod element of length l is given by (GARDONIO; BRENNAN, 2004, p. 416)

$$R_{\mathrm{LL}} = -\frac{\cot(kl)}{\omega S\sqrt{E\rho}}.$$

If this is larger than the transfer receptance within a frequency band, then there is attenuation, and if it is smaller there is amplification. A similar qualitative analysis can be made by comparing the damped peaks in Figs. 3.6(ii) and 3.6(iii). The point receptance is greater for a thinner rod than for a thicker rod (because of the cross-sectional area), hence attenuation occurs from left to right for the asymmetric cell shown in Fig. 3.3(b.i), but there is amplification from left to right for the asymmetric cell shown in Fig. 3.3(b.ii). The receptance mismatch between the elements in the cell of a periodic structure is the key to the phenomenon (CREMER *et al.*, 2005, p. 344; GRAFF, 1991, p. 84).

Figure 3.6. Attenuation band and bounding frequencies analysis of a periodic structure comprising multiple asymmetric cells with area ratio (a) $\alpha = 2$ and (b) $\alpha = 0.5$. (i) Displacement transmissibility. (ii) Point receptance and (iii) transfer receptance. Thick gray lines correspond to structure with $N = 3$ and thin black lines to $N = 6$.



Source: author.

3.4 ATTENUATION THROUGH SYMMETRIC AND ASYMMETRIC MONO-COUPLED STRUCTURES

To fully understand the difference between symmetric and asymmetric finite periodic structures, it is convenient to investigate how vibrations change throughout the system. This can be examined by determining the displacement transmissibility between each cell. These levels can be illustrated graphically for structures consisting of both cell configurations. This is accomplished by modifying the transfer matrix method, which is presented in this section in agreement with the work conducted by Carneiro Jr. *et al.* (2021).

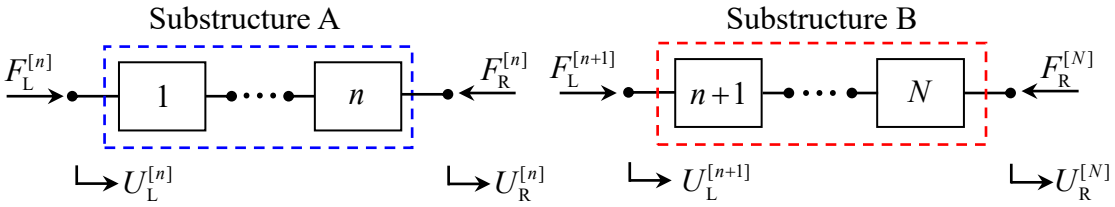
Consider the structure shown in Fig. 3.7, partitioned as shown, such that the vibration can be calculated between the n-th and $(n+1)$-th cell. The equations relating the forces and displacements on either side of substructures A and B are respectively given by $\mathbf{q}_{\mathrm{R}}^{[\mathrm{A}]} = \mathbf{T}^{[\mathrm{A}]}\mathbf{q}_{\mathrm{L}}^{[\mathrm{A}]}$ and $\mathbf{q}_{\mathrm{R}}^{[\mathrm{B}]} = \mathbf{T}^{[\mathrm{B}]}\mathbf{q}_{\mathrm{L}}^{[\mathrm{B}]}$, where

$$\mathbf{T}^{[\mathrm{A}]} = \begin{bmatrix} T_{\mathrm{LL}}^{[\mathrm{A}]} & T_{\mathrm{LR}}^{[\mathrm{A}]} \\ T_{\mathrm{RL}}^{[\mathrm{A}]} & T_{\mathrm{RR}}^{[\mathrm{A}]} \end{bmatrix} \quad \text{and} \quad \mathbf{T}^{[\mathrm{B}]} = \begin{bmatrix} T_{\mathrm{LL}}^{[\mathrm{B}]} & T_{\mathrm{LR}}^{[\mathrm{B}]} \\ T_{\mathrm{RL}}^{[\mathrm{B}]} & T_{\mathrm{RR}}^{[\mathrm{B}]} \end{bmatrix}$$

are the transfer matrices of substructures A and B respectively, which can be calculated in the same way that is described in Sec. 3.3. Applying the boundary conditions $\mathbf{q}_{\mathrm{R}}^{[\mathrm{A}]} = \mathbf{q}_{\mathrm{L}}^{[\mathrm{B}]}$, and $F_{\mathrm{R}}^{[\mathrm{B}]} = 0$ results in (CARNEIRO JR. *et al.*, 2021)

$$\frac{U_{\mathrm{R}}^{[\mathrm{A}]}}{U_{\mathrm{L}}^{[\mathrm{A}]}} = \frac{1}{T_{\mathrm{LL}}^{[\mathrm{A}]} + \dfrac{T_{\mathrm{LR}}^{[\mathrm{B}]} T_{\mathrm{RL}}^{[\mathrm{A}]}}{T_{\mathrm{LL}}^{[\mathrm{B}]}}} . \tag{3.30}$$

Figure 3.7. Partition of the structure to determine the vibration between the periodic cells or substructures.



Source: Carneiro Jr. *et al.* (2021) adapted.

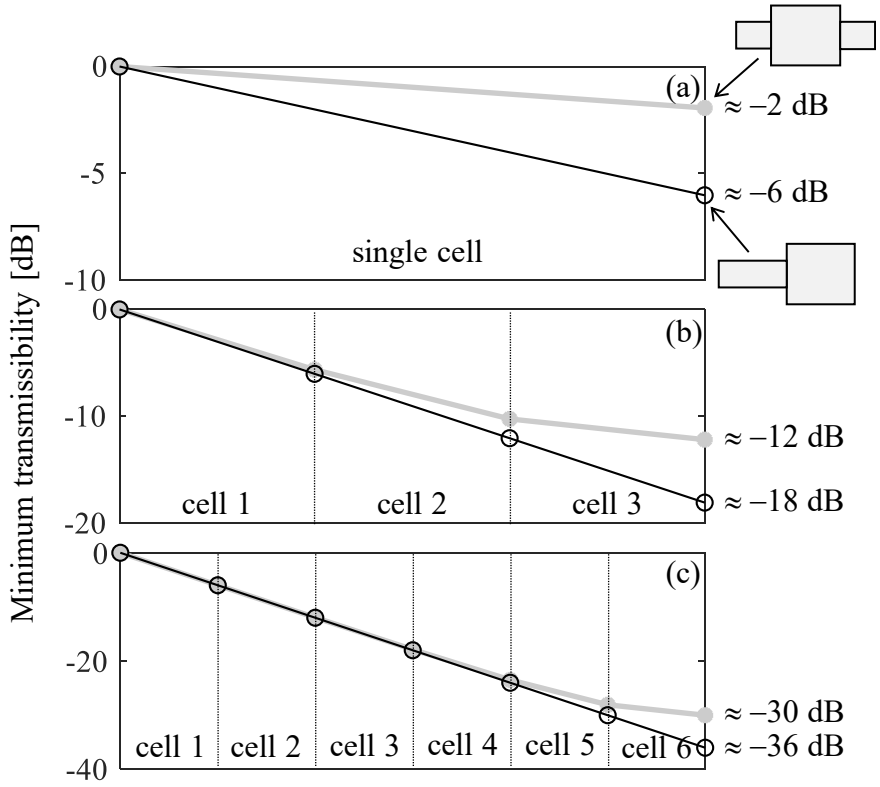
Figure 3.8 illustrates the modulus of Eq. (3.30) for configurations consisting of 1, 3, and 6 symmetric and asymmetric cells, at a frequency where the transmissibility of the entire structure reaches its minimum, *i.e.*, $l/\lambda = 1/4$. The figure demonstrates that the most significant disparity in attenuation (approximately 6 dB) between structures composed of symmetric and asymmetric cells is mainly due to the cell at the end of the structure opposite to the excitation source. The vibration levels at most of the other positions are similar. For instance, in Fig. 3.8(c), which shows the vibration levels for a structure with 6 cells, the vibration levels in the first 3 cells are almost identical for structures comprised of either symmetric or asymmetric cells, with the levels slowly diverging in the final two cells.

The preceding discussions have demonstrated that for a finite structure comprising N cells, utilising asymmetric cells proves more advantageous than symmetric ones. This holds true when the cells are positioned such that the thinner rods are oriented towards the end containing the excitation source, as illustrated in Fig 3.3(b.i). This configuration yields superior results, with a higher maximum attenuation within the attenuation band and a broader frequency range of attenuation. To quantify the disparity in minimum transmissibility between the two structures, one can divide Eq. (3.29) by Eq. (3.22), resulting in

$$\left| \frac{\dfrac{U_{\mathrm{R}}^{[N]}}{U_{\mathrm{L}}^{[1]}}^{[\mathrm{Asy}]}}{\dfrac{U_{\mathrm{R}}^{[N]}}{U_{\mathrm{L}}^{[1]}}^{[\mathrm{Sym}]}} \right|_{\min} = \frac{\alpha^{N} + \alpha^{-N}}{2\alpha^{N}}, \tag{3.31}$$

which tends to $1/2$ or -6 dB as α^N becomes large. Consequently, a configuration comprising N asymmetric cells can achieve a maximum attenuation that is up to 6 dB higher than an equivalent arrangement of symmetric cells. Whilst there is no straightforward expression for determining the boundary frequencies of the attenuation band as function of N, it is possible to establish upper and lower bounds. The upper bound corresponds to that of a single cell, as described by Eq. (3.27), whereas the lower bound aligns with the stop band frequencies given by Eq. (3.20).

Figure 3.8. Minimum displacement transmissibility between the excitation at the left of the structure and the ends of the cells for (a) 1 cell, (b) 3 cells, and (c) 6 cells. The thick grey line is for symmetric cells and the thin black line is for asymmetric cells, both with $\alpha = 2$.

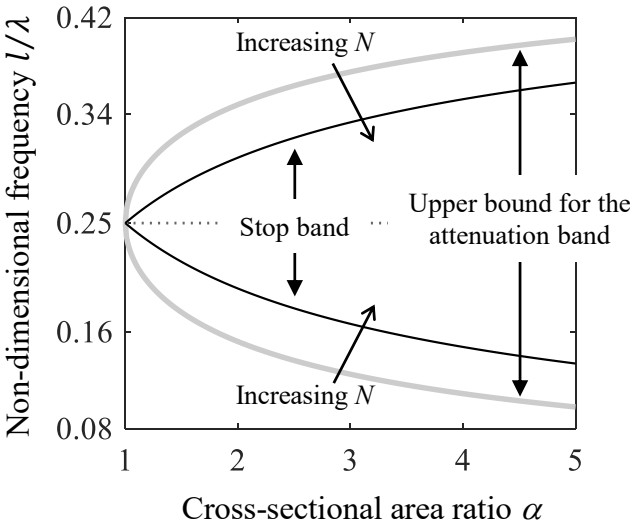


Source: Carneiro Jr. *et al.* (2021) adapted.

Expressions for the boundary frequencies for the lowest stop band of the structure comprising symmetric cells are given in Table 3.1, as are the upper and lower bounds for the lowest attenuation band for the structure comprising asymmetric cells. Also tabulated are the expressions for the minimum transmissibility within these bands for both types of structure.

The relationship between boundary frequencies and area ratio is depicted in Fig. 3.9. It demonstrates that when $\alpha > 2$, then a change in α has minimal impact on the attenuation band. However, as the number of cells increases, the attenuation band narrows. In the limiting scenario where $N \to \infty$, the attenuation band becomes identical to the stop band. This convergence occurs because an infinite structure is fundamentally composed of elements "a" and "b" regardless of their arrangement. The configuration of these elements becomes significant when transitioning to *real* structures and applying *finite* boundary conditions.

Figure 3.9. The attenuation band for the asymmetric cell and the stop band for the symmetric cell as a function of the area ratio α. The upper bound corresponds to the attenuation band for a single asymmetric cell.



Source: Carneiro Jr. *et al.* (2021) adapted.

Table 3.1. Key features of the lowest stop and attenuation bands for structures containing a finite array of N symmetric and asymmetric cells respectively.

Structure	Attenuation band form	Boundary frequencies			Minimum transmissibility
		$\left.\frac{l}{\lambda}\right\|_{\text{lower}}$	$\left.\frac{l}{\lambda}\right\|_{\text{upper}}$	$\left.\frac{l}{\lambda}\right\|_{\text{min}}$	$\left.\left\|\frac{U_{\text{R}}^{[N]}}{U_{\text{L}}^{[1]}}\right\|\right\|_{\text{min}}$
Symmetric – Fig. 3.3(a)	Stop band	$\frac{1}{\pi}\tan^{-1}\left(\frac{1}{\sqrt{\alpha}}\right)$	$\frac{1}{\pi}\tan^{-1}\left(\sqrt{\alpha}\right)$		$\frac{2}{\alpha^N+\alpha^{-N}}$
Asymmetric – Fig. 3.3(b.i)	Upper bound	$\frac{1}{2\pi}\tan^{-1}\left(\sqrt{\frac{2}{\alpha-1}}\right)$	$\frac{1}{4}+\frac{1}{2\pi}\tan^{-1}\left(\sqrt{\frac{\alpha-1}{2}}\right)$	$\frac{1}{4}$	$\frac{1}{\alpha^N}$
	Lower bound ($N\to\infty$)	$\frac{1}{\pi}\tan^{-1}\left(\frac{1}{\sqrt{\alpha}}\right)$	$\frac{1}{\pi}\tan^{-1}\left(\sqrt{\alpha}\right)$		

Source: Carneiro Jr. *et al.* (2021) adapted.

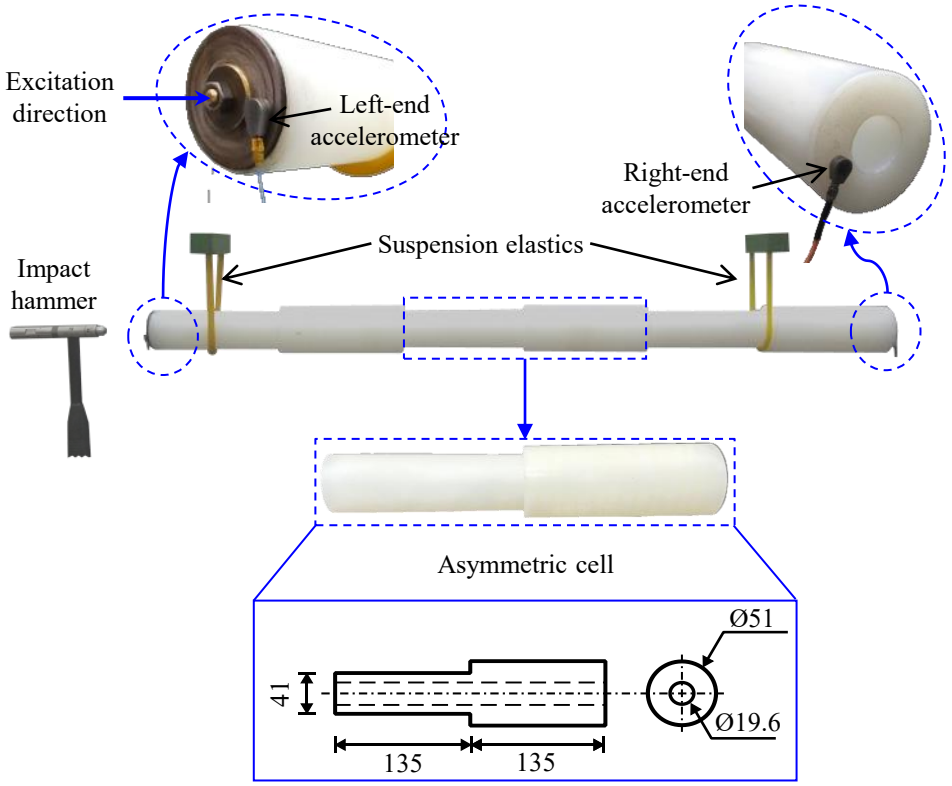
3.5 EXPERIMENTAL VALIDATION

Laboratory-based experiments were conducted to support the theoretical development described in previous sections. To achieve this objective, the expressions listed in Tab. 3.1 were used as design tools for periodic structures. The experimental structure was designed such that the upper limit of the lowest attenuation band did not occur at very high frequencies and the structure remained relatively compact. Nylon was chosen as the material that resulted in a theoretical wavenumber $k = 0.004f$, where f is the frequency in Hertz. The cell length was determined to be 270 mm by setting the minimum frequency of the attenuation band to $f|_{\text{min}} = 3$ kHz, noting that at this frequency $l/\lambda|_{\text{min}} = 1/4$, where $\lambda|_{\text{min}} = 2\pi/0.004\, f|_{\text{min}}$. Assuming length restrictions, for example, that the total length of the structure does not exceed one meter, the number of cells can be easily found, and in this case, $N = 3$ was determined. Finally, the area ratio can be determined from the number of cells and a design parameter that defines the minimum transmissibility required for $f|_{\text{min}}$. From Eq. (3.29), for a structure with three cells and an area ratio $\alpha = 1.71$, a minimum transmissibility of -14 dB was predicted.

The periodic structure was suspended horizontally using elastic bands to ensure a free-free boundary condition within the frequency range of interest and an impact test was conducted. Figure 3.10 shows the experimental setup. Note that the rod used was machined from a solid nylon tube, and therefore the metal tip was used at the excitation ends, to ensure a precisely impact that excited the structure longitudinally. Also note that the accelerometers were positioned away from the centre and aligned with each other. The technical details are presented in Appendix B.

The experimental transmissibilities are presented in Fig. 3.11, alongside the theoretical predictions calculated using Eq. (3.14) with a loss factor of 0.04. This specific loss factor was selected to provide the best match between the peaks in the experimental and theoretical predictions. Figure 3.11(a) shows the transmissibility for the condition where the cells are oriented in the direction to provide a range of frequencies in which there is vibration attenuation. In contrast, Fig. 3.11(b) shows the transmissibility when the cells are oriented in the opposite direction ($\alpha = 1/1.71$) such that there is amplification rather than attenuation within the same frequency range.

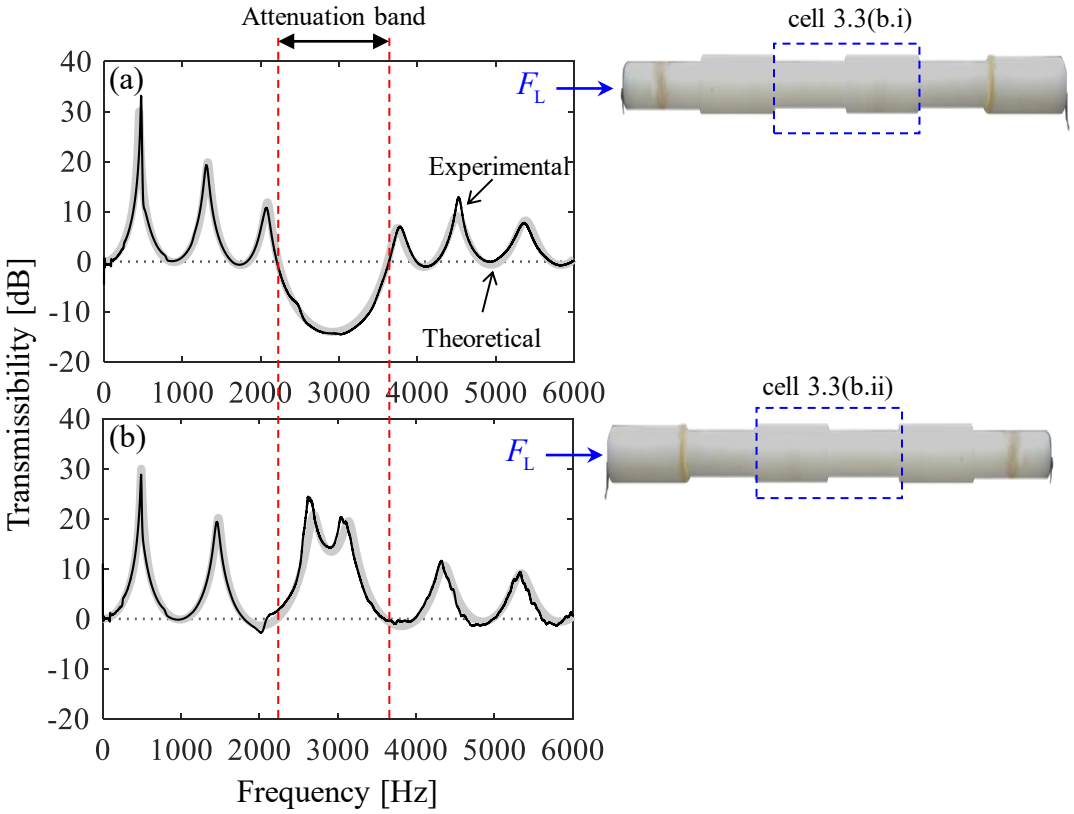
Figure 3.10. Experimental setup showing a periodic structure consisting of three nylon asymmetric cells, with the inset giving the dimensions of a single cell. The structure was excited with the impact hammer on the centre line of the structure at the left- and right-hand ends, and the transmissibility was measured using the left and right accelerometers.



Source: author.

The experimental results reveal a minimum measured transmissibility of -14.3 dB, which is consistent with the theoretical prediction of -14 dB. Table 3.2 summarises the key features of the experimental results in terms of attenuation band and minimum transmissibility. It is clear from Fig. 3.11 and the table that there is very good agreement between the developed theory and experiment. This agreement indicates that the proposed models are robust and can be used with confidence to permit the study of other structural configurations using numerical simulations and periodic structures design. Moreover, the results highlight a critical distinction between finite and infinite structures: whilst the latter primarily concerns the suppression of wave propagation, the former necessitates careful consideration of cell orientation for optimal performance.

Figure 3.11. Comparison of experimental results with theoretical developments. (a) cells oriented to give an attenuation band ($\alpha = 1.71$). (b) cells oriented to give a band of frequencies in which there is amplification ($\alpha = 0.58$). Experiment results, thin black line; theoretical, thick grey line. Figures on the right are photos of the investigated structure.



Source: Carneiro Jr. *et al.* (2021) adapted.

Table 3.2. Summary of the experimental results in terms of attenuation band and minimum transmissibility compared with the predictions and bound limits.

Attenuation band	Boundary frequencies			Minimum transmissibility
	$f\|_{\text{lower}}$ [Hz]	$f\|_{\text{upper}}$ [Hz]	$f\|_{\text{min}}$ [Hz]	$\left\|U_R^{[3]}/U_L^{[1]}\right\|_{\text{min}}$ [dB]
Upper bound – Eq. (3.27a,b)	1985	4036		
Predicted – Fig. 3.11(a)	2225	3620	2918	-14
Measured – Fig. 3.11(a)	2206	3638	3016	-14.3
Lower bound – Eq. (3.20c,d)	2690	3344		

Source: Carneiro Jr. *et al.* (2021) adapted.

3.6 ON THE OTHER CONDITIONS OF THE PERIODIC CELL

The discussions conducted thus far have used geometric discontinuities as the basis for the analysis. It is natural then to question other forms of discontinuity, such as elements with different material properties, the coupling of external elements, or even different boundary conditions. This section sheds light on this issue.

Initially, consider an extreme case of discontinuity, in which the elements of the cell vary in geometry and material. This structure can be evaluated by its transmissibility in a manner analogous to that described in Sec. 3.3. However, for the investigation conducted here, it is more convenient to return to the approach of Sec. 3.4. In this sense, this cell is subdivided into two substructures, A and B, resulting in Eq. (3.30). Note that Eq. (3.30) can be rewritten in the form of

$$\frac{U_{\mathrm{R}}^{[\mathrm{A}]}}{U_{\mathrm{L}}^{[\mathrm{A}]}}=\frac{1}{T_{\mathrm{LL}}^{[\mathrm{A}]}+D_{\mathrm{LL}}^{[\mathrm{B}]}T_{\mathrm{RL}}^{[\mathrm{A}]}}=\frac{1}{T_{\mathrm{LL}}^{[\mathrm{A}]}+\dfrac{R_{\mathrm{RL}}^{[\mathrm{A}]}}{R_{\mathrm{LL}}^{[\mathrm{B}]}}}. \tag{3.32}$$

Equation (3.32) is a powerful tool for investigating the most varied cell configurations because substructures A and B can assume various forms of mono-coupled elements. From this expression, it follows that displacement transmissibility is reciprocal to force transmissibility. If $D_{\mathrm{LL}}^{[\mathrm{B}]}=0$, Eq. (3.32), reduces to $1/T_{\mathrm{LL}}^{[\mathrm{A}]}$. It is clear from this that the greater the receptance mismatch $R_{\mathrm{RL}}^{[\mathrm{A}]}/R_{\mathrm{LL}}^{[\mathrm{B}]}$, the lower is the displacement transmissibility in A. This analysis is the finite equivalent of the observation of impedance ratio commonly performed based on waves in infinite systems (SANTOS, 2018, p. 38; CREMER *et al.*, 2005, p. 344; GRAFF, 1991, p. 84).

In the aforementioned example,

$$\frac{R_{\mathrm{RL}}^{[\mathrm{A}]}}{R_{\mathrm{LL}}^{[\mathrm{B}]}}=\frac{\alpha\varepsilon}{\kappa\sin\left(k_{\mathrm{A}}l\right)\cot\left(k_{\mathrm{A}}l\kappa\right)}$$

where $\varepsilon = E_B/E_A$ is a ratio of Young's modulus and $\kappa = k_B/k_A = \sqrt{\varepsilon\,\rho_A/\rho_B}$ is wavenumber ratio. This increases linearly with the area ratio, but not with the material properties ratio, being significantly more sensitive to this. As the phase velocity changes for each element, the natural frequencies also change. Typically, a cell composed of nylon in A and steel in B has a ratio of properties approximately to $\varepsilon \approx 66$ and $\kappa \approx 3$, therefore for each natural frequency of B there is κ times natural frequencies of A. Applying these parameters in this example, for the same frequency range, this asymmetric cell of material discontinuity presents three attenuation bands with a minimum transmissibility lower than that of a geometric discontinuity structure with an area ratio equivalent to ε/κ.

Equation (3.32) was also used by Carneiro Jr. *et al.* (2021) to investigate other boundary conditions, such as the coupling of concentrated elements at the ends of periodic structures. This research suggests that lumped parameters prove beneficial when the connected structure does not add a significant dynamic load. Moderate levels of stiffness or damping are unlikely to have a profound effect on the attenuation band because this region is likely to manifest at relatively high frequencies (above 1 kHz) for periodic rods (CARNEIRO JR. *et al.*, 2021).

3.7 CHAPTER REMARKS

In this chapter, the vibration of mono-coupled structures composed of symmetric and asymmetric rods was investigated. In these analyses, the transfer matrix method based on the dynamic stiffness and receptance approach, as described in Chapter 2, was applied. The finite periodic structure, the object of study in this chapter, was investigated based on its fundamental cell part. The transfer matrix for the uniform elements was determined from the governing equations of longitudinal motion in waveguides. The cell is composed of two elements with identical material properties but different cross-sectional areas, which were configured in such a way as to constitute symmetry or asymmetry. Of particular interest was the behaviour of the structure in terms of the frequency range in which there was vibration attenuation and maximum attenuation within this range. The applied methodology allowed the description of the cells from the displacement transmissibility in simple expressions, with which it was possible to predict the maximum attenuation and bandwidth of the attenuation band, both for a single cell and for multiple cells.

It was found that it is advantageous to use asymmetric rather than symmetric cells. However, research has demonstrated the significance of positioning cells such that the thinner rod element within each cell is situated nearer the source; otherwise, a narrow amplification band occurs. A configuration featuring properly aligned asymmetric cells exhibited a wider attenuation band than that composed of symmetric cells. Additionally, it demonstrates a maximum attenuation in displacement transmissibility from one end of the configuration to the other of approximately 6 dB. Nevertheless, as the number of cells increases, the attenuation band narrows, gradually approaching that of the symmetric cell configuration. This convergence ultimately matches the stop band of an infinite configuration, regardless of whether it comprises symmetric or asymmetric cells.

To assess the physical insights of this conclusion, an investigation of the transmissibility along the structure was conducted. Research revealed that the overall maximum attenuation of the entire structure is calculated by multiplying the maximum attenuation values of each individual cell. This implies that the maximum attenuation for every cell, measured in decibels (dB), is not influenced by the adjacent cells and can be added together to determine the total attenuation of the complete structure. From this observation, it also follows that the difference in the attenuation level between the symmetrical and asymmetrical structures is evident in the last cell.

Theoretical developments were validated using laboratory-based experimental work. The experiment considered a structure composed of three asymmetric cells oriented in such a way as to produce an attenuation band, and in the undesirable case, to produce an amplification band. There was very good agreement between the experimental and theoretical results, emphasising the convergence between the boundary frequencies and minimum transmissibility, measured and predicted.

A structure with asymmetric cells, in which the periodicity is simply due to a change in the cross-sectional area, is particularly effective in reducing the vibration transmission. Therefore, asymmetry can be considered a strategy for enhancing the attenuation performance of finite periodic structures. However, the correct orientation – or truncation – of the cells, is necessary; otherwise, the vibration will use its uncanny knack to find ways to circumvent obstacles in its path. Nevertheless, the discussions have primarily addressed internal discontinuities within the cell. Is it possible to apply a similar strategy to external discontinuities? What effects might this type of discontinuity have on improving attenuation bands? The next Chapter aims to answer these questions.

4 CONTROLLING VIBRATION TRANSMISSION IN A BEAM WITH EXTERNAL DISCONTINUITIES

4.1 INTRODUCTION

The desirable effect of vibration control using periodic structures is primarily due to the interaction of waves with discontinuities in the propagation medium. Discontinuities in designed periodic systems can be categorized into two main forms: internal and external (MEAD, 1999a). The former, as explored in Chapter 3, may involve a change in the cross-section of the cell or a spring between the connecting ends of the cell subelements. The latter, by contrast, consists of simple additions at a single connection point between the cell subelements, such as a concentrated mass, a grounded spring, or combinations of these. This chapter focuses on investigating this latter form.

This chapter examines vibration propagation control in thin beams with external discontinuities, designed using translational and rotational neutralisers. Leveraging the principles of Euler-Bernoulli beam theory, it explores wave dynamics in infinite and semi-infinite beams and analyses dynamic stiffness and receptance matrices, providing expressions for finite beams. It is known that the neutraliser induces a dip in displacement transmissibility, corresponding to an anti-resonance in the frequency response function between the source and receiver (CLEANTE *et al*., 2022; GONÇALVES *et al*., 2021). As observed in wave transmission in infinite beams, this dip does not occur at the neutraliser's natural frequency (RUGHUNANAN *et al.*, 2020; TOIT *et al.*, 2021). However, whether the mechanism responsible for this dip in finite beams is the same as that for the zero-wave transmission coefficient in infinite beams remains unclear, and this issue is addressed in this chapter. The results presented in this chapter were published in Carneiro Jr. *et al.* (2025).

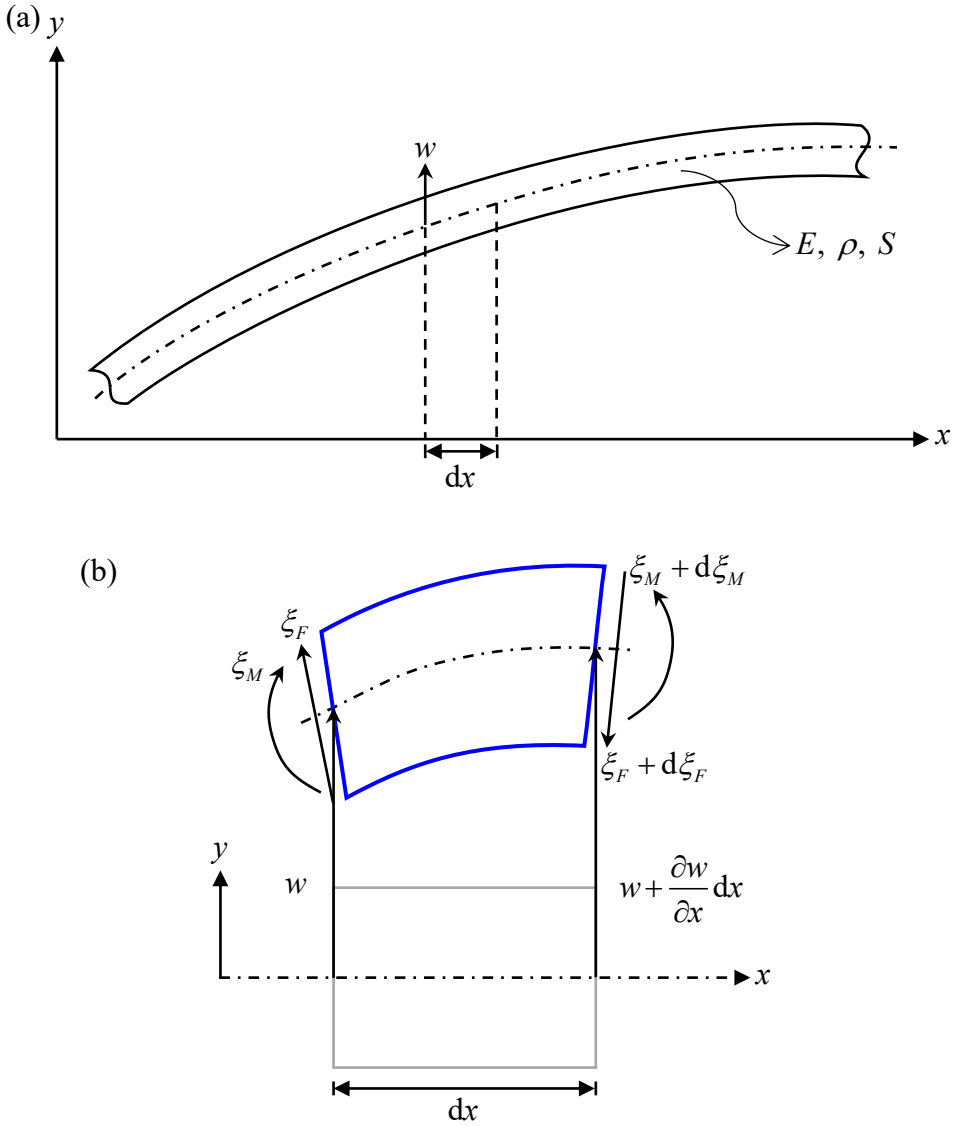
4.2 MODELLING UNIFORM BEAMS UNDER BENDING VIBRATION

4.2.1 Free wave motion in beams

In this section, bending (or flexural) waves are considered. Here, the classical Euler-Bernoulli theory for beams is invoked. Consider a slender beam subjected to transverse motion as shown in Fig. 4.1. The first assumption is that the beam sections vibrate orthogonally with

the neutral axis, and both transverse and rotational displacements occur. This means that the rotational distortion due to shear is considered negligible compared with the bending deformation; therefore, pure bending vibration is considered here. Furthermore, it results that the relationship between the bending moment and curvature is given by $\partial^2 w/\partial x^2 = -\xi_M / EI$, in which $\xi_M(x,t)$ is the bending moment, and I is the beam second moment of area (GRAFF, 1991).

Figure 4.1. Vibration of a Euler–Bernoulli beam. (a) Beam under free vibration and properties. (b) Displacements and deformations in bending.



Source: Cremer (2005) adapted.

The summation of the shear forces acting on the infinitesimal element shown in Fig. 4.1(b) is expressed by (GRAFF, 1991),

$$\xi_F - \left(\xi_F + \frac{\partial \xi_F}{\partial x} \mathrm{d}x \right) = -\rho S \mathrm{d}x \frac{\partial^2 w}{\partial t^2}, \tag{4.1a}$$

where $w(x,t)$ is the translational displacement, which relates with the rotation of a cross-section through the small angle $\theta(x) = \partial w / \partial x$. Equation (4.1a) reduces it to

$$\frac{\partial \xi_F}{\partial x} + \rho S \frac{\partial^2 w}{\partial t^2} = 0. \tag{4.1b}$$

Note the absence of body forces in Eqs. (4.1).

The second assumption is that the rotary inertia is relatively small and can be neglected. It follows that the summation of the moments acting on the element is given by $\xi_F = \partial \xi_M / \partial x$. Combining this with Eq. (4.1b), assuming *EI* constant, and the established hypotheses yield the governing equation of the Euler-Bernoulli beam, given by

$$EI \frac{\partial^4 w}{\partial x^4} + \rho S \frac{\partial^2 w}{\partial t^2} = 0. \tag{4.2}$$

Assuming harmonic motion of the form $w(x,t) = W(x) \mathrm{e}^{\mathrm{j}\omega t}$, Eq. (4.2) becomes

$$\frac{\mathrm{d}^4}{\mathrm{d}x^4} W(x) + k^4 W(x) = 0, \tag{4.3}$$

where $k^4 = \omega^2 \left(\rho S / EI\right)$ is the beam wavenumber. This implies that the beam phase velocity is given by $c = \omega^{1/2} \left(EI/\rho S\right)^{1/4}$, which depends on frequency, and therefore, is refers to a dispersive medium, as discussed in Sec. 2.2.1.

Equation (4.3) is a fourth-order differential equation; thus, it has four solutions. The solution to Eq. (4.3) is given by (BRENNAN *et al*., 2016)

$$w(x,t) = \left(A^{+}\mathrm{e}^{-\mathrm{j}kx} + B^{+}\mathrm{e}^{-kx} + A^{-}\mathrm{e}^{\mathrm{j}kx} + B^{-}\mathrm{e}^{kx}\right)\mathrm{e}^{\mathrm{j}\omega t}, \tag{4.4}$$

where A^{+} and A^{-} represent the amplitudes of waves propagating in the positive and negative x-directions, respectively. These components are analogous to the longitudinal waves observed in rods. However, in the case of beams, two additional solutions, denoted as B^{+} and B^{-}, arise. These correspond to the amplitudes of evanescent waves, which decay in the positive and negative x-directions, respectively. Evanescent waves are characterized by their decay with both frequency and distance (confined near discontinuities), and their inability to propagate energy unless they interact with one another (BOBROVNITSKII, 1992; MEAD, 1982).

4.2.2 Wave transmission of an infinite beam

To obtain the core of the interaction between the vibration in the beam and discontinuity, consider the infinite beam shown in Fig. 4.2. This structure extends from infinity to infinity and is excited by a harmonic force $\xi_F(t) = F\mathrm{e}^{\mathrm{j}\omega t}$. Before the discontinuity represented by device $\mathbf{D}^{[\mathrm{d}]}$ is attached to the structure, there is no reflection influence, and the motion at any point $x < 0$ on the beam is given by

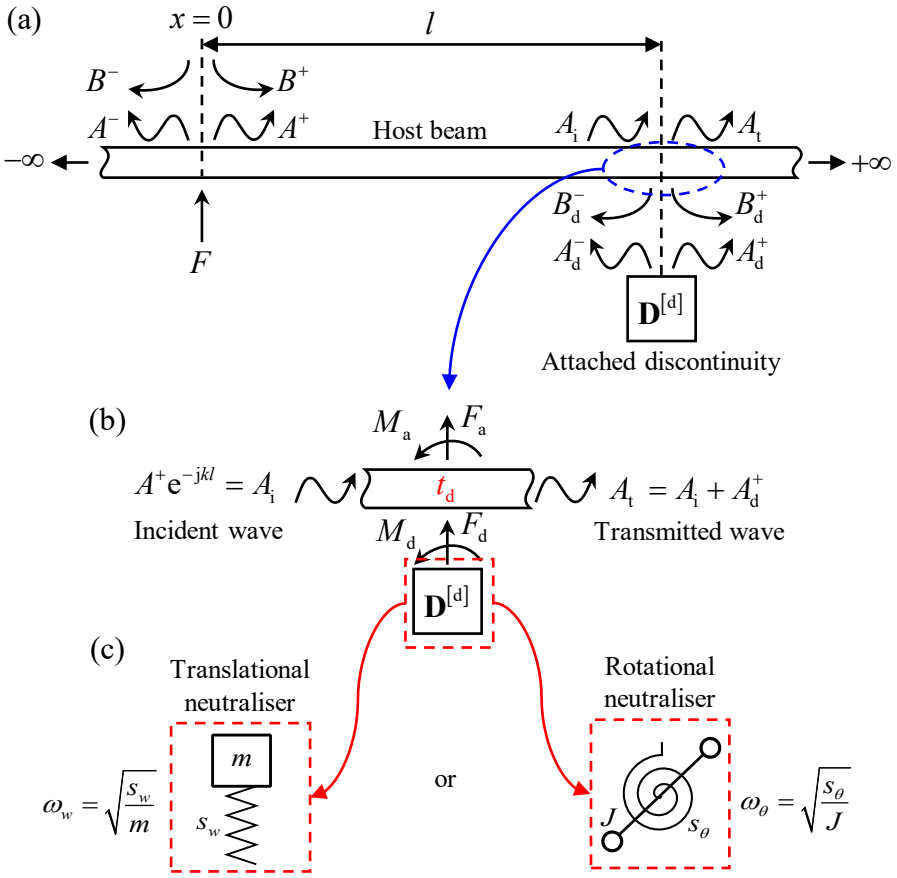
$$W^{-}(x) = A^{-}\mathrm{e}^{\mathrm{j}kx} + B^{-}\mathrm{e}^{kx} \tag{4.5a}$$

and at $x > 0$ is given by

$$W^{+}(x) = A^{+}\mathrm{e}^{-\mathrm{j}kx} + B^{+}\mathrm{e}^{-kx}\,. \tag{4.5b}$$

In these equations, the time component was omitted for clarity.

Figure 4.2. Host beam with an attached discontinuity. (a) Infinite beam and wave components generated by the source and the discontinuity. (b) Section of the beam in the vicinity of the attachment, showing the incident and reflected waves generated by the discontinuity, among which the right-going propagating waves compose the transmitted wave. (c) Types of couplings considered, these being translational and rotational neutralisers.



Source: author.

The four unknown terms in Eq. (4.5) are determined by applying the boundary conditions. The continuity relation at $x = 0$ gives that the transverse displacement to the left of the applied force is equal to the transverse displacement to the right of the applied force. The

same is true for the rotational displacement $\Theta(x) = \mathrm{d}W(x)/\mathrm{d}x$. The equilibrium conditions are that shear force is equal to the applied force, and bending moment to the left of the applied force is equal to bending moment to the right of the applied force. These conditions result in

$$A^{+} = A^{-} = \mathrm{j}B^{+} = \mathrm{j}B^{-} = -\frac{F}{4EIk^3}.$$

By substituting this into Eq. (4.5b), we obtain the point dynamic stiffness of the infinite beam given by

$$\frac{F}{W^{\pm}} = -2EIk^3\left(1-\mathrm{j}\right) = D_{\infty,w}. \tag{4.6}$$

As in the case of the rod in the previous Chapter, this dynamic stiffness is informative regarding the effective dynamic behaviour of the structure. Substituting the wavenumber into Eq. (4.6), this will be expressed as $D_{\infty,w} = -\omega^2\left(\rho S\,\lambda/\pi\right) + 2\mathrm{j}\omega\rho Sc$, which indicates that the resistance to the imposed force is seen as an effective mass $\left(\rho S\,\lambda/\pi\right)$ in series with a frequency-dependent damper $\left(2\rho Sc\right)$ (GARDONIO; BRENNAN, 2004; MEAD, 1999a).

Similarly, if instead of a force, the beam is excited with an harmonic moment $\xi_M(t) = M\mathrm{e}^{\mathrm{j}\omega t}$, by applying the boundary conditions, the resulting rotational dynamic stiffness will be expressed by

$$\frac{M}{\Theta^{\pm}} = 2EIk\left(1+\mathrm{j}\right) = D_{\infty,\theta}. \tag{4.7}$$

This is equivalent to an effective rotational spring in parallel with an effective rotational damper (GARDONIO; BRENNAN, 2004; MEAD, 1999a).

4.2.2.1 Wave transmission with an attached discontinuity

Consider now that an element is connected to the beam, imposing a discontinuity, as shown in Fig. 4.2(b). This coupled device is described by $\mathbf{f}_{\mathrm{d}} = \mathbf{D}^{[\mathrm{d}]}\mathbf{u}_{\mathrm{d}}$,

$$\begin{Bmatrix} F_{\mathrm{d}} \\ M_{\mathrm{d}} \end{Bmatrix} = \begin{bmatrix} D_w & 0 \\ 0 & D_\theta \end{bmatrix} \begin{Bmatrix} W_{\mathrm{d}} \\ \Theta_{\mathrm{d}} \end{Bmatrix}, \tag{4.8}$$

where D_w and D_θ are a translational and a rotational dynamic stiffnesses, respectively, with translation and rotation assumed to be uncoupled. This configuration allows the investigation of different types of attachments, such as concentrated mass, rotational inertia, translational and rotational grounded springs, or even translational or rotational neutralisers. Note that either D_w and/or D_θ can be 0 depending upon which type, and condition of device is attached. Here, it is considered that they are coupled individually in each investigation to facilitate physical interpretation.

Although Fig. 4.2 illustrates a force applied to the beam, as explained in the previous section, the excitation could come from a moment or even a combination of both. Therefore, it is more convenient to refer to the excitation as a source. The waves generated by the excitation force (source) propagates up to the discontinuity. Assuming that the frequency is high enough, such that the evanescent waves are localised close to the source, only the propagating wave $A^{+} = -\mathrm{j}F/4EIk^3$ impinges on the device. At this position this wave has propagated a distance l, so its value is $A_{\mathrm{is}} = A^{+}\,\mathrm{e}^{-\mathrm{j}kl}$. As this is the only wave that is incident, then $A_{\mathrm{i}} = A_{\mathrm{is}}$, where A_{i} is the sum of the right-going incident waves.

When A_{i} impinges the device, four waves are generated as shown in the figure, due its motion. They are left-going propagating and evanescent waves given by A_{d}^{+} and B_{d}^{+} respectively, and right-going propagating and evanescent waves given by A_{d}^{-} and B_{d}^{-} respectively. Because the beam is considered to be infinite in each direction, the waves

generated by the device propagate away and do not return. The net transmitted wave A_t is the superposition of the incident wave A_i and the wave generated by the device A_d^+, so that

$$A_\mathrm{t} = A_\mathrm{i} + A_\mathrm{d}^+ . \tag{4.9}$$

This wave can also be written as $A_\mathrm{t} = t_\mathrm{d} A_\mathrm{i}$ where t_d is the transmission coefficient of the attachment, given by (MACE, 1984)

$$t_w = 1 + \frac{\mathrm{j}D_w}{4EIk^3 - D_w\left(1+\mathrm{j}\right)} \text{ and } t_\theta = 1 + \frac{\mathrm{j}D_\theta}{4EIk + D_\theta\left(1-\mathrm{j}\right)} \tag{4.10a,b}$$

for translational and rotational devices, respectively. Equation (4.9) demonstrates that the transmitted wave is zero if $A_\mathrm{d}^+ = -A_\mathrm{i}$, which occurs when $t_\mathrm{d} = 0$.

By applying force equilibrium and continuity of motion at the attachment position, the right-going propagating wave is found to be given by $A_\mathrm{d}^+ = \left(t_w - 1\right) A_\mathrm{i}$ and $A_\mathrm{d}^- = \left(t_\theta - 1\right) A_\mathrm{i}$, for a translational attachment and for a rotational attachment, respectively (MACE, 1984; MEAD, 1982). Combining these with Eq. (4.9), and normalising the attached dynamic stiffnesses as $\hat{D}_w = D_w / EIk^3$ and $\hat{D}_\theta = D_\theta / EIk$, gives

$$\frac{A_\mathrm{t}}{A_\mathrm{is}} = \frac{A_\mathrm{t}}{A_\mathrm{i}} = \frac{4 - \hat{D}_w}{4 - \hat{D}_w\left(1+\mathrm{j}\right)} \text{ and } \frac{A_\mathrm{t}}{A_\mathrm{is}} = \frac{A_\mathrm{t}}{A_\mathrm{i}} = \frac{4 + \hat{D}_\theta}{4 + \hat{D}_\theta\left(1-\mathrm{j}\right)}, \tag{4.11a,b}$$

i.e. the wave transmission ratio.

Essential physical insights can be extracted from Eq. (4.11a,b). Note that if $\mathrm{Re}\left\{\hat{D}_w\right\} \gg 4$, the modulus of the transmitted wave amplitude is $1/\sqrt{2}$ the incident wave amplitude modulus. This is because the local dynamic stiffness constrains the transverse motion, and the power associated with the shear force does not transmit to the right part of the

beam. A similar effect is observed in Eq. (4.11b) if $\mathrm{Re}\left\{\hat{D}_\theta\right\} \gg 4$, so that the power associated with the bending moment does not transmit beyond the discontinuity (MEAD, 1999a).

It is clear from the numerator in Eq. (4.11a,b), to obtain the zero-transmission condition, the attached dynamic stiffnesses must satisfy

$$D_w = 4EIk^3 \text{ and } D_\theta = -4EIk\,. \qquad (4.12a,b)$$

Equation (4.12a) is fulfilled if the real part of the transverse dynamic stiffness is positive, whereas Eq. (4.12b) if the real part of the rotational dynamic stiffness is negative. This means that D_w must have stiffness-like behaviour, and D_θ must have mass-like behaviour. From a qualitative perspective, this is coherent because this stiffness behaviour *resonates* with the effective mass of the beam in the same way that the mass behaviour (rotary inertia) effect resonates with the effective rotational stiffness of the beam.

Appendix C presents the theoretical development of the previous discussion based on the coupling of simple lumped parameters, such as mass and grounded springs. From an engineering point of view, these elements may not be suitable, since while the former adds mass to the host system, the latter constrains the system. In this sense, neutralisers emerge as feasible alternatives to solve problems in the field.

4.2.2.2 Vibration neutraliser effects as the imposed discontinuity

Consider the coupling as shown in Fig. 4.2(c), in which it is possible to assume either a translational neutraliser or a rotational neutraliser. In simplified terms, neutralisers consist of a resonating appendage, such as a mass-spring system, normally undamped. If the attachment is dissipative it is more commonly referred to as a vibration absorber (DAYOU, 2006). This effect, which depends on the natural frequency of the neutraliser, can be used to suppress vibrations close to an excitation frequency or to control vibrations near a troublesome resonance frequency (BRENNAN; FERGUSON, 2004). If the attachment is an undamped translational neutraliser then (CARNEIRO JR. *et al*., 2025)

$$D_w = \frac{-\omega^2 m s_w}{\left(s_w - \omega^2 m\right)} = -s_w \frac{\left(\omega^2/\omega_w^2\right)}{1-\left(\omega^2/\omega_w^2\right)} \tag{4.13a}$$

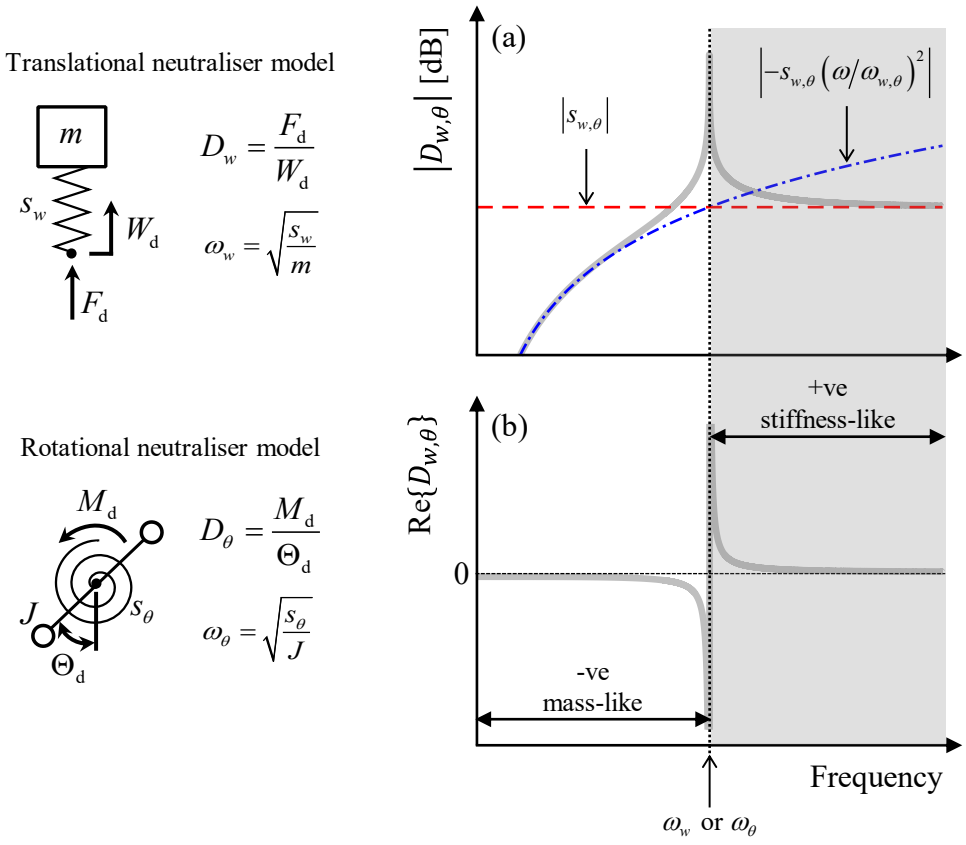
and the undamped rotational neutraliser

$$D_\theta = \frac{-\omega^2 J s_\theta}{\left(s_\theta - \omega^2 J\right)} = -s_\theta \frac{\left(\omega^2/\omega_\theta^2\right)}{1-\left(\omega^2/\omega_\theta^2\right)}, \tag{4.13b}$$

in which m, s_w, J and s_θ are mass, translational stiffness, rotational inertia and rotational stiffness, respectively. The natural frequencies of the neutralisers are given by $\omega_w = \sqrt{s_w/m}$ and $\omega_\theta = \sqrt{s_\theta/J}$.

The literature indicates that when a neutraliser is connected to a host structure, it creates a condition that suppresses vibrations at a specific frequency, referred to as the tuned frequency (KELA; VÄHÄOJA, 2009). This phenomenon is associated with the resonant condition described by Eq. (4.12a,b). To demonstrate how a translational or rotational neutraliser can achieve the desired stiffness-like or mass-like behaviour, the dynamic stiffness of an undamped neutraliser, as expressed in Eq. (4.13a,b), is plotted in Fig. 4.3. The figure illustrates that a neutraliser exhibits a mass-like behaviour below its natural frequency, as $\omega_{w,\theta} \gg \omega$ and $D_{w,\theta} \approx -s_{w,\theta}\left(\omega/\omega_{w,\theta}\right)^2$, which is real and negative (denoted in -ve shaded area). Conversely, above its natural frequency, the neutraliser exhibits a stiffness-like behaviour, as $\omega \gg \omega_{w,\theta}$ and $D_{w,\theta} \approx s_{w,\theta}$, which is real and positive (denoted in the +ve shaded area). This region is highlighted by the shaded area.

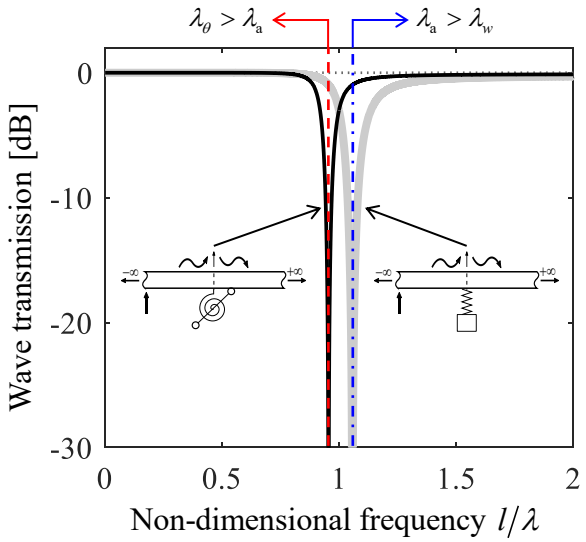
Figure 4.3. Typical behaviour of the dynamic stiffness (a) modulus and (b) real part of either a translational or rotational vibration neutraliser.



Source: author.

The behaviour of the infinite beam with each neutraliser is illustrated by examining the ratio of the transmitted waves A_t to the propagating incident wave A_{is} generated by the lateral force. These ratios are shown in Fig. 4.4, combining Eqs. (4.11a,b) and Eqs. (4.13a,b), respectively. In this figure the properties of the normalised translational and rotational neutralisers were chosen such that $s_w = 4EI\left(2\pi/\lambda_w\right)^3$ and $s_\theta = 4EI\left(2\pi/\lambda_\theta\right)$, in which $\lambda_w = \lambda_\theta = l$ are the wavelength when the beam is excited at the neutralisers natural frequencies.

Figure 4.4. Infinite beam wave transmission ratio for an attached translational neutraliser, in thick grey line, and rotational neutraliser, in thin black line.



Source: author.

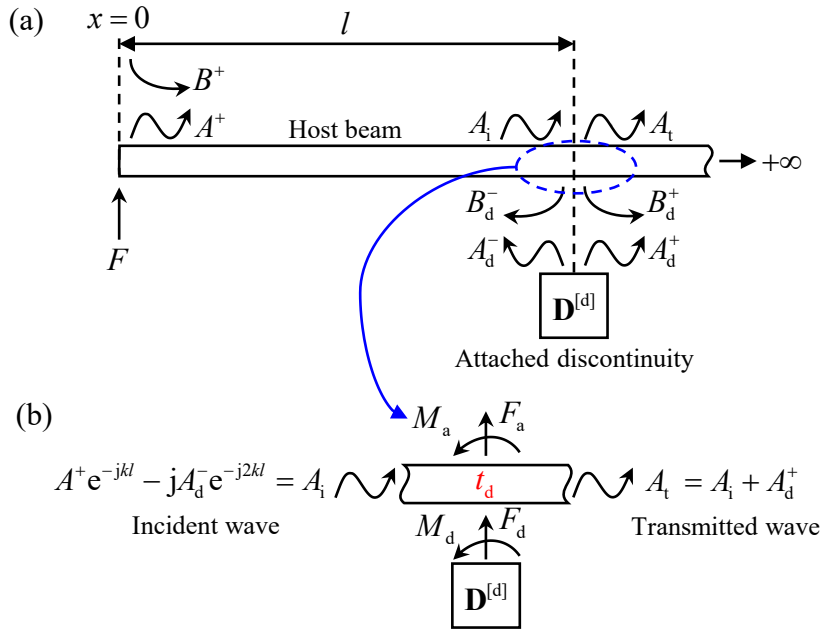
It is clear in Fig. 4.4 that, there is a significant reduction in the transmitted wave at a single frequency for each device, which has wavelength λ_a. Note that this frequency is different from the neutraliser's natural frequency, i.e, $l/\lambda = 1$. This occurs when either $\left|4 - \hat{D}_w\right| = 0$ or $\left|4 + \hat{D}_\theta\right| = 0$ for the reasons discussed previously. Away from this frequency, the neutraliser only has a marginal effect on the transmitted wave, as discussed in (BRENNAN, 1999; SALLEH; BRENNAN, 2007).

4.2.3 Wave transmission of semi-infinite beam with an attached discontinuity

Consider now the case shown in Fig. 4.5. In this case, the right of the device, the beam is assumed to extend to infinity, but there is a boundary to the left of the device that imposes a reflecting interface. The wave generated by the source is now $A^+ = -(1+\mathrm{j})F/2EIk^3$. Thus the wave A_d^- generated by the interaction of the incident wave with the discontinuity is reflected from the boundary and propagates back to the discontinuity, so that the net incident wave is the superposition of these two waves and is given by $A_i = A^+ \mathrm{e}^{-\mathrm{j}kl} - \mathrm{j}A_d^- \mathrm{e}^{-\mathrm{j}2kl}$. Note that the A_d^- wave undergoes a phase change of $2kl$ as it propagates to the left boundary and returns to the

discontinuity plus it has a phase delay of $90°$ due to reflection from the free boundary (MACE, 1984). As in the infinite beam case $A_{is} = A^{+}\,\mathrm{e}^{-jkl}$.

Figure 4.5. Host beam with an attached discontinuity. (a) Semi-infinite beam and wave components generated by the source and the discontinuity. (b) Section of the beam in the vicinity of the attachment, showing the incident and reflected waves generated by the discontinuity, among which the right-going propagating waves compose the transmitted wave.



Source: author.

The transmitted wave is again given by Eq. (4.9) in terms of the net incident wave, but this net incident wave depends on the interference between the directly excited wave A^{+} and the reflection of the wave A_{d}^{-} induced by the device from the end of the beam.

The transmission coefficient is given by Eq. (4.10a,b) in terms of the sum of the incident wave and the wave generated by the neutraliser. Noting that $A_{d}^{-} = \pm A_{d}^{+}$, then $A_{t} = A_{is} + A_{d}^{+}\left(1 \mp \mathrm{j}\,\mathrm{e}^{-\mathrm{j}2kl}\right)$, for translational or rotational neutralisers, respectively. By applying force equilibrium and continuity of motion, the right-going propagating wave is found to be given in terms of the wave generated by the excitation as (CARNEIRO JR. *et al.*, 2025)

$$A_{\mathrm{d}}^{+}=\frac{\left(t_w-1\right)A_{\mathrm{is}}}{1+\mathrm{j}\mathrm{e}^{-\mathrm{j}2kl}\left(t_w-1\right)}\ \text{and}\ A_{\mathrm{d}}^{+}=\frac{\left(t_\theta-1\right)A_{\mathrm{is}}}{1+\mathrm{j}\mathrm{e}^{-\mathrm{j}2kl}\left(1-t_\theta\right)} \tag{4.14a,b}$$

for a translational and a rotational attachment respectively. Combining these with Eq. (4.9) and the normalised form of the dynamic stiffnesses gives the wave transmission ratios

$$\frac{A_{\mathrm{t}}}{A_{\mathrm{is}}}=\frac{4-\hat{D}_w}{4-\hat{D}_w\left[1+\mathrm{j}\left(1-\mathrm{j}\mathrm{e}^{-\mathrm{j}2kl}\right)\right]} \tag{4.15a}$$

and

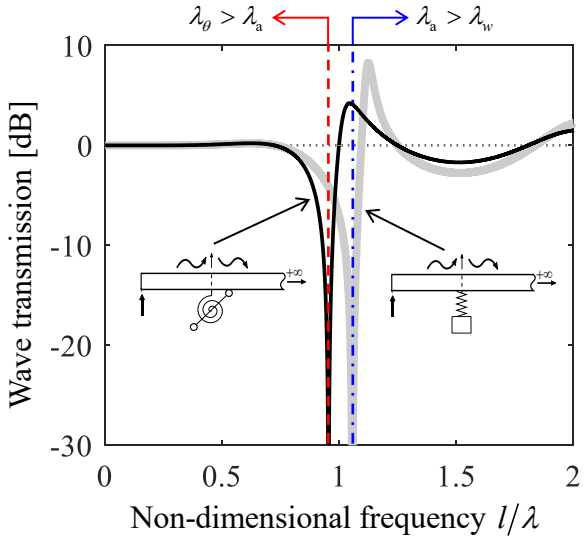
$$\frac{A_{\mathrm{t}}}{A_{\mathrm{is}}}=\frac{4+\hat{D}_\theta}{4+\hat{D}_\theta\left[1-\mathrm{j}\left(1-\mathrm{j}\mathrm{e}^{-\mathrm{j}2kl}\right)\right]}. \tag{4.15b}$$

Unlike the infinite system, note that in this case $A_{\mathrm{t}}/A_{\mathrm{is}}\neq A_{\mathrm{t}}/A_{\mathrm{i}}$ is given by Eqs. (4.15a,b). Comparing Eqs. (4.11a,b) for the infinite beam with Eqs. (4.15a,b) for the semi-infinite beam, it can be seen that the numerators are the same but the denominators are different. If the beam is infinite and the dynamic stiffness of the attachment is chosen so that the numerator is zero, then the denominators of Eqs. (4.11a,b) are $\mp\mathrm{j}4$, respectively; in the semi-infinite beam case, the denominators of Eqs. (4.15a,b) are $\mp 4\mathrm{j}\left(1-\mathrm{j}\mathrm{e}^{-\mathrm{j}2kl}\right)$, respectively. This is zero if the wave A_{d}^{-} generated by the device is reflected from the left boundary such that it is in anti-phase with the wave A_{d}^{+}, as discussed by Carneiro Jr. *et al.* (2025). Accordingly, this is clearly a function of frequency and the position of the attached device. If a neutraliser is attached, this effect will result to be a frequency where the neutraliser cannot cause a dip in the transmission, because it is located at a node of a standing wave originating at the free end (CARNEIRO JR. *et al*., 2025).

Figure 4.6 shows the wave transmission ratio for the semi-infinite beam with attached translational and rotational neutralisers, which are described in the same way as discussed in

the previous section. The behaviour of the semi-infinite beam is similar to the infinite beam, but there are other frequencies where the wave transmission ratio is either less than unity or greater than unity. This is because the wave A_{d}^{-} generated by the neutraliser is reflected from the left-hand boundary and combines either destructively or constructively with the wave A_{is} generated by the source.

Figure 4.6. Semi-infinite beam wave transmission ratio for an attached translational neutraliser, in thick grey line, and rotational neutraliser, in thin black line.



Source: author.

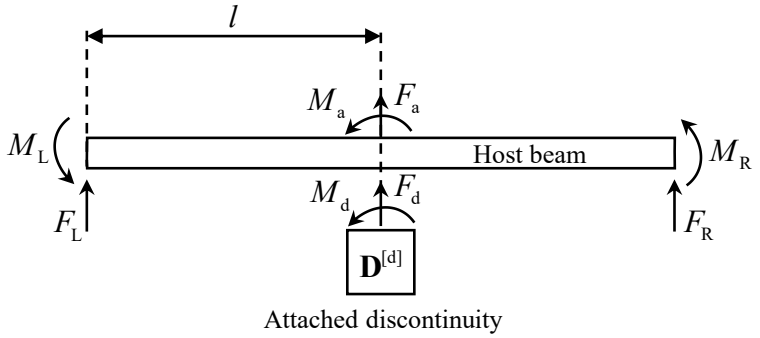
4.2.4 Modelling a finite beam with an attached discontinuity

Building on the understanding of the behaviour and physical principles of infinite and semi-infinite structures, the investigation now shifts to finite beams. The objective is to identify the additional effects that structural truncation introduces and to evaluate their implications for vibration control.

The general system of interest is illustrated in Fig. 4.7, which shows a finite beam of total length $2l$. The vibration is induced by a source and then transmitted to a remote part of the structure (the receiver). In between them, at a distance l from the source, it is attached the device, that may modify the vibration transmission. It is known that, if the device is a neutraliser, by positioning it at the source would induce vibration suppression at all other points

of the structure at the natural frequency of the neutraliser, while positioning it on the receiver results in suppression at that point, again at the natural frequency of the neutraliser (BRENNAN; FERGUSON, 2004). These cases are not considered here, because it may not be practicable to place the neutraliser at either the source or receiver positions.

Figure 4.7. Schematic of a finite Euler-Bernoulli beam with a device attached at point a.



Source: author.

The system is modelled using the dynamic stiffness/receptance approach, as presented in Chapter 2. The bare host beam is described by

$$\begin{Bmatrix} \mathbf{u}_\mathrm{L} \\ \mathbf{u}_\mathrm{a} \\ \mathbf{u}_\mathrm{R} \end{Bmatrix} = \begin{bmatrix} \mathbf{R}_\mathrm{LL} & \mathbf{R}_\mathrm{La} & \mathbf{R}_\mathrm{LR} \\ \mathbf{R}_\mathrm{aL} & \mathbf{R}_\mathrm{aa} & \mathbf{R}_\mathrm{aR} \\ \mathbf{R}_\mathrm{RL} & \mathbf{R}_\mathrm{Ra} & \mathbf{R}_\mathrm{RR} \end{bmatrix} \begin{Bmatrix} \mathbf{f}_\mathrm{L} \\ \mathbf{f}_\mathrm{a} \\ \mathbf{f}_\mathrm{R} \end{Bmatrix}, \tag{4.16}$$

where the response vectors are given by $\mathbf{u}_\mathrm{L} = \{W_\mathrm{L} \quad \Theta_\mathrm{L}\}^\mathrm{T}$, $\mathbf{u}_\mathrm{a} = \{W_\mathrm{a} \quad \Theta_\mathrm{a}\}^\mathrm{T}$ and $\mathbf{u}_\mathrm{R} = \{W_\mathrm{R} \quad \Theta_\mathrm{R}\}^\mathrm{T}$; and force vectors are given by $\mathbf{f}_\mathrm{L} = \{F_\mathrm{L} \quad M_\mathrm{L}\}^\mathrm{T}$, $\mathbf{f}_\mathrm{a} = \{F_\mathrm{a} \quad M_\mathrm{a}\}^\mathrm{T}$ and $\mathbf{f}_\mathrm{R} = \{F_\mathrm{R} \quad M_\mathrm{R}\}^\mathrm{T}$. The subscripts L, a and R refer to the left-hand, appendage and right-hand beam positions, respectively. The inner receptance matrix $\mathbf{R}_{ij}$ can be determined by applying the boundary conditions and are expressed by (CARNEIRO JR. *et al*., 2025)

$$\mathbf{R}_{\mathrm{LL}} = \frac{1}{EIk\mathrm{H}}\begin{bmatrix} \mathrm{Q}_1 & \mathrm{G}_1 \\ \mathrm{G}_1 & \mathrm{K}_1 \end{bmatrix},\ \mathbf{R}_{\mathrm{La}} = \mathbf{R}_{\mathrm{aL}}{}^{T} = \frac{1}{EIk\mathrm{H}}\begin{bmatrix} \mathrm{V}_1 & \mathrm{P}_1 \\ \mathrm{P}_2 & \mathrm{V}_2 \end{bmatrix}, \tag{4.17a,b}$$

$$\mathbf{R}_{\mathrm{LR}} = \mathbf{R}_{\mathrm{RL}}{}^{T} = \frac{1}{EIk\mathrm{H}}\begin{bmatrix} \mathrm{Q}_2 & \mathrm{G}_2 \\ -\mathrm{G}_2 & \mathrm{K}_2 \end{bmatrix},\ \mathbf{R}_{\mathrm{aR}} = \mathbf{R}_{\mathrm{Ra}}{}^{T} = \frac{1}{EIk\mathrm{H}}\begin{bmatrix} \mathrm{V}_1 & -\mathrm{P}_2 \\ -\mathrm{P}_1 & \mathrm{V}_2 \end{bmatrix}, \tag{4.17c,d}$$

$$\mathbf{R}_{\mathrm{RR}} = \frac{1}{EIk\mathrm{H}}\begin{bmatrix} \mathrm{Q}_1 & -\mathrm{G}_1 \\ -\mathrm{G}_1 & \mathrm{K}_1 \end{bmatrix} \text{ and } \mathbf{R}_{\mathrm{aa}} = \frac{1}{EIk\mathrm{H}}\begin{bmatrix} \mathrm{J}_1 & 0 \\ 0 & \mathrm{J}_2 \end{bmatrix}, \tag{4.17e,f}$$

where

$$\begin{aligned}
\mathrm{H} &= \cos(2kl)\cosh(2kl) - 1, \\
\mathrm{Q}_1 &= \frac{1}{k^2}\big(\sin(2kl)\cosh(2kl) - \cos(2kl)\sinh(2kl)\big), \\
\mathrm{Q}_2 &= \frac{1}{k^2}\big(\sin(2kl) - \sinh(2kl)\big), \\
\mathrm{G}_1 &= -\frac{1}{k}\big(\sin(2kl)\sinh(2kl)\big), \\
\mathrm{G}_2 &= \frac{1}{k}\big(\cos(2kl) - \cosh(2kl)\big), \\
\mathrm{K}_1 &= \sin(2kl)\cosh(2kl) + \cos(2kl)\sinh(2kl), \\
\mathrm{K}_2 &= \sin(2kl) + \sinh(2kl), \\
\mathrm{V}_1 &= \frac{1}{k^2}\big(\cos(kl) + \cosh(kl)\big)\big(\sin(kl)\cosh(kl) - \cos(kl)\sinh(kl)\big), \\
\mathrm{V}_2 &= \big(\cos(kl) + \cosh(kl)\big)\big(\sin(kl)\cosh(kl) + \cos(kl)\sinh(kl)\big), \\
\mathrm{P}_1 &= -\frac{1}{k}\big(\sin(kl) + \sinh(kl)\big)\big(\sin(kl)\cosh(kl) + \cos(kl)\sinh(kl)\big), \\
\mathrm{P}_2 &= \frac{1}{k}\big(\sin(kl) - \sinh(kl)\big)\big(\sin(kl)\cosh(kl) - \cos(kl)\sinh(kl)\big), \\
\mathrm{J}_1 &= \frac{1}{k^2}\big(\cos(kl)\cosh(kl) + 1\big)\big(\sin(kl)\cosh(kl) - \cos(kl)\sinh(kl)\big),
\end{aligned}$$

and

$$\mathrm{J}_2 = \big(\cos(kl)\cosh(kl) + 1\big)\big(\sin(kl)\cosh(kl) + \cos(kl)\sinh(kl)\big).$$

Of particular interest is to evaluate the structure in terms of displacement transmissibility. Hence, the receptances of the structure with the attachment must be written. If the device is now connected to the host beam, and assuming the description expressed by Eq. (4.8), then $\mathbf{f}_{\mathrm{a}} = -\mathbf{f}_{\mathrm{d}}$ and $\mathbf{u}_{\mathrm{a}} = \mathbf{u}_{\mathrm{d}}$. Assuming for simplicity that the right-hand side is free, so that $\mathbf{f}_{\mathrm{R}} = \mathbf{0}$, the resulting equations can be solved for the receptances of the host structure and the dynamic stiffness matrix of the imposed discontinuity giving

$$\mathbf{u}_{\mathrm{L}} = \left[\mathbf{R}_{\mathrm{LL}} - \mathbf{R}_{\mathrm{La}} \mathbf{D}^{[\mathrm{d}]} \left(\mathbf{I} + \mathbf{R}_{\mathrm{aa}} \mathbf{D}^{[\mathrm{d}]} \right)^{-1} \mathbf{R}_{\mathrm{aL}} \right] \mathbf{f}_{\mathrm{L}} \tag{4.18a}$$

and

$$\mathbf{u}_{\mathrm{R}} = \left[\mathbf{R}_{\mathrm{RL}} - \mathbf{R}_{\mathrm{Ra}} \mathbf{D}^{[\mathrm{d}]} \left(\mathbf{I} + \mathbf{R}_{\mathrm{aa}} \mathbf{D}^{[\mathrm{d}]} \right)^{-1} \mathbf{R}_{\mathrm{aL}} \right] \mathbf{f}_{\mathrm{L}} \,. \tag{4.19b}$$

Equations (4.19a,b) can be used to determine the transmissibility of motion between the source and the receiver for a given force excitation vector $\mathbf{f}_{\mathrm{L}}$. Combining these for the case when the beam is excited by an external force of amplitude F_{L} at the left end ($M_{\mathrm{L}} = 0$), results in

$$\frac{W_{\mathrm{R}}}{W_{\mathrm{L}}} = \frac{\mathbf{R}_{\mathrm{RL}}(1,1) + D_w \left[\mathbf{R}_{\mathrm{RL}}(1,1) \mathbf{R}_{\mathrm{aa}}(1,1) - \mathbf{R}_{\mathrm{Ra}}(1,1) \mathbf{R}_{\mathrm{aL}}(1,1) \right]}{\mathbf{R}_{\mathrm{LL}}(1,1) + D_w \left[\mathbf{R}_{\mathrm{LL}}(1,1) \mathbf{R}_{\mathrm{aa}}(1,1) - \mathbf{R}_{\mathrm{La}}(1,1) \mathbf{R}_{\mathrm{aL}}(1,1) \right]}, \tag{4.20a}$$

when a translation device is used, and

$$\frac{W_{\mathrm{R}}}{W_{\mathrm{L}}} = \frac{\mathbf{R}_{\mathrm{RL}}(1,1) + D_\theta \left[\mathbf{R}_{\mathrm{RL}}(1,1) \mathbf{R}_{\mathrm{aa}}(2,2) - \mathbf{R}_{\mathrm{Ra}}(1,2) \mathbf{R}_{\mathrm{aL}}(2,1) \right]}{\mathbf{R}_{\mathrm{LL}}(1,1) + D_\theta \left[\mathbf{R}_{\mathrm{LL}}(1,1) \mathbf{R}_{\mathrm{aa}}(2,2) - \mathbf{R}_{\mathrm{La}}(1,2) \mathbf{R}_{\mathrm{aL}}(2,1) \right]}, \tag{4.20b}$$

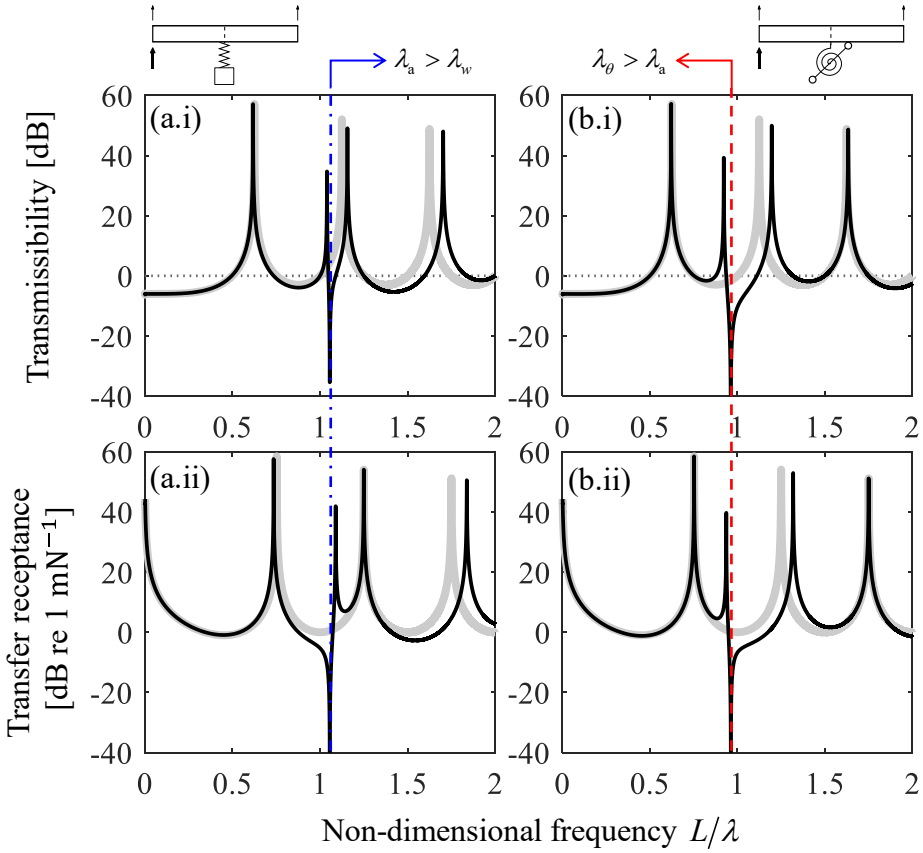
when a rotational device is used. Note that the procedure to obtain Eqs. (4.20a,b) can also be applied in an analogous way to obtain the transmissibility of angular displacements, or even for the case in which the excitation is a bending moment.

4.2.4.1 Vibration neutraliser effects as the imposed discontinuity

In this section, consider that instead of a generic device, neutralisers are attached to the beam, such as those described by Eqs. (4.14a,b). The effect of attaching the neutralisers individually is illustrated in Fig. 4.8. In this figure the properties of the normalised translational and rotational neutralisers were chosen such that $s_w = 4EI\left(2\pi/\lambda_w\right)^3$, $s_\theta = 4EI\left(2\pi/\lambda_\theta\right)$ and $\lambda_w = \lambda_\theta = 2l$. The translational displacement transmissibility and transfer receptance curves are presented. Along with the structure with the neutraliser, the curves for the bare beam are also shown, in thick grey lines. To limit the peaks response, a loss factor of $\eta = 0.001$ is assumed to add some damping to the structure.

It can be seen in Fig. 4.8 that the main effect of the neutraliser is to create a dip in the transmissibility, which is equivalent to an anti-resonance of the transfer receptance $W_{\mathrm{R}}/F_{\mathrm{L}}$ at frequency ω_{a}. It should be noted that the anti-resonances occur at a different frequency from the natural frequency of the neutralisers, although they are close. For a translational neutraliser the dip occurs at a frequency greater than its natural frequency and for a rotational neutraliser the dip occurs at a frequency less than its natural frequency, as in the case infinite and semi-infinite. However, if the translational neutraliser is attached to the beam at either the source in L or receiver in R, then an anti-resonance occurs at the natural frequency of the neutraliser.

Figure 4.8. Comparison of the effect that either a (a) translational or (b) rotational vibration neutraliser, has on a free-free beam, excited by a force at one end, in thin black lines, with a bare beam in thick grey lines. (i) Displacement transmissibility. (ii) Transfer receptance.



Source: author.

To investigate the way in which the neutraliser creates a dip in the displacement transmissibility, it is convenient to consider the case where the evanescent waves on the beam are confined to the ends of the beam, the excitation location and the position where the neutraliser is attached. This occurs at high frequencies when there is at least half wavelength between the neutraliser and the ends of the beam. In this case $\sinh(kl) \approx \cosh(kl)$ as discussed in (GONÇALVES *et al.*, 2007, 2018). Accordingly, after some algebraic manipulation the modified receptances in Eqs. (4.20a,b) results in (CARNEIRO JR. *et al.*, 2025)

$$\frac{W_{\mathrm{R}}}{W_{\mathrm{L}}} \approx \frac{4-\hat{D}_w}{4\sqrt{2}\cos\left(2kl+\dfrac{\pi}{4}\right)-\hat{D}_w\left[1-2\sin(2kl)\right]}, \tag{4.21a}$$

when a translational neutraliser is used, where $\hat{D}_w = D_w / EIk^3$, and

$$\frac{W_{\mathrm{R}}}{W_{\mathrm{L}}} \approx \frac{4 + \hat{D}_\theta}{4\sqrt{2}\cos\left(2kl + \frac{\pi}{4}\right) + \hat{D}_\theta\left[1 + 2\cos\left(2kl\right)\right]} \tag{4.21b}$$

when a rotational neutraliser is used, where $\hat{D}_\theta = D_\theta / EIk$.

When the respective neutralisers are attached, the dips in the displacement transmissibilities shown in Fig. 4.8 occur at the anti-resonance frequencies of the beam ω_{a} in the transfer receptances between the force F_{L} and the displacement W_{R} . Note that the anti-resonance occurs at a different frequency when either a translational or rotational neutraliser is attached.

It is important to note that the forms of the numerator in Eqs. (4.21a,b) are the same as in Eqs. (4.11a,b) and Eqs. (4.15a,b). Table 4.1 summarises these equations. This demonstrates that when the frequency is high enough, such that the evanescent waves at the ends of the beam and at the neutraliser do not significantly interact with each other, the anti-resonance in the transfer receptance is due to the suppression of a right-going propagating wave by the neutraliser, *i.e.* the transmission coefficient of the neutraliser is zero at this frequency (CARNEIRO JR. *et al*., 2025). In other words, this effect depends only on the local interaction between the attached device dynamic stiffness and the dynamic stiffness of the host bare beam at the attachment point.

Table 4.1. Expressions for the displacement transmissibilities and wave transmission ratios.

Structure		Expression	
		Translational neutraliser	Rotational neutraliser
		Wave transmission ratios	
Infinite: Eqs. (4.11a,b)	$\dfrac{A_\mathrm{t}}{A_\mathrm{is}} =$	$\dfrac{4-\hat{D}_w}{4-\hat{D}_w\left(1+\mathrm{j}\right)}$	$\dfrac{4+\hat{D}_w}{4+\hat{D}_w\left(1-\mathrm{j}\right)}$
Semi-infinite: Eqs. (4.15a,b)	$\dfrac{A_\mathrm{t}}{A_\mathrm{is}} =$	$\dfrac{A_\mathrm{t}}{A_\mathrm{is}} = \dfrac{4-\hat{D}_w}{4-\hat{D}_w\left[1+\mathrm{j}\left(1-\mathrm{j}\mathrm{e}^{-\mathrm{j}2kl}\right)\right]}$	$\dfrac{A_\mathrm{t}}{A_\mathrm{is}} = \dfrac{4-\hat{D}_w}{4-\hat{D}_w\left[1+\mathrm{j}\left(1-\mathrm{j}\mathrm{e}^{-\mathrm{j}2kl}\right)\right]}$
		Transmissibility	
Finite: Eqs. (4.21a,b)	$\dfrac{W_\mathrm{R}}{W_\mathrm{L}} =$	$\dfrac{4-\hat{D}_w}{4\sqrt{2}\cos\left(2kl+\dfrac{\pi}{4}\right)-\hat{D}_w\left[1-2\sin\left(2kl\right)\right]}$	$\dfrac{4+\hat{D}_\theta}{4\sqrt{2}\cos\left(2kl+\dfrac{\pi}{4}\right)+\hat{D}_\theta\left[1+2\cos\left(2kl\right)\right]}$

Source: Carneiro Jr. *et al.* (2025) adapted.

Therefore, the dip in transmissibility is governed by the relation in Eq. (4.12a,b). Setting Eq. (4.12a) for the dynamic stiffness of the neutraliser D_w, which is given in Eq. (4.13a) results in (BRENNAN, 1999)

$$\left(\frac{\omega_\mathrm{a}}{\omega_w}\right)^2 = 1+\mu_w\left(\frac{\omega_\mathrm{a}}{\omega_w}\right)^{\frac{1}{2}}, \tag{4.22a}$$

where $\mu_w = (\pi/2)m/(\rho S\lambda_w)$, which is $\pi/2$ times the ratio of the neutraliser mass to the mass in one wavelength of the beam at the natural frequency of the neutraliser.

Similarly, setting Eq. (4.12b) for the dynamic stiffness of the rotational neutraliser, results in (CARNEIRO JR. *et al*., 2025)

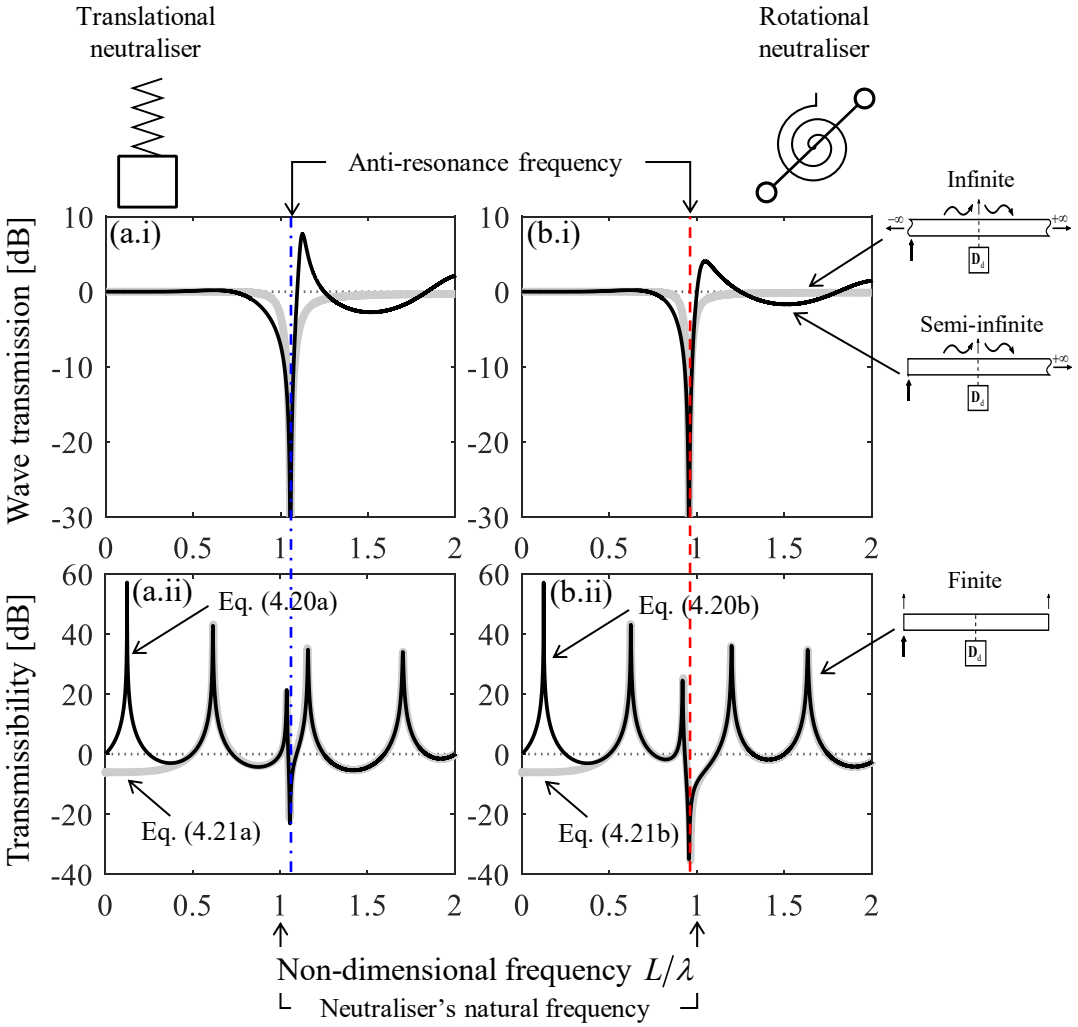
$$\left(\frac{\omega_\mathrm{a}}{\omega_\theta}\right)^2 = 1-\chi_\theta\left(\frac{\omega_\mathrm{a}}{\omega_\theta}\right)^{\frac{1}{2}}, \tag{4.22b}$$

where $\chi_\theta = s_\theta/[8\pi(EI/\lambda_\theta)]$, which is $1/8\pi$ times the ratio of the neutraliser stiffness to the representative stiffness in one wavelength of the beam at the natural frequency of the neutraliser. If $\mu_w \ll 1$, then $\left(\omega_\mathrm{a}/\omega_w\right)^{1/2} \approx 1$, so that $\omega_\mathrm{a} \approx (1+\mu_w/2)\omega_w$ and if $\chi_\theta \ll 1$ then $\omega_\mathrm{a} \approx (1-\mu_\theta/2)\omega_\theta$ (CARNEIRO JR. *et al*., 2025). Equations (4.22a,b) can be used as design parameters.

Figure 4.9 presents the theoretical comparison between the expressions for the infinite, semi-infinite and finite systems. As in Figs. 4.4, 4.6, and 4.8, the neutralisers are chosen so that their mass ratios $\mu_w = \chi_\theta = 0.2$, and their natural frequencies are such that the finite beam length ($L = 2l$) is equal to a wavelength at this frequency, *i.e.*, $L/\lambda_w = L/\lambda_\theta = 1$. The dip in the transmissibility in each case is evident and coincides with the zero-transmission effect when either $\left|4-\hat{D}_w\right| = 0$ or $\left|4+\hat{D}_\theta\right| = 0$. It is also clear that for a translational (rotational) neutraliser this occurs at a frequency greater than (less than) the natural frequency of the neutraliser. It is

important to note that if the neutraliser includes damping, it cannot exhibit a purely mass-like or stiffness-like behaviour, which limits the depth of the dip in transmissibility.

Figure 4.9. Theoretical curves for infinite, semi-infinite and finite beams based on the expressions in Table 4.1. (b) Translational neutraliser; and (b) rotational neutraliser. (i) Infinite and semi-infinite beams wave transmission ratio. (ii) Displacement transmissibility.



Source: Carneiro Jr. *et al.* (2025) adapted.

4.3 EXPERIMENTAL DEMONSTRATIONS

In this section some experimental results are presented to support the theoretical study. The experiments were restricted to the translational neutraliser as this was easier to implement and would validate the main idea presented in this chapter. A long beam whose ends were placed in sandboxes to suppress wave reflections from the ends was considered. The intention was to create conditions for the beam to behave as though it was infinite in the considered frequency range. A similar experiment was also conducted on a beam in which only one end was placed in a sandbox, to simulate the conditions of a semi-infinite beam. The displacement transmissibility of a free-free beam excited by a force at one end, with a translational neutraliser attached to the centre of the beam, was measured to validate the theoretical predictions. The complete experimental setup and other technical details are presented in the Appendix B.

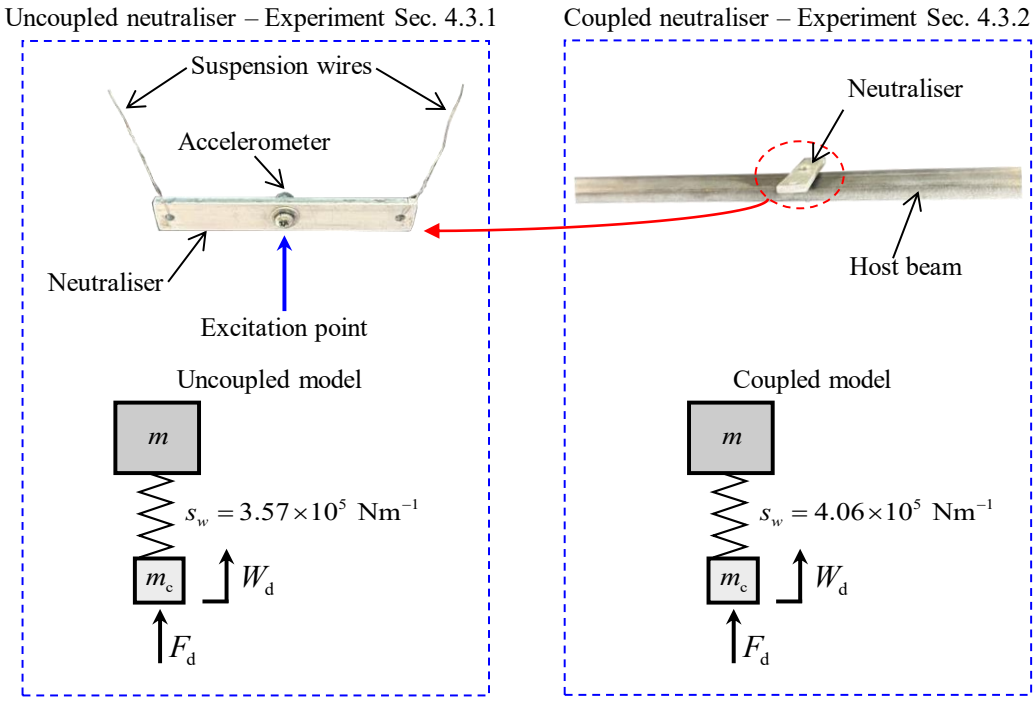
4.3.1 Characterisation of the neutraliser

The translational neutraliser was realised through a free-free aluminium beam which was bolted to the hosting beam at its central position with a washer between the neutraliser and the beam. This arrangement is shown in the upper right part of Fig. 4.10. Part of the neutraliser beam mass acts as the "active" mass of the neutraliser *m*, and the other part acts as the "dead" mass m_c, attached to the host beam. In the frequency range of interest, the neutraliser can be modelled as a spring with stiffness s_w, sandwiched between two masses as shown in the bottom part of Fig. 4.10. The analysis conducted in (KIDNER; BRENNAN, 1999; XIAO *et al*., 2013a), shows that the active mass is approximately 60% of the neutraliser beam mass, while the dead mass is about 40%. The dynamic stiffness of the beam-like neutraliser is thus given by

$$D_w = -\omega^2 m_c + \frac{-\omega^2 m s_w}{s_w - \omega^2 m}. \tag{4.23}$$

As an effect of the coupling to the host beam, the parameters of the neutralizer may differ from those of the uncoupled system. To characterise this device, two models were investigated as shown in Fig. 4.10: coupled and uncoupled.

Figure 4.10. Models to characterise the dynamic behaviour of the beam-like neutraliser.

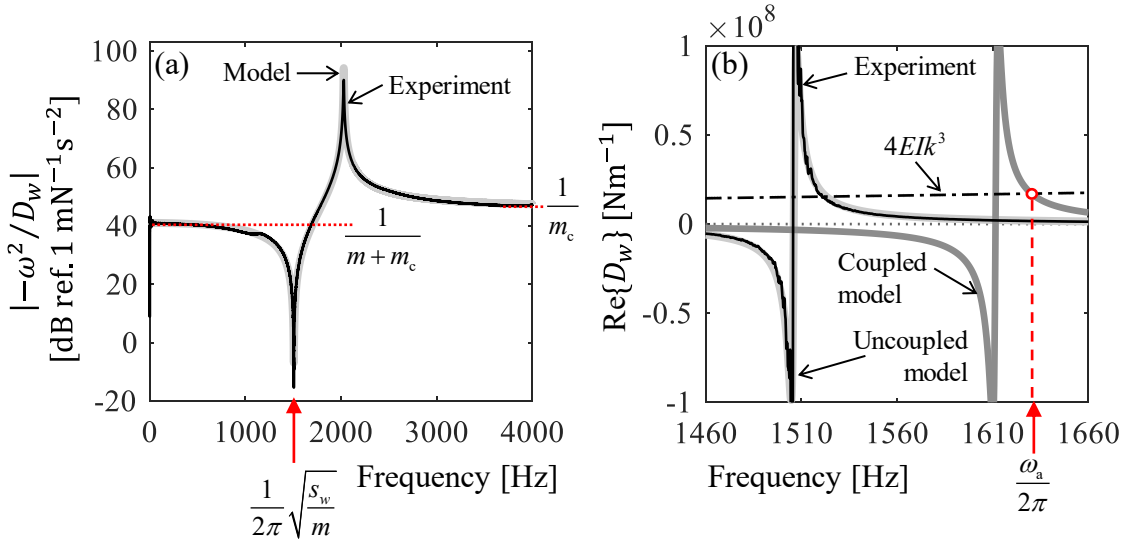


Source: author.

The accelerance of the neutraliser disconnected from the beam was measured. The experimental set up is shown in the upper left part of Fig. 4.10, which depicts the neutraliser suspended at its ends by thin cords to simulate free-free boundary conditions. An accelerometer was attached to the centre of the beam-like neutraliser and it was excited with an impact hammer. The measured modulus of the accelerance is plotted in Fig. 4.11(a) in thin black line. The accelerance based on Eq. (4.23) is also plotted in thick light grey line. The dead mass is determined from the high frequency asymptote as shown in the figure. The low frequency asymptote is used to determine the total mass of the neutraliser, as shown in the figure, from which the active mass can be determined. The anti-resonance frequency marked in the figure is used, together with knowledge of the active mass, to determine the neutraliser stiffness. The resulting values are approximately $m_c = 4.87$ g, $m = 3.96$ g, and $s_w = 3.57\times10^5$ Nm^{-1}. To match the amplitudes of the resonance peaks in the model and experiment, a loss factor of 0.0018 was used in the model.

The real part of the measured and modelled dynamic stiffness of the neutraliser in the limited frequency range of 1460 – 1660 Hz are plotted in Figs. 4.11(b). Two theoretical curves are presented in these figures in addition to the experimental result. The light grey line represents the dynamic stiffness of the translational neutraliser uncoupled from the host beam. The dark grey line represents the dynamic stiffness of neutraliser with an increased stiffness due to the reduction in length of the neutraliser beam which occurs when it is connected to the host beam. From these graphs, it can be seen that the model reproduces the behaviour of the translational uncoupled neutraliser very well.

Figure 4.11. Measurements to characterise the dynamic behaviour of the beam-like neutraliser. (a) Comparison between the neutraliser theoretical and experimental accelerances. (b) Real part of the measured and modelled dynamic stiffness of the neutraliser. Experimental results in solid black lines and theoretical results in solid grey lines.



Source: Carneiro Jr. *et al.* (2025) adapted.

Figure 4.11(b) also shows the real part of the required dynamic stiffness of a neutraliser to suppress the incident wave when the neutraliser is connected to the host beam (coupled model), or, equivalently, to cause a sharp dip in the displacement transmissibility of the beam (dash-dot line). As discussed in Section 4.2, this is when $D_w = 4EIk^3$. It can be seen that this equals the dynamic stiffness of the uncoupled neutraliser when the frequency is 1523 Hz, which corresponds to a neutraliser with a natural frequency of approximately 1506 Hz. In the experimental results with the neutraliser coupled to the beam, which are discussed in the next

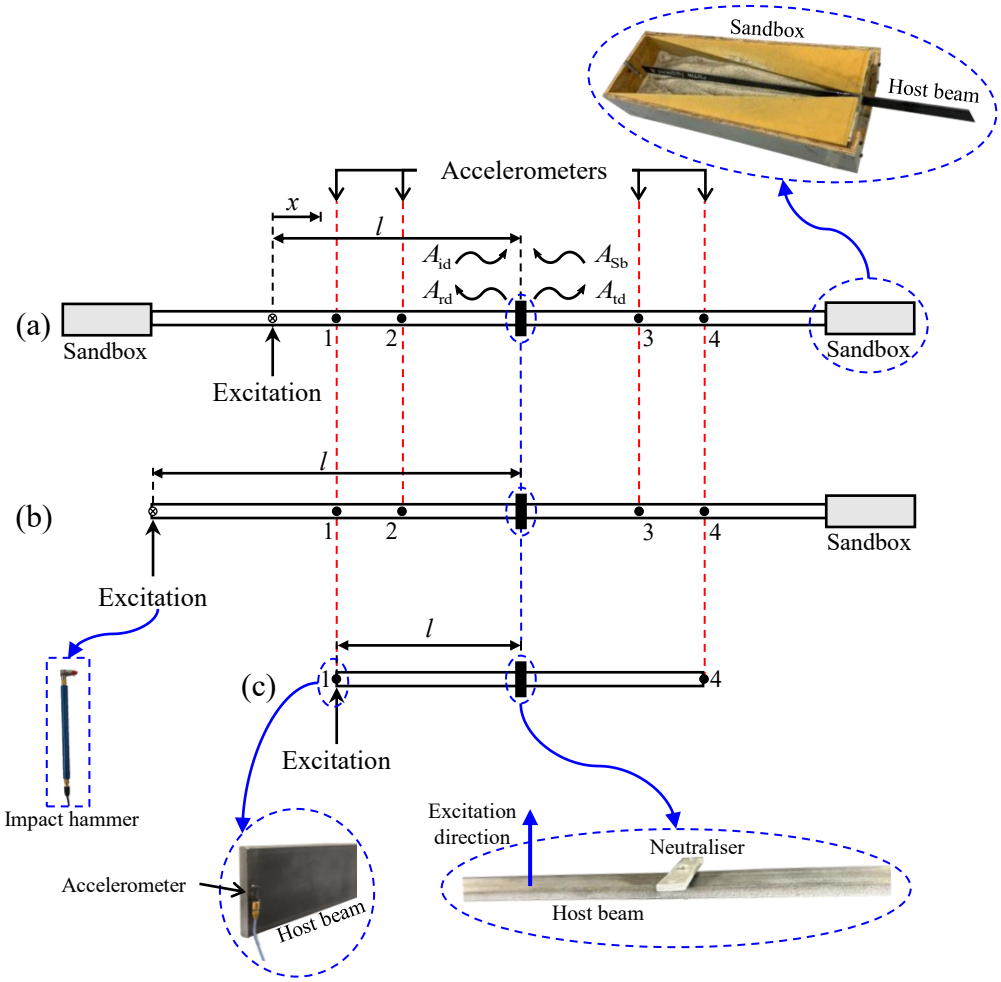
subsection, the dip in the displacement transmissibility occurs at approximately 1630 Hz, which corresponds to a neutraliser with a natural frequency of 1612 Hz. The difference between the natural frequency of the uncoupled neutraliser to its natural frequency when coupled to the host beam, is due partly to the connection between the neutraliser and the host beam through a washer, which has a diameter of approximately 4.4 mm. This means that the effective neutraliser length is reduced. The ratio of the natural frequencies $(1612/1506)$ is proportional to the square root of the increase in neutraliser stiffness, which is approximately 7%. As the neutraliser stiffness is inversely proportional to the cube of the length, the corresponding neutraliser length is reduced by approximately 5% or 4 mm, which compares well with the diameter of the actual washer used in the experiment. The conclusion from this part of the experimental work is that the two-mass and spring model, shown in the bottom right part of Fig. 4.10, has values $m_{\mathrm{c}} = 4.87$ g, $m = 3.96$ g, and $s_w = 4.06\times10^5$ Nm^{-1}, respectively.

4.3.2 Host beam with neutraliser attached

Once the neutraliser had been characterised experimentally, it was then attached to three configurations of the host beam to verify the theoretical analysis described in Section 4.2. Figure 4.11 shows the schematic of the experimental setup.

To examine the local behaviour of the beam close to the neutraliser, wave transmission across the neutraliser was measured. The incident wave A_{is} and the transmitted wave A_{t} were determined from two acceleration measurements between the excitation force and the neutraliser at positions 1 and 2, and two acceleration measurements downstream of the neutraliser at positions 3 and 4. Wave reflections were suppressed from each end of the beam by using sandboxes to simulate infinite conditions, and then one sandbox was removed upstream of the neutraliser to simulate a semi-infinite beam.

Figure 4.12. Experimental setup (not to scale) (a) infinite beam (sandbox at each end of the host beam), (b) semi-infinite beam (sandbox at one end of the host beam), and (c) finite beam.



Source: Carneiro Jr. *et al.* (2025) adapted.

The relationship between the incoming and outgoing waves A_{id}, A_{rd}, A_{td}, to and from the neutraliser at high frequencies, and the reflected from the sandbox, A_{Sb} are related to the measured accelerances by (MACE; HALKYARD, 2000)

$$\begin{Bmatrix} A_{id} \\ A_{rd} \\ A_{td} \\ A_{Sb} \end{Bmatrix} = \frac{F}{-\omega^2} \begin{bmatrix} e^{-jk_{exp}(x_1-l)} & e^{jk_{exp}(x_1-l)} & 0 & 0 \\ e^{-jk_{exp}(x_2-l)} & e^{jk_{exp}(x_2-l)} & 0 & 0 \\ 0 & 0 & e^{-jk_{exp}(x_3-l)} & e^{jk_{exp}(x_3-l)} \\ 0 & 0 & e^{-jk_{exp}(x_4-l)} & e^{jk_{exp}(x_4-l)} \end{bmatrix}^{-1} \begin{Bmatrix} \tilde{A}_1 \\ \tilde{A}_2 \\ \tilde{A}_3 \\ \tilde{A}_4 \end{Bmatrix}, \tag{4.24}$$

where x_i is the distance between the measurement points and the excitation point, and $\tilde{\mathrm{A}}_i(\omega)$ is the accelerance between the acceleration measured at the *i*-th point and the excitation force *F*. The distance l is the distance between the excitation point and neutraliser, which is $1.72\,\mathrm{m}$ for the infinite beam and 3.25 m for the semi-infinite beam. In the matrix in Eq. (4.24) k_{exp} is the wavenumber of the host beam that was determined experimentally to be $k_{\mathrm{exp}} \approx 0.93\sqrt{f}$ from the phase measured between positions 1 and 4, with the neutraliser removed on the infinite beam. The corresponding theoretical value obtained from the beam properties is $k \approx 0.92\sqrt{f}$.

The results for the infinite beam are shown in Fig. 4.12(a), together with the prediction from the model. In this case, the reflections at the anechoic terminations are small and the equivalence between the theoretical and experimental wave amplitudes $A_{\mathrm{t}}/A_{\mathrm{is}} = B_{\mathrm{t}}/B_{\mathrm{i}}$ was assumed.

For the semi-infinite beam, the wave incident on the neutraliser A_{id} determined using Eq. (4.24) is not the wave generated by the force as it is in the infinite beam case. It contains also the contribution from the left-going wave generated by the neutraliser, which is subsequently reflected from the left-hand boundary. In this case $A_{\mathrm{rd}} = A_{\mathrm{d}}^{-}$ because the reflected wave from the sandbox A_{Sb} is very small. The equivalent expression to Eq. (4.15a) is therefore $A_{\mathrm{t}}/A_{\mathrm{is}} = A_{\mathrm{td}}\Big/\left(A_{\mathrm{id}} - \mathrm{j}A_{\mathrm{rd}}\,\mathrm{e}^{-\mathrm{j}2k_{\mathrm{exp}}l}\right)$.

Figure 4.12(a) and (b) present the comparisons of the experimental curves with the theoretical curves predicted respectively by Eq. (4.11a) and Eq. (4.15a) for the systems used in the experiments. The curves show good agreement. The multiple oscillations observed in the experimental results are due to the interactions of the induced waves and the waves reflected from the sandboxes, as perfect anechoic terminations were not achieved.

The last experiment consisted of measuring the acceleration transmissibility of a 1.1 m long steel beam with the neutraliser attached to its mid-point. To simulate free-free boundary conditions, the beam was suspended vertically by thin wires. The host beam was excited at one end and the accelerations at each end of the beam were measured as shown in Fig. 4.11(c).

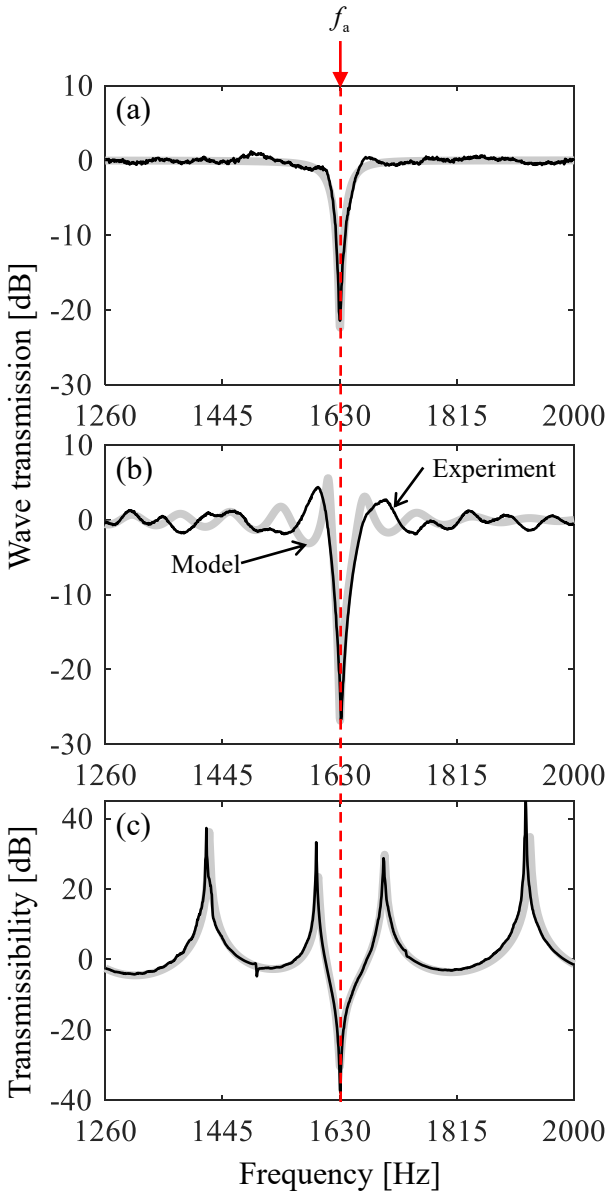
The measured transmissibility of the beam is plotted in Fig. 4.12(c) as thin black lines. The theoretical result is also plotted as a thick grey line using the approximate model of Eq. (4.21a), also including the effect of the mass of the accelerometers at the ends of the host beam,

in which the dynamic stiffness model of the neutraliser determined in Sec. 4.3.1 has been used. The material loss factor of the host beam and neutraliser were estimated to be 0.001 and 0.0015 by matching the theoretical and experimental peaks and dip, respectively. The dip in the transmissibility occurs at approximately $f_{\mathrm{a}} \approx 1630\ \mathrm{Hz}$, which is consistent with the results from the previous subsection.

At the coupled neutraliser natural frequency (approximately 1612 Hz) the bending wavelength of the host beam is approximately 0.17 m, which means that the mass of the beam per wavelength is approximately 258 g. The active mass of the neutraliser estimated is 3.96 g. This means that the mass ratio in Eq. (4.22a) is equal to $\mu_w = (\pi/2) m/\rho S \lambda_w \approx 0.024$. Using the approximate expression $f_{\mathrm{a}} \approx (1+\mu_w/2) f_w$ given in Sec. 4.2.4.1, implies that the dip (or anti-resonance) occurs at a frequency about 1.2% greater than the natural frequency of the neutraliser.

Comparing the plots in Fig. 4.12, it can be seen that the frequency at which the dip occurs in the wave transmission ratio coincides with the dip in the transmissibility, demonstrating that the physical mechanism behind the anti-resonance is due to the wave suppression by the neutraliser.

Figure 4.13. Experimental measurements, in thin black lines, and theoretical model, in thick grey lines, for wave transmission ratio on (a) infinite and (b) semi-infinite beams; and transmissibility of a (c) finite beam.



Source: Carneiro Jr. *et al.* (2025) adapted.

4.4 LOCAL RESONANCE EFFECT IN BEAMS AND RODS

The previous sections have discussed vibration control in beams, particularly through the use of a neutraliser. Neutralisers are commonly employed in engineering systems to control structural vibrations. Nearly a century has passed since their theoretical description by Ormondroyd and Den Hartog (ORMONDROYD; DEN HARTOG, 1928), and they have been extensively studied to enhance their frequency range of operation and robustness (RAHIMI *et al*., 2020).

In general applications, the tuned frequency, at which no vibration is transmitted, corresponds to the neutraliser's natural frequency. This holds true for mono-coupled structures. However, this may not apply when controlling flexural vibrations in beams. At the neutraliser's natural frequency, the beam behaves as if it is pinned or hinged, depending on the type of neutraliser, whether translational or rotational. Observing the transmissibility, the inclusion of a neutraliser in structures such as rods results in the emergence of a dip in the frequency response function between the source and receiver. This dip, corresponding to an anti-resonance, occurs at the neutraliser's natural frequency. In beams, a similar effect on transmissibility, caused by the influence on transfer receptance, is observed. However, this does not occur for the same reason and not at the neutraliser's natural frequency, as shown in the previous sections.

Although the phenomena observed in both rods and beams are effective local resonance effects, the control mechanisms associated with each waveguide differ. As discussed in Section 4.2.2.1 and by Mead (1982, 1999), simple lumped parameters, such as grounded springs and rotary masses, can result in the zero-transmission effect. In rods, this effect only arises with the inclusion of a resonant system, this is, the neutraliser. A qualitative method to infer this is to evaluate the effective behaviour of each system. The beam responds effectively to force excitation as a mass in series with a damper; thus, the inclusion of a stiffness-like element satisfies the resonance condition. Conversely, the rod exhibits an effective damping behaviour, as expressed in Eq. (3.8), which necessitates a mass-spring system for the resonance effect to occur.

4.5 CHAPTER REMARKS

This chapter has presented a comprehensive study on the control of vibration propagation in thin beams with external discontinuities, highlighting the theoretical and experimental aspects of vibration neutralisers. The analysis demonstrated how discontinuities, modelled as dynamic stiffness elements, influence wave transmission in both infinite and finite beam configurations.

Using the wave-based approach it was demonstrated that there is a significant reduction in the transmitted wave for infinite and semi-infinite beams when either $\left|4-\hat{D}_w\right|=0$ or $\left|4+\hat{D}_\theta\right|=0$. Using the dynamic stiffness and receptance matrix approach, the displacement transmissibility expressions for the finite beam were determined. An approximate expression for the transmissibility was also derived by applying high-frequency approximation, which proved to be effective at $l/\lambda>1$ when the frequency is high enough, such that the evanescent waves at the ends of the beam and at the neutraliser do not significantly interact with each other.

Combining the discussions of the different approaches, it was found that the zero-transmission effect coincides with the dip in the displacement transmissibility for the finite beam. Therefore, the anti-resonance in the transfer receptance is due to the propagating wave generated by the neutraliser cancelling the incident wave that results in net zero wave transmission. This means that the effect depends only on the local interaction between the attached device dynamic stiffness and the dynamic stiffness of the host bare beam at the attachment point.

The investigation of the effects of the boundary conditions led to determining the frequency and distance relationship between the excitation and the neutraliser, in which the reflected left-going wave generated by the neutraliser combines either destructively or constructively with the wave generated by the source. Consequently, there will be a frequency where the neutraliser cannot cause an anti-resonance in the transfer receptance, *i.e.* a dip in the displacement transmissibility. The theoretical developments were supported by experimental results, which demonstrated that the local effect occurs at the same frequency regardless of the boundary condition downstream of the attached device.

A deep understanding of the control parameters in vibration transmission in beams is an important tool for applying the phenomenon investigated in the next chapter as a strategy for improving the attenuation bands.

5 EFFECTS OF COUPLING LOCAL RESONANCE BAND AND BRAGG STOP BAND IN BEAMS

5.1 INTRODUCTION

Modern structural designs consider the multiple factors associated with the application. In civil engineering, there is a growing number of architectural design forms favouring unorthodox and/or very slender structures, which require dynamic analyses, far beyond the traditional only statics considerations (MESKOURIS *et al*., 2019). In this context, many studies have been dedicated to methods for modelling and mitigating vibrations. An alternative method has emerged in recent decades from the investigation of the coupling effects of Bragg and the local resonance effect stop bands, resulting in the so-called super stop bands or ultra-wide stop band (BHATT; BANERJEE, 2023). However, this approach does not have its control parameters and physical behaviour defined as a band broadening technique in finite multi-coupled structures. Addressing these gaps constitutes the primary objective of this chapter.

In this chapter, the approaches described in Chapter 2 and the theoretical developments in Chapter 3 are applied to fill the aforementioned knowledge gap. The aim is to investigate the dynamics of finite Euler-Bernoulli beam with an external discontinuity, which is a translational or rotational vibration neutraliser, configured to produce the coupling effect of the stop bands due to local resonance and the Bragg scattering.

5.2 COUPLING LOCAL RESONANCE BAND AND BRAGG BAND GAP: THE SUPER ATTENUATION BAND

In this section, the fundamental concept of the super attenuation band phenomenon is presented. The work conducted by Cleante *et al.* (2022) is used as base line to demonstrate the effect under investigation in a simpler system, that is, a mono-coupled structure. Consider a homogeneous rod of length $2l$, to which a discontinuity is attached at its central point as shown in Fig. 5.1. The transfer matrix of this system is described as $\mathbf{T} = \mathbf{T}^{[\mathrm{rod}]}\mathbf{T}^{[\mathrm{d}]}\mathbf{T}^{[\mathrm{rod}]}$, in which $\mathbf{T}^{[\mathrm{rod}]}$ is given by Eq. (3.12) and

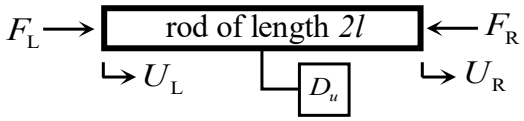
$$\mathbf{T}^{[\mathrm{d}]} = \begin{bmatrix} 1 & D_u \\ 0 & 1 \end{bmatrix}.$$

After some manipulation, the transmissibility is given by

$$\frac{U_{\mathrm{R}}}{U_{\mathrm{L}}} = \frac{1}{\cos\left(2k_{\mathrm{r}}l\right) + D_u \cos\left(k_{\mathrm{r}}l\right)\sin\left(k_{\mathrm{r}}l\right)}, \tag{5.1}$$

where, exclusively in this chapter, $k_{\mathrm{r}} = \omega\sqrt{\rho/E}$ is the rod wavenumber and D_u denotes the dynamic stiffness of the discontinuity.

Figure 5.1. General rod with an attached device at it central point.



Source: author.

The coupled discontinuity can take the form of a grounded spring, concentrated mass, or an undamped axial neutraliser, such as the structures in the lower part of Fig. 5.2. For these elements $D_u = s_u$, $D_u = -\omega^2 m$ and $D_u = -\omega^2 m s_u/(s_u - \omega^2 m)$, respectively (GARDONIO; BRENNAN, 2004). Figure 5.2 presents the transmissibility curves for these structures as a function of the dimensionless frequency $l/\lambda = k_{\mathrm{r}}l/2\pi$, assuming a loss factor of 0.01 in the wavenumber to control peak amplitudes.

In Figure 5.2(a), the first row illustrates the transmissibility for the case in which a neutraliser is coupled to the rod under three different conditions. In case (i), the neutraliser is tuned so that, at its natural frequency $\omega_u = \sqrt{s_u/m}$, its dynamic stiffness is equivalent to s_u. In case (iii), the neutraliser is adjusted such that its dynamic stiffness at its natural frequency equals $\omega_u^2 m$. These figures reveal two distinct regions where the transmissibility is less than unity (0 dB), and referred as attenuation bands. The first attenuation band, characterized by a sharp dip in transmissibility, is governed by the local resonance effect, and its dip frequency corresponds to the natural frequency of the neutraliser. The second attenuation band, which exhibits a narrow bandwidth and a smooth curve, is primarily controlled by the stiffness of the

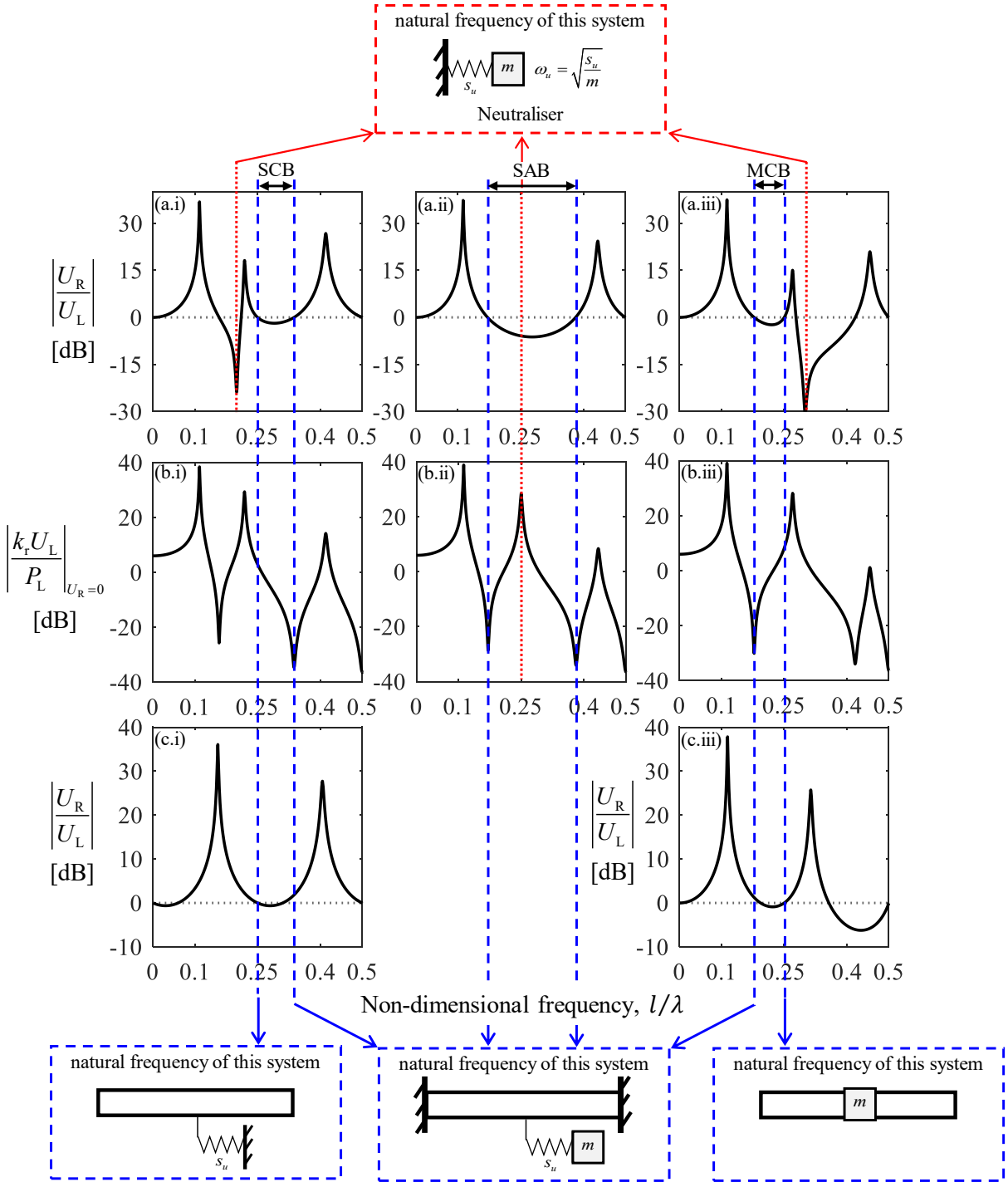
neutraliser (when above the dip and denoted as SCB – Fig. 5.2(i)) or by the mass of the neutraliser (when below the dip frequency and denoted as MCB – Fig. 5.2(iii)).

Figure 5.2(a.ii) illustrates the condition in which the neutraliser is tuned such that its natural frequency coincides with the natural frequency of the host structure. In this case, only a single attenuation region is observed within the examined frequency range. This region is characterized by a broad bandwidth and smooth attenuation band, leading to its designation as the super attenuation band (SAB).

As discussed in Section 2.4.2, the dynamic behaviour of the structure can be inferred from receptances. From that section, the boundary frequencies corresponding to the conditions explored in Fig. 5.2(a) can be analysed using the drive-point receptances. The resonance of the free-free receptances indicates the boundary frequency that corresponds to the free-free natural frequency of the structure. However, the boundary frequency at which the free-free receptances have equal magnitudes does not allow a direct analogous physical interpretation. In this case, the boundary condition $U_{\mathrm{R}} = 0$ is imposed, and the point receptance at the free end is analysed. These curves are depicted in Figure 5.2(b). This allows access to the physical interpretation from resonances and anti-resonances, and in the latter, it is possible to verify the correspondence with the natural frequency of the fixed-fixed structure.

Figure 5.2(c) presents the transmissibility when a (i) grounded spring and (iii) a concentrated mass are coupled under the same dynamic stiffness conditions as those applied to the neutraliser. By comparing the corresponding attenuation bands in Fig. 5.2(a.i) and 5.2(a.iii), the influence of these elements on transmissibility control becomes evident.

Figure 5.2. Dynamic behaviour, expressed in the form of transmissibility and drive-point receptance, of the rod with different types of couplings. (a) Transmissibility for an attached axial neutraliser with dynamic characteristics of (i) stiffness, (ii) combined and (iii) mass. (b) Point receptance of the system in (a) imposing displacement restriction at the right end. (c) transmissibility for an attached (i) grounded spring and (iii) concentrated mass.



Source: author.

These results corroborate previous works (CLEANTE *et al*., 2022; GONÇALVES *et al*., 2021) to summarize the super attenuation band behaviour as follows.

- When a periodic structure is assembled (*N* rods with neutralisers), the Bragg effect will be observed in the SCB and MCB, reducing the minimum transmissibility but without changing the bandwidth of these regions.
- The super attenuation band emerges when Bragg and local resonance effects are combined.
- The key condition is to attach the neutraliser at a nodal point of the host cell and tuning its natural frequency to the free-free natural frequency of the host cell.

It is noteworthy that the super attenuation band does not have maximum attenuation (minimum transmissibility) as pronounced as the local resonance effect band exclusively. However, SAB has an attenuation greater than that of the Bragg band, which increases as the number of cells increases (as does the Bragg band), maintaining a broader bandwidth. Furthermore, the reduction in the number of amplification peaks for the same frequency band should also be notable when the SAB is formed.

The ω_u/ω_r ratio, where ω_r is the rod natural frequency, can be used to define a parameter that relates the cell length to the corresponding wavelengths λ_u and λ_r of the structure at these respective frequencies. This implies that for each neutraliser configuration, the ratio of the form $l/\lambda_u = (\omega_u/\omega_r) l/\lambda_r$. Such a parameter enables alternative perspectives for physical interpretation, particularly in the context of the continuous finite systems analysed in this study.

As observed in the rod presented in this section, the inclusion of a neutraliser induces a local resonance effect, which manifests as an anti-resonance in the transfer receptance and as a dip in the transmissibility. This effect is the same as that discussed in Chapter 4. However, the control parameters in this multi-coupled system differ, and their influence on the formation of the super attenuation band must be thoroughly investigated.

5.3 THE FORMATION OF THE SUPER ATTENUATION BAND IN SINGLE-SPAN BEAMS

In this section, the formation of the super attenuation band is discussed in terms of the neutraliser referred to in Sec. 4.2.2.2. To create a local resonance effect in beams it is not necessary to have an attached neutraliser but elements that behave as transverse stiffness or rotational mass, as discussed in the Chapter 4. In fact, assuming that the excitation frequency is high enough to confine the evanescent waves close to the discontinuities, the dip in the transmissibility is controlled by Eq. (4.12a,b), this is,

$$4EIk^3 - D_w = 0 \quad \text{and} \quad 4EIk + D_\theta = 0 .$$

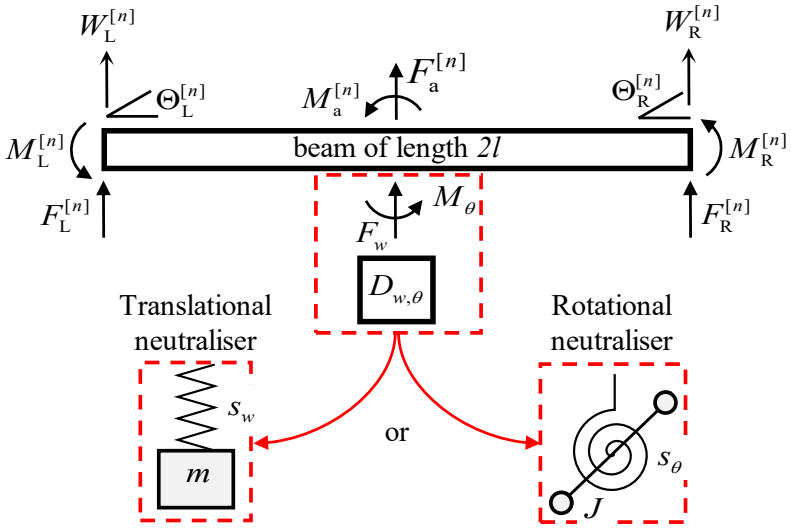
From these relations, it follows that it is possible to adjust the neutraliser parameters so that the local resonance effect occurs at the desired frequency.

The model for a single-span beam with a neutraliser/discontinuity coupled at its midpoint is described in Sec. 4.2.4 and is reproduced here as shown in Fig. 5.3. The transmissibility is expressed by Eq. (4.20a,b). From Eqs. (4.13a,b), the non-dimensional dynamic stiffness of these devices can be conveniently rewritten as

$$\hat{D}_w = -4\mu_w \frac{\left(\lambda_w/\lambda\right)^4}{1-\left(\lambda_w/\lambda\right)^4} \quad \text{and} \quad \hat{D}_\theta = -4\chi_\theta \frac{\left(\lambda_\theta/\lambda\right)^4}{1-\left(\lambda_\theta/\lambda\right)^4}, \tag{5.2a,b}$$

which makes explicit the relationship between the wavelengths λ and $\lambda_{w,\theta}$, the latter being the wavelength at which the beam is excited at the translational or rotational neutraliser natural frequency, respectively. Note that $\lambda_{w,\theta}$ is a constant parameter for each neutraliser configuration. As in the previous chapter $\mu_w = \left(\pi/2\right)m/(\rho S\lambda_w)$ and $\chi_\theta = s_\theta/[8\pi\left(EI/\lambda_\theta\right)]$.

Figure 5.3. Single-span beam with discontinuity attached force and displacements components. The attachment is assumed to be a translational or a rotational neutraliser.



Source: author.

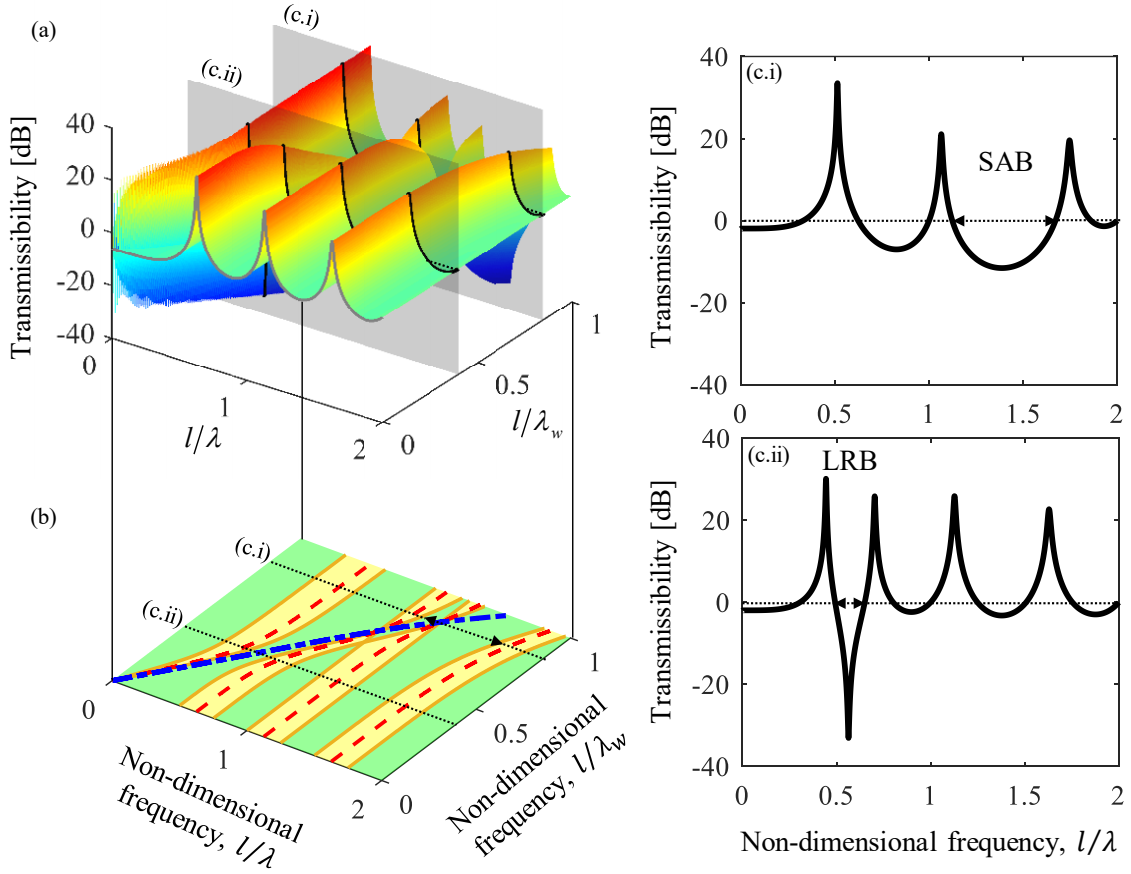
The condition under which a translational neutraliser is coupled to the beam is initially investigated. Figure 5.4 presents methods of visualising the behaviour of the structure in focus, with the transmissibility curves varying as a function of the non-dimensional frequency parameter l/λ_w. It is important to emphasise that this figure has an instructive nature since each l/λ_w implies a different system, that is, a different neutraliser set, which is better evaluated from Figs. 5.4(b-c). In all the cases, the curves were obtained from Eq. (4.20a) and assumed a loss factor of 0.02 to write the complex wavenumber and control the peak.

Figure 5.4(b) shows the top view of Fig 5.4(a), considering a reference plane when the transmissibility is equal to one unit or 0 dB. In this figure, the regions in yellow and green correspond to the areas where the transmissibility is above (amplification) and below (attenuation) 0 dB, respectively. The red dotted lines correspond to the transmissibility peaks and the blue dash-dotted lines correspond to the transmissibility dip. Figure 5.4(c) represents the transmissibility under particular conditions of l/λ_w, which is indicated in Fig 5.4(a) by the shaded planes and in Fig. 5.4(b) by the dotted black lines.

In condition (i), the system is tuned to produce the super attenuation band, a region highlighted by the arrows and characterised by the smoothness of the transmissibility curve and the increase in bandwidth. Condition (ii), however, presents an untuning, and the local resonance region (LRB) is evident. This observation method guarantees comprehensive analysis of the structure. While the *top view* is advantageous in viewing tuning conditions given

a frequency range, the *front view* (Figs. 5.4(c)) allows evaluation of the attenuation level and interpretation of the dynamic behaviour of the system.

Figure 5.4. Methods of visualizing transmissibility. (a) Composite view. (b) Top view with reference to a unit. (c) Transmissibility of the shaded planes indicated in (a) – front views.



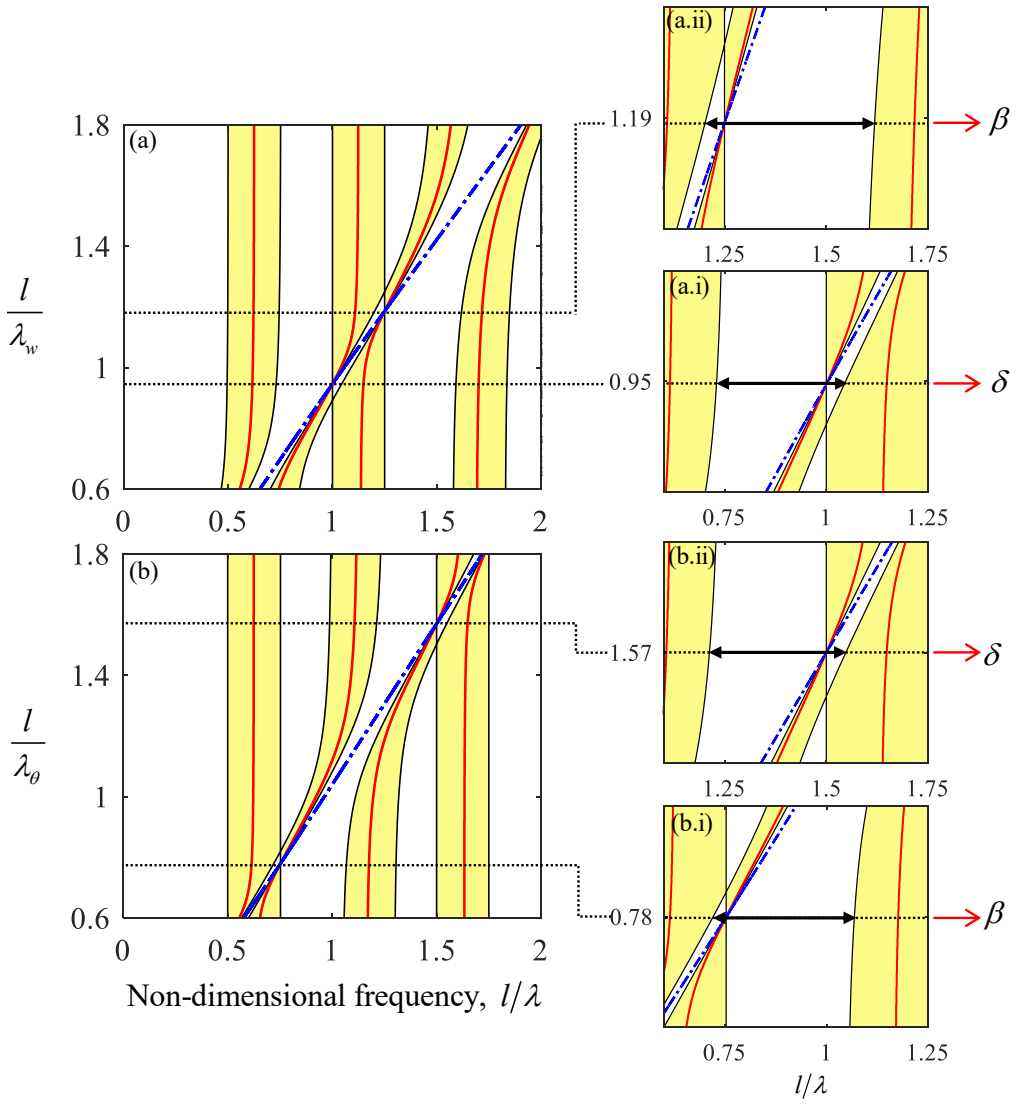
Source: author.

5.3.1 The tuning conditions of the super attenuation band

The top views of Eqs. (4.20a) and (4.20b) are plotted in Fig. 5.5 for (a) a translational neutraliser and (b) a rotational neutraliser. It is assumed $\mu_w = 0.2$ and $\chi_\theta = 0.2$. In this figure, the yellow regions indicate the amplification bands and the white areas are the attenuation bands. The blue dash-dotted lines correspond to the transmissibility dip. For each of the conditions evaluated, the formation of the super attenuation band is highlighted by the black arrows. The column of figures on the right show details of the indicated regions where the super attenuation band forms.

The super attenuation band emerges when two attenuation bands merge due to an overlap of the peak, dip, and frequency band curves. This phenomenon suggests the union of a local resonance band with a Bragg band (resulting from either the mass or stiffness effects). The LRB is characterised by the presence of a dip curve, whereas the Bragg band is distinguished by the constancy of one of its boundary frequencies, either at the natural frequency of the host structure, $l/\lambda \approx (i+1/2)/2$ for $i = 1,\ 2,\ 3,\ \ldots$, for the free-free bare beam (BLEVINS, 1979) or at the frequencies $l/\lambda = i/2$, for $i = 1,\ 2,\ 3,\ \ldots$. These frequencies serve as the tuning frequencies of the SAB.

Figure 5.5. Transmissibility top views assuming (a) a translational neutraliser with $\mu_w = 0.2$ and (b) rotational neutraliser with $\chi_\theta = 0.2$; and close-up in the (i) δ and (ii) β tuning conditions.



Source: author.

As illustrated in Figs. 5.5(a) and 5.5(b), the tuning frequencies vary depending on the type of the coupled device. However, they always appear in pairs within a specified periodic frequency range. Each tuning condition pair consists of a natural frequency and the frequencies related to $l/\lambda = i/2$, for $i = 1,\ 2,\ 3,\ \ldots$.

To analyse each tuning condition of the super attenuation band indicated in Fig. 5.5, examine the (a) transmissibilities and (b) their corresponding receptances, as presented in Fig. 5.6. In this analysis, a translational neutraliser is assumed, and the resulting system curves are depicted as solid lines. For comparison, the transmissibility and point receptance of the host structure (bare beam) are indicated by dashed dotted lines.

The configuration in which the lowest-frequency SAB forms occurs at (i) $l/\lambda_w = 0.946$, where the tuning frequency is $l/\lambda_{\text{tun}} = 1$. This condition, highlighted by the vertical dotted lines, is referred to as the tuning condition δ. At this tuning frequency, the anti-resonances align, indicating that the transverse displacement at the beam ends tends to be minimal, with the right end exhibiting even smaller absolute motion than the left.

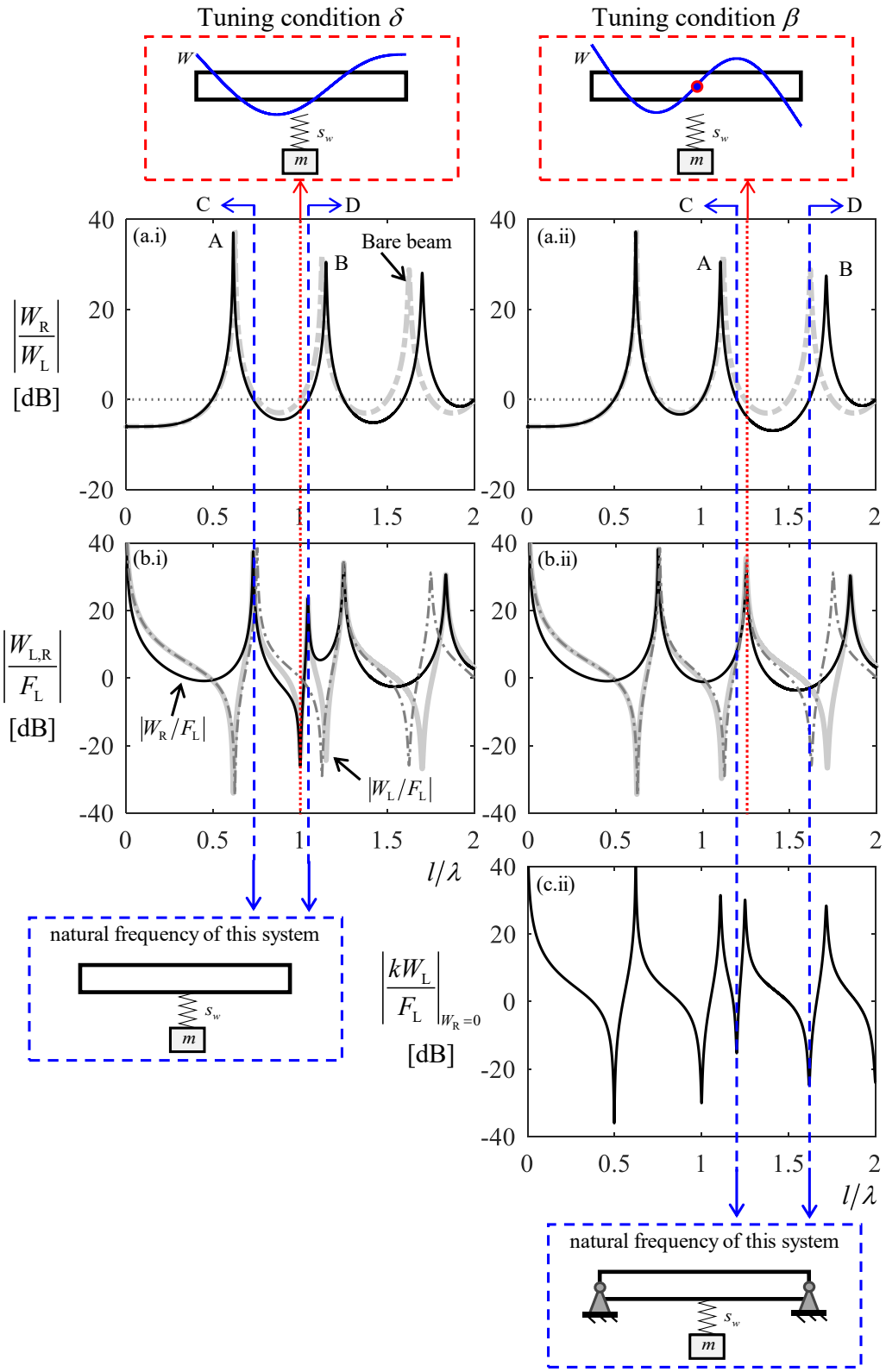
The second tuning condition, referred to as β, is characterised by parameters (ii) $l/\lambda_w = 1.186$, where the tuning frequency is $l/\lambda_{\text{tun}} = 1.25$. At this frequency, a combination of resonances occurs, converging with the resonance of the bare beam. Even in the absence of damping, although resonance indeterminacy exists, their quotients remain defined and finite. As indicated by the transmissibility, this results in a reduction in the relative motion between the beam ends.

Within the SAB, there are amplification peaks A and B on either side of the target bandwidth. However, the boundary frequencies C and D differ between the tuning conditions. Under the δ condition, C and D correspond to the natural frequencies of the system. By contrast, in the β condition, C and D are the frequencies at which the magnitudes of the receptances are equal. To investigate this latter case, a pin is assumed at the right end, and the point receptance of the modified system is determined and plotted in Figure 5.6(c.ii). As indicated by the dashed vertical lines, C and D converge to anti-resonances in this system, suggesting that in the β tuning condition, they correspond to the natural frequency of the beam-neutraliser system when both ends are pinned. Furthermore, in both the δ and β conditions, the target bandwidth was chosen to encompass the first and second natural frequencies of the host structure, respectively.

The upper section of Fig. 5.6 illustrates the operational deflection shapes of the host beam at the tuning frequencies, depicted as solid blue lines. These deflection shapes were determined by applying continuity and equilibrium conditions. In the δ tuning condition, the device is not attached to a nodal point of the host structure, whereas in the β tuning condition, it is positioned at a nodal point.

Notably, β tuning corresponds to the behaviour observed in previous studies on mono-coupled systems. Under this condition, vibration is distributed between the neutraliser and the downstream section of the structure. These components act proportionally on the attachment point, maintaining it motionless. Conversely, δ tuning leverages the local effect of the neutraliser, leading to a condition that converges to the natural frequency of a system with constrained ends (pinned-pinned beam with neutraliser).

Figure 5.6. Super attenuation band formation using a translational neutraliser with $\mu_w = 0.2$ and (i) $l/\lambda_w = 0.946$ and (ii) $l/\lambda_w = 1.186$. (a) Transmissibility. (b) Point (grey) and transfer (black) receptances. (c) Point receptance with constrained right-end system. Solid lines and dash-dot lines refer to the system and bare host beam, respectively.



Source: author.

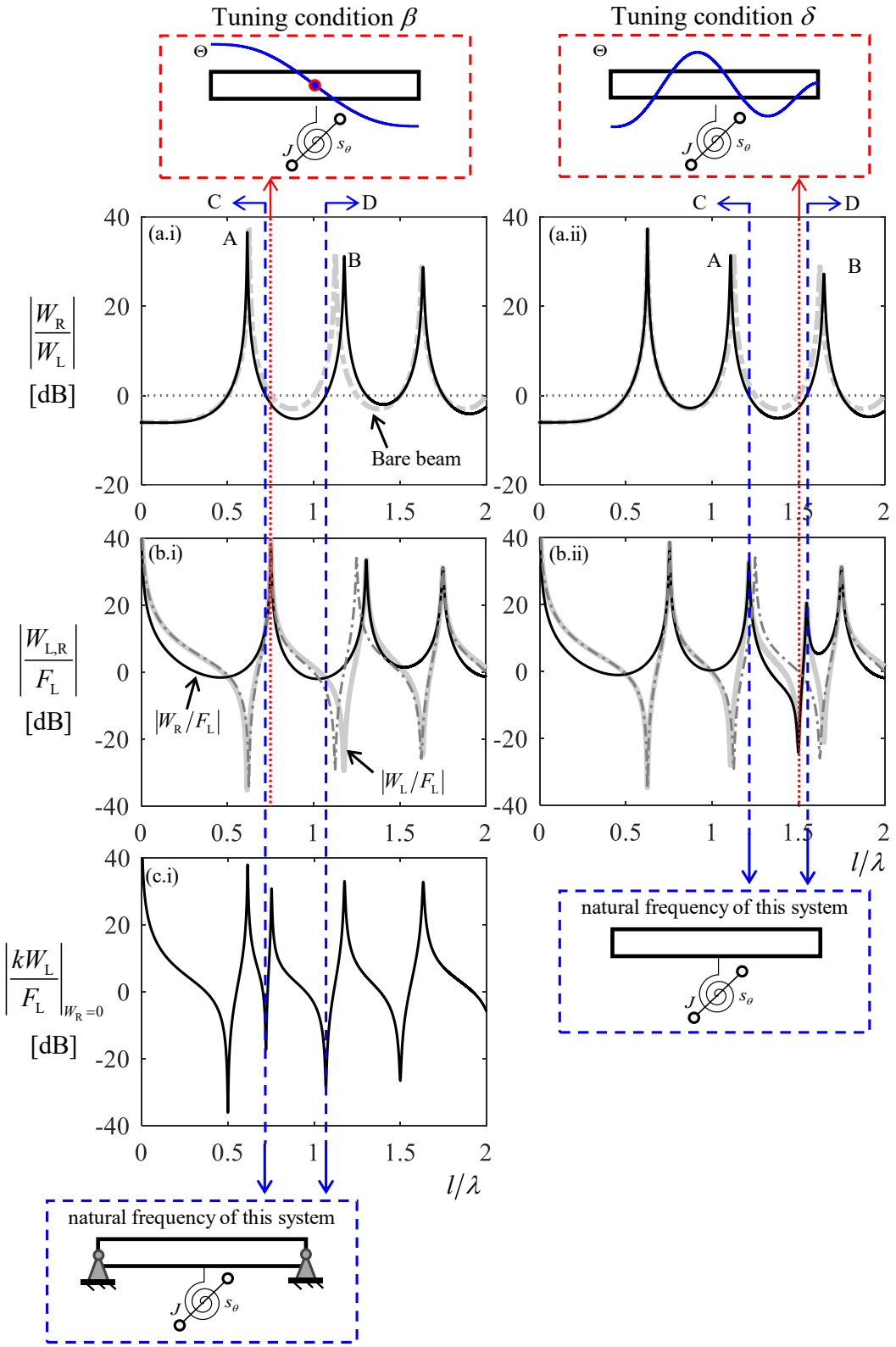
A similar analysis is conducted for the case where a rotational neutraliser is coupled to the beam using the conditions expressed in Fig. 5.5(b). The transmissibility and the corresponding receptances of this system are shown in Fig. 5.7. In this scenario, the β tuning condition occurs in the lower frequency region at $l/\lambda_{\text{tun}} = 0.75$, corresponding to the first natural frequency of the structure. This frequency is associated with the anti-symmetric mode of the rotational motion of the host bare beam, as illustrated in the upper section of Figure 5.7. Consequently, coupling occurs at the nodal points.

In contrast, the δ tuning condition occurs at $l/\lambda_{\text{tun}} = 1.5$. The observed behaviour in this case is similar to that of a system with a translational neutraliser, where the device is not positioned at a nodal point and a SAB forms owing to the anti-resonances match.

The key observations from Figures 5.6 and 5.7 can be summarised as follows:

- Tuning condition β: the device is attached to a node in the translational displacement for translational acting device or a node in the rotation for a rotational acting device. The tuning frequency is the natural frequency of the structure when the neutraliser is not attached.
- Tuning condition δ: the device is attached to an off-node position. The tuning frequency is anti-resonances in the point and in transfer receptances of the free-free-structure occur at the same frequency. This is a pinned-pinned natural frequency for the beam. (In a rod, it is a fixed-fixed natural frequency).
- Frequencies A and B are the transmissibility peaks on either side of the targeted bandwidth. These correspond to the anti-resonance frequencies in the point receptance of the free-free structure.
- Frequencies C and D are the boundary frequencies for transmissibility attenuation band. These correspond to the anti-resonance frequencies in the free-pinned structure for the condition β and the resonance frequencies of the free-free structure for the condition δ.

Figure 5.7. Supper attenuation band formation using a rotational neutraliser with $\chi_\theta = 0.2$ and (i) $l/\lambda_\theta = 0.780$ and (ii) $l/\lambda_\theta = 1.570$. (a) Transmissibility. (b) Point (grey) and transfer (black) receptances. (c) Point receptance with constrained right-end system. Solid lines and dash-dot lines refer to the system and bare host beam, respectively.



Source: author.

5.3.2 Discussions on tuning conditions

To assess the fundamental effect of the neutraliser and the beam interaction on the super attenuation band formation, it is convenient to rewrite the relationships in terms of the receptances. In this sense, consider the receptance matrix of the host beam given by Eq. (4.16). From Eq. (4.19), the interaction between the structure and the translational neutraliser allows writing,

$$\frac{W_{\mathrm{R}}}{F_{\mathrm{L}}} = \mathbf{R}_{\mathrm{RL}}(1,1) - \frac{\mathbf{R}_{\mathrm{Ra}}(1,1)\mathbf{R}_{\mathrm{aL}}(1,1)}{\mathbf{R}_{\mathrm{aa}}(1,1) + 1/D_w}. \tag{5.3}$$

The condition of $l/\lambda_{\mathrm{tun}} = 1$, as shown in Fig. 5.6(i), implies $\left|W_{\mathrm{R}}/F_{\mathrm{L}}\right| \to 0$, thus $\mathbf{R}_{\mathrm{RL}}(1,1)\left(\mathbf{R}_{\mathrm{aa}}(1,1) + 1/D_w\right) - \mathbf{R}_{\mathrm{aL}}(1,1)^2 = 0$ or

$$D_w = \frac{\mathbf{R}_{\mathrm{RL}}(1,1)}{\mathbf{R}_{\mathrm{aL}}(1,1)^2 - \mathbf{R}_{\mathrm{RL}}(1,1)\mathbf{R}_{\mathrm{aa}}(1,1)}. \tag{5.4}$$

Note that the right part of Eq. (5.4) depends solely on the relationships of the host beam. Replacing Eq. (4.13a) in (5.4), the ideal physical parameter for this tuning condition is determined and given by,

$$\left(\frac{\omega}{\omega_w}\right)^2 = \frac{\Delta_w}{\Delta_w - s_w}, \tag{5.5}$$

where $\Delta_w = \mathbf{R}_{\mathrm{RL}}(1,1)\Big/\left(\mathbf{R}_{\mathrm{aL}}(1,1)^2 - \mathbf{R}_{\mathrm{RL}}(1,1)\mathbf{R}_{\mathrm{aa}}(1,1)\right)$.

As discussed, the tuning condition shown in Fig. 5.6(ii), with $l/\lambda_{\mathrm{tun}} = 1.25$ implies matching resonance frequencies. Like the procedure with the tuning frequency $l/\lambda_{\mathrm{tun}} = 1$, the relationship of left-end motion and excitation can be rewritten in terms of the receptances of the host beam so that (see Eq. 4.18)

$$\frac{W_{\mathrm{L}}}{F_{\mathrm{L}}} = \mathbf{R}_{\mathrm{LL}}(1,1) - \frac{\mathbf{R}_{\mathrm{La}}(1,1)\mathbf{R}_{\mathrm{aL}}(1,1)}{\mathbf{R}_{\mathrm{aa}}(1,1) - 1/D_w}. \tag{5.6}$$

Setting the denominator to zero determines that $D_w = -1/\mathbf{R}_{\mathrm{aa}}(1,1)$. Substituting Eq. (4.13a) in this expression, we obtain the ideal physical parameter to form the super attenuation band at β tuning condition, which is given by

$$\left(\frac{\omega}{\omega_w}\right)^2 = \frac{\mathrm{B}_w}{\mathrm{B}_w - s_w}, \tag{5.7}$$

where $\mathrm{B}_w = -1/\mathbf{R}_{\mathrm{aa}}(1,1)$.

The same procedure used for the translational neutraliser is applied to the coupled rotational neutraliser. In this case, Equation (4.18) and (4.19) allows the point and transfer receptances to be expressed, respectively, as

$$\frac{W_{\mathrm{L}}}{F_{\mathrm{L}}} = \mathbf{R}_{\mathrm{LL}}(1,1) - \frac{\mathbf{R}_{\mathrm{La}}(1,2)\mathbf{R}_{\mathrm{aL}}(2,1)}{\mathbf{R}_{\mathrm{aa}}(2,2) - 1/D_\theta}$$

and

$$\frac{W_{\mathrm{R}}}{F_{\mathrm{L}}} = \mathbf{R}_{\mathrm{RL}}(1,1) - \frac{\mathbf{R}_{\mathrm{Ra}}(1,2)\mathbf{R}_{\mathrm{aL}}(2,1)}{\mathbf{R}_{\mathrm{aa}}(2,2) + 1/D_\theta}.$$

For the β tuning condition (resonance matching), the tuning parameter is given by

$$\left(\frac{\omega}{\omega_\theta}\right)^2 = \frac{\mathrm{B}_\theta}{\mathrm{B}_\theta - s_\theta}, \tag{5.8}$$

where $\mathrm{B}_\theta = -1/\mathbf{R}_{\mathrm{aa}}(2,2)$. Similarly, for the δ tuning condition (anti-resonance matching), the tuning parameter is given by

$$\left(\frac{\omega}{\omega_\theta}\right)^2 = \frac{\Delta_\theta}{\Delta_\theta - s_\theta}, \tag{5.9}$$

where $\Delta_\theta = \mathbf{R}_{\mathrm{RL}}(1,1)\Big/\left(\mathbf{R}_{\mathrm{aL}}(2,1)^2 - \mathbf{R}_{\mathrm{RL}}(1,1)\mathbf{R}_{\mathrm{aa}}(2,2)\right)$.

Equations (5.5), (5.7), (5.8) and (5.9) mean that the super attenuation band is formed under the respective conditions when there is a combination of the dynamic stiffness of the coupling with an effective dynamic stiffness of the host beam, given by the properties $\Delta_{w,\theta}$ and $\mathrm{B}_{w,\theta}$.

For a mono-coupled system composed of symmetric cells, the bounding frequencies of the attenuation bands can be identified with the natural frequencies of a single cell under boundary conditions with free- and fixed-ends (GONÇALVES *et al*., 2021; MEAD, 1975a). Mead (1975) observed that this property holds for certain symmetric multi-coupled systems, requiring the enforcement of some constraints. In a bi-coupled structure, such as the beam studied here, the boundary frequencies can be interpreted as the natural frequencies of a beam under the pinned-pinned boundary conditions, which can be determined by the roots of the determinant expressed by (MEAD, 1975b),

$$\left|\mathbf{R}_{\mathrm{LL}}(1,1) \pm \mathbf{R}_{\mathrm{RL}}(1,1)\right| = 0\,. \tag{5.10}$$

This behaviour was shown in Figs. 5.6 and 5.7. Following this statement, the modes of vibration of this symmetric system will be symmetric or antisymmetric; hence the union of two attenuation zones implies the coalescence of two natural frequencies and, therefore, the coalescence of two vibration modes. Therein lies the physical insight of the phenomenon and the tuning conditions.

5.4 ON THE FORMATION OF THE SUPPER ATTENUATION BAND IN OTHER SOURCE AND RESPONSE CONDITIONS

The discussions in the previous section focused on a specific response and source condition – translational displacement and shear force, respectively. However, alternative conditions can also be explored to form the super attenuation band, such as considering a bending moment as the source and angular displacement as the response. This section examines these alternative source-response combination for the beam with attached neutraliser.

Equations (4.18) and (4.19) can be combined, with the appropriate boundary conditions applied, to derive the transmissibilities $W_{\mathrm{R}}/W_{\mathrm{L}}\big|_{M_{\mathrm{L}}=0}$, $\Theta_{\mathrm{R}}/\Theta_{\mathrm{L}}\big|_{M_{\mathrm{L}}=0}$, $W_{\mathrm{R}}/W_{\mathrm{L}}\big|_{F_{\mathrm{L}}=0}$, and $\Theta_{\mathrm{R}}/\Theta_{\mathrm{L}}\big|_{F_{\mathrm{L}}=0}$. Notably, $W_{\mathrm{R}}/W_{\mathrm{L}}\big|_{M_{\mathrm{L}}=0}$ is expressed in Equations (4.20a,b) and was utilized in the subsequent investigations. The top views of transmissibilities $\Theta_{\mathrm{R}}/\Theta_{\mathrm{L}}\big|_{M_{\mathrm{L}}=0}$, $W_{\mathrm{R}}/W_{\mathrm{L}}\big|_{F_{\mathrm{L}}=0}$ and $\Theta_{\mathrm{R}}/\Theta_{\mathrm{L}}\big|_{F_{\mathrm{L}}=0}$ are shown in Fig. 5.8, under the conditions in which the previously described neutralisers are attached to the beam. In this figure the parameters are $\mu_w = 0.2$ and $\chi_\theta = 0.2$, and the first two conditions δ and β for super attenuation band formation are highlighted with dotted horizontal lines and double arrows.

By analysing Fig. 5.8(a) in conjunction with Fig. 5.5, it can be observed that in the β tuning condition, the SAB forms for both degrees of freedom, W and Θ. This effect also occurs under the other conditions presented in Fig. 5.8. Additionally, note that Fig. 5.8(a.i) is identical to Fig. 5.8(b.i), and the same holds for Figs. 5.8(a.ii) and 5.8(b.ii).

To better understand the underlying physics of the observed behaviours, approximate transmissibility expressions for high frequencies are derived by applying the hypotheses presented in Section 4.2.4.1. Accordingly, the approximate rotational transmissibility in response to a force is given by

$$\left.\frac{\Theta_{\mathrm{R}}}{\Theta_{\mathrm{L}}}\right|_{M_{\mathrm{L}}=0} \approx \frac{4-\hat{D}_w}{4\sin\left(2kl\right)-\sqrt{2}\hat{D}_w\sin\left(2kl+\dfrac{\pi}{4}\right)} \tag{5.11a}$$

and

$$\left.\frac{\Theta_{\mathrm{R}}}{\Theta_{\mathrm{L}}}\right|_{M_{\mathrm{L}}=0} \approx \frac{4+\hat{D}_\theta}{4\sin\left(2kl\right)+\sqrt{2}\hat{D}_\theta\sin\left(2kl-\dfrac{\pi}{4}\right)}. \tag{5.11b}$$

The translational transmissibility in response to a bending moment is given by

$$\left.\frac{W_{\mathrm{R}}}{W_{\mathrm{L}}}\right|_{F_{\mathrm{L}}=0} \approx \frac{4-\hat{D}_w}{-4\sin\left(2kl\right)+\sqrt{2}\hat{D}_w \sin\left(2kl+\frac{\pi}{4}\right)} \tag{5.12a}$$

and

$$\left.\frac{W_{\mathrm{R}}}{W_{\mathrm{L}}}\right|_{M_{\mathrm{L}}=0} \approx \frac{4+\hat{D}_\theta}{-4\sin\left(2kl\right)-\sqrt{2}\hat{D}_\theta \sin\left(2kl-\frac{\pi}{4}\right)}; \tag{5.12b}$$

while the rotational transmissibility is expressed by

$$\left.\frac{\Theta_{\mathrm{R}}}{\Theta_{\mathrm{L}}}\right|_{F_{\mathrm{L}}=0} \approx \frac{4-\hat{D}_w}{4\sqrt{2}\sin\left(2kl+\frac{\pi}{4}\right)-\hat{D}_w\left[1+2\cos\left(2kl\right)\right]} \tag{5.13a}$$

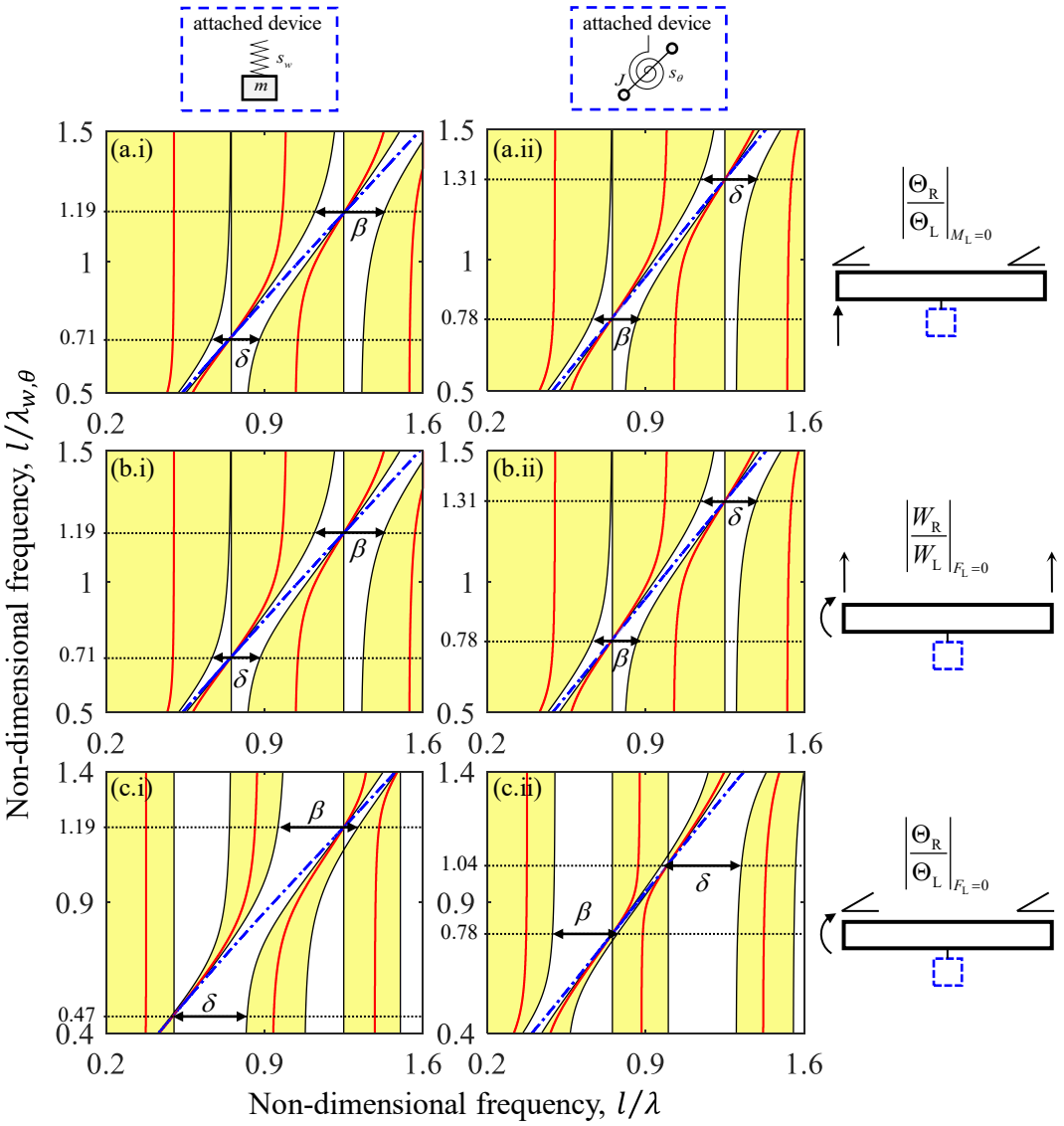
and

$$\left.\frac{\Theta_{\mathrm{R}}}{\Theta_{\mathrm{L}}}\right|_{F_{\mathrm{L}}=0} \approx \frac{4+\hat{D}_\theta}{4\sqrt{2}\sin\left(2kl+\frac{\pi}{4}\right)+\hat{D}_\theta\left[1+2\sin\left(2kl\right)\right]}. \tag{5.13b}$$

The transmissibility numerator is related to the transfer receptance numerator, hence the anti-resonance in it is controlled by the local interaction with the host beam and the neutraliser (as shown in Chapter 4). The transmissibility denominator is related to the point receptance numerator, hence the anti-resonance at this point is controlled by the interaction with the force applied by the source. This effect can be illustrated by comparing Eq. (5.11a) with Eq. (5.13a), in which a phase difference of one-eighth wavelength is observed. Due to these relationships, the super attenuation band will occur under different conditions depending on the coupled device and the source excitation type.

By comparing the magnitudes of the *cross* transmissibilities in Eqs. (5.11a,b) and (5.12a,b), the equivalence observed in Figs. 5.8(a) and 5.8(b), for their respective attached devices, becomes evident. The term "cross" is used here to refer to the transmissibility of a given degree of freedom in response to a source that directly interacts with another degree of freedom.

Figure 5.8. Transmissibility top views assuming attached neutralisers. (i) Translational neutraliser with $\mu_w = 0.2$ and (ii) rotational neutraliser with $\chi_\theta = 0.2$. (a) rotational displacement for a force source. (b) translational displacement for a moment source. (c) rotational displacement for a moment source.



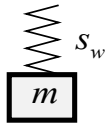
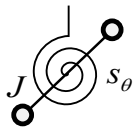
Source: author.

At β tuning condition the supper attenuation band occurs for both motions, thus being considered an ideal tuning condition. As investigated by Cleante *et al.* (2022), it is also in this condition that the SAB is formed in symmetrical mono-coupled systems. This effect can also be interpreted in the beam because at these tuning frequencies the beam presents an antisymmetric mode for translation and a symmetric mode for rotation, or vice versa, which

implies that the attachment point is effectively pinned or hinged: the neutraliser reacts with only one of the energy propagation mechanisms.

Table 5.1 summarises the tuning conditions for the different tuning frequencies and systems, over which the pattern repeats indefinitely. Furthermore, it is worth mentioning that with the correct adjustment of the rotational neutraliser, it is possible to obtain the supper attenuation band in a lower frequency range than in the system with a translational neutraliser. In fact, as the discussions in the previous chapter, an absorber is not needed, but simple elements such as a grounded spring or inertial mass are required. The latter presents a practical advantage over translational neutralisers or grounded springs, especially when considering large structures such as space satellites; however, the transverse effect of these masses must be considered.

Table 5.1. Formation of the super attenuation band in a rod and single-span beam under different conditions.

Host structure	Attached device (effective behaviour)	Source excitation	Displacement transmissibility	Tuning frequencies			
Rod	 (neutraliser)	Force	U_R/U_L	$l/\lambda = 0.25$	$l/\lambda = 0.5$	$l/\lambda = 0.75$	$l/\lambda = 1$
				β	δ	β	δ
Beam	 (stiffness-like)	Force	W_R/W_L	$l/\lambda = 0.5$	$l/\lambda = 0.75$	$l/\lambda = 1$	$l/\lambda = 1.25$
						δ	β
			Θ_R/Θ_L		δ		β
		Moment	W_R/W_L		δ		β
			Θ_R/Θ_L	δ			β
	 (mass-like)	Force	W_R/W_L		β		
			Θ_R/Θ_L		β		δ
		Moment	W_R/W_L		β		δ
			Θ_R/Θ_L		β	δ	

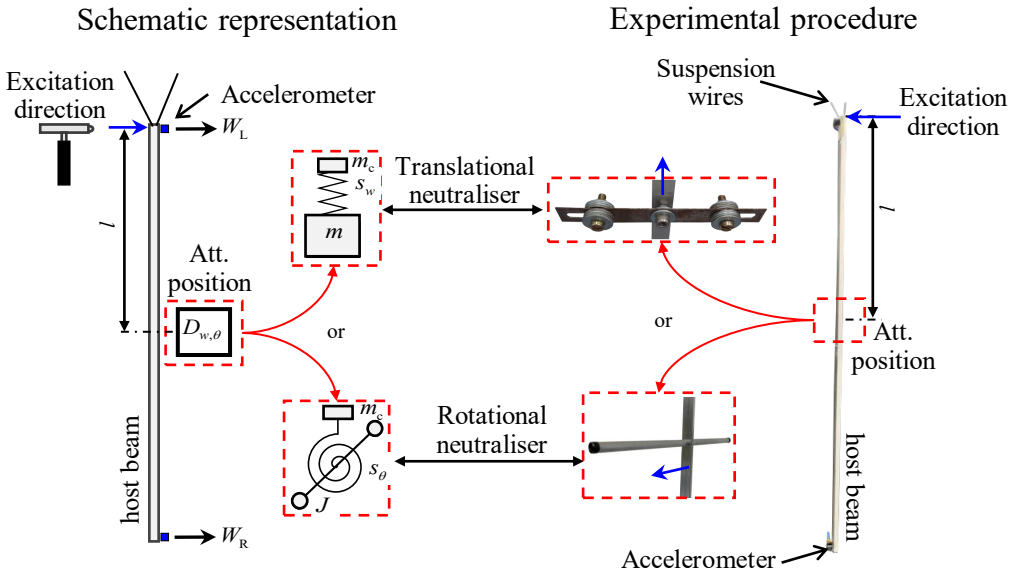
Source: author.

5.5 EXPERIMENTAL DEMONSTRATIONS

In this section, laboratory-based experiments were conducted to support the theoretical investigation and validate modelling predictions. Three different devices were considered and evaluated under different tunning conditions, which produce the stiffness- and mass-like behaviour, as shown in Fig. 5.9: a beam-like translational vibration neutraliser, and a beam-like rotational neutraliser. In these real elements, the translational effect of the coupling mass, acting together with the "dead" mass m_c in parallel with the device's dynamic stiffness, must be considered. In all cases, the host structure consists of a 500×12.6×3.15 mm long single span aluminium beam. The attached devices and beam properties can be found in Appendix B.4, as well the equipment details.

The beam was suspended vertically by thin wires to simulate free-free boundary conditions. Two accelerometers were attached to the host beam's upper- (W_L) and bottom-hand (W_R) ends, and an impact hammer was used to excite the structure. The transmissibility was calculated from the measured transversal accelerances, by averaging the measurements from 10 impacts, for the two systems configurations.

Figure 5.9. Experimental setup (not to scale) showing the schematic representation of the system and its experimental implementation.



Source: author.

5.5.1 Super attenuation band with a translational vibration neutraliser

The experiment concerns a single beam span with a translational vibration neutraliser attached in its centre point. The neutraliser consists of a 120×14.9×1.55 mm steel beam with masses of 20.3 g attached at each end. To adjust the system tuned frequency, the position of the concentrated masses could be adjusted in-situ. The characterization of the neutraliser properties was determined using the same procedure as that presented in Sec. 4.3.1, in which the dynamic stiffness of this element was expressed by

$$D_w = -\omega^2 m_c + \frac{-\omega^2 m s_w}{s_w - \omega^2 m}.$$

In this case, the masses of the set of bolt, washer and nut with the neutraliser beam, realise a total coupling-dead mass attached to the host structure of $m_c = 19$ g. The active mass was estimated as $m = 40.6$ g. The stiffness was adjusted by positioning the tip masses. Using the predictions described in Tab. 5.1 and solving $4EIk^3 - D_w = 0$ (Eq. (4.12a)) for the desired tuning frequency, the stiffnesses were estimated. This means adjusting the anti-resonance in the transfer receptance to converge with the tuning frequency $\omega_{\text{tun}} = 2\pi f_{\text{tun}}$.

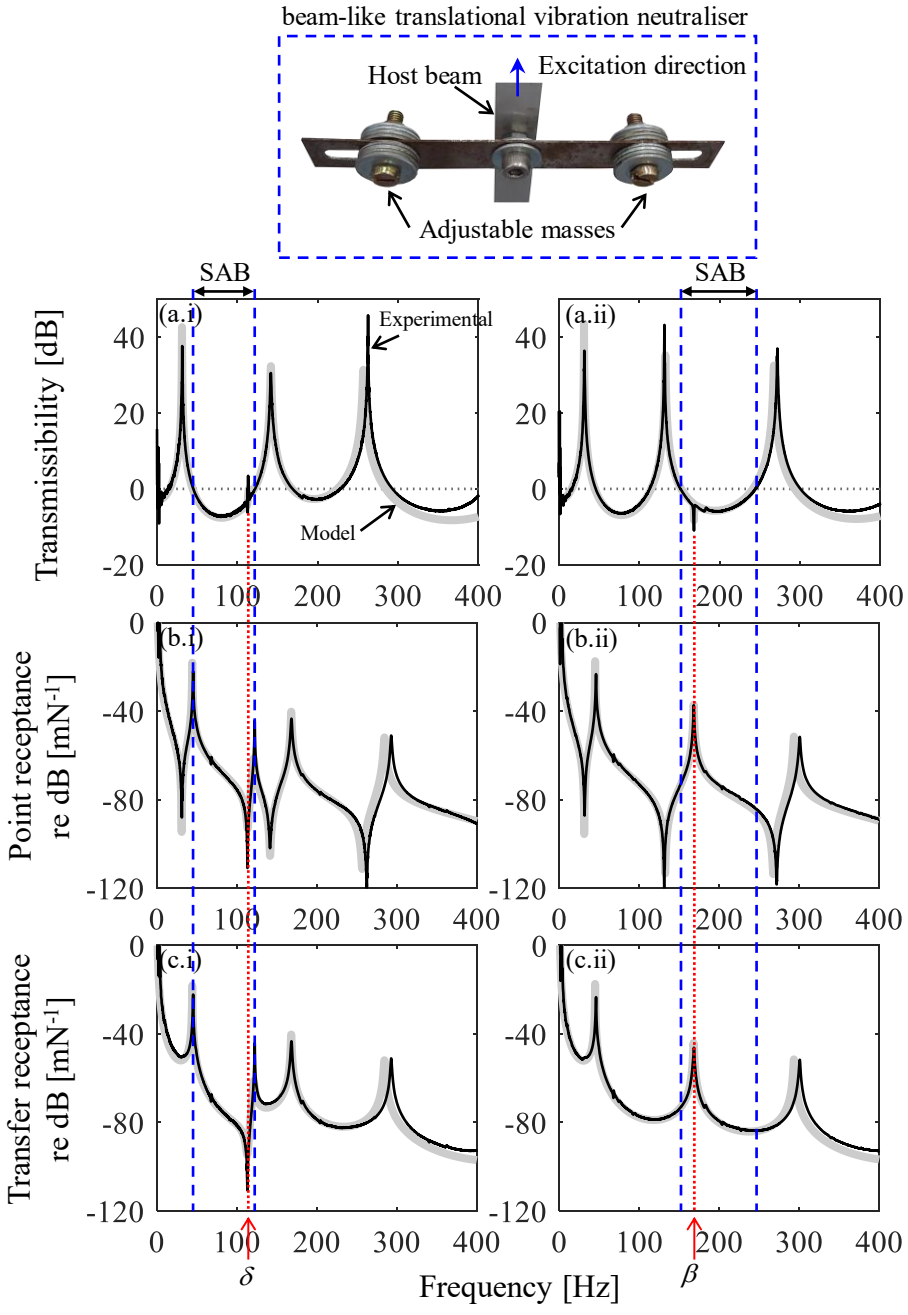
To achieve the tuning condition $l/\lambda_{\text{tun}} = 1$, the two masses were positioned at a distance of 48 mm from the centre of the neutraliser to give a dip frequency of $f_a = f_{\text{tun}} = 113.3$ Hz and, consequently, an estimated stiffness of $s_w = 11.704$ kNm^{-1}. To achieve the tuning condition $l/\lambda_{\text{tun}} = 1.25$, the two masses were positioned at a distance of 38 mm from the centre of the neutraliser to give a dip frequency of $f_a = f_{\text{tun}} = 168.5$ Hz and an estimated stiffness of $s_w = 25.453$ kNm^{-1}. The material loss factor is found for the beam and neutraliser by matching the experimental data, which are 0.005, 0.02 ($l/\lambda_{\text{tun}} = 1$) and 0.002 ($l/\lambda_{\text{tun}} = 1.25$), respectively.

The measured accelerances, conveniently converted to receptance, and their respective transmissibilities for the cases when $l/\lambda_{\text{tun}} = 1$ and $l/\lambda_{\text{tun}} = 1.25$ are shown, respectively, in Figs. 5.10(i) and 5.10(ii) in thin black lines. In these figures, thick grey lines correspond to predictions using the developed model. For the two configurations, the predictions and the

experimental results are in very good agreement up to a frequency of approximately 300 Hz. Above this frequency, the poor agreement is probably due to moment added by the vibration absorber to the host beam that the current model was not able to capture.

In this frequency range of interest, the formation of the super attenuation band in both configurations is evident. Note that complete smoothing of the curve is not achieved in Figs. 5.10(a.i) and 5.10(a.ii). At the tuning frequencies, approximately 113 Hz and 168 Hz, a peak and a dip are observed, respectively. The peak in case (i) arises due to slight imprecision in the tuning, whereas the dip in case (ii) results from the damping effect, as discussed by Cleante *et al.* (2022). Specifically, if the damping in the neutraliser exceeds that of the host beam, a peak will occur; if the damping in the neutraliser is lower, a dip will be observed; and if the damping levels are equal, complete smoothing will be achieved. Consequently, condition (ii), where the damping of the neutraliser is lower than that of the beam, is the more favourable scenario.

Figure 5.10. Experimental results for the super attenuation band using a translational neutraliser. (a) Translational displacement transmissibilities. (b) Point and (c) transfer receptances. Tuning conditions (i) δ and (ii) β. Model in grey thick solid lines and measurement in thin black lines.



Source: author.

5.5.2 Super attenuation band with a rotational vibration neutraliser

In this experiment, a rotational vibration neutraliser is attached to the beam, as shown in Fig. 5.9. This rotational device consists of two aluminium tubular arms connected through the beam by a screw. The arms have an inner diameter of 6.3 mm, outer diameter of 9.4 mm, and an individual length of 94.3 mm. A group of nuts and washers make up the mass at the ends of the arm. The tuning frequency can be adjusted by changing the arm length and/or the mass at the ends. For this case, the masses were varied so that the super attenuation band could be observed under three different tuning conditions. Technical experimental details are presented in Appendix B.4.

The dynamic stiffness of the neutraliser is determined from the equation of motion, considering the mass contribution at the end. For this, it is assumed that, at the attachment point, only the bending moment interacts and that the transverse motion of the device (*i.e.*, the axial motion of the beam) is negligible. Additionally, it is assumed that the inertial contributions smaller than 1/3 of the neutraliser arm mass are negligible. The theory behind these assumptions is presented in Appendix D, from which it is determined that the dynamic stiffness of the beam-like rotational neutraliser is expressed by

$$D_\theta = \frac{-\omega^2 J_{\text{eq}} s_{\text{eq}}}{3s_{\text{eq}} - \omega^2 J_{\text{eq}}}, \tag{5.14}$$

where $J_{\text{eq}} = \left(3m + m_{\text{arm}}\right) l_{\text{arm}}^2$ is the equivalent mass moment of inertia and $s_{\text{eq}} = 3EI/l_{\text{arm}}$ is the equivalent rotational stiffness. The subscript "arm" refers to the arm properties and m is the adjustable mass at the end of the arm.

As in the translational neutraliser, there is also a translational effect of the "dead" mass in this case. As described in Appendix D, this effect is given by $D_w = -\omega^2 \left(3m_{\text{c}} + m_{\text{arm}}\right)$, in which m_{c} is the screw mass that connect the arms. This is assimilated in the model in parallel with the rotational effect, acting as a concentrated mass on the host beam.

Figure 5.11 presents the experimental and theoretical results obtained. For both cases, $s_{\text{eq}} = 681.63$ Nm , since the tuning was done by adjusting the masses at the tip of the neutraliser arms. To tune in the first δ condition, this is $f_{\text{tun}} = 202.3$ Hz $(l/\lambda = 1.5)$, the mass was

$m = 8.86$ g, which resulted in $J_{eq} = 4.0258\ 10^{-4}$ kgm^2. For the β case, $f_{tun} = 274.8$ Hz ($l/\lambda = 1.75$) the mass was adjusted to $m = 2.74$ g, and therefore $J_{eq} = 2.3949\ 10^{-4}$ kgm^2. These tuning conditions are shown, respectively, in Figs. 5.11(i) and 5.11(ii), and for the two configurations, the model and the experimental results are in good agreement.

The material loss factor is found for the beam and neutraliser by matching the experimental data, which are 0.005, 0.004 (i) and 0.05 (ii), respectively. Again, the complete smoothing of the curves is evident from the dip in (i) and the peak in (ii), which highlight the effect of the relationship between the damping of the host structure and the neutraliser.

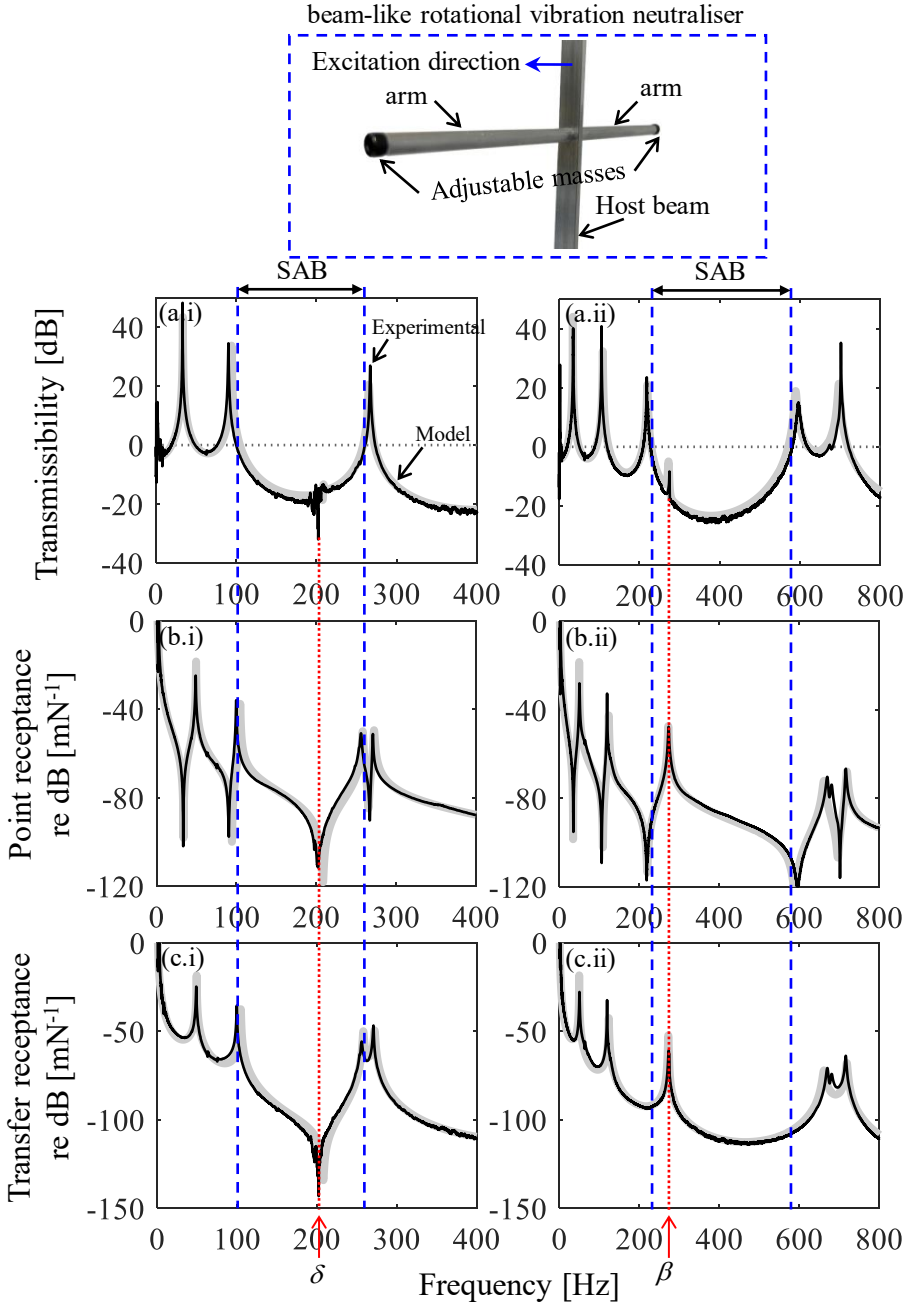
The key results of the experiments and predictions conducted in these sections are summarised in Table 5.2. The boundary frequencies presented in this table are highlighted in Fig. 5.10 and 5.11 by the vertical dashed and dotted lines.

Table 5.2. Comparison between the experimental and theoretical super attenuation band boundary frequencies for the single-span beam under different conditions.

Attached device	Tuning condition		Boundary frequencies [Hz]		
			Tuning	Lower	Upper
Translational neutraliser	δ	Measured	113.4	45.2	122.0
		Predicted	114.1	44.4	120.9
	β	Measured	168.1	151.1	244.9
		Predicted	168.1	152.2	241.4
Rotational neutraliser	δ	Measured	202.3	100.2	260.6
		Predicted	207.8	104.9	258.3
	β	Measured	274.8	227.5	580.7
		Predicted	272.5	229.5	570.6

Source: author.

Figure 5.11. Experimental results for the super attenuation band using a rotational neutraliser. (a) Translational displacement transmissibilities. (b) Point and (c) transfer receptances. Tuning conditions (i) δ and (ii) β. Model in grey thick solid lines and measurement in thin black lines.

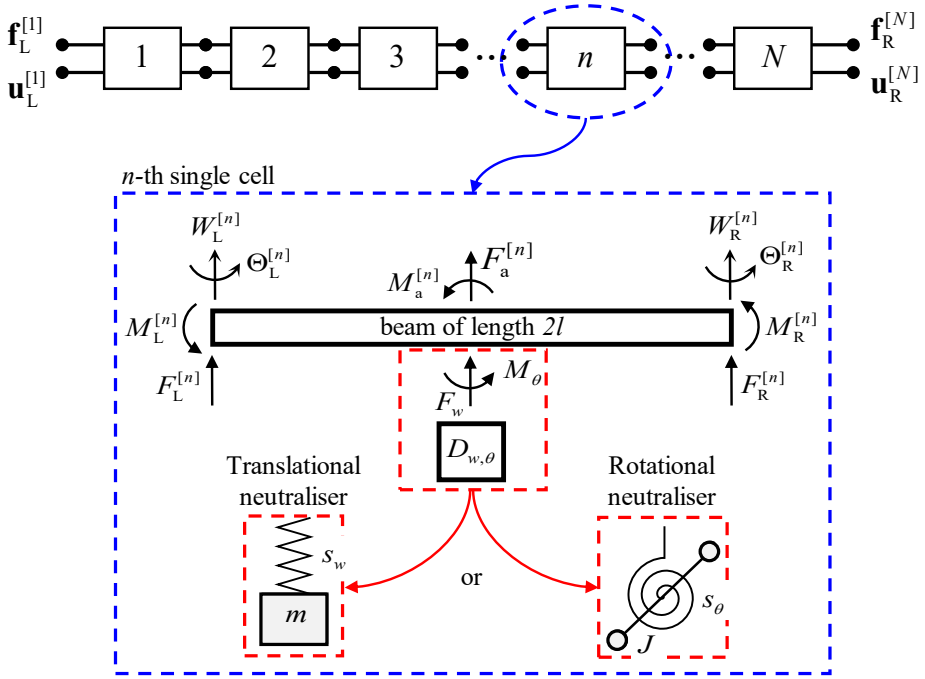


Source: author.

5.6 ON THE FORMATION OF THE SUPER ATTENUATION BAND IN PERIODIC BEAMS

After investigating the super attenuation band phenomenon in a single-span beam, this structure can be extended to form a periodic system, as illustrated in Figure 5.12. This section examines the system depicted in the figure to determine whether the conditions and control parameters governing SAB remain consistent with the theoretical framework established for a single cell.

Figure 5.12. General periodic beam with translational or rotational vibration neutraliser attached to centre of the *n*-th cell.



Source: author.

The system is modelled using the dynamic stiffness approach as described in Chapter 2. Appling the continuity and equilibrium relations between cells, the complete structure receptance matrix $\mathbf{R}^{[\mathrm{str}]}$ can be obtained. A direct way to obtain transmissibility is by applying the boundary conditions to this receptance matrix. In this sense, considering the right end free and applying a harmonic force to the left end, the transverse displacement transmissibility will be expressed by

$$\frac{W_{\mathrm{R}}^{[N]}}{W_{\mathrm{L}}^{[1]}} = \frac{R(j,1)}{R(1,1)}. \tag{5.15}$$

The indices $(j,1)$ and $(1,1)$, in which $j = 4N+1$, denote the respective row and column elements of the matrix $\mathbf{R}^{[\mathrm{str}]}$. Note that $R(1,1)$ is the point receptance and $R(j,1)$ is the transfer receptance. These relationship is used to investigate the proposed system.

Figures 5.13 and 5.14 present the numerical results for a three-cell structure, considering the coupling of a translational and rotational neutraliser, respectively. As shown in the top views of the transmissibility in Figures 5.13(a) and 5.14(a), the super attenuation band is present only under the δ condition for both periodic and single-span beams. In contrast, under the $l/\lambda_{w,\theta}$ condition, where β tuning occurs for a single cell, SAB formation does not occur.

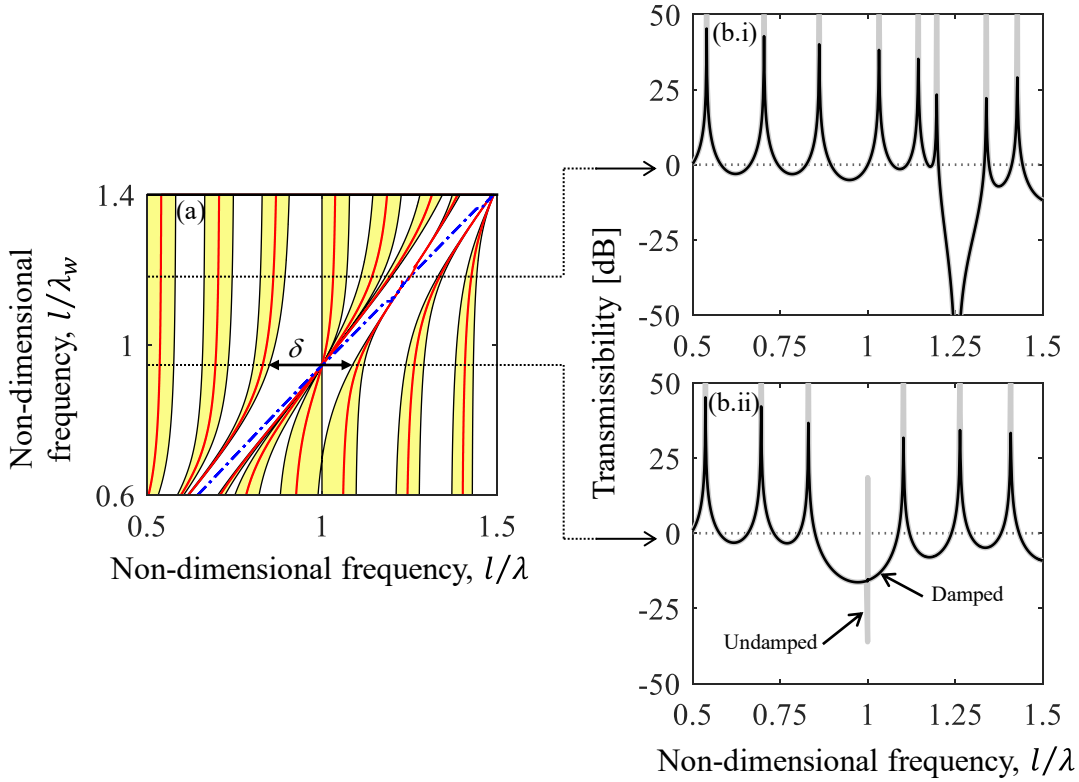
Figures 5.13(b) and 5.14(b) shows the transmissibility curves for specific $l/\lambda_{w,\theta}$ conditions, highlighted by dotted lines. These curves, shown in thick grey lines, do not account for any form of damping. The same configurations are also plotted in thin black lines, incorporating light structural damping with a loss factor of 0.001. Notably, in case (i), which corresponds to β tuning in a single-span beam, the effect of the local resonance is evident. In configuration (ii), the SAB is not effectively formed. However, when damping is present in the host structure, the asymptotic behaviour at the tuning frequency is smoothed, *i.e.*, controlled receptance response amplitudes, and leading to the formation of a *quasi*-super attenuation band.

The absence of a fully developed SAB in multi-coupled periodic structures is attributed to the mode coalescence absence, occurring effect similar to the structural mode veering. This phenomenon, initially described in the literature as aberration, is the approximation and sudden veering of frequency curves instead of crossing and is controlled by the coupling characteristics between the system, which modifies the behaviour of the eigenvalues and eigenvectors near the deviation (DAO *et al*., 2023; LEISSA, 1974; LIU, 2002). Mode coalescence occurred in symmetric mono-coupled structures and single-span symmetric beams under tuning conditions. However, in periodic beams, the absence of this effect prevents the coupling of attenuation bands, thereby inhibiting SAB formation.

It is important to emphasise that, although damping can facilitate the formation of a quasi-SAB, increasing the number of cells also enhances the precision required for tuning the

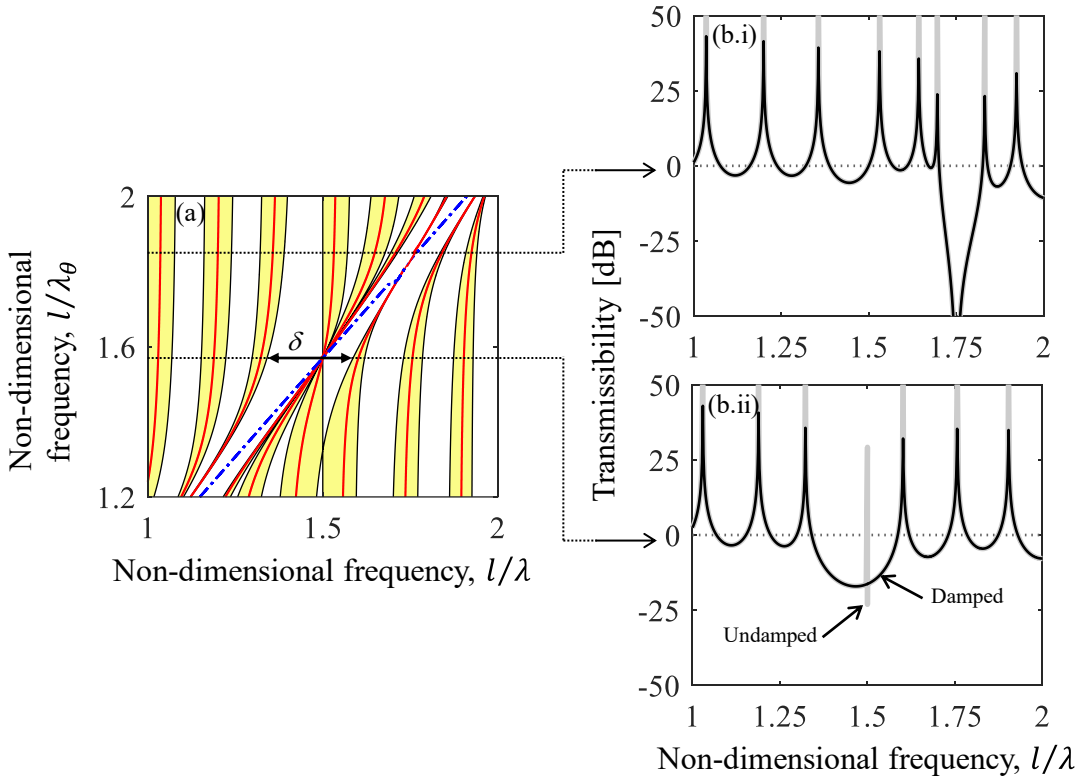
parameter configuration. For instance, in the cases presented in Figures 5.13(b.ii) and 5.14(b.ii), $l/\lambda_w = 0.94596$ and $l/\lambda_\theta = 1.56995$.

Figure 5.13. Translational displacement transmissibility of a finite periodic beam of three cells with translational neutralisers. (a) Top view of the transmissibility as a function of l/λ_w. (b) Transmissibility in the specific configurations in (i) $l/\lambda_w = 0.94596$ and (ii) $l/\lambda_w = 1.18610$. Thick grey lines, without structural damping, and thin black lines with loss factor of 0.001.



Source: author.

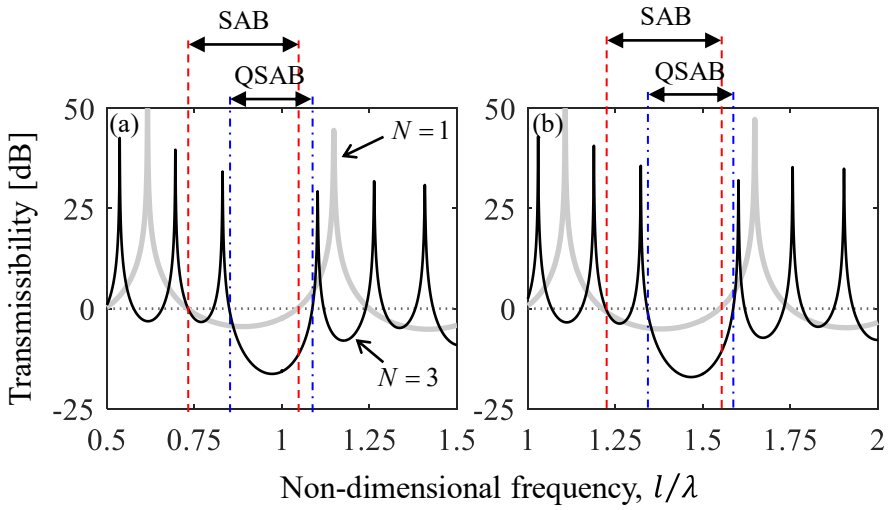
Figure 5.14. Translational displacement transmissibility of a finite periodic beam of three cells with rotational neutralisers. (a) Top view of the transmissibility as a function of l/λ_θ. (b) Transmissibility in the specific configurations in (i) $l/\lambda_\theta = 1.56995$ and (ii) $l/\lambda_\theta = 1.83250$. Thick grey lines, without structural damping, and thin black lines with loss factor of 0.001.



Source: author.

Figure 5.15 combines the transmissibility curves presented in the previous sections for the single-span beam with those for the three-cell structure. Note that as the number of cells increases, the minimum transmissibility decreases, as expected. On the other hand, the bandwidth of the attenuation bands also decreases. Note also that the boundary frequencies of the quasi-super attenuation band (QSAB) have shifted to higher frequencies, due to the dispersive nature of the beam, but the tuning frequency remains the same.

Figure 5.15. Translational displacement transmissibility of a finite periodic beam with (a) translational neutraliser and (b) rotational neutraliser, assuming $N=1$, in thick grey lines; and $N=3$ in thin black lines.



Source: author.

5.7 CHAPTER REMARKS

In this chapter, the effects of coupling Bragg stop band with the local resonance effect band in multi-coupled structures were investigated. These effects were leveraged to create a broad and smooth attenuation region in the transmissibility curves, minimizing resonance peaks within the attenuation band. The host structure was modelled as a Euler-Bernoulli beam with translational and rotational neutralisers configured to induce a phenomenon known as the super attenuation band.

The transmissibility of a single-span beam with coupled devices was determined using the receptance approach. Of particular interest is the formation of super attenuation bands in the lower frequency regions. The results indicated the existence of two such bands, arising from distinct tuning conditions: the β condition and the δ condition. However, both conditions primarily resulted from the interaction between the vibration modes of the structure. The β condition occurs when the anti-resonance in the transfer receptances – caused by the local resonance effect – coincides with both the natural frequency of the system when the device is coupled at a nodal point and the natural frequency of the host structure in the absence of the device. In contrast, in the δ condition, the device is attached to an off-node position, and the tuning frequency is anti-resonances in the point and transfer receptances of the free-

free structure to occur at the same frequency, which is a pinned-pinned natural frequency for the beam. This finding extends those of previous studies on mono-coupled systems.

For each tuning condition, the $\Delta_{w,\theta}$ and $B_{w,\theta}$ parameters were identified, representing a matching of the dynamic stiffness of the coupled device and an effective dynamic stiffness relation of the host structure. These control parameters provide a practical basis for the design of such systems. In addition, the investigations provided physical interpretations of the explored systems at the boundary frequencies of the super attenuation bands formed under each tuning condition.

The experimental results confirmed the theoretical predictions, highlighting the importance of precise tuning to achieve optimal behaviour. The translational and rotational neutralisers exhibited distinct yet complementary behaviours, with the rotational neutraliser offering advantages in the higher frequency ranges. Moreover, the findings emphasise the role of damping in shaping the transmissibility characteristics, influencing whether a peak or dip appears at the target tuning frequency. The observed effects align with those of previous analyses conducted for mono-coupled systems.

Extending the examination to periodic beams, this is, multiple cells, it was observed that while the super attenuation band effect is preserved in single-span beams, periodic structures introduce additional complexities due to the absence of mode coalescence. These effects can inhibit the complete formation of the super attenuation band. Despite this limitation, careful tuning and structural damping can mitigate the impact, leading to quasi-super attenuation bands (QSAB) in δ tuning condition, thereby enabling effective vibration suppression in practical applications.

This chapter provides a comprehensive framework for understanding and harnessing the super attenuation band phenomenon in structural design. The insights gained herein offer valuable guidelines for optimising vibration mitigation in engineering applications from civil structures to aerospace components. Future studies should explore adaptive tuning strategies and non-periodic approaches.

6 FINAL REMARKS

This chapter concentrates the main conclusions of this thesis, accompanied by its summary. This chapter also presents some recommendations for future work and a list of published knowledge contributions related to the developments of this thesis.

6.1 MAIN CONCLUSIONS

Although the study of periodic systems dates back to more than a century, the field remains an open space for exploration and the development of new perspectives. Fundamental engineering principles, which serve as the foundation for technological advancement, are at the core of this thesis. By integrating the physical principles with practical constraints, this study offers new insights into the performance limits of linear periodic structures.

This thesis explores alternative approaches to enhance the vibration attenuation in finite one-dimensional periodic structures. Mono-coupled structures are modelled as rods, whereas multi-coupled structures follow the Euler-Bernoulli beam model. Two strategies, each with distinct primary effects, were investigated. The first focuses on the role of symmetry and asymmetry in unit cells and their influence on the attenuation bands through the Bragg effect. The second approach examined the coupling of Bragg scattering and local resonance effects.

The theoretical foundations necessary for analysing periodic structures were established in Chapter 2. Key methods, including wave propagation analysis, receptance, dynamic stiffness, and transfer matrices, provided a solid framework for identifying pass bands, stop bands, and attenuation zones in finite systems. The relationship between the dispersion diagrams and transmissibility was also explored, confirming that attenuation bands share boundary frequencies with stop bands, provided that assumptions of linearity, symmetry, and a sufficiently large number of cells hold.

Following the delineation of the methodology, the initial strategy was implemented on rod systems, as discussed in Chapter 3, where periodicity arose from variations in the cross-sectional area. This study examined the impact of asymmetric unit cells on vibration attenuation, demonstrating that asymmetric configurations significantly improve attenuation bands compared to symmetric configurations. However, the positioning of the cells is crucial, and for optimal attenuation, the thinner rod element within each cell must be placed closer to

the vibration source. Otherwise, an amplification band may occur. Numerical and analytical formulations were used to derive optimal geometric parameters and closed-form expressions for transmissibility, and experimental validation confirmed that properly oriented asymmetric cells outperform symmetric cells in both bandwidth and transmissibility reduction.

The second strategy investigates the combination of the Bragg stop bands and local resonance effects. The behaviour of local resonance differs between mono-coupled and multi-coupled systems. This was demonstrated in Chapter 4, which developed the control theory and physical notions for the local resonance effect in beams. The local resonance effect was induced by external discontinuities, which were assumed to be translational and rotational neutralisers. Combining the discussions of the different approaches, wave-based and receptance, it was found that the zero-transmission effect (in infinite and semi-infinite structures) coincide with the dip in the displacement transmissibility for the finite beam. Therefore, the anti-resonance in the transfer receptance, that is the local resonance effect, is due to the propagating wave generated by the discontinuity cancelling the incident wave that results in net zero wave transmission, in accordance with the conditions $\left|4-\hat{D}_w\right|=0$ or $\left|4+\hat{D}_\theta\right|=0$. Therefore, the effect depends only on the local interaction between the attached device dynamic stiffness and the dynamic stiffness of the host bare beam at the attachment point.

Following the establishment of the theory of vibration control utilizing the local resonance effect in beams, research efforts have concentrated on the development of the super attenuation band. This attenuation region, characterised by its smooth response (without resonance peaks or zero transmissibility) and wide bandwidth, results from the coupling of the Bragg and local resonance bands.

Chapter 5 further discusses the conditions under which this super attenuation band forms and highlights two specific tuning criteria: the β condition and the δ condition. These conditions primarily resulted from the interaction between the vibration modes of the structure. However, these conditions are valid primarily for single-span beams (single-cell structures).

For the investigation of the super attenuation band formation in periodic symmetric beams, it was found that the absence of mode coalescence can inhibit the complete formation of the super attenuation band. Despite this limitation, careful tuning and structural damping can mitigate the detrimental effect, leading to quasi-super attenuation bands in δ tuning condition, thereby enabling effective vibration suppression in practical applications.

The overarching conclusion of this thesis is that the attenuation performance of conventional periodic structures can be significantly enhanced by using the proposed strategies. However, the inherent limitations of each approach should be carefully considered. Additionally, these findings demonstrate that the field of linear periodic structures extends beyond what is currently explored in the literature. This study emphasises the importance of investigating finite systems while maintaining a connection to the physical insights derived from infinite systems.

6.2 RECOMMENDATIONS FOR FURTHER WORK

This thesis presented the effects of asymmetry and stop band coupling separately. Investigations into the combination of these strategies may be a good direction for future work. The recommendation would be to start with the formation of the super attenuation band in mono-coupled periodic structures of asymmetric cells and then advance to multi-coupled structures. The discussions presented in this thesis, for each of the phenomena explored, serve as a theoretical foundation for these investigations. Additionally, formation of the super attenuation band with strategies of quasi-periodic structures or rainbow structures is recommended. Furthermore, in the case of beams, it is also recommended to further investigate the determination of the transfer matrix for N periodic cells using the Cayley-Hamilton theorem.

6.3 LIST OF PUBLICATIONS

This section presents a list of publications as result of the work developed and presented in this thesis.

- Articles in indexed Journals:

  J.P. Carneiro Jr, M.J. Brennan, P.J.P. Gonçalves, V.S. Sorokin, V.G. Cleante, B. R. Mace. *Controlling vibration propagation in a thin beam using a neutraliser*. **Journal of Sound and Vibration**, v. 602, p. 118947, 2025.

  J.P. Carneiro Jr, M.J. Brennan, P.J.P. Gonçalves, V.G. Cleante, D.D. Bueno, R.B. Santos. *On the attenuation of vibration using a finite periodic array of rods comprised of either symmetric or asymmetric cells*. **Journal of Sound and Vibration**, v. 511, p. 116217, 2021.

R.B. Santos, J.P. Carneiro Jr, C.G. Gonsalez-Bueno, B.S. Lucca, D.D. Bueno. *On the number of cells for flexural vibration suppression in periodic beams*. **Meccanica**, v. 56, p. 2813-2823, 2021.

V.G. Cleante, M.J. Brennan, P.J.P. Gonçalves, J.P. Carneiro Jr. *On the formation of a super stop-band in finite mono-coupled periodic structures using an array of vibration absorbers: Controlling parameters and physical insight*. **Mechanical Systems and Signal Processing**, v. 180, p. 109383, 2022.

- Book Chapters:

V.G. Cleante, M.J. Brennan, P.J.P. Gonçalves, J.P. Carneiro Jr. *On the formation of a super attenuation band in a mono-coupled finite periodic structure comprising asymmetric cells*. **Mechanisms and Machine Science: Recent Trends in Wave Mechanics and Vibrations**. Cham: Springer International Publishing, 2022. p. 703-712.

- Full Papers and Abstracts in Conference Proceedings:

J.P. Carneiro Jr., V.G. Cleante, P.J.P. Gonçalves, M.J. Brennan, V.S. Sorokin. *On the non-conventional use of vibration absorber/neutralisers in beams to form a super attenuation band*. In: **XIV International Conference on Recent Advances in Structural Dynamics**. The Institute of Sound and Vibration Research, 2024.

J.P. Carneiro Jr., V.G. Cleante, P.J.P. Gonçalves, M.J. Brennan. *Strategies to enhance the attenuation band in finite beams using periodic attachments*. In: **INTER-NOISE and NOISE-CON Congress and Conference Proceedings**. Vol. 267. No. 1. Institute of Noise Control Engineering, 2023.

J.P. Carneiro Jr., P.J.P. Gonçalves, M.J. Brennan, V.S. Sorokin, V.G. Cleante, B.R. Mace, D. Toit. *On the dynamic behaviour of finite and infinite beams with lumped parameter attachments*. In: **27th International Congress of Mechanical Engineering, COBEM**. Brazilian Society of Mechanical Sciences and Engineering, 2023.

J.P. Carneiro Jr., V.G. Cleante, P.J.P. Gonçalves, M.J. Brennan. *Attenuation of Vibration and Mass Reduction using a Finite Hollow Periodic Rod*. In: **42nd Ibero-Latin-American Congress on Computational Methods in Engineering, CILAMCE,** 2021.

J.P. Carneiro Jr., V.G. Cleante, P.J.P. Gonçalves, M.J. Brennan. *Predicting Attenuation Characteristics on Finite Periodic Pinned Supported Beam Structures*, In: **26th International Congress of Mechanical Engineering, COBEM**. Brazilian Society of Mechanical Sciences and Engineering, 2021.

J.P. Carneiro Jr., R.B. Santos, D.D. Bueno. *Analysis of suppression of longitudinal vibrations in rods with material periodicity*. In: **25th International Congress of Mechanical Engineering, COBEM**. Brazilian Society of Mechanical Sciences and Engineering, 2019.

V.G. Cleante, J.P. Carneiro Jr., M.J. Brennan, P.J.P. Gonçalves. *On the formation of a super attenuation band in a beam*. In. **Proceedings of the XIX International Symposium on Dynamic Problems of Mechanics DINAME**. Brazilian Society of Mechanical Sciences and Engineering, 2023.

B.R. Mace, J.P. Carneiro Jr, D. Toit, P.J.P. Gonçalves, V.S. Sorokin, M.J. Brennan, V.G. Cleante. *Energy transmission through finite periodic structures*. In: **13th International Symposium on Vibrations of Continuous Systems**. Alberta, Canada, 2023.

V.G. Cleante, J.P. Carneiro Jr., D.A. Rade, P.J.P. Gonçalves, M.J. Brennan, T.P. Waters. *Forming a super attenuation band in a beam-like structure using an array of moment resonators*. In: **XIV International Conference on Recent Advances in Structural Dynamics**. The Institute of Sound and Vibration Research, 2024.

V.G. Cleante, D.A. Rade, M.J. Brennan, P.J.P. Gonçalves, J.P. Carneiro Jr. *A strategy to form super attenuation bands in beams using arrays of resonators*. In: **27th International Congress of Mechanical Engineering, COBEM**. Brazilian Society of Mechanical Sciences and Engineering, 2023.

REFERENCES

Airbus A300 fuselage. Deutsches Museum, 2024.

AL BA'BA'A, H. B.; WILLEY, C. L.; CHEN, V. W.; JUHL, A. T.; NOUH, M. Theory of Truncation Resonances in Continuum Rod-Based Phononic Crystals with Generally Asymmetric Unit Cells. **Advanced Theory and Simulations**, [s. l.], v. 6, n. 2, 2023.

AL BA'BA'A, H.; NOUH, M.; SINGH, T. Dispersion and topological characteristics of permutative polyatomic phononic crystals. **Proceedings of the Royal Society A: Mathematical, Physical and Engineering Sciences**, [s. l.], v. 475, n. 2226, p. 20190022, 2019.

ALMEIDA, V. F.; LIMA, V. D.; ARRUDA, J. R. F. Applying the phononic crystal concept to the intake muffler of a refrigeration compressor. **Applied Acoustics**, [s. l.], v. 194, p. 108800, 2022.

ALVES PIRES, F.; WANDEL, M.; THOMAS, C.; DECKERS, E.; DESMET, W.; CLAEYS, C. Improving the Sound Transmission Loss of an Aircraft Ceiling Panel by Locally Resonant Metamaterials. In: 2022, **Anais**... [s.l: s.n.]

BANERJEE, A.; DAS, R.; CALIUS, E. P. Waves in Structured Mediums or Metamaterials: A Review. **Archives of Computational Methods in Engineering**, [s. l.], v. 26, n. 4, p. 1029–1058, 2019.

BHATT, A.; BANERJEE, A. Flexural Wave Propagation in Rigid Elastic Combined Metabeam. **Journal of Vibration and Acoustics**, [s. l.], v. 145, n. 1, 2023.

BLEVINS, R. D. **Formulas for natural frequency and mode shape.**, 1979.

BLOCH, F. Uber die Quantenmechanik der Elektronen in Kristallgittern. **Zeitschrift fur Physik**, [s. l.], v. 52, n. 7–8, p. 555–600, 1929.

BOBROVNITSKII, Y. I. Letters To the Editor on the Energy Flow in Evanescent Waves. **Journal of Sound and Vibration**, [s. l.], v. 152, n. 1, p. 175–176, 1992.

BORN, M. Lattice dynamics and X-ray scattering. **Proceedings of the Physical Society**, [s. l.], v. 54, n. 4, p. 362–376, 1942.

BOUKADIA, R. F.; DECKERS, E.; CLAEYS, C.; ICHCHOU, M.; DESMET, W. A wave-based optimization framework for 1D and 2D periodic structures. **Mechanical Systems and Signal Processing**, [s. l.], v. 139, p. 106603, 2020.

BRAGG, W. H.; BRAGG, W. L. The reflection of X-rays by crystals. **Proceedings of the Royal Society of London. Series A, Containing Papers of a Mathematical and Physical Character**, [s. l.], v. 88, n. 605, p. 428–438, 1913.

BRENNAN, M. J. Control of flexural waves on a beam using a tunable vibration neutraliser. **Journal of Sound and Vibration**, [s. l.], v. 222, n. 3, p. 389–407, 1999.

BRENNAN, M. J.; ELLIOTT, S. J.; PINNINGTON, R. J. The dynamic coupling between piezoceramic actuators and a beam. **The Journal of the Acoustical Society of America**, [s. l.], v. 102, n. 4, p. 1931–1942, 1997.

BRENNAN, M. J.; FERGUSON, N. S. Vibration control. In: FAHY, F.; WALKER, J. (Eds.). **Advanced Applications in Acoustics, Noise and Vibration**. 1st. ed. [s.l.] : CRC Press, 2004. p. 530–580.

BRENNAN, M. J.; TANG, B. **Virtual Experiments in Mechanical Vibrations**. First ed. [s.l.] : John Wiley & Sons Ltd, 2023.

BRENNAN, M. J.; TANG, B.; ALMEIDA, F. C. L. Wave Motion in Elastic Structures. In: LOPES JUNIOR, V.; STEFFEN JR., V.; SAVI, M. (Eds.). **Dynamics of Smart Systems and Structures**. First ed. Cham: Springer International Publishing, 2016. p. 41–63.

BRILLOUIN, L. **Wave Propagation in Periodic Structures Electric Filters and Crystal Lattices**. 2. ed. [s.l.] : Dover Publications, Inc., 1953.

CARNEIRO JR., J. P.; BRENNAN, M. J.; GONÇALVES, P. J. P.; SOROKIN, V. S.; CLEANTE, V. G.; MACE, B. R. Controlling vibration propagation in a thin beam using a neutraliser. **Journal of Sound and Vibration**, [s. l.], v. 602, p. 118947, 2025.

CARNEIRO JR., J. P.; CLEANTE, V. G.; GONÇALVES, P. J. P.; BRENNAN, M. J. Attenuation of Vibration and Mass Reduction using a Finite Hollow Periodic Rod. In: 42ND IBERO-LATIN-AMERICAN CONGRESS ON COMPUTATIONAL METHODS IN ENGINEERING, CILAMCE 2021, **Anais**... [s.l: s.n.], 2021a

CARNEIRO JR., J. P.; CLEANTE, V. G.; GONÇALVES, P. J. P.; BRENNAN, M. J. Predicting attenuation characteristics on finite periodic pinned supported beam structures. In: PROCEEDINGS OF THE 26TH INTERNATIONAL CONGRESS OF MECHANICAL ENGINEERING 2021, **Anais**... : ABCM, 2021b.

CARNEIRO JR., J. P.; CLEANTE, V. G.; GONÇALVES, P. J. P.; BRENNAN, M. J. Strategies to enhance the attenuation band in finite beams using periodic attachments. In: INTER-NOISE AND NOISE-CON CONGRESS AND CONFERENCE PROCEEDINGS 2023, Auckland, New Zealand. **Anais**... Auckland, New Zealand. 2023.

CARNEIRO JR, J. P.; BRENNAN, M. J.; GONÇALVES, P. J. P.; CLEANTE, V. G.; BUENO, D. D.; SANTOS, R. B. On the attenuation of vibration using a finite periodic array of rods comprised of either symmetric or asymmetric cells. **Journal of Sound and Vibration**, [s. l.], v. 511, p. 116217, 2021.

CENEDESE, M.; BELLONI, E.; BRAGHIN, F. Interaction of Bragg scattering bandgaps and local resonators in mono-coupled periodic structures. **Journal of Applied Physics**, [s. l.], v. 129, n. 12, p. 124501, 2021.

CHENG Z.; SHI, Z.; CHENG, Z. B.; SHI, Z. F. Composite periodic foundation and its application for seismic isolation. **Earthquake Engineering and Structural Dynamics**, [s. l.], v. 47, n. 4, p. 925–944, 2017.

CLEANTE, V. G.; BRENNAN, M. J.; GONÇALVES, P. J. P.; CARNEIRO JR., J. P. On the formation of a super stop-band in finite mono-coupled periodic structures using an array of

vibration absorbers: Controlling parameters and physical insight. **Mechanical Systems and Signal Processing**, [s. l.], v. 180, 2022.

CLEANTE, V. G.; BRENNAN, M. J.; PAUPITZ GONÇALVES, P. J.; CARNEIRO JR., J. P. On the Formation of a Super Attenuation Band in a Mono-coupled Finite Periodic Structure Comprising Asymmetric Cells. In: [s.l: s.n.]. p. 703–712, 2023.

CREMER, L.; HECKL, M.; PETERSSON, B. A. T. **Structure-borne sound: Structural vibrations and sound radiation at audio frequencies**. 3 Ed. ed. Berlin. Germany: Springer, 2005.

CREMER, L.; HECKL, M.; UNGAR, E. E. **Structure-Borne Sound**. First ed. [s.l.] : Springer-Verlag Berlin Heidelberg GmbH, 1973.

CREMER, L.; LEILICH, H. O. Zur theorie der biegekettenleiter. **Archiv der elektrischen Ubertragung**, [s. l.], v. 7, p. 261–270, 1953.

CUNHA, L. R. **Robust bandgaps for vibration control in periodic structures**. 2017. Université Bourgogne Franche-Comté; Federal University of Uberlandia., [s. l.], 2017.

DA SILVA, C. A. X.; SOROKIN, V.; BRENNAN, M. J.; GONÇALVES, P. J. P. The dynamic behaviour of a finite periodic structure comprising either symmetric or asymmetric exponential- and conical-shaped rods. **Journal of Sound and Vibration**, [s. l.], p. 118741, 2024.

DAL POGGETTO, V. F.; SERPA, A. L. Flexural wave band gaps in a ternary periodic metamaterial plate using the plane wave expansion method. **Journal of Sound and Vibration**, [s. l.], v. 495, p. 115909, 2021.

DAO, G.; YOUHONG, S.; GUANGYU, L.; ZEGEN, W.; XIN, D.; WEIGUANG, S.; QIUSHI, W.; TENGFEI, W.; YUANJIN, J.; KAI, Z.; JINSONG, Z. Frequency veering between car body and under-chassis equipment of railway vehicles in vertical bending mode. **Mechanical Systems and Signal Processing**, [s. l.], v. 185, p. 109768, 2023.

DAYOU, J. Fixed-points theory for global vibration control using vibration neutralizer. **Journal of Sound and Vibration**, [s. l.], v. 292, n. 3–5, p. 765–776, 2006.

DOMADIYA, P. G.; MANCONI, E.; VANALI, M.; ANDERSEN, L. V; RICCI, A. Numerical and experimental investigation of stop-bands in finite and infinite periodic one-dimensional structures. **Journal of Vibration and Control**, [s. l.], v. 22, n. 4, p. 920–931, 2016.

DUHAMEL, D.; MACE, B. R.; BRENNAN, M. J. Finite element analysis of the vibrations of waveguides and periodic structures. **Journal of Sound and Vibration**, [s. l.], v. 294, n. 1–2, p. 205–220, 2006.

ECONOMOU, E. N.; SIGALAS, M. Stop bands for elastic waves in periodic composite materials. **The Journal of the Acoustical Society of America**, [s. l.], v. 95, n. 4, p. 1734–1740, 1994.

FABRO, A.; MENG, H.; CHRONOPOULOS, D. Correlated disorder in rainbow metamaterials for vibration attenuation. **Proceedings of the Institution of Mechanical Engineers, Part C: Journal of Mechanical Engineering Science**, [s. l.], v. 235, n. 14, p.

2610–2621, 2021.

FABRO, A. T.; FERGUSON, N. S.; MACE, B. R. Wave propagation in slowly varying waveguides using a finite element approach. **Journal of Sound and Vibration**, [s. l.], v. 442, p. 308–329, 2019.

FAHY, F.; GARDONIO, P. **Sound and Structural Vibration**. Second ed. [s.l.] : Elsevier, 2007.

FAHY, F.; WALKER, J. **Advanced Applications in Acoustics, Noise and Vibration**. [s.l.] : CRC Press, 2004.

FARAJIAN, M.; KHODAKARAMI, M. I.; SHARAFI, P. Effect of MetaFoundation on the Seismic Responses of Liquid Storage Tanks. **Applied Sciences 2022, Vol. 12, Page 2514**, [s. l.], v. 12, n. 5, p. 2514, 2022.

GARDONIO, P.; BRENNAN, M. J. On the origins ad development of mobility and impedance method in structural dynamics. **Journal of Sound and Vibration**, [s. l.], v. 249, n. 3, p. 557–573, 2002.

GARDONIO, P.; BRENNAN, M. J. Mobility and impedance methods in structural dynamics. In: FAHY, F.; WALKER, J. (Eds.). **Advanced Applications in Acoustics, Noise and Vibration**. 1. ed. London: Spon Press, 2004. p. 389–447.

GONÇALVES, P. J. P.; BRENNAN, M. J.; CLEANTE, V. G. Predicting the stop-band behaviour of finite mono-coupled periodic structures from the transmissibility of a single element. **Mechanical Systems and Signal Processing**, [s. l.], v. 154, 2021.

GONÇALVES, P. J. P.; BRENNAN, M. J.; ELLIOTT, S. J. Numerical evaluation of high-order modes of vibration in uniform Euler–Bernoulli beams. **Journal of Sound and Vibration**, [s. l.], v. 301, n. 3–5, 2007.

GONÇALVES, P. J. P.; PEPLOW, A.; BRENNAN, M. J. Exact expressions for numerical evaluation of high order modes of vibration in uniform Euler-Bernoulli beams. **Applied Acoustics**, [s. l.], v. 141, 2018.

GONSALEZ-BUENO, C. G. **An investigation into the way in which longitudinal and flexural waves interact with corrosion-like damage**. 2019. State University of São Paulo (UNESP). School of Engineering, [s. l.], 2019.

GOPALAKRISHNAN, S.; RAUT, M. S. Longitudinal wave propagation in one-dimensional waveguides with sinusoidally varying depth. **Journal of Sound and Vibration**, [s. l.], v. 463, p. 114945, 2019.

GRAFF, K. F. **Wave Motion in Elastic Solids**. First ed. [s.l.] : Dover Publications, Inc., 1991.

HAN, L.; ZHANG, Y.; NI, Z. Q.; ZHANG, Z. M.; JIANG, L. H. A modified transfer matrix method for the study of the bending vibration band structure in phononic crystal Euler beams. **Physica B: Condensed Matter**, [s. l.], v. 407, n. 23, p. 4579–4583, 2012.

HAO, S.; WU, Z.; LI, F.; ZHANG, C. Numerical and experimental investigations on the band-gap characteristics of metamaterial multi-span beams. **Physics Letters, Section A: General,**

Atomic and Solid State Physics, [s. l.], v. 383, n. 36, p. 126029, 2019.

HIBBELER, R. **Engineering Mechanics: Statics**. 14th. ed. [s.l.] : Pearson, 2015.

HOANG, T.; DUHAMEL, D.; FORET, G. Wave finite element method for waveguides and periodic structures subjected to arbitrary loads. **Finite Elements in Analysis and Design**, [s. l.], v. 179, p. 103437, 2020.

HOLLKAMP, J. P.; SEN, M.; SEMPERLOTTI, F. Analysis of dispersion and propagation properties in a periodic rod using a space-fractional wave equation. **Journal of Sound and Vibration**, [s. l.], v. 441, p. 204–220, 2019.

HU, G.; C. M. AUSTIN, A.; SOROKIN, V.; TANG, L. Metamaterial beam with graded local resonators for broadband vibration suppression. **Mechanical Systems and Signal Processing**, [s. l.], v. 146, p. 106982, 2021.

HULL, A. J.; CRAY, B. A. Response of infinite length rods and beams with periodically varying area. **Journal of Sound and Vibration**, [s. l.], v. 333, n. 20, p. 4960–4976, 2014.

HUSSEIN, M. I.; LEAMY, M. J.; RUZZENE, M. Dynamics of Phononic Materials and Structures: Historical Origins, Recent Progress, and Future Outlook. **Applied Mechanics Reviews**, [s. l.], v. 66, n. 4, 2014.

HUTTON, D. V. **Fundamentals of finite element analysis**. First ed. [s.l.] : McGraw-Hill Science/Engineering/Math, 2003.

IQBAL, M.; KUMAR, A. Analysis of bending waves and parametric influence on band gaps in periodic track structure. **Materials Today: Proceedings**, [s. l.], v. 113, p. 235–239, 2024.

JOHN, S. Strong localization of photons in certain disordered dielectric superlattices. **Physical Review Letters**, [s. l.], v. 58, n. 23, p. 2486–2489, 1987.

KELA, L.; VÄHÄOJA, P. Recent Studies of Adaptive Tuned Vibration Absorbers/Neutralizers. **Applied Mechanics Reviews**, [s. l.], v. 62, n. 6, 2009.

KIDNER, M.; BRENNAN, M. J. J. Improving the performance of a vibration neutraliser by actively removing damping. **Journal of Sound and Vibration**, [s. l.], v. 221, n. 4, p. 587–606, 1999.

KUSHWAHA, M. S. Classical band structure of periodic elastic composites. **International Journal of Modern Physics B**, [s. l.], v. 10, n. 09, p. 977–1094, 1996.

LAGE, Y. E.; NEVES, M. M.; MAIA, N. M. M.; TCHERNIAK, D. Force transmissibility versus displacement transmissibility. **Journal of Sound and Vibration**, [s. l.], v. 333, n. 22, p. 5708–5722, 2014.

LANGLEY, R. S. On the Modal Density and Energy Flow Characteristics of Periodic Structures. **Journal of Sound and Vibration**, [s. l.], v. 172, n. 4, p. 491–511, 1994. a.

LANGLEY, R. S. One-parameter scaling in weakly disordered one-dimensional systems. **Journal of Physics: Condensed Matter**, [s. l.], v. 6, n. 40, p. 8259–8268, 1994. b.

LANGLEY, R. S. On The Forced Response Of One-dimensional Periodic Structures: Vibration Localization By Damping. **Journal of Sound and Vibration**, [s. l.], v. 178, n. 3, p. 411–428, 1994. c.

LANGLEY, R. S.; BARDELL, N. S.; LOASBY, P. M. The optimal design of near-periodic structures to minimize vibration transmission and stress levels. **Journal of Sound and Vibration**, [s. l.], v. 207, n. 5, p. 627–646, 1997.

LEE, J.; THOMPSON, D. J. Dynamic stiffness formulation, free vibration and wave motion of helical springs. **Journal of Sound and Vibration**, [s. l.], v. 239, n. 2, p. 297–320, 2001.

LEI, Z.; LIU, T. Wave finite element method based on isogeometric analysis for periodic structures. **Journal of Physics D: Applied Physics**, [s. l.], v. 57, n. 24, p. 245301, 2024.

LEISSA, A. W. On a curve veering aberration. **Zeitschrift für angewandte Mathematik und Physik ZAMP**, [s. l.], v. 25, n. 1, p. 99–111, 1974.

LI, Y.; XIAO, Y.; GUO, J.; ZHU, Z.; WEN, J. Single-phase metabeam for three-directional broadband vibration suppression. **International Journal of Mechanical Sciences**, [s. l.], v. 234, p. 107683, 2022.

LI, Z.; WANG, X. Wave propagation in a dual-periodic elastic metamaterial with multiple resonators. **Applied Acoustics**, [s. l.], v. 172, p. 107582, 2021.

LIAO, L.; YAO, S.; ZHU, Y.; MA, R.; LI, Y. Topological design of hexagonal lattice phononic crystals for vibration attenuation combined fast plane wave expansion method with elite seed strategy genetic algorithm. **Results in Physics**, [s. l.], v. 59, p. 107562, 2024.

LIU, L.; HUSSEIN, M. I. Wave Motion in Periodic Flexural Beams and Characterization of the Transition Between Bragg Scattering and Local Resonance. **Journal of Applied Mechanics**, [s. l.], v. 79, n. 1, 2012.

LIU, X. L. Behaviour of Derivatives of Eigenvalues and Eigenvectors in Curve Veering and Mode Localization and their relation to close eigenvalues. **Journal of Sound and Vibration**, [s. l.], v. 256, n. 3, p. 551–564, 2002.

LIU, Z.; ZHANG, X.; MAO, Y.; ZHU, Y. Y.; YANG, Z.; CHAN, C. T.; SHENG, P. Locally Resonant Sonic Materials. **Science**, [s. l.], v. 289, n. 5485, p. 1734–1736, 2000.

LUO, H.; ZHANG, X.; LU, X.; CHEN, K. Bandgap analysis of partial-interaction composite beams periodically attached vibration absorbers. **International Journal of Mechanical Sciences**, [s. l.], v. 267, p. 109006, 2024.

MACE, B. R. Wave reflection and transmission in beams. **Journal of Sound and Vibration**, [s. l.], v. 97, n. 2, p. 237–246, 1984.

MACE, B. R.; CARNEIRO JR., J. P.; TOIT, D. Du; GONÇALVES, P. J. P.; SOROKIN, V. S.; BRENNAN, M. J.; CLEANTE, V. G. Energy transmission through finite periodic structures. In: 13TH INTERNATIONAL SYMPOSIUM ON VIBRATIONS OF CONTINUOUS SYSTEMS 2023, Alberta, Canada. **Anais**... Alberta, Canada.

MACE, B. R.; DUHAMEL, D.; BRENNAN, M. J.; HINKE, L. Finite element prediction of

wave motion in structural waveguides. **The Journal of the Acoustical Society of America**, [s. l.], v. 117, n. 5, p. 2835–2843, 2005.

MACE, B. R.; HALKYARD, C. R. Time domain estimation of response and intensity in beams using wave decomposition and reconstruction. **Journal of Sound and Vibration**, [s. l.], v. 230, n. 3, p. 561–589, 2000.

MAIA, N. M. M.; SILVA, J. M. M.; RIBEIRO, A. M. R. The transmissibility concept in multi-degree-of-freedom systems. **Mechanical Systems and Signal Processing**, [s. l.], v. 15, n. 1, p. 129–137, 2001.

MCMAHON, K. J. A Comparison of the Transfer Matrix Method and the Finite Element Method for the Calculation of the Transmission Loss in a Single Expansion Chamber Muffler by. **Tesis**, [s. l.], 2014.

MEAD, D. J. A general theory of harmonic wave propagation in linear periodic systems with multiple coupling. **Journal of Sound and Vibration**, [s. l.], v. 27, n. 2, p. 235–260, 1973.

MEAD, D. J. Wave propagation and natural modes in periodic systems: I. Mono-coupled systems. **Journal of Sound and Vibration**, [s. l.], v. 40, n. 1, p. 1–18, 1975. a.

MEAD, D. J. Wave propagation and natural modes in periodic systems: II. Multi-coupled systems, with and without damping. **Journal of Sound and Vibration**, [s. l.], v. 40, n. 1, p. 19–39, 1975. b.

MEAD, D. J. Structural wave motion. In: WHITE, R. G.; WALKER, J. G. (Eds.). **Noise and Vibration**. 1. ed. Southampton: Ellis Horwood, 1982. v. 1p. 207–226.

MEAD, D. J. **Passive Vibration Control**. London, England: John Wiley and Sons Ltd, 1999. a.

MEAD, D. J. Receptance and Dynamic Stiffness. In: **Passive Vibration Control**. First ed. [s.l.] : John Wiley & Sons Ltd, 1999. b. p. 71–98.

MEAD, D. J.; BANSAL, A. S. Mono-coupled periodic systems with a single disorder: Free wave propagation. **Journal of Sound and Vibration**, [s. l.], v. 61, n. 4, p. 481–496, 1978.

MEAD, D. J. M. Wave propagation in continuous periodic structures: research contributions from Southampton, 1964--1995. **Journal of sound and vibration**, [s. l.], v. 190, n. 3, p. 495–524, 1996.

MEAD, D. J.; WILBY, E. F. The random vibrations of a multi-supported heavily-damped beam. **The Shock and Vibration Bulletin**, [s. l.], v. 35, n. 3, p. 45–55, 1965.

MENCIK, J.-M. A wave finite element approach for the analysis of periodic structures with cyclic symmetry in dynamic substructuring. **Journal of Sound and Vibration**, [s. l.], v. 431, p. 441–457, 2018.

MENCIK, J.-M. M. New advances in the forced response computation of periodic structures using the wave finite element (WFE) method. **Computational Mechanics**, [s. l.], v. 54, n. 3, p. 789–801, 2014.

MESKOURIS, K.; BUTENWEG, C.; HINZEN, K.-G.; HÖFFER, R. **Structural Dynamics with Applications in Earthquake and Wind Engineering**. Berlin, Heidelberg: Springer Berlin Heidelberg, 2019.

MILES, J. W. Vibrations of Beams on Many Supports. **Journal of the Engineering Mechanics Division**, [s. l.], v. 82, n. 1, 1956.

MUHAMMAD; LIM, C. W. From Photonic Crystals to Seismic Metamaterials: A Review via Phononic Crystals and Acoustic Metamaterials. **Archives of Computational Methods in Engineering**, [s. l.], v. 29, n. 2, p. 1137–1198, 2022.

NEWTON, I. **Philosophiae naturalis principia mathematica**. [s.l.] : Jussu Societatis Regiae ac Typis Josephi Streater. Prostat apud plures bibliopolas, 1687.

NICOLETTI, R.; BACHOUR, R. S. Natural Frequencies and Band Gaps of Periodically Corrugated Beams. **Journal of Vibration and Acoustics**, [s. l.], p. 1–22, 2020.

NOBREGA, E. D.; GAUTIER, F.; PELAT, A.; DOS SANTOS, J. M. C. C. Vibration band gaps for elastic metamaterial rods using wave finite element method. **Mechanical Systems and Signal Processing**, [s. l.], v. 79, p. 192–202, 2016.

NUNES, A. W.; DA SILVA, S.; RUIZ, A. Exact general solutions for the mode shapes of longitudinally vibrating non-uniform rods via Lie symmetries. **Journal of Sound and Vibration**, [s. l.], v. 538, p. 117216, 2022.

O'HARA, G. J. Mechanical Impedance and Mobility Concept. **The Journal of the Acoustical Society of America**, [s. l.], v. 39, n. 6_Supplement, p. 1237–1237, 1966.

ORMONDROYD, J.; DEN HARTOG, J. P. The Theory of the Dynamic Vibration Absorber. **Transactions of the American Society of Mechanical Engineers**, [s. l.], v. 49–50, n. 2, 1928.

OSTACHOWICZ, W.; KUDELA, P.; KRAWCZUK, M.; ZAK, A. **Guided Waves in Structures for SHM**. [s.l: s.n.].

PARK, S.; YAN, R. F.; MATLACK, K. H. Characteristics of truncation resonances in periodic bilayer rods and beams with symmetric and asymmetric unit cells. **The Journal of the Acoustical Society of America**, [s. l.], v. 155, n. 2, p. 791–802, 2024.

RAGHAVAN, L.; PHANI, A. S. Local resonance bandgaps in periodic media: Theory and experiment. **The Journal of the Acoustical Society of America**, [s. l.], v. 134, n. 3, p. 1950–1959, 2013.

RAHIMI, F.; AGHAYARI, R.; SAMALI, B. Application of Tuned Mass Dampers for Structural Vibration Control: A State-of-the-art Review. **Civil Engineering Journal**, [s. l.], v. 6, n. 8, p. 1622–1651, 2020.

RAYLEIGH, R. S. On the maintenance of vibrations by forces of double frequency, and on the propagation of waves through a medium endowed with a periodic structure. **The London, Edinburgh, and Dublin Philosophical Magazine and Journal of Science**, [s. l.], v. 24, n. 147, p. 145–159, 1887.

ROSA, M. I. N.; DAVIS, B. L.; LIU, L.; RUZZENE, M.; HUSSEIN, M. I. Material vs.

structure: Topological origins of band-gap truncation resonances in periodic structures. **Physical Review Materials**, [s. l.], v. 7, n. 12, p. 124201, 2023.

ROSA, M. I. N.; GUO, Y.; RUZZENE, M. Exploring topology of 1D quasiperiodic metastructures through modulated LEGO resonators. **Applied Physics Letters**, [s. l.], v. 118, n. 13, 2021.

RUBIN, S. Mechanical Immittance- and Transmission-Matrix Concepts. **The Journal of the Acoustical Society of America**, [s. l.], v. 41, n. 5, p. 1171–1179, 1967.

RUGHUNANAN, L.; MACE, B.; SOROKIN, V.; DU TOIT, D. On the behaviour of infinite, periodic, mono-coupled waveguides using a transmission coefficient phase method. **Mechanical Systems and Signal Processing**, [s. l.], v. 135, p. 106409, 2020.

SALLEH, H.; BRENNAN, M. J. J. Control of flexural waves on a beam using a vibration neutraliser: Effects of different attachment configurations. **Journal of Sound and Vibration**, [s. l.], v. 303, n. 3–5, p. 501–514, 2007.

SANTOS, R. B. **An alternative approach to design periodic rods**. 2018. São Paulo State University (UNESP), School of Engineering, [s. l.], 2018.

SANTOS, R. B.; BERRES, G.; INMAN, D. J.; GONSALEZ-BUENO, C. G.; BUENO, D. D. A practical approach to evaluate periodic rods composed of cells with geometric and material periodicity. **Journal of Sound and Vibration**, [s. l.], v. 553, p. 117646, 2023.

SANTOS, R. B.; CARNEIRO JR., J. P.; GONSALEZ-BUENO, C. G.; LUCCA, B. S. De; BUENO, D. D. On the number of cells for flexural vibration suppression in periodic beams. **Meccanica**, [s. l.], v. 56, n. 11, p. 2813–2823, 2021.

SEN GUPTA, G. Natural flexural waves and the normal modes of periodically-supported beams and plates. **Journal of Sound and Vibration**, [s. l.], v. 13, n. 1, p. 89–101, 1970.

SEN GUPTA, G. Natural frequencies of periodic skin-stringer structures using a wave approach. **Journal of Sound and Vibration**, [s. l.], v. 16, n. 4, p. 567–580, 1971.

SHENG, P.; FANG, X.; WEN, J.; YU, D. Vibration properties and optimized design of a nonlinear acoustic metamaterial beam. **Journal of Sound and Vibration**, [s. l.], p. 115739, 2020.

SIGALAS, M. M.; ECONOMOU, E. N. Elastic and acoustic wave band structure. **Journal of Sound and Vibration**, [s. l.], v. 158, n. 2, p. 377–382, 1992.

SILVA, P. B. Dynamic analysis of periodic structures via wave-based numerical approaches and substructuring techniques. [s. l.], n. February, p. 192, 2015.

SILVA, T. M. P.; CLEMENTINO, M. A.; DE SOUSA, V. C.; DE MARQUI, C. An Experimental Study of a Piezoelectric Metastructure With Adaptive Resonant Shunt Circuits. **IEEE/ASME Transactions on Mechatronics**, [s. l.], v. 25, n. 2, p. 1076–1083, 2020.

STRUTT, J. W. **The Theory of Sound - Volume I**. London, England: Macmillan and CO., 1877.

SUGINO, C.; LEADENHAM, S.; RUZZENE, M.; ERTURK, A. On the mechanism of bandgap formation in locally resonant finite elastic metamaterials. **Journal of Applied Physics**, [s. l.], v. 120, n. 13, 2016.

TOIT, D. Du; MACE, B.; SOROKIN, V.; RUGHUNANAN, L. Control of bending wave transmission through an uncoupled force and moment neutraliser. **Journal of Sound and Vibration**, [s. l.], v. 508, p. 116219, 2021.

URGUEIRA, A. P. V.; ALMEIDA, R. A. B.; MAIA, N. M. M. On the use of the transmissibility concept for the evaluation of frequency response functions. **Mechanical Systems and Signal Processing**, [s. l.], v. 25, n. 3, p. 940–951, 2011.

WAKI, Y.; MACE, B. R.; BRENNAN, M. J. Numerical issues concerning the wave and finite element method for free and forced vibrations of waveguides. **Journal of Sound and Vibration**, [s. l.], v. 327, n. 1–2, p. 92–108, 2009.

WALLIS, R. F. Effect of Free Ends on the Vibration Frequencies of One-Dimensional Lattices. **Physical Review**, [s. l.], v. 105, n. 2, p. 540–545, 1957.

WANG, F.; LU, Y.; LEE, H. P.; MA, X. Vibration and noise attenuation performance of compounded periodic struts for helicopter gearbox system. **Journal of Sound and Vibration**, [s. l.], v. 458, p. 407–425, 2019.

WANG, G.; WAN, S.; HONG, J.; LIU, S.; LI, X. Enhancement of the vibration attenuation characteristics in local resonance metamaterial beams: Theory and experiment. **Mechanical Systems and Signal Processing**, [s. l.], v. 188, p. 110036, 2023.

WEI, J. PETYT, M. A method of analyzing finite periodic structures, part 2: comparison whit infinite periodic structure theory. **Journal of sound and vibration**, [s. l.], v. 202, p. 571–583, 1997.

XIAO, Y.; MACE, B. R.; WEN, J.; WEN, X. Formation and coupling of band gaps in a locally resonant elastic system comprising a string with attached resonators. **Physics Letters A**, [s. l.], v. 375, n. 12, p. 1485–1491, 2011.

XIAO, Y.; WEN, J. Closed-form formulas for bandgap estimation and design of metastructures undergoing longitudinal or torsional vibration. **Journal of Sound and Vibration**, [s. l.], v. 485, p. 115578, 2020.

XIAO, Y.; WEN, J.; WANG, G.; WEN, X. Theoretical and Experimental Study of Locally Resonant and Bragg Band Gaps in Flexural Beams Carrying Periodic Arrays of Beam-Like Resonators. **Journal of Vibration and Acoustics**, [s. l.], v. 135, n. 4, 2013. a.

XIAO, Y.; WEN, J.; WEN, X. Broadband locally resonant beams containing multiple periodic arrays of attached resonators. **Physics Letters A**, [s. l.], v. 376, n. 16, p. 1384–1390, 2012. a.

XIAO, Y.; WEN, J.; WEN, X. Flexural wave band gaps in locally resonant thin plates with periodically attached spring–mass resonators. **Journal of Physics D: Applied Physics**, [s. l.], v. 45, n. 19, p. 195401, 2012. b.

XIAO, Y.; WEN, J.; YU, D.; WEN, X. Flexural wave propagation in beams with periodically attached vibration absorbers: Band-gap behavior and band formation mechanisms. **Journal of**

Sound and Vibration, [s. l.], v. 332, n. 4, p. 867–893, 2013. b.

YABLONOVITCH, E. Inhibited Spontaneous Emission in Solid-State Physics and Electronics. **Physical Review Letters**, [s. l.], v. 58, n. 20, p. 2059–2062, 1987.

YEH, S. L.; HARNE, R. L. Origins of broadband vibration attenuation empowered by optimized viscoelastic metamaterial inclusions. **Journal of Sound and Vibration**, [s. l.], v. 458, p. 218–237, 2019.

YING, Z. G.; NI, Y. Q. Dynamic characteristics of infinite-length and finite-length rods with high-wave-number periodic parameters. **JVC/Journal of Vibration and Control**, [s. l.], v. 24, n. 11, p. 2344–2358, 2018.

YU, D.; LIU, Y.; ZHAO, H.; WANG, G.; QIU, J. Flexural vibration band gaps in Euler-Bernoulli beams with locally resonant structures with two degrees of freedom. **Physical Review B**, [s. l.], v. 73, n. 6, p. 064301, 2006.

YU, D.; WEN, J.; ZHAO, H.; LIU, Y.; WEN, X. Vibration reduction by using the idea of phononic crystals in a pipe-conveying fluid. **Journal of Sound and Vibration**, [s. l.], v. 318, n. 1–2, p. 193–205, 2008.

APPENDIX A. DETERMINATION OF THE TRANSFER MATRIX FOR A MONO-COUPLED PERIODIC STRUCTURE CONTAINING N CELLS (EQ. (3.13))

This appendix demonstrates how to obtain the transfer matrix in the form of Eq. (3.13), for the periodic structure as shown in the top part of Fig. 3.3, which consists of *N* mono-coupled identical cells. This method can be found in Gonçalves *et al.* (2021). The structure transmissibility matrix given in Eq. (2.15) can be written as $\mathbf{T}^{[\mathrm{str}]} = \left[\mathbf{T}^{[\mathrm{cell}]}\right]^N$. The Cayley-Hamilton theorem states that eigenvalues to the *N*-power ($\varphi_{1,2}^N$) are a linear combination of the eigenvalues $\varphi_{1,2}$. Now, the eigenvalues are related in that $\varphi_1 = \varphi$ and $\varphi_2 = 1/\varphi$, so that

$$\varphi_1^N = \varphi^N = a\left(\varphi + \frac{1}{\varphi}\right) + b\left(\varphi - \frac{1}{\varphi}\right) \tag{A.1a}$$

and

$$\varphi_2^N = \frac{1}{\varphi^N} = a\left(\varphi + \frac{1}{\varphi}\right) - b\left(\varphi - \frac{1}{\varphi}\right), \tag{A.1b}$$

where *a* and *b* are constants. Note that $\varphi + 1/\varphi = 2\cosh(\psi)$ and $\varphi - 1/\varphi = 2\sinh(\psi)$, because $\varphi = \mathrm{e}^{\psi}$ (see Sec. 2.4). Solving Eq. (A.1a,b) results in

$$a = \frac{\cosh(N\psi)}{2\cosh(\psi)} \quad \text{and} \quad b = \frac{\sinh(N\psi)}{2\sinh(\psi)}. \tag{A.2a,b}$$

Note that $\cosh\psi = \left(T_{\mathrm{LL}} + T_{\mathrm{RR}}\right)/2 = \Delta$, which is related to the eigenvalues of $\mathbf{T}$ by $\varphi_{1,2} = \Delta \pm \sqrt{\Delta^2 - 1}$.

Another consequence of the Cayley-Hamilton theorem is that Eqs. (A.1a,b) remain valid if either of the eigenvalues is replaced by $\mathbf{T}$, so that

$$\mathbf{T}^N = a\left[\mathbf{T} + \mathbf{T}^{-1}\right] + b\left[\mathbf{T} - \mathbf{T}^{-1}\right]. \tag{A.3}$$

Noting that $\mathbf{T}$ is the transfer matrix of a single cell, and $\mathbf{T}^{-1}$ is the inverse of this matrix, Eqs. (A.2a,b) and (A.3) combine to give

$$\mathbf{T}^{[\mathrm{str}]} = \mathbf{T}^N = \begin{bmatrix} \cosh(N\psi) - (T_{\mathrm{LL}} - T_{\mathrm{RR}})\dfrac{\sinh(N\psi)}{2\sinh(\psi)} & \dfrac{T_{\mathrm{LR}}\sinh(N\psi)}{\sinh(\psi)} \\ \dfrac{T_{\mathrm{RL}}\sinh(N\psi)}{\sinh(\psi)} & \cosh(N\psi) + (T_{\mathrm{LL}} - T_{\mathrm{RR}})\dfrac{\sinh(N\psi)}{2\sinh(\psi)} \end{bmatrix}. \tag{A.4}$$

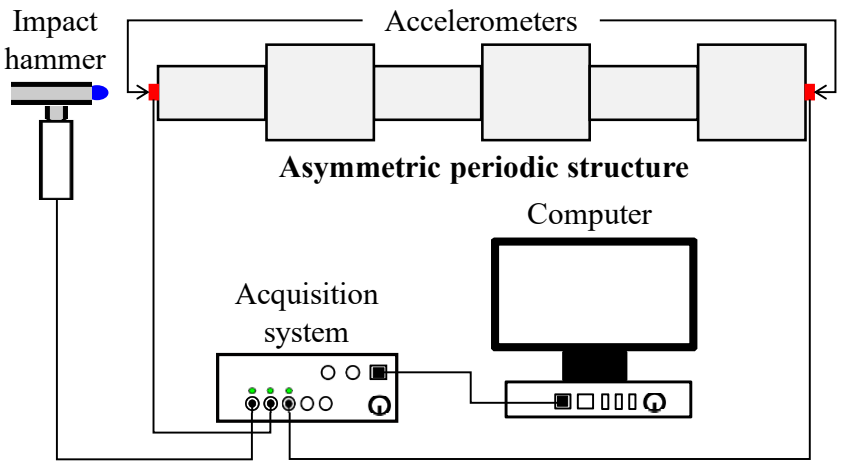
APPENDIX B. SUPPLEMENTARY DETAILS OF EXPERIMENTAL PROCEDURES AND ADDITIONAL RESULTS

This appendix presents the details of the experimental procedures conducted in the different systems discussed in this thesis. In all experiments detailed in this thesis and presented in this appendix, Young's modulus and loss factor properties were determined by fitting theoretical and experimental curves, *i.e.*, knowing the nominal values provided by manufacturers, these parameters were adjusted to best fit the frequency response curves measured. Density properties followed the manufacturers' nominal values, while lengths, widths, and thicknesses were measured directly using suitable conventional measuring instruments.

B.1. EXPERIMENTAL DETAILS FOR THE PROCEDURE ON A PERIODIC ROD COMPOSED OF THREE ASYMMETRICAL CELLS

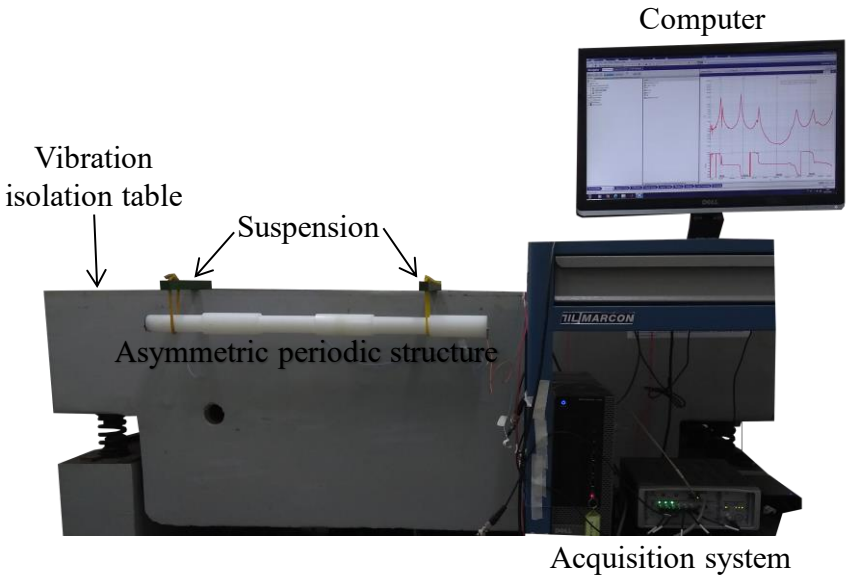
The experimental details of the procedure discussed in Sec. 3.3 are summarized in Tables B.1 and B.2. Figure B.1 and B.2 presents the experimental scheme and photograph setup.

Figure B.1. Schematic illustration of the experimental setup.



Source: author.

Figure B.2. Experimental setup photograph.



Source: author.

Table B.1. Experimental setup.

Equipment	Model
Impact hammer	PCB type 086C04
Accelerometer at left-end	Dytran type 3225F1
Accelerometer at right-end	PCB type 352A25
Acquisition system	LMS SCADAS mobile (Test Lab)
System setup	
Frequency resolution [Hz]	0.781
Bandwidth [Hz]	6400
Measurement averaging	10 impacts

Source: author.

Table B.2. Periodic rod properties

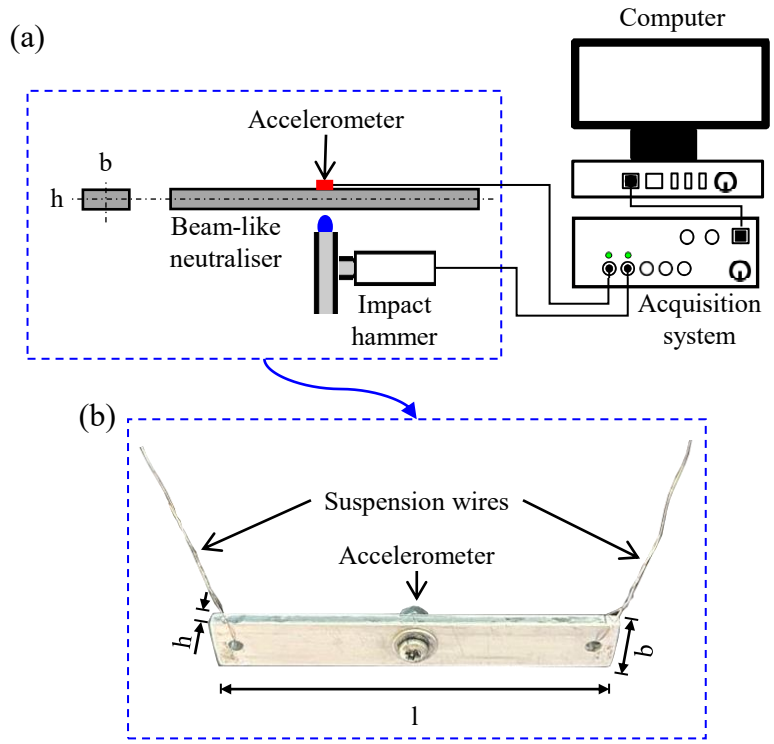
Property	Value	
	Segment a	Segment b
Young's Modulus [N/m^2]	$2.9x10^9$	
Density [kg/m^3]	1130	
Material loss factor	0.04	
Length [mm]	135	
Inner diameter [mm]	19.6	
Outer diameter [mm]	41	51

Source: author.

B.2. EXPERIMENTAL DETAILS FOR THE PROCEDURE ON A BEAM-LIKE VIBRATION NEUTRALISER

The experimental details of the procedure discussed in Sec. 4.3.1 are summarized in Tables B.3 and B.4. Figure B.3 presents the experimental setup for the characterisation of the neutraliser.

Figure B.3. Schematic illustration of the experimental setup



Source: author.

Table B.3. Equipment setup.

Equipment	Model
Impact hammer	PCB type 086E80
Accelerometer	PCB type 352C23
Acquisition system	Dewesoft
System setup	
Frequency resolution [Hz]	0.2
Bandwidth [Hz]	5000
Measurement averaging	10 impacts

Source: author.

Table B.4. Neutraliser properties.

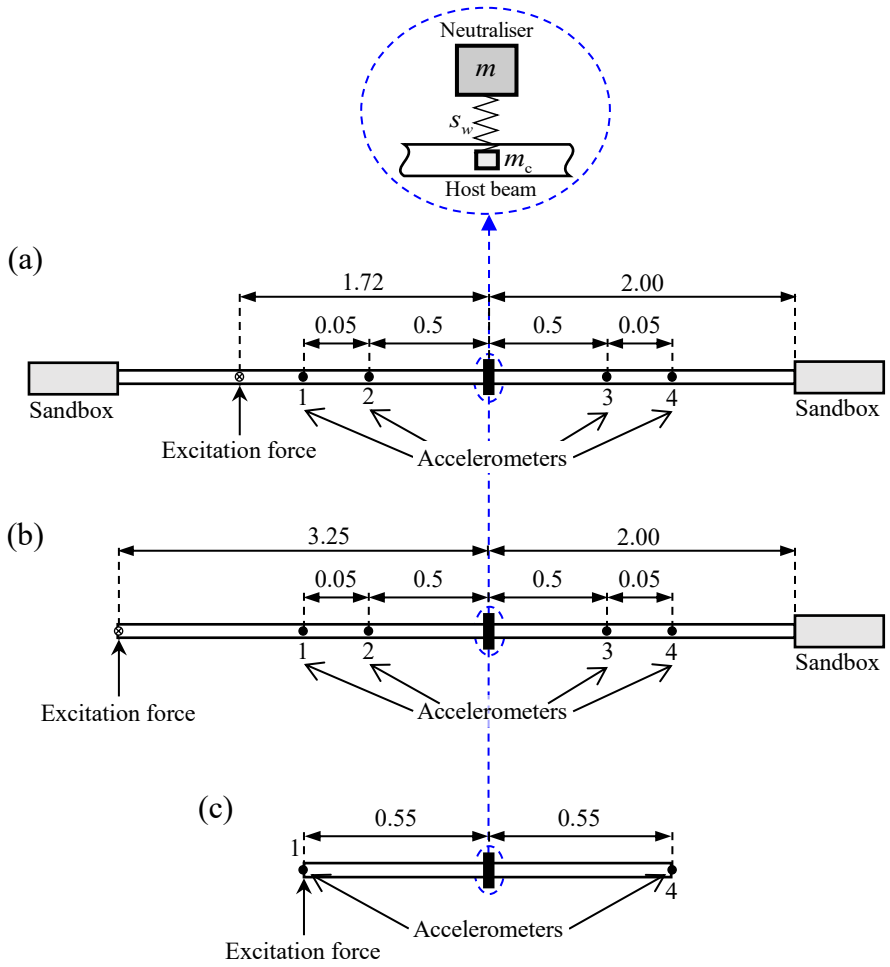
Property	Value
Young's Modulus [N/m^2]	$66x10^9$
Density [kg/m^3]	2700
Material loss factor	0.0018
Length (l) [mm]	79.4
Width (b) [mm]	12
Thickness (h) [mm]	3

Source: author.

B.3. EXPERIMENTAL DETAILS FOR THE PROCEDURE ON AN INFINITE, SEMI-INFINITE AND FINITE BEAM

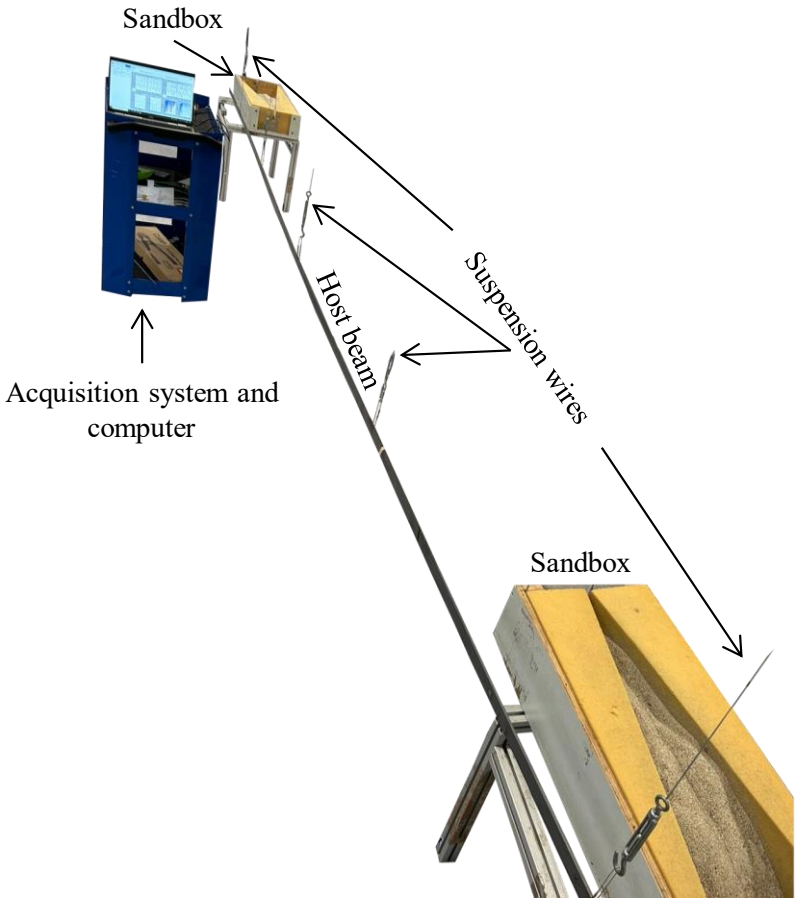
Figure B.4 shows the experimental setup for the host beam system with neutraliser, under the conditions with anechoic terminations and finite condition as discussed in Sec. 4.3.2. Figures B.5 and B.6 present photographs of the experimental setup. Tables B.5 and B.6 summarises the details of the experimental procedure.

Figure B.4. Experimental setup (not to scale) on a (a) infinite beam (sandbox at each end of the host beam), (b) semi-infinite beam (sandbox at one end of the host beam), and (c) finite beam.



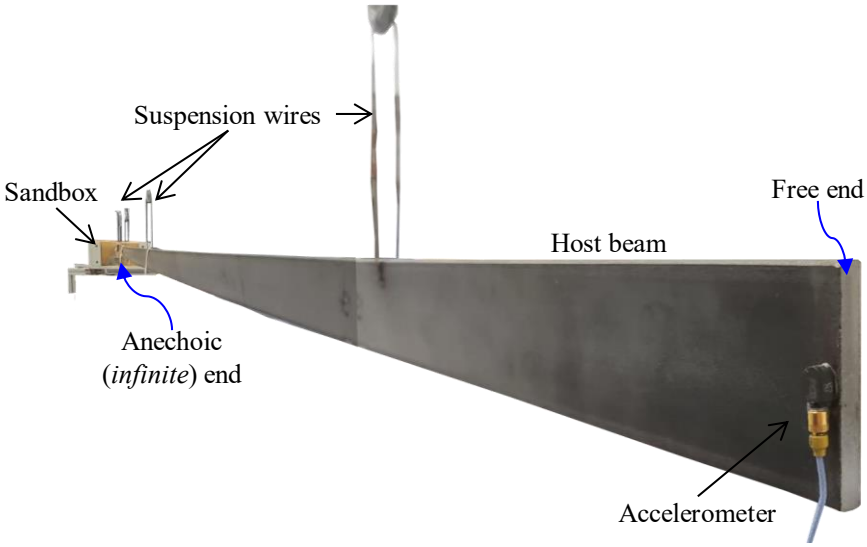
Source: author.

Figure B.5. Experimental setup photograph.



Source: author.

Figure B.6. Photograph demonstrating the arrangement for simulating semi-infinite boundary conditions.



Source: author.

Table B.5. Equipment setup.

Equipment	Model
Impact hammer	PCB type 086E80
Accelerometer	PCB type 352C23
Acquisition system	Data Physics QUATTRO
System setup	
Frequency resolution [Hz]	0.78
Bandwidth [Hz]	5000
Measurement averaging	10 impacts

Source: author.

Table B.6. Host beam properties.

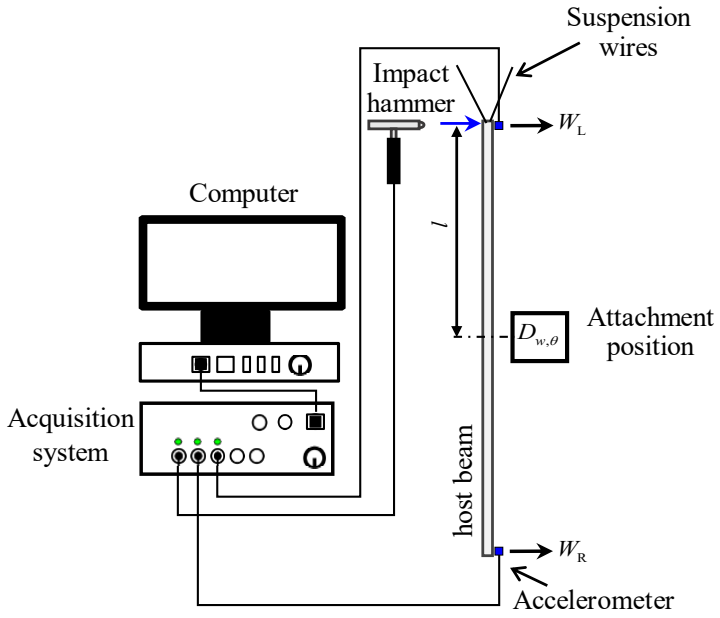
Property	Value
Young's Modulus [N/m^2]	$195x10^9$
Density [kg/m^3]	7500
Material loss factor	0.001
Length [m]	6
Width [mm]	40.5
Thickness [mm]	5

Source: author.

B.4. EXPERIMENTAL DETAILS FOR THE PROCEDURE ON THE FORMATION OF THE SUPER ATTENUATION BAND

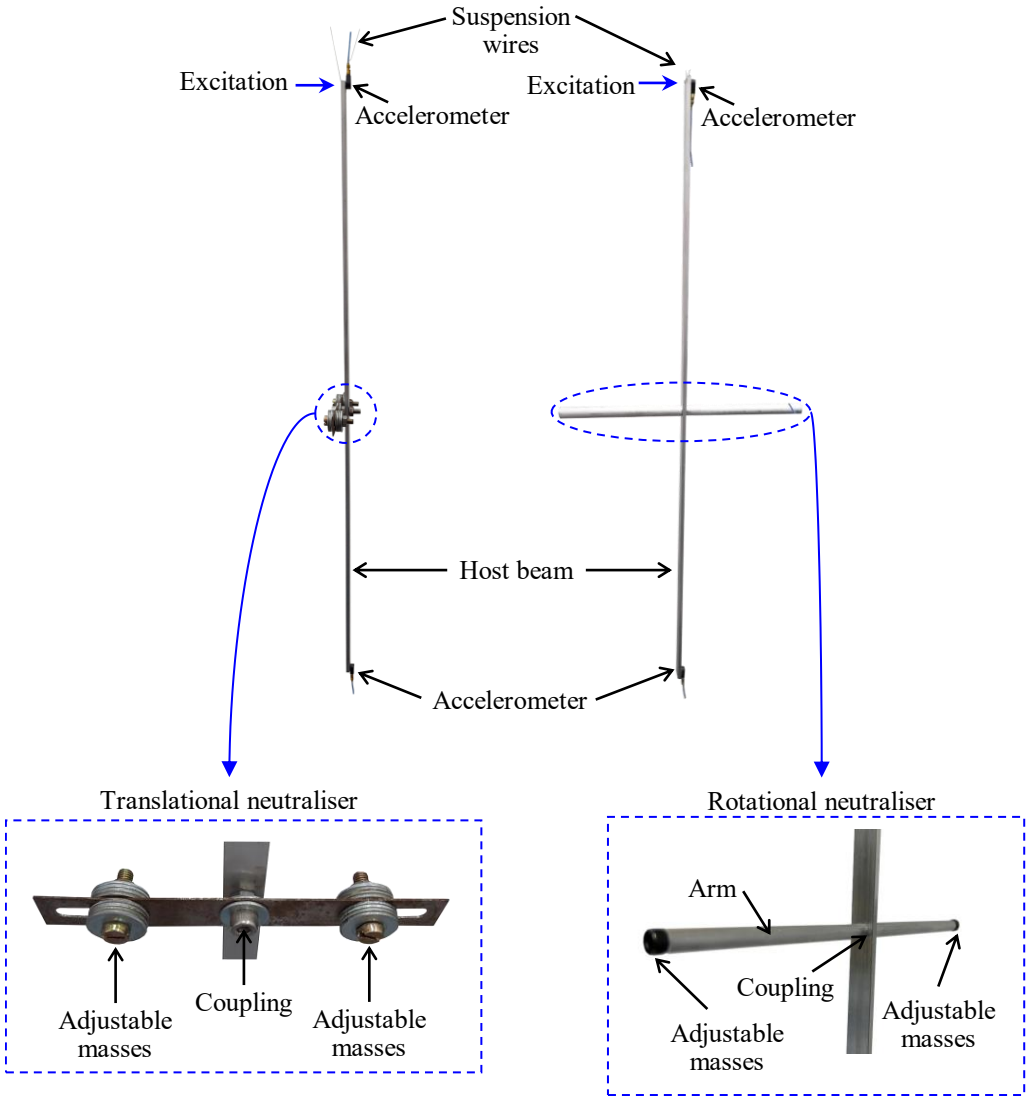
This section presents the experimental details for the experimental work discussed in Sec. 5.5, in which translational and rotational vibration neutralisers are attached in the centre point of a free-free beam and tuned to form the super attenuation band. Figure B.4 shows the experimental setup for the host beam system with neutraliser. Tables B.7 and B.8 summarises the details of the experimental equipment and devices.

Figure B.7. Experimental setup (not to scale) of a finite beam with attachments at its centre position.



Source: author.

Figure B.8. Photograph of the physical system used in the experiments with translational (left) and rotational (right) neutralizer. Dashed boxes show details of the coupled devices.



Source: author.

Table B.7. Equipment setup

Equipment	Model	
Impact hammer	PCB type 086C04	
Accelerometer	PCB type 332C22	
Acquisition system	LMS SCADAS (Test Lab)	
System setup		
Neutraliser type	Translational	Rotational
Frequency resolution [Hz]	0.125	0.976
Bandwidth [Hz]	512	8000
Measurement averaging	10 impacts	

Source: author.

Table B.8. Host beam and neutraliser properties.

Property	Value		
	Beam	Translational	Rotational
Young's Modulus [N/m^2]	68x10^9	195x10^9	70x10^9
Density [kg/m^3]	2700	7500	2700
Material loss factor	0.005	0.02 (δ) 0.002 (β)	0.004 (δ) 0.05 (β)
Length [m]	0.5	0.120	0.188
Width [mm]	12.60	14.9	
Thickness [mm]	3.15	1.55	
Inner diameter [mm]			6.3
Outer diameter [mm]			9.4

Source: author.

APPENDIX C. EFFECTS OF ATTACHING LUMPED PARAMETERS ON BEAMS

Chapter 4 investigated the effects of discontinuities in infinite and finite beams, using neutralisers to demonstrate these effects. In this appendix the investigation is presented in terms of simple lumped parameters to corroborate the theoretical development of the aforementioned chapter.

C.1. WAVE TRANSMISSION ACROSS DISCONTINUITIES IN AN INFINITE BEAM

This section and further discussions regarding different types of discontinuities in infinite beams through wave analysis can be found in the text book (MEAD, 1999a).

The magnitude of the wave transmitted across the discontinuity divided by the magnitude of the incident wave gives the transmission ratio, as shown in Fig. 4.2(b), and is expressed by Eqs. (4.11a,b), this is,

$$\frac{A_{\mathrm{t}}}{A_{\mathrm{i}}} = \frac{4 - \hat{D}_w}{4 - \hat{D}_w\left(1 + \mathrm{j}\right)} \quad \text{and} \quad \frac{A_{\mathrm{t}}}{A_{\mathrm{i}}} = \frac{4 + \hat{D}_\theta}{4 + \hat{D}_\theta\left(1 - \mathrm{j}\right)},$$

where $\hat{D}_w = D_w / EIk^3$ and $\hat{D}_\theta = D_\theta / EIk$ are normalised translational and rotational dynamic stiffnesses, respectively.

Equations (4.11a,b) make it possible to extract important insights into the behaviour of the beam subject to a translational or rotational discontinuity. Note that if the discontinuity is simple support (Eq. (4.11a)), the transverse motion will be zero at the attachment point, and the shear force the due to the incident wave will not transmit power into the right part of the beam, so if $\hat{D}_w \gg 4$, the modulus of the transmitted wave amplitude is $1/\sqrt{2}$ times the incident wave amplitude magnitude. A similar effect is observed in Eq. (4.11b) if the discontinuity prevents only rotational motion, so that the bending moment due to the incident wave does not transmit power.

As discussed in Sec. 4.2.2.1 the value of $1/\sqrt{2}$ can be reduced if the translational dynamic stiffness is real and positive, *i.e.*, it has stiffness-like behaviour, or the rotational dynamic stiffness is real and negative, so it portrays mass-like behaviour.

To illustrate this effect, consider as discontinuity a concentrated mass in Eq. (4.11a), such that $\hat{D}_w = -2\pi m/(\rho S\lambda)$, which is the ratio of the mass m, to the beam mass of approximately one-sixth of wavelength λ. The transmission ratio for this condition is shown in Fig. C.1 for the thick grey solid line. Note that at small values of $\hat{D}_w$, or low frequencies, the transmission tends to 1 or 0 dB. At large values of $\hat{D}_w$, or high frequencies, there is a maximum transmission reduction of -3 dB, *i.e.*, $|A_t/A_i| = 1/\sqrt{2}$.

Consider now that a grounded spring of stiffness s_w is attached to the beam, so $\hat{D}_w = s_w/EI\left(2\pi/\lambda\right)^3$ and the transmission ratio curve takes the form shown in the thin black line in Fig. C.1. In this case, for small values of $\hat{D}_w$, or high frequencies, there is no effective transmission reduction, but for large values of $\hat{D}_w$, or low frequencies, the resulting maximum transmission reduction is $|A_t/A_i| = 1/\sqrt{2}$.

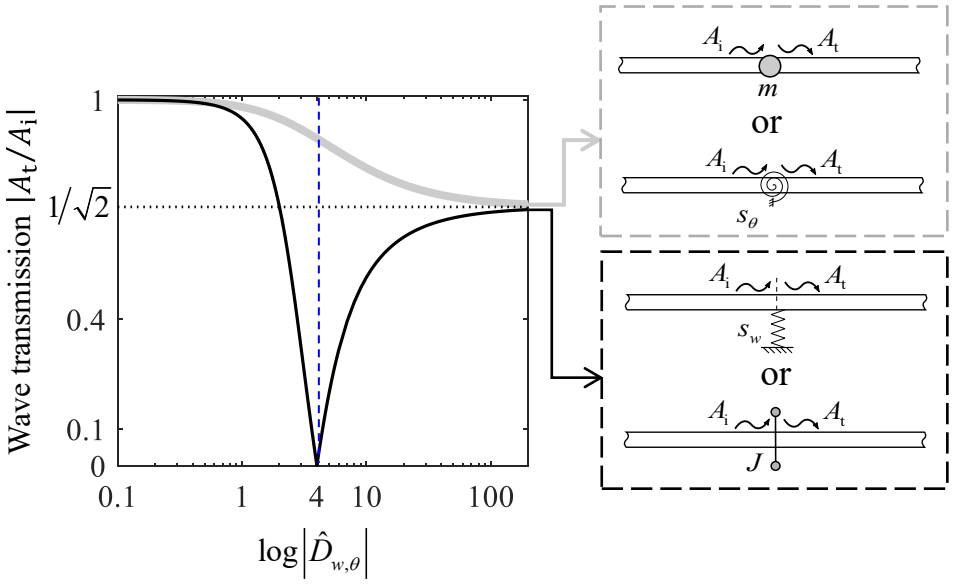
Assume now that the discontinuity consists of a grounded rotational spring of stiffness s_θ or a pure moment of inertia J with mass m. The non-dimensional dynamic stiffness of these elements can be written as $\hat{D}_\theta = s_\theta\lambda/(2\pi EI)$ or $\hat{D}_\theta = -J/[\rho S\left(\lambda/2\pi\right)^3]$. This rotational devices are also plotted in Fig. C.1. Setting these into Eq. (4.11b) results in an algebraic equivalence for the mass and grounded spring discontinuities, this is, the transmission ratio for a point mass-type discontinuity is algebraically equal to the transmission ratio for a grounded rotational spring-type discontinuity; in other words

$$\left|\frac{A_t}{A_i}\right|_m = \left|\frac{A_t}{A_i}\right|_{s_\theta} = \frac{4+\hat{D}_{w,\theta}}{\sqrt{\hat{D}_{w,\theta}^2+\left(4+\hat{D}_{w,\theta}\right)^2}}. \tag{C.1a}$$

Similarly, the transmission ratios for the inertial discontinuity is algebraically equal to the grounded translational spring discontinuity, so

$$\left|\frac{A_\mathrm{t}}{A_\mathrm{i}}\right|_{s_w} = \left|\frac{A_\mathrm{t}}{A_\mathrm{i}}\right|_{J} = \frac{4-\hat{D}_{w,\theta}}{\sqrt{\hat{D}_{w,\theta}^2+\left(4-\hat{D}_{w,\theta}\right)^2}}. \tag{C.1b}$$

Figure C.1. Wave transmission ratio for beam with discontinuity consisting of a concentrated mass or grounded rotational spring, thick grey line; and grounded translational spring or pure moment of inertia, thin black line.



Source: author.

Whatever it is, a large mass or a very stiff spring, at large values of $\hat{D}_{w,\theta}$ all motion associated with the respective discontinuity, transverse or rotational, is constrained and therefore behaves like a pinned or sliding support. However, the grounded translational spring and the inertia can, at a particular frequency, when $\left|\hat{D}_{w,\theta}\right| = 4$, effectively prevent all transversal and rotational motion. This condition is highlighted by the dip in the transmission ratio and can be easily interpreted by setting the numerator of Eqs. (4.11a,b) to 0. In fact, by solving these (as expressed in Eqs. (4.12a,b)), at this frequency, the translational spring resonates with the effective mass of the beam in the form of

$$\omega_w\big|_{\text{dip}} = \sqrt{\frac{s_w}{2\rho S\lambda/\pi}}\,. \tag{C.2a}$$

By solving $4-\hat{D}_\theta = 0$, the effective rotational stiffness of the beam resonates with the pure moment of inertia in the form,

$$\omega_\theta\big|_{\text{dip}} = \sqrt{\frac{8\pi EI/\lambda}{J}}\,. \tag{C.2b}$$

This effective mass, which is approximately 0.64 of the beam mass of one wavelength, is given by the real part of the point dynamic stiffness of the infinite beam excited with an harmonic force. The effective rotational stiffness, in turn, is obtained from the real part of the point dynamic stiffness of the infinite beam excited with an harmonic bending moment and corresponds to 8π times the beam stiffness of one wavelength.

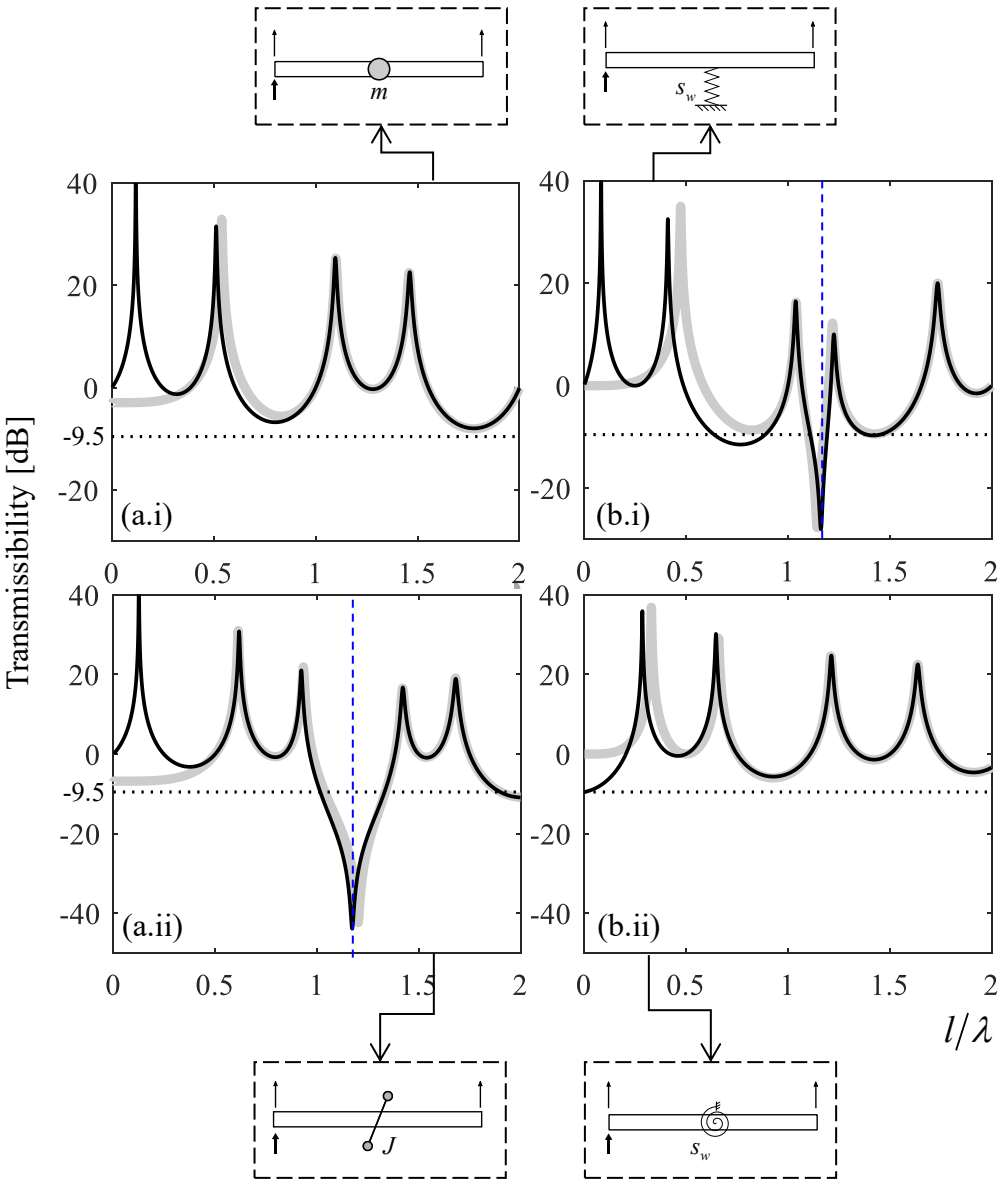
C.2. TRANSMISSIBILITY OF FINITE BEAM WITH EXTERNAL DISCONTINUITIES

The physical insight extracted from the previous wave-based analysis can also be inferred from the transmissibility analysis, as in Sec. 4.2.4. In this regard, consider the transmissibilities for the finite beam in Fig. 4.7 given by Eqs. (4.20a,b) and the approximated transmissibilities given by Eqs. (4.21a,b).

Assume in Eq. (4.21a) that $\hat{D}_w \to \infty$, this results in $|W_{\text{R}}/W_{\text{L}}| \approx 1/\left(1-2\sin\left(2kl\right)\right)$, which corresponds to the approximate transmissibility for the structure when the discontinuity consists of a pinned support. Note that, in this case, the minimum transmissibility value will be $1/3$ or approximately -9.5 dB. Now, assume in Eq. (4.21b) that $\hat{D}_\theta \to \infty$. In this case, Eq. (4.21b) can be written as $|W_{\text{R}}/W_{\text{L}}| \approx 1/\left(1+2\sin\left(2kl\right)\right)$. Again, the minimum transmissibility corresponds to $1/3$, but now the expression is equivalent to the approximate transmissibility of a structure where the discontinuity consists of sliding support.

To investigate each lumped parameter as in previous section, consider the translational dynamic stiffnesses given by the same expression, that is, $\hat{D}_w = -2\pi m/(\rho S\lambda)$ and $\hat{D}_w = s_w \big/ [EI\left(2\pi/\lambda\right)^3]$ for the mass and grounded spring, respectively. Consider also the rotational dynamic stiffnesses given by $\hat{D}_\theta = s_\theta \lambda/(2\pi EI)$ and $\hat{D}_\theta = -J\big/[\rho S\left(\lambda/2\pi\right)^3]$, for the grounded spring and rotary inertia, respectively. Figure C.2 presents transmissibility curves for these four discontinuities, as a function of the non-dimensional frequency parameter l/λ. It is assumed $m = \rho Sl$, $s_w = 1550\,EI/l^3$, $J = m\left(0.1l\right)^2$ and $s_\theta = 15.50\,EI/l$. As expected, only the translational grounded spring and the rotary inertia present local resonance behaviour. Note that, for the shown frequency range, the single concentrated mass and the rotational spring do not exceed the value $1/3$ (≈ -9.5 dB).

Figure C.2. Transmissibility for finite beams with different types of (a) mass-like and (b) stiffness-like behaviours. (i) Translational and (ii) rotational discontinuities. Complete transmissibility, Eqs. (4.20a,b), in grey thick lines and approximated form transmissibility, Eqs. (4.21a,b), in black thin lines.



Source: author.

APPENDIX D. THEORETICAL AND EXPERIMENTAL ANALYSIS OF BEAM-LIKE ROTATIONAL NEUTRALISER

The theoretical study of the factors that control vibration in beams presents the resonant interaction between the beam and a mass with rotational inertia. This interaction occurs from the resonance between the attached inertia (mass-like behaviour) and the effective stiffness of the host beam subject to the moment (spring-like behaviour). In fact, a condition observed in the frequency response function of the structure at which the transmission of wave through this element will be null and independent of the boundary condition after the moment of inertia, *i.e.*, the host beam can be finite, semi-infinite or infinite (see Chapter 4). This phenomenon has varied practical implications, mainly in terms of vibration attenuation. However, moving away from theoretical observation and evaluating real systems, the attached rotational element does not behave exclusively as a pure moment of inertia. This appendix discusses this effect and develops expressions that can be used to model a beam-like moment neutraliser.

D.1. THE PURE ROTARY INERTIA AND THE PRACTICAL BEHAVIOUR

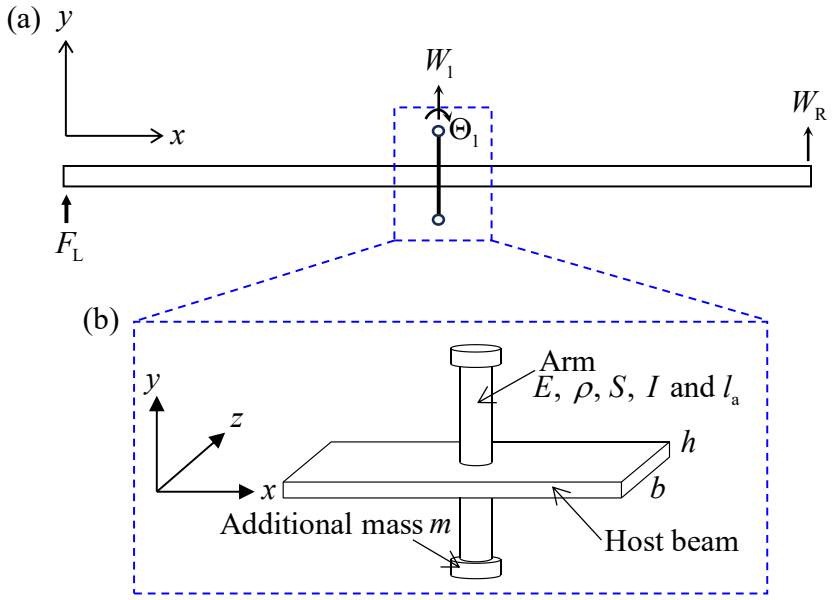
Consider that in a free-free slender beam, a mass with rotational inertia is attached at its central point. Figure D.1 presents the system and a detail in D.1(b). The host beam has a cross-section of width b and thickness h. At a point $x = 0$, far from the discontinuity, a source induces transverse excitation and the response is measured at the right end at $x = L$, where L is the beam length.

The attached device is composed of two parts, as shown in the force diagram in Fig. D.2. The first part refers to the arm with Young's Modulus E, density ρ, cross-sectional area S, second moment of area I and length l. The second part is an additional mass m at the free end. A concentrated mass m_c is assumed at the end coupled to the beam due to the translational reaction of the coupling and the mass of the device. Note that Fig. D.2 only highlights half of the element since it is symmetrical, but it must be considered that the total moment of inertia reacting to the movement of the host beam is given by the sum of the individual moments of each part of the element. Therefore, considering pure inertia, the dynamic stiffness matrix of the device at the coupling point will be given by

$$\begin{Bmatrix} F_1 \\ M_1 \end{Bmatrix} = \begin{bmatrix} D_w & 0 \\ 0 & D_\theta \end{bmatrix} \begin{Bmatrix} W_1 \\ \Theta_1 \end{Bmatrix}, \tag{D.1}$$

where W and Θ are, respectively, the transverse and rotational displacements at that point (1).

Figure D.1. Beam with a rotational device attached. (a) Schematic representation of the designed beam structure with imposed force and measured displacement. (b) Detail on the attached device.



Source: author.

The translational and rotational dynamic stiffnesses are

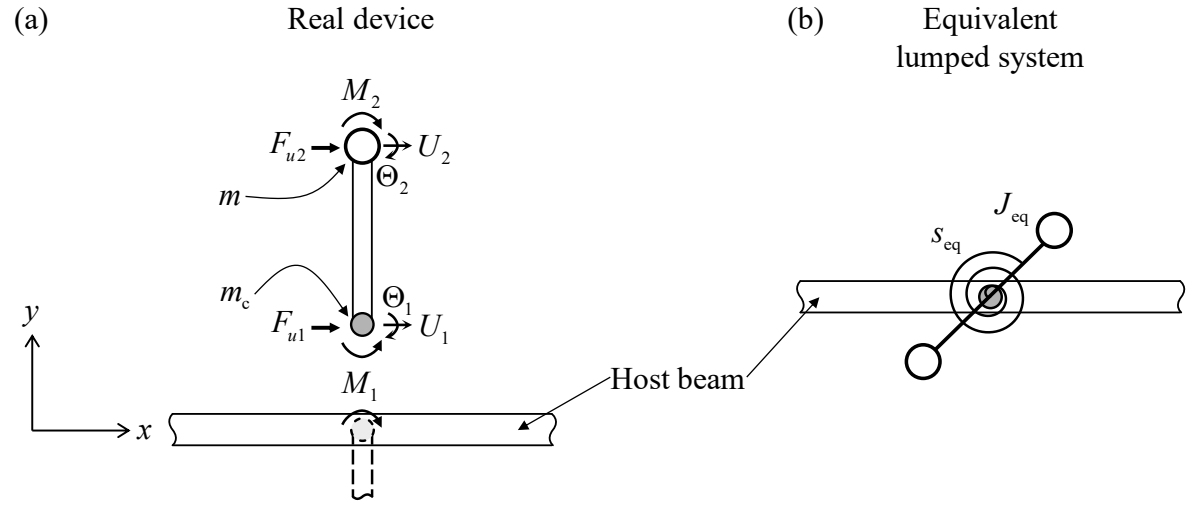
$$D_w = -\omega^2 m_c \tag{D.2a}$$

and

$$D_\theta = -\omega^2 \left(\frac{1}{3} \rho S l + m \right) l^2 . \tag{D.2b}$$

In other words, Eq. (D.2b) is given by the sum of effects of the arm and the additional mass. This moment of inertia of the arm is easily found in textbooks such as Hibbeler (2015), assuming the distance between the centre of gravity of this additional mass is l.

Figure D.2. Schematic representation of the beam-like moment resonator. (a) Real separated device diagram. (b) Approximated lumped system.



Source: author.

An experimental work is conducted in this system. The experimental setup is shown in Fig. D.3 and the beam and device properties are in Table D.1. In this case, the device was made with a threaded bar with a diameter of 4.4 mm, and the masses at the free end were composed of a set of nuts and washers. Figure D.4 presents the experimental results, in thin black lines, and theoretical results, in thick grey lines, for the bare host beam and for the beam system with the rotational inertia device attached. Theoretical transfer accelerances were obtained from the dynamic stiffness and receptance matrix method (see Chapter 2). The experimental FRF were obtained by the software SCADAS (Appendix B). The properties of Table 1 were assumed and the concentrated mass was given by $m_c = m + \rho Sl + m_n$, where m_n refers to the mass of the coupling washers and nuts (see Fig. D.3).

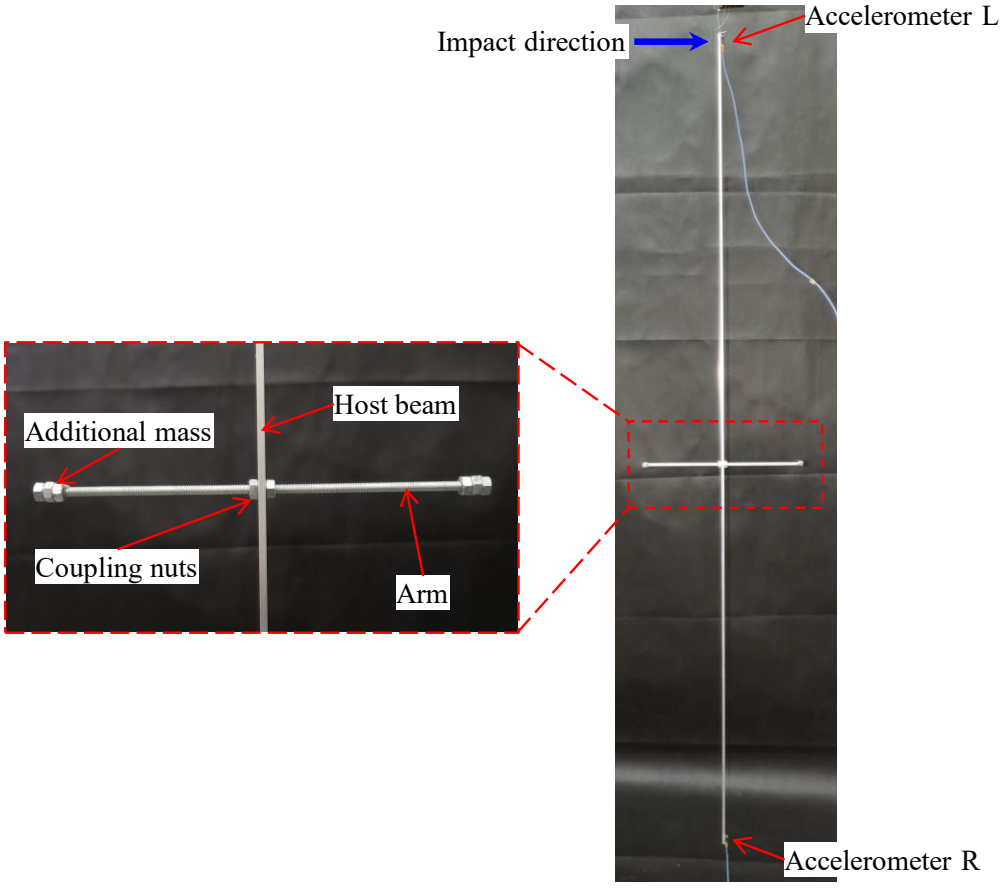
The results for the structure without discontinuity show excellent convergence, however, this convergence does not occur between the curves for the system with discontinuity. This significant difference between experimental results and theoretical predictions indicates that the real element does not behave as a pure moment of inertia. This is because the coupled device is not infinitely rigid, *i.e.*, the lumped element model does not consider the flexibility that the arm presents.

Table D.1. Properties of the host beam and attached device

Property	Value	
	Beam	Device
Young's Modulus [N/m^2]	70×10^9	195×10^9
Density [kg/m^3]	2700	8000
Material loss factor	0.005	0.005
Length [mm]	1000	184.9
Width [mm]	12.6	
Thickness [mm]	3.15	
Diameter [mm]		4.4
Masses [g]	53.6	3.3

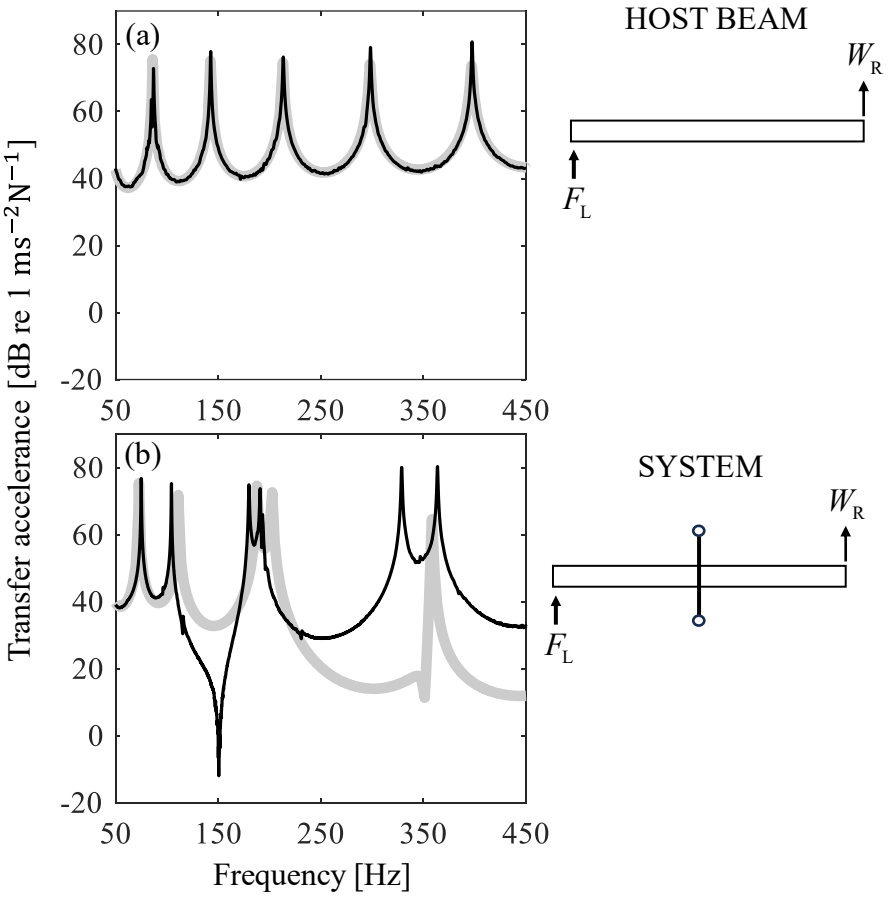
Source: author.

Figure D.3. Experimental setup and device details.



Source: author.

Figure D.4. Experimental and theoretical results comparison. (a) Bare host beam. (b) Beam with attached device system. Experimental transfer accelerance in thin black lines. Theoretical transfer accelerance in thick grey lines.



Source: author.

D.2. MODELLING THE BEAM-LIKE ROTATIONAL NEUTRALISER

Alternatively, the attached rotary inertia can be modelled as a continuous system. In this sense, the element is assumed to be an Euler-Bernoulli beam subject to the forces and displacement represented in Fig. D.2(a). The shear force on the host beam that acts at point 1 have the same intensity and opposite direction to the force indicated by Eq. (D.1) and applies to the device an axial motion in the y direction (F_1). The element is also subject to bending moments M_1 and M_2, in addition to translational forces F_{u1} and F_{u2} that induce displacements U_1 and U_2. Note that F_{u1} and U_1 correspond to the force and axial displacement acting on the host beam. The equation of motion in frequency domain is given by (HUTTON, 2003)

$$\left[\mathbf{K}-\omega^2\mathbf{M}\right]\mathbf{u}=\mathbf{f}\,, \tag{D.3}$$

where $\mathbf{u}=\{W_1,U_1,\Theta_1,W_2,U_2,\Theta_2\}^{\mathrm{T}}$ is the displacements vector, $\mathbf{f}=\{F_1,F_{u1},M_1,F_2,F_{u2},M_2\}^{\mathrm{T}}$ is the loads vector. The mass and stiffness matrices, described by the finite element method, are expressed by

$$\mathbf{M}=\frac{\rho Sl}{420}\begin{bmatrix} 140(3\mu_c+1) & 0 & 0 & 70 & 0 & 0 \\ 0 & 156 & 22l & 0 & 54 & -13l \\ 0 & 22l & 4l^2 & 0 & 13l & -3l^2 \\ 70 & 0 & 0 & 140(3\mu+1) & 0 & 0 \\ 0 & 54 & 13l & 0 & 12(35\mu+13) & -22l \\ 0 & -13l & -3l^2 & 0 & -22l & 4l^2 \end{bmatrix} \tag{D.4a}$$

and

$$\mathbf{K}=\frac{EI}{l^3}\begin{bmatrix} \chi & 0 & 0 & -\chi & 0 & 0 \\ 0 & 12 & 6l & 0 & -12 & 6l \\ 0 & 6l & 4l^2 & 0 & -6l & 2l^2 \\ -\chi & 0 & 0 & \chi & 0 & 0 \\ 0 & -12 & -6l & 0 & 12 & -6l \\ 0 & 6l & 2l^2 & 0 & -6l & 4l^2 \end{bmatrix}. \tag{D.4b}$$

The stiffness parameter $\beta = Sl^2/I$ expresses the ratio between the characteristic axial stiffness (ES/l) and the characteristic flexural stiffness (EI/l^3). The parameters $\mu = m/m_{\text{arm}}$ and $\mu_{\text{c}} = m_{\text{c}}/m_{\text{arm}}$ express the mass ratios of the additional mass and the concentrated mass to the arm mass $m_{\text{a}} = \rho Sl$, respectively.

Assuming that the axial motion in the host beam is negligible and that point 2 is free - therefore only the force F_1 and the bending moment M_1 act on the element. Applying these boundary conditions in Eq. (D.3), the system of equations can be solved by substitution, or another method. The resulting translational dynamic stiffness is given by

$$\frac{F_1}{W_1\left(EI/l^{\,3}\right)} = \frac{-\Omega^2\left[12\chi\left(1+\mu_{\text{c}}+\mu\right)-\Omega^2\left(1+4\mu_{\text{c}}+4\mu+12\mu_{\text{c}}\mu\right)\right]}{4\left(\chi-\Omega^2\left(1+3\mu\right)\right)} \tag{D.5a}$$

and the rotational dynamic stiffness

$$\frac{M_1}{\Theta_1\left(EI/l\right)} = \frac{-\Omega^2\left[\Omega^4\left(15\mu+1\right)+\Omega^2\left(39{,}600\mu-5{,}200\right)+4{,}536{,}000\mu+1{,}512{,}000\right]}{300\left[\Omega^4\left(1+12\mu\right)-72\Omega^2\left(17+70\mu\right)+15{,}120\right]}, \tag{D.5b}$$

where $\Omega^2 = \omega^2/\left(EI/l^3/m_{\text{arm}}\right)$ is a non-dimensional frequency parameter. Note that Equation (D.5a,b) is normalized to obtain the non-dimensional form of these dynamic stiffnesses. Equations (D.5a,b) provide the dynamic behaviour of the device under the described boundary conditions, and the powers and large coefficients indicate which parameters control the expressions.

Consider now that the mass matrix approximation

$$\mathbf{M} \approx \begin{bmatrix} \mu_c+1/3 & 0 & 0 & 0 & 0 \\ 0 & 0 & 0 & 0 & 0 \\ 0 & 0 & \mu+1/3 & 0 & 0 \\ 0 & 0 & 0 & \mu+1/3 & 0 \\ 0 & 0 & 0 & 0 & 0 \end{bmatrix}, \tag{D.6}$$

this is, setting to zero the matrix terms smaller than 1/3 of the mass of the arm. Solving Eq. (D.3) for this matrix and same boundary conditions, the approximated translational and rotational dynamics stiffnesses obtained will be given, respectively, by

$$\frac{F_1}{W_1\left(EI/l^{3}\right)}=\frac{-\Omega^2\left[3\chi\left(2+3\mu_c+3\mu\right)-\Omega^2\left(1+3\mu_c\right)\left(1+3\mu\right)\right]}{3\left[3\chi-\Omega^2\left(1+3\mu\right)\right]} \tag{D.7a}$$

and

$$\frac{M_1}{\Theta_1\left(EI/l\right)}=\frac{-3\Omega^2\left(\frac{1}{3}+\mu\right)}{3-\Omega^2\left(\frac{1}{3}+\mu\right)}. \tag{D.7b}$$

Note that if the characteristic flexural stiffness of the arm is sufficiently large such that $\Omega^2 \ll 1$, or at low frequencies, Eq. (D.7a,b) approaches respectively

$$\left.\frac{F_1}{W_1\left(EI/l^3\right)}\right|_{\text{High stiff.}} \approx -\Omega^2\left(\frac{2}{3}+\mu_c+\mu\right) \tag{D.8a}$$

and

$$\left.\frac{M_1}{\Theta_1\left(EI/l\right)}\right|_{\text{High stiff.}} \approx -\Omega^2\left(\frac{1}{3}+\mu\right). \tag{D.8b}$$

On the other hand, if the characteristic stiffness is very small $\Omega^2 \gg 1$, or at very high frequencies, Eq. (D.7a,b) approaches respectively

$$\left.\frac{F_1}{W_1\left(EI/l^3\right)}\right|_{\text{High-freq.}} \approx -\Omega^2\left(\frac{1}{3}+\mu_c\right) \tag{D.9a}$$

and

$$\left.\frac{M_1}{\Theta_1\left(EI/l\right)}\right|_{\text{High-freq.}} \approx 3\,. \tag{D.9b}$$

Equations (D.8a,b) and (D.9a,b) can be proven from the first-order series expansion, under the specified conditions. Note that the dynamic translational stiffness has mass-like behaviour (real part negative and dependent on frequency) in both conditions. Rotational dynamic stiffness, on the other hand, has mass-like behaviour when the stiffness is large or at low frequencies, with Eq. (D.8b) being equivalent to Eq. (D.2b), and spring-like behaviour (real part positive and independent on frequency) at high frequencies.

Figure D.5 shows the dynamic stiffness values for the developed expression, assuming the parameters presented in Table D.1 and $m_{\text{c}} = m_{\text{n}} = 4.3\ \text{g}$. This representation allows observation of the frequency regions where the device behaves like a mass or spring. Note that Eq. (D.7a,b) is an approximation of a single-DOF equivalent to a rotational vibration neutraliser. This approximation is valid because, as expected, the anti-resonance of the transfer acceleration occurs in the region where the discontinuity behaves like a mass with rotational inertia (approximately 150 Hz; see Fig. D.4(b)). Therefore, it can be assumed that the translational dynamic stiffness can be expressed using Eq. (D.9a) or in the dimensional form

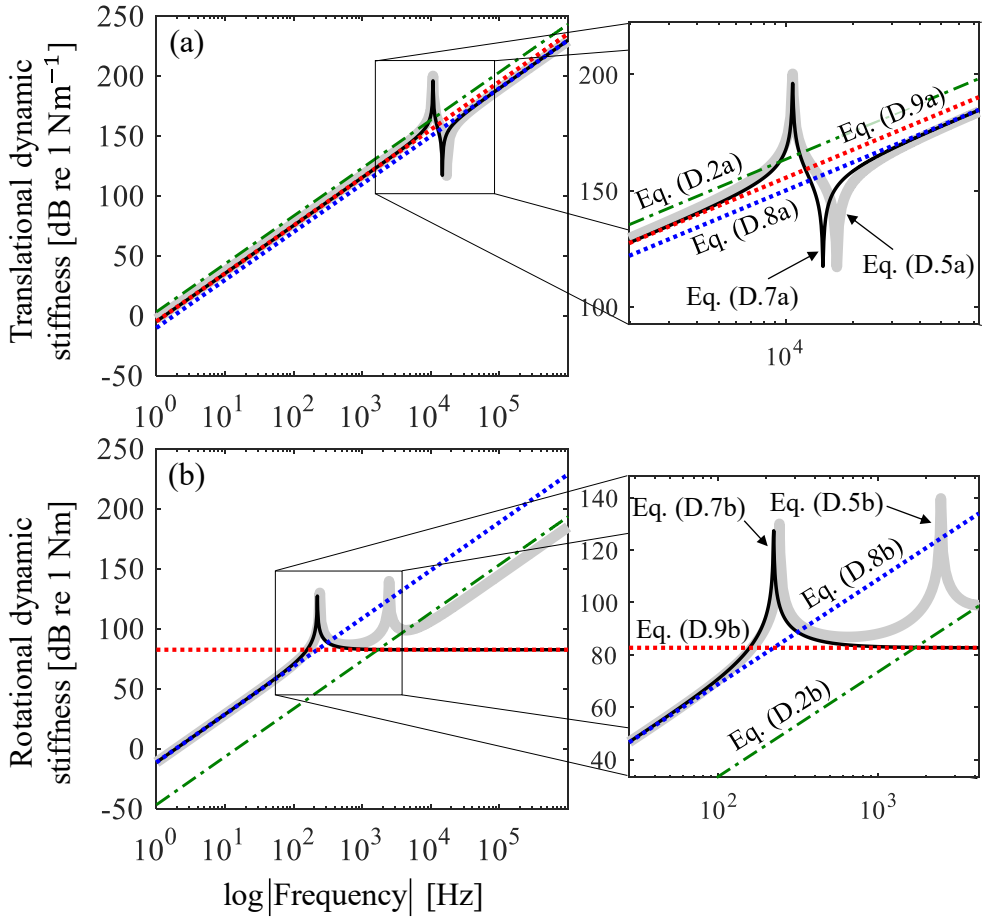
$$D_w = -\omega^2\left(m_{\text{arm}} + 3m_{\text{c}}\right) \tag{D.10a}$$

and the rotational dynamic stiffness is expressed by Eq. (D.7b) or in the dimensional form

$$D_\theta = \frac{-\omega^2 J_{\text{eq}} s_{\text{eq}}}{3s_{\text{eq}} - \omega^2 J_{\text{eq}}}\,, \tag{D.10b}$$

where $J_{\text{eq}} = \left(3m + m_{\text{arm}}\right)l^2$ is the equivalent mass moment of inertia and $s_{\text{eq}} = 3EI/l$ is the equivalent rotational stiffness.

Figure D.5. Different forms of the (a) translational and (b) rotational dynamic stiffnesses. Expressions given by Eqs. (D.2a,b) in dash-dot lines, Eqs. (D.5a,b) in solid grey thick lines, Eqs. (D.7a,b) in solid thin lines, Eqs. (D.8a,b) in blue dotted lines and Eqs. (D.9a,b) in red dotted lines.



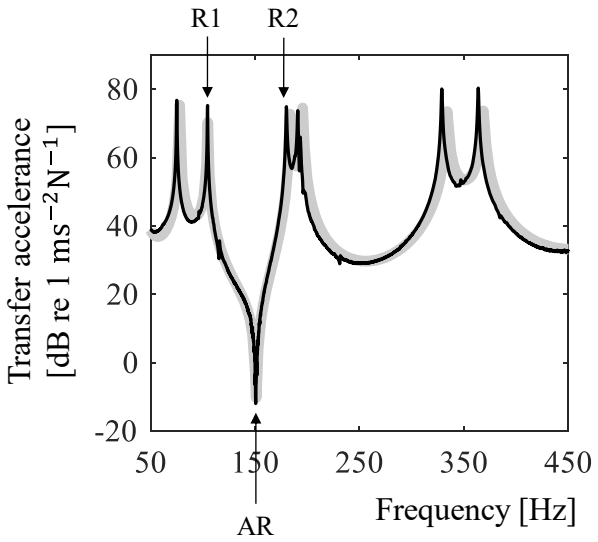
Source: author.

Equation (D.10) substituted into Eq. (D.1) provides the dynamic stiffness matrix that couples to the host beam. The simplified model is shown in Fig. D.2(b). A comparison of this theoretical model with the experimental results is shown in Fig. D.6, where the curves show excellent convergence. The experimental anti-resonance (AR) occurs at 150.6 Hz and the theoretical AR occurs at 151.8. The experimental resonances R1 and R2 occur respectively at 104.5 Hz and 180 Hz, respectively, whereas their theoretical pairs occur at 104.7 Hz and 183.6 Hz.

The discussions presented in these studies demonstrate that although a mass with pure rotational inertia alone produces the effect of local resonance, the rigidity of this element significantly interferes with the model and cannot be ignored. Hence, the resulting behaviour

is that of a moment vibration neutraliser, which can be tuned by adjusting the length of the device arm and the additional mass at the end. An alternative to approximate the neutraliser behaviour to pure inertia is to increase the relationship between the stiffness and mass of the arm, such as by using an arm with a tubular cross-section instead of a solid one.

Figure D.6. Experimental and theoretical results comparison for the system shown in Fig. D.3 and assuming the model expressed by Eq. (D.10). Experimental transfer accelerance in thin black line and theoretical transfer accelerance in thick grey lines.



Source: author.